Reviews in Mineralogy & Geochemistry
Vol. 60, pp. 83-219, 2006
Copyright © Mineralogical Society of America

Understanding the Lunar Surface and Space-Moon Interactions

Paul Lucey[1], Randy L. Korotev[2], Jeffrey J. Gillis[1], Larry A. Taylor[3], David Lawrence[4], Bruce A. Campbell[5], Rick Elphic[4], Bill Feldman[4], Lon L. Hood[6], Donald Hunten[7], Michael Mendillo[8], Sarah Noble[9], James J. Papike[10], Robert C. Reedy[10], Stefanie Lawson[11], Tom Prettyman[4], Olivier Gasnault[12], Sylvestre Maurice[12]

[1]University of Hawaii at Manoa, Honolulu, Hawaii, U.S.A.
[2]Washington University, St. Louis, Missouri, U.S.A.
[3]University of Tennessee, Knoxville, Tennessee, U.S.A.
[4]Los Alamos National Laboratory, Los Alamos, New Mexico, U.S.A.
[5]Smithsonian Institution, Washington D.C., U.S.A.
[6]Lunar and Planetary Laboratory, Univ. of Arizona, Tucson, Arizona, U.S.A.
[7]University of Arizona, Tucson, Arizona, U.S.A.
[8]Boston University, Cambridge, Massachusetts, U.S.A.
[9]Brown University, Providence, Rhode Island, U.S.A.
[10]University of New Mexico, Albuquerque, New Mexico, U.S.A.
[11] Northrop Grumman, Van Nuys, California, U.S.A.
[12]Centre d'Etude Spatiale des Rayonnements, Toulouse, France

Corresponding authors e-mail:
Paul Lucey <lucey@higp.hawaii.edu> *Randy Korotev <korotev@wustl.edu>*

1. INTRODUCTION

The surface of the Moon is a critical boundary that shapes our understanding of the Moon as a whole. All geologic mapping and remote sensing techniques utilize only the outermost portion of the Moon. Before leaving the Moon for study in our laboratories, all lunar samples that have been studied existed at or very near the surface. With the exception of the deeply probing geophysical techniques, our understanding of the interior of the Moon is derived from surficial, but not superficial, information, coupled with geologic reasoning. While the surface is the upper boundary of the lunar crust, it is the lower boundary layer of the tenuous lunar atmosphere and constitutes both a source and a sink for atmospheric gases. The surface is also where the Moon interacts with the space environment, causing changes in the physical nature of lunar materials, and provides a laboratory for the study of processes that occur on all airless bodies.

The data obtained remotely by the Galileo, Clementine, and Lunar Prospector missions, as well as data derived from lunar meteorites, have resulted in major changes to our understanding of global distributions of chemistry and rocks. This chapter summarizes the current understanding of this critical interface, the surface of the Moon, in its role as the lower boundary of the lunar atmosphere, the upper boundary of the crust, and the window through which we view, through remote sensing, the composition of the crust and the history of the Moon. In this post-Lunar Prospector time, the view of the Moon has changed, lending new perspectives to lunar samples and lunar processes. But the New View will likely remain in flux as we continue to digest the results from these recent space missions and move forward to a new era of lunar exploration.

1529-6466/06/0060-02$15.00 DOI: 10.2138/rmg.2006.60.2

Despite the freshness of our perspective, this is an important moment to capture, before the next generation of lunar scientists are forced to relearn old lessons. We can examine the new data through the lens of the Apollo era with its hard won lessons and years of anticipation of new data such as is now in our hands. We can attack these new data with tools forged for other missions that did not aim at the Moon. In addition to capturing a snapshot of rapidly evolving new scientific perspectives on the Moon, this Chapter will present an overview of the materials that constitute the surface of the Moon and its interior—its rocks and minerals and the regolith that constitutes the entire outer surface of the Moon. The new discoveries in the space weathering of the lunar soil aids the further understanding and quantification of the remotely sensed observations, and provide their ground-truth.

Of necessity, this chapter is a snapshot of a field in flux, but not a new field, one lacking introspection. An integration of data obtained during the last 30+ years is revealed herein. It will become apparent to the reader that new views of the Moon have been accrued by the coalition of several planetary science disciplines focused on a common cause, the science of the Moon.

Excellent and detailed reviews of lunar rocks, minerals, and soils have been presented in the *Lunar Sourcebook* (1991) and in *Planetary Materials* (1998). Readers seeking a more thorough treatment of these topics are referred to these monumental books.

2. THE LUNAR REGOLITH

Regolith is the term for the layer or mantle of fragmental and unconsolidated rock material, whether residual or transported and of highly varied character, that nearly everywhere forms the surface. This definition applies to the surface of all heavenly bodies, including the Moon and Earth. The entire lunar surface consists of a layer of regolith that completely covers the underlying bedrock, except perhaps on some very steep-sided crater walls and lava channels, where bedrock may be exposed. All samples collected by the Apollo and Luna Missions, as well as the lunar meteorites, are from the regolith; no "bedrock" was sampled directly in place. The lunar regolith is the product of the more than 4 billion years of impacts of meteoroids, big and small, into the Moon.

The lunar regolith is the boundary layer between the solid Moon and the matter and energy that fill the solar system. It contains information about both of these regions, and the complexities of studying the regolith are exceeded only by its importance to understanding the Moon and the space environment around it. The regolith is the source of virtually all our information about the Moon. All direct measurements of physical and chemical properties of lunar material have been made on samples collected from the regolith. Remotely sensed X-ray fluorescence, optical and infrared spectra, and gamma-ray signals come from the very top of the lunar regolith; in fact, from depths of no more than 20 μm, 1 mm, and 10–20 cm respectively (Adler et al. 1973; Metzger et al. 1973; Pieters 1983; Morris 1985). In addition, because of its surficial, unconsolidated, and fine-grained nature, it is likely that the regolith will be the raw material used for construction, mining, road building, and resource extraction when permanent lunar bases are established. As a resource, the lunar regolith is far more useful and accessible than the underlying "bedrock."

The lunar regolith also preserves information from beyond the Moon. Trapped in the solid fragments that make up the regolith are atoms from the Sun and cosmic-ray particles from beyond the solar system. In the regolith, data about the nature and evolution of the Moon are mixed with other records. These records include the composition and early history of the sun, and the nature and history of cosmic rays. The regolith also contains information about the rate at which meteoroids and cosmic dust have bombarded the Moon and, by inference, the Earth. Unscrambling these intertwined histories is a major challenge—and a major reward—of lunar research.

2.1. Some properties of lunar regolith and soil

We review here a few first-order properties of lunar regolith that are important for subsequent discussion. Although *soil* and *regolith* are terms that are sometimes used interchangeably, lunar *soil* usually refers to the fine portion of the regolith, operationally, the <1-mm grain-size fraction. Lunar soil is somewhat cohesive and dark gray to light gray in color. The mean grain size of lunar soils ranges from 40 to 800 μm and averages between 60 and 80 μm. Using conventional terrestrial descriptions, most lunar regolith samples would correspond to pebble- or cobble-bearing silty sands. Sorting values (the standard deviation of Folk 1968) range from 1.99 to 3.73 ϕ. In other words, lunar soils are poorly to very poorly sorted because mechanisms such as wind and water that sort terrestrial sediments do not occur on the Moon. There is also an inverse correlation between mean grain size and sorting (standard deviation); the coarsest samples are the most poorly sorted. Soils from all the Apollo sites are nearly symmetrically to coarsely skewed (skewness = 0–0.3). Exceptions to these generalizations are soils dominated by pyroclastic (volcanic) ash, which are finer-grained (mean grain sizes of ~40 μm) and better sorted ($\sigma = 1.6$ to 1.7 ϕ) than impact-produced soils.

The lunar regolith consists of fragments of igneous intrusive and extrusive rocks, crystalline impact-melt rocks that texturally resemble igneous rocks, various types of crystalline and glassy breccias produced by meteoroid impacts, mineral grains derived from rocks and breccias as a result of impact processes, glassy and crystallized spherules of volcanic origin, impact glass (spherules, ropy glass, glass coatings, glass fragments), meteorites, meteoritic metal, and agglutinates.

Agglutinates are a special and common lithic component of the lunar regolith, one that was unanticipated and that has no terrestrial analog, a direct result of the lack of an atmosphere on the Moon, which does not slow impinging micrometeorites. (Fig. 2.1). Each agglutinate particle is produced during the collision between a micrometeoroid traveling at 15–30 km/s and lunar regolith. Agglutinates, sometimes called glass-welded aggregates in early literature, consist of lithic and mineral fragments welded together by the glass formed as the small volume of resulting impact melt quenches. Agglutinates are mostly glassy, with complex morphologies and high vesicularity. The vesicles form from release of solar-wind implanted gases (Section 8) during the nearly instantaneous heating and melting of fined-grained surface regolith. Agglutinates make up a high proportion of the lithic fragments in lunar soils, about 25–30 vol% on average, although their abundances may range from essentially zero on the ejecta of a fresh impact crater to about 65 vol% in a mature soil (Section 9).

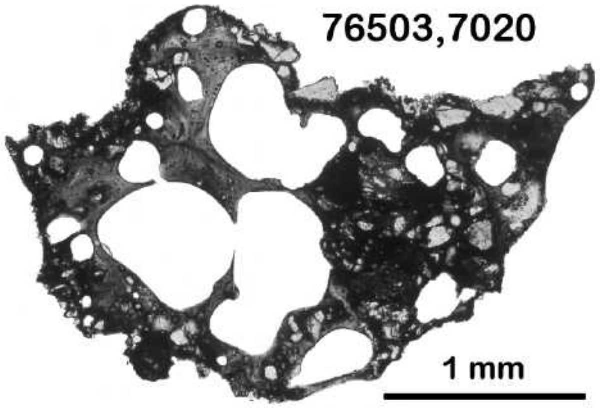

Figure 2.1. Photomicrograph of a thin section of an agglutinate from the Apollo 17 regolith (76503,7020; Jolliff et al. 1996). The particle is 3 mm in longest dimension. Most agglutinates are much smaller.

3. LUNAR SAMPLES

Nearly all of the direct information about the Moon's minerals, chemical composition, and age have been derived from samples. There are three classes of lunar samples available for study: (1) rocks and (2) soils collected on the six U.S. Apollo and three Russian Luna missions, and (3) lunar meteorites. A total of 382 kg of samples were collected on the Apollo missions (July, 1969, to December, 1972) and 0.3 kg on the Luna missions (September, 1970, to August, 1976). About 70% of the mass of the Apollo collection consists of rocks >1 cm in diameter; the rest is in the form of *fines* (<1 mm) and *coarse fines* (1–10 mm, but see Section 3.3). About 27 kg of lunar meteorites have been found to date (Section 3.2).

3.1. Apollo rock samples

In the study of terrestrial rocks, geologists typically collect samples by chipping, cutting, or drilling rocks that are several kilograms in mass from outcrops. As noted above (and perhaps with one exception, an Apollo 15 basalt), all lunar rock samples are isolated, loose rocks that were displaced by impacts from the locations where they originally formed. Most compositional and petrographic data that exist for lunar rocks are based on rocks that are small by terrestrial standards. Of the approximately 1500 numbered rocks collected on the Apollo missions (i.e., rocks >1 cm in diameter), 66 exceeded 1 kg in mass; the largest was 11.7 kg. About half (180 kg) of the total mass of material (382 kg) collected on the Apollo missions consists of >1-kg rocks. Of the numbered rock samples, the mean mass is about a quarter of a kilogram. Many of the numbered rocks, however, are less than a gram in mass. Tens of thousands of small lithic fragments (<1 cm) occur in the regolith samples and these have provided important information on the relative abundance of rock types in the regolith as well as a few unique types of rocks. The largest rock from the Luna missions is only about a gram in mass. Only 5 of ~37 lunar meteorites exceed 1 kg (some as more than one stone). Some rock types discussed here (e.g., alkali anorthosite and granite/felsite) are known only from small clasts in breccias or lithic fragments in the regolith. Before the discovery of the lunar meteorites, very low-Ti basalt was known only as small rock fragments.

For geochemical studies of terrestrial rocks, samples of several kilograms are pulverized and small subsamples of the resulting powder are analyzed to obtain data that are representative of the whole rock. In stark contrast, NASA has not pulverized any Apollo rocks and only small subsamples have been allocated to investigators for chemical analysis because of the rarity of lunar rocks. Most compositional data for lunar rocks have been obtained from fragments of a few tens of milligrams (sometimes smaller, e.g., Luna rocks) to, at most, a few grams (only for a few large Apollo rocks). Similarly, petrographic thin sections of all but the largest Apollo rocks are typically <1 cm^2 in area. For these reasons, compositional or petrographic results for different samples of a given "rock" can be expected to differ. The only lunar rock that is generally available in pulverized form is a portion of the MAC 88105 lunar meteorite (Lindstrom et al. 1991).

Each Apollo rock was given a 5-digit sample number. As an illustration, examples of some well known Apollo rock samples from each of the six missions are 10017 (Apollo 11 basalt), 12013 (Apollo 12 complex breccia), 14310 (Apollo 14 impact-melt rock), 15415 (Apollo 15 anorthosite), 65015 (Apollo 16 impact-melt breccia), and 72415 (Apollo 17 dunite). For the first four missions, the first two digits provide the key to the mission number; for the latter two missions, only the first digit provides the key. For Apollo 16 and 17, the second number represented the station at which the sample was collected. The last of the five numbers signifies the nature of the sample. Numbers of '5' and above represent rocks >1 cm; the number '0' refers to a soil, with '1' indicating the <1 mm sieved fraction, '2' the 1–2 mm fraction, '3' the 2–4 fraction, and '4' the 4–10 "rocklets." Luna samples provided to NASA for distribution use the same scheme, with numbers of the form 21xxx, 22xxx, and 24xxx representing the Luna 16, 20, and 24 missions, respectively.

3.2. Lunar meteorites

Since the end of the Apollo and Luna missions, numerous rocks have been found on Earth that are pieces of the Moon. All of the lunar meteorites known at this time (Table 2.1) are rocks that experienced a sequence of improbable events (Korotev et al. 2003a): They were blasted off the Moon by the impact of meteoroids, they eventually fell to Earth at remote locations (some up to several million years after they left the Moon), they were found by humans, and they were recognized to be of lunar origin. The first lunar meteorite to be so recognized was ALHA 81005 in 1982. Its identification as a piece of the Moon was uncontroversial (Marvin 1983 and other papers therein) because of our acquired experience with the Apollo and Luna samples. It is not known where on the Moon any of the lunar meteorites originated and it is not known with certainty how many impacts on the Moon launched the 37 currently known lunar meteorites (Table 2.1). The number of source craters is almost certainly a high fraction of the number of meteorites, however (Korotev et al. 2003b).

3.3. Lunar regolith and soil samples

During the Apollo and Soviet Luna missions, regolith samples were obtained with scoops, drive tubes, and rotary drill cores (Allton 1989). Apollo scoop samples were taken from near the surface (<10 cm depth) as well as from trenches as deep as 30 cm. Scoop and trench samples range in mass from tens of grams to several kilograms, although most are several hundred grams in mass. The number of distinct samples of surface and trench soils range from 2 at Apollo 11 to 68 at Apollo 17. With each successive Apollo mission, the distance separating the most distant collection points increased, from 10–30 m for Apollo 11 to 11 km for Apollo 17. A total of 24 drive tubes and cores (10 cm to 3 m in length) were taken on six Apollo missions and one on each of the three Luna missions. The compositional database for surface and trench soils is poorest for Apollo 12 and Apollo 15 samples.

As with the rocks, NASA assigned each scoop and trench sample and each core or drive tube section a unique 5-digit number. Some nominal samples of "soil" are fines derived largely from a disaggregation of a single rock or abrasion of rocks after collection (e.g., samples 10011, 12057, 67700, 73130, 76320), not true regolith. Most Apollo scoop and trench samples were passed through sieves of 10 mm, 4 mm, 2 mm, and 1 mm mesh size in the curatorial facility at the NASA Johnson Space Center. Each of the sub-cm grain-size fractions was assigned a new sample number and any fragment that was held by the 1-cm sieve was treated as a "rock" and given a unique sample number. In this section, "sample" is usually reserved for a mass of regolith with a distinct NASA 5-digit sample number. "Subsample" refers to that small portion of a sample allocated to an investigator or analyzed by some technique. Because of concerns about contamination and sample rarity, NASA did not pulverize or split by conventional sample splitting techniques masses of soil prior to allocation.

Soil from some regolith cores and drive tubes was also passed through a 0.25-mm sieve, and some investigators sieved or otherwise sized the <1-mm material in their own laboratories to obtain sub-millimeter grain-size fractions (e.g., McKay et al. 1974; Laul et al. 1988). Most chemical and physical measurements on lunar soil have been made only on subsamples of material that passed through a 1-mm sieve, i.e., the *<1-mm fines* or *fine fines*. Unless otherwise stated, nearly all available compositional data are based on subsamples of <1-mm fines. For the Luna samples and Apollo core samples, data are usually for <0.25-mm fines, however. Most petrographic data are only for grain-size fractions of even an narrower range, e.g., 90–150 μm (e.g., Heiken et al. 1973; Heiken and McKay 1974).

Coarse fines is a term that has been used to refer to both 1–10-mm and 4–10-mm material. With few exceptions (e.g., Jolliff et al. 1991a, 1996), data for bulk composition or other bulk properties of material in the 1–2 mm, 2–4 mm, and 4–10-mm grain-size fractions are nonexistent because of the problem of obtaining small, representative samples of coarse-

Table 2.1. List of lunar meteorites and some of their properties, in approximate order of increasing Al_2O_3 concentration, as of October 2005 (after Korotev et al. 2003b).

N	**name**	**lunar rock type**	**mass (g)**	**TiO$_2$ (%)**	**Al$_2$O$_3$ (%)**	**FeO (%)**	**MgO (%)**	***Mg´* (%)**	**Th µg/g**
mare basalts									
1	Dhofar 287	mare basalt &	154	*2.8*	*8.4*	*22.*	*13.*	*52.*	*0.9*
		regolith breccia		n.a.	n.a.	n.a.	n.a.	n.a.	n.a.
2	Northwest Africa 032/479	mare basalt	~456	3.1	9.2	22.	7.8	39.	2.0
3	Asuka 881757	mare basalt	442	2.4	9.8	23.	6.3	33.	0.4
4	LAP/02205/02224/02226/ 02436/03632	mare basalt	1875	3.2	9.9	22.	6.3	34.	2.0
5	Yamato 793169	mare basalt	6	2.2	10.8	22.	5.9	33.	0.7
KREEP impact-melt breccia									
6	Sayh al Uhaymir 169	impact-melt breccia &	206	2.2	15.9	10.7	11.1	65	32.7
		regolith breccia		2.5	17.4	11.1	7.9	56	8.4
"mixed"(feldspathic-basaltic) breccias									
7	Northwest Africa 773	olivine gabbro &	633	0.3	4.7	19.4	26.3	71.	1.3
		regolith breccia		0.9	9.0	19.0	13.6	56.	2.1
8	Kalahari 008/009	fragmental breccia &	13,500	n.a.	13.	16.	8.5	49.	n.a.
		regolith breccia	598	n.a.	28.	4.5	4.4	64.	
9	EET 87521/96008	fragmental breccia	84	0.8	14.	18.	8.	43.	0.9
10	Northwest Africa 3136	regolith breccia	95	1.2	14.	15.	10.	55.	1.3
11	QUE 94281	regolith breccia	23	0.7	16.	14.	8.3	52.	0.9
12	MET 01210	regolith breccia	23	1.6	17.	16.	6.1	40.	0.9
13	Yamato 793274/981031	regolith breccia	195	0.7	18.	12.	8.9	56.	1.1
14	Calcalong Creek	regolith breccia	19	0.8	21.	9.	*8.*	*60.*	4.
15	Yamato 983885	regolith breccia	289	0.5	22.	9.	8.	62.	2.
feldspathic breccias									
16	ALHA 81005	regolith breccia	31	0.27	25.9	5.5	8.2	73.	0.31
17	Yamato 791197	regolith breccia	52	0.34	26.2	6.2	6.1	64.	0.34
18	Northeast Africa 001	regolith breccia	262	0.27	26.4	5.6	5.6	64.	0.24
19	PCA 02007	regolith breccia	22	0.29	26.5	6.2	6.9	66.	0.41
20	Dhofar 025/301/304/308	regolith breccia	772	0.30	27.	4.9	6.6	71.	0.6
21	"specimen 1153"	regolith breccia	?	*0.18*	*27.*	*5.2*	*3.9*	*57.*	n.a.
22	Dar al Gani 262	regolith breccia	513	0.21	27.9	4.5	5.5	68.	0.39
23	QUE 93069/94269	regolith breccia	25	0.25	28.3	4.4	4.6	65.	0.52
24	Yamato 82192/82193/86032	fragm. or reg. breccia	712	0.19	28.5	4.4	5.2	68.	0.20
25	Dar al Gani 400	regolith breccia	1425	0.18	28.5	3.6	4.8	70.	0.34
26	MAC 88104/88105	regolith breccia	724	0.24	28.7	4.3	4.1	63.	0.39
27	Dhofar 026/457–468	granulitic breccia	709	0.2	28.8	4.3	4.8	67	0.39
28	Northwest Africa 482	impact-melt breccia	1015	0.17	29.1	3.8	4.2	66.	0.23
29	Dhofar 302/303/305/306/307/ 309/310/311/489/730/731/ 908/909/911/950/1085	impact-melt breccia	1041	*0.14*	*29.*	*3.*	*5.*	*75.*	*0.06*
30	Dhofar 081/280/910/1224	fragmental breccia	572	*0.12*	*32.*	*3.1*	*2.6*	*60.*	*0.2*
31	Dar al Gani 996	fragmental ? breccia	12	n.a.	n.a.	n.a.	n.a.	n.a.	n.a.
32	Dhofar 490/1084	fragmental breccia	124	n.a.	n.a.	n.a.	n.a.	n.a.	n.a.
33	Dhofar 733	granulitic? breccia	459	n.a.	n.a.	n.a.	n.a.	n.a.	n.a.
34	Dhofar 925/960/961	impact melt ? breccia	106	n.a.	n.a.	n.a.	n.a.	n.a.	n.a.

ALHA = Allen Hills, EET = Elephant Moraine, LAP = LaPaz Icefield, MAC = MacAlpine Hills, MET = Meteorite Hills; PCA = Pecora Escarpment, QUE = Queen Alexandra Range. Multiple meteorites listed on the same line are known or suspected to be terrestrially paired (different fragments of a single meteorite fall); other unrecognized pairings might exist. In particular, pairing relationships among the various Dhofar meteorites are not well established. Concentration values in italics are uncertain. *Mg´* = bulk mole % Mg/(Mg+Fe). Data from many literature sources and unpublished data (R. L. Korotev).

grained material. Many properties of lunar soil, e.g., composition and spectral reflectance (Sections 9.5, 10.4.4), are a function of grain size. Thus for some purposes, data derived from the <1-mm *fines* may not be comparable to data for other grain-size fractions or data obtained remotely on exposed surface material.

3.4. The mare-highlands dichotomy and KREEP

3.4.1. The dichotomy. One of the best-known concepts in lunar geoscience is that the Moon has two types of surfaces, the highlands or terra (land) and the maria (seas; singular: mare). The mare-terra dichotomy originates from early astronomical observations that the light-colored areas of the Moon are rugged and mountainous and the dark areas are smooth like water, circular, and occur at lower elevation. Largely as a result of the Apollo, Clementine, and Lunar Prospector missions, it is now known that the highlands consist largely of feldspathic rocks termed *anorthosite*. The highlands are rugged because they are old and have experienced impacts by countless meteoroids. The maria are smooth because volcanic magmas were extruded into the low spots resulting from the largest and deepest impacts after the most intense period of meteoroid bombardment had ended. The maria are darker than the highlands because the basalts of the maria are richer in iron than the anorthosites of the highlands.

Despite the mixed etymology, lunar scientists usually use the terms *mare* and *highlands* to refer to the two types of surfaces and samples derived from them. For various reasons, the distinction, which appears to be conveniently black and white or low and high, is not always easily or accurately applicable to all situations. For example, there is not the one-to-one correspondence among elevation, landform morphology, composition, and geologic history that one might expect from a simple dichotomy in topography or albedo. Some areas of morphologic highlands are actually at low elevation, some rocks that are not mare basalts are also not feldspathic, and many places on the lunar surface the regolith consists of material of both highlands and mare origin. With regard to samples, the term *nonmare* is commonly used refer to rocks that are clearly not of mare volcanic origin but for which the relationship to the feldspathic highlands is not clear or firmly established (e.g., Warren and Wasson 1977).

Geochemically, the mare-highlands dichotomy is inadequate because three general compositional groups of common rocks occur (Fig. 2.2). Basalts, demonstrably from the maria, are rich in Fe. Rocks and breccias from the feldspathic highlands are rich in aluminum. However, a great many rocks and breccias in the Apollo collection have intermediate concentrations of Fe and Al, but are much richer in incompatible elements than mare basalts or feldspathic breccias. Such rocks are not simple mixtures of materials of the feldspathic highlands and the maria but are a third type of material. Subsequent discussion requires a brief introduction to one of the most crucial, but confusing, concepts in lunar geoscience: KREEP.

3.4.2. KREEP. Incompatible elements are those lithophile (rock-loving) elements that do not fit into the crystal structure of the major rock-forming minerals. As a consequence, incompatible elements tend to become increasingly concentrated in the residual liquid phase as a magma solidifies. Many types of terrestrial igneous rocks and many samples from the Apollo collection have high to very high concentrations of incompatible elements compared to meteorites. Large regions of the near-side lunar surface are enriched in Th, a quintessential incompatible element, by factors of 100–300 over chondritic meteorites (Plate 2.1). These simple observations indicate that both the Earth and Moon differentiated to a much greater degree than did the asteroids.

A distinguishing characteristic of the Moon, however, is that in nearly all lunar samples that have moderate to high concentrations of incompatible elements, the ratio of the concentrations of any two incompatible elements is nearly always the same. It is as though there is but one carrier of incompatible elements, concentrations of incompatible elements in that material are very high, and the samples contain variable proportions of that material. This simple characteristic is one of the important geochemical arguments used to support the hypothesis of a global magma

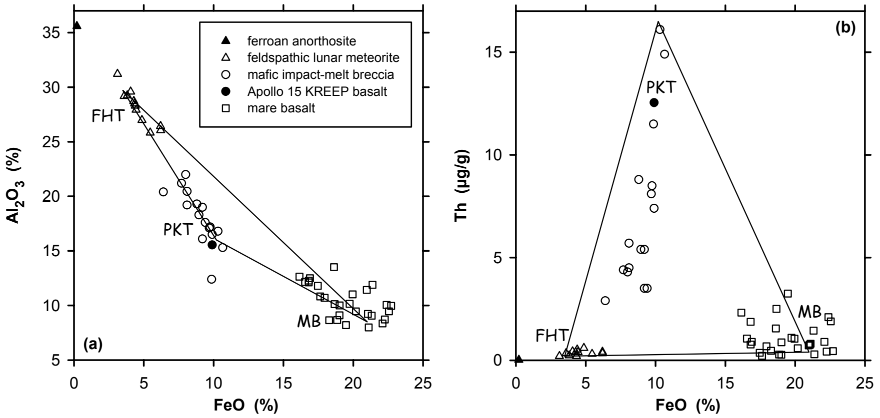

Figure 2.2. Geochemical variations among lunar samples corresponding to three "terrane" types that represent compositional extremes among common rocks of the Apollo missions: (1) Feldspathic Highlands Terrane (FHT), (2) Procellarum KREEP Terrane (PKT) (see Chapter 3), and (3) mare basalts (MB). The FHT is represented here by the feldspathic lunar meteorites (Korotev et al. 2003b) and highly feldspathic ferroan anorthosite (sample 15415), which have very low Th concentrations. The PKT is represented by Apollo 15 KREEP basalt and mafic impact-melt breccias, which are dominated by material (KREEP) with a noritic composition and high concentrations of incompatible elements such as Th. Each point represents one the 12 compositional groups defined by Korotev (2000) among samples from Apollo 14, 15, 16, and 17. The most Fe- and Th-rich ones are from Apollo 12 and 14 (Korotev 2000). The MB points each represent the mean of one of the major lunar basalt types. The triangles shown on these plots, are the same as those of Figures 2.5, 2.11, 2.12, 2.13, and 2.14.

ocean (e.g., Warren 1985). In this model the incompatible-element-rich material is, or derives from, the last liquid to solidify starting with a mostly or entirely molten Moon. Because these observations about lunar samples that are rich in incompatible elements (1) had no terrestrial analog, (2) were made very early in the study of lunar samples when lunar geochemistry was not well understood, (3) and the first materials to be recognized with these properties were glasses and breccias, not igneous rocks, the samples and the implied chemical component were given a non-standard designation: KREEP (Hubbard et al. 1971). The word is an acronym for K (potassium), REE (rare-earth elements), and P (phosphorous) which, along with Th and U, are among the many incompatible elements that are characteristic of materials identified as KREEP.

As a noun, KREEP usually refers to a rock, residual liquid, or chemical component (real or imaginary) that has concentrations of incompatible elements like those of samples that are rich in incompatible elements from Apollo 12 and Apollo 14. However, the term is not well defined or consistently used, and even experienced lunar geoscientists disagree on a definition and what the term means. Because the term KREEP has been applied to any and all materials with high concentrations of incompatible elements, largely regardless of major-element composition or whether the materials are igneous rocks, polymict samples (breccias, impact glass, regolith), or regions of the surface observed form orbit, its use sometimes obscures petrogenetic and chemical differences that, in fact, do occur among such materials.

As discussed in more detail below, samples identified as KREEP or as containing a large component of KREEP are usually noritic or basaltic in composition (Fig. 2.2, 2.3), although some are troctolitic (Shervais et al. 1988). The lithologic carriers of the chemical signature of KREEP in most Apollo regoliths are Fe- and Mg-rich impact-melt breccias and glasses. KREEP also occurs as a feldspathic basalt (Dymek 1986) with igneous texture at the Apollo 15 site, and some rocks of Apollo 17 have also been identified as KREEP basalt (Ryder et al.

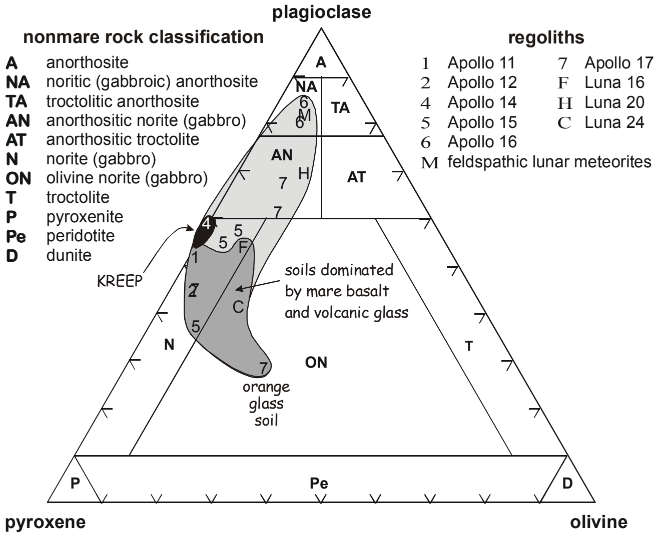

Figure 2.3. Normative mineralogy (idealized mass fraction based on chemical composition) of the three major minerals of lunar regolith converted to estimated modal mineralogy (volume fraction). Although lunar soil is composed mainly of plagioclase, pyroxenes, and olivine (most lunar regolith contain <5% ilmenite and other minerals), known soils occupy only a small portion (shaded region) of the triangle. For Apollo 11 (1) and 14 (4) and the three Luna missions (F, H, and C), a single point is plotted representing the mean composition of soil from each of those sites. For Apollo 16 (6), the two points represent the means of mature soils from the Cayley Plains and soils from North Ray crater (closer to plagioclase apex). For Apollo 15 (5) and 17 (7), the three points represent the compositional extremes; all other soils from either of these sites would plot within the triangle formed by these three points. The point for feldspathic lunar meteorites (M) is based on the mean composition of Table 2.1. The field for KREEP is based on Apollo 15 KREEP basalt and the Th-rich impact-melt breccias of Apollo 12, 14, and 15. The classification of Stöffler et al. (1980) for lunar highlands rocks is shown by the various fields (anorthositic norite, etc.). The classification does not strictly apply to soils dominated by mare basalt and volcanic glass.

1977; Salpas et al. 1987). The issue of "what is KREEP?" has been confused because the most common types of KREEP rocks are polymict breccias that vary substantially in major-element composition and some of which have greater concentrations of incompatible elements than their apparently igneous counterparts (Korotev 2000; Section 5.2.2). Many samples that are said to "contain KREEP" are polymict breccias or regoliths that contain clasts of impact-melt breccia of KREEP composition. However, even some mare basalts are described as containing KREEP as an assimilant (Dickinson et al. 1985; Neal et al. 1988; Anand et al. 2003).

More extensive discussions and summaries of the petrogenesis and significance of KREEP can be found elsewhere in this volume (Chapters 3 and 4) and in Schonfeld (1974), McKay and Weill (1977), Palme (1977), Hawke and Head (1978), Warren and Wasson (1979), Taylor (1982), Warren (1985), Dymek (1986), Haskin and Warren (1991), Ryder (1994), Warren (1998), Jolliff (1998), Wieczorek and Phillips (2000), Korotev (2000), and Korotev and Gillis (2001). The summary of McKay et al. (1986) is particularly enlightening.

4. LUNAR MINERALOGY

This section provides a summary of lunar mineralogy derived from direct examination of lunar samples. Even though the lunar samples were collected from a spatially limited region of the Moon, impacts have redistributed material over the lunar surface so there is a finite probability at any location on the surface of the Moon of obtaining material that formed at any other location. Also the Apollo samples provide a basis for understanding lunar mineralogy within the context of parent-body history and processes. For these reasons, the roster of lunar minerals is not expected to differ significantly in the unsampled regions except perhaps at the lunar poles for reasons described below. The lunar meteorites, which are random samples of the lunar surface that were "redistributed" by impacts to the extreme, confirm this expectation. Thus far no common minerals have been found in lunar meteorites that are not present in the Apollo collection (discounting terrestrial alteration products). With few exceptions, the minerals found on the Moon and their chemistry constitute a subset of known minerals that occur on Earth and that are consistent with the specific settings, history, and origin of the Moon. For a detailed coverage of mineralogy based on lunar samples, see Smith and Steele (1976), Papike et. al. (1991, 1998), and Papike (1998).

Minerals have provided the keys to understanding lunar rocks because their compositions and atomic structures reflect the physical and chemical conditions under which the rocks formed. Analyses of lunar minerals, combined with the results of laboratory experiments, have enabled scientists to determine key parameters—temperature, pressure, cooling rate, and the partial pressures of such gases as oxygen, sulfur, and carbon monoxide—that existed during formation of the lunar rocks. The array of minerals found in the lunar samples demonstrates strong differences between the Earth and Moon, at least since formation. The lack of water-bearing minerals shows the Moon is extremely dry; the samples are depleted in moderately volatile elements such as Na; the presence of metallic iron and details of the oxidation state of various elements in lunar minerals shows the Moon has very reducing conditions with oxygen fugacity near and mostly below the Fe-FeO buffer. High pressure phases unrelated to shock are not found at the Moon's surface.

As on the Earth, we recognize that minerals that occur on the surface of the Moon may not represent its deep interior because few delivery mechanisms exist to bring deep-seated solid materials to the lunar surface. On Earth, mantle materials are borne by kimberlites or diamond-bearing pipes that have sampled the Earth's mantle, but these occurrences are extremely rare. Similar features either do not occur or have not been recognized on the Moon. Asteroidal impacts may have excavated deep seated material in some areas, but no such material has been recognized in the sample collection. However, there is indirect evidence that garnet, a mineral not found in the samples, may occur in the Moon's mantle (see Chapter 3).

One area where there may yet be significant additions to the lunar mineral suite is in regions where hydrogen has been concentrated in the regolith, preserved by burial, and subjected to enough heat to form H-bearing minerals. Remote sensing has detected H at the lunar poles that may have been added to the Moon by many plausible sources, including cometary impacts or by solar wind implantation. Other volatile elements could have been added in the same events. The rare occurrences of volatile-element-bearing phases such as iron oxyhydroxides and carbonates in lunar samples (if indeed they formed on the Moon) may give evidence to these processes. The H deposits are most significant near the lunar poles and are at least partly associated with permanently shadowed locations in impact craters which may have acted as cold-traps (Watson et al. 1961; Feldman et al. 2001).

The most common minerals found in the lunar samples are the silicates plagioclase feldspar $(Ca,Na)(Al,Si)_4O_8$, pyroxene, $(Ca,Fe,Mg)_2Si_2O_6$, and olivine $(Mg,Fe)_2SiO_4$. Potassium feldspar ($KAlSi_3O_8$) and the silica (SiO_2) minerals (e.g., quartz), although abundant on Earth, are notably rare on the Moon. Minerals containing ferric iron (Fe^{3+}) and carbonate (CO_3^{2-}) are absent on the Moon. The most striking aspect of lunar mineralogy, however, is the lack of minerals that contain water, such as phyllosilicate clays, micas, amphiboles, and oxyhydroxides. These minerals may yet be found near the lunar poles where increased H concentrations occur, but these minerals would not be indicative of Moon-wide processes or compositions.

After the silicate minerals, oxide minerals are next in abundance. They are particularly concentrated in the mare basalts, and they can make up more than 20% by volume of these rocks. The most abundant oxide mineral is ilmenite, $(Fe,Mg)TiO_3$, a black, opaque mineral that is the carrier of high TiO_2 concentrations of many mare basalts. The second most abundant oxide mineral, spinel, has a widely varying composition and actually consists of a complex series of solid solutions. Members of this series include: chromite, $FeCr_2O_4$; ulvöspinel, Fe_2TiO_4; hercynite, $FeAl_2O_4$; and spinel (*sensu stricto*), $MgAl_2O_4$ (Table 2.2). Another oxide phase, which is only abundant in Ti-rich lunar basalts, is a mineral first described from the Moon, armalcolite $(Fe,Mg)Ti_2O_5$.

Two additional minerals are noteworthy because, although they occur only in small amounts, they are important indicators of a highly reducing, low-oxygen environment under which the lunar rocks formed. Native iron (Fe) is ubiquitous in lunar rocks, and commonly contains small amounts of Ni and Co. Troilite, relatively pure FeS, is a common minor component; it holds most of the sulfur in lunar rocks. As a result of selective volatilization of silica by meteoroid bombardment, some high-alumina and silica-poor glasses occur in the regolith (Naney et al. 1976), as well as new minerals resulting from this process, yoshiokaite, a Ca-Al silicate (Vaniman and Bish 1990) and hapkeite, an Fe_2Si phase (Anand et al. 2004).

4.1. Silicate minerals

Silicate minerals are the most abundant minerals in the lunar crust. Modal data for mineral grains in regoliths show the predominance of silicate minerals, especially pyroxene, plagioclase feldspar, and olivine (Table 2.2). It is expected that in some regions of the Moon the range of abundance is likely to be greater, especially in anorthosite terrains where the abundance of feldspar could locally approach 100%.

4.1.1. Pyroxene. Pyroxenes are the most chemically complex of the major silicate phases in lunar rocks and their chemistry records conditions of formation and evolutionary history of rocks in which they occur. Pyroxenes are compositionally variable solid solutions and they contain most of the major elements present in the host rocks. Lunar pyroxenes are primarily "quadrilateral" in that their compositions are defined within the compositional space bounded by enstatite-ferrosilite-diopside-hedenbergite. The most common varieties are hypersthene, augite, and pigeonite.

For a review of pyroxene crystal chemistry, see Papike (1987). Briefly, in the pyroxene structure, the M1 and M2 sites provide a range of atomic environments; as a result, pyroxenes can accommodate a wide variety of cations, and these cations reflect much of the chemistry and crystallization history of the rocks in which they occur. Ca, Na, Mn, Mg, and Fe^{2+} are accommodated in the large, distorted six- to eight-coordinated M2 site; Mn, Fe^{2+}, Mg, Cr^{3+}, Cr^{2+}, Ti^{4+}, Ti^{3+}, and Al occur in the six-coordinated M1 site; and Al and Si occupy the small, tetrahedral site. Potassium is too large to be accommodated in any of the pyroxene crystallographic sites at low pressure.

Although the major elements that define the pyroxene quadrilateral plot (Ca, Mg, and Fe) show important variations, the other, less abundant elements also show important trends. In lunar pyroxenes, these other elements include Al, Ti, and Cr. Reduced valence states for some Ti cations (including some Ti^{3+}) and Cr cations (including some Cr^{2+}) are important indications of very low oxygen fugacity during the crystallization of lunar rocks.

Lunar pyroxenes also show evidence of substantial *subsolidus* reactions (i.e., recrystallization and other changes that take place below melting temperatures). Considerable work has been done to interpret the resulting features. It was discovered soon after the return of the Apollo 11 samples that subsolidus exsolution of two distinct pyroxenes, augite and pigeonite, had taken place within originally uniform pyroxene crystals (e.g., Ross et al. 1970). This process produced distinctive microscopic and submicroscopic exsolution lamellae, i.e.,

Table 2.2. Lunar mineralogy summary.

Major minerals		
Pyroxene		
orthopyroxene	$(Mg,Fe)_2Si_2O_6$	
clinopyroxene	$(Ca,Mg,Fe)_2Si_2O_6$	
Plagioclase	$(Ca,Na,K)Al_2Si_2O_8$	
Olivine	$(Mg,Fe)_2SiO_4$	
Ilmenite	$FeTiO_3$	
Minor/accessory minerals		
K-feldspar	$(K,Ba)AlSi_3O_8$	
Phosphates		
apatite	$Ca_5(PO_4)_3(F,Cl)$	
whitlockite (RE-merrillite)	$Ca_{18-x}(Mg,Fe)_2(Y,REE)_xNa_{2-x}(P,Si)_{14}O_{56}$	
monazite	$(La,Ce,Nd)PO_4$	
farringtonite	$(Mg,Fe)_3(PO_4)_2$	(tentative—65785 Sp. Troct.)
graftonite	$(Fe,Mn,Ca)_3(PO_4)_2$	(not verified)
Pyroxenoid		
pyroxferroite	$Ca_{1/7}Fe_{6/7}SiO_3$	
Silica (SiO_2) polymorphs: cristobalite, quartz, tridymite		
Spinels[1]		
pleonaste	$(Mg,Fe)(Al,Cr)_2O_4$	Mg>Fe, Al>>Cr (“normal” spinel)
chromite	$(Fe,Mg)(Cr,Al)_2O_4$	ideally $Fe^{2+}Cr_2O_4$ (“normal” spinel)
ulvöspinel	Fe_2TiO_4	inverse ($TiFe_2O_4$)
Sulfides		
troilite	FeS	
sphalerite	ZnS	
wurtzite	ZnS	see Bogatikov et al. (2001)
Ti-bearing minerals other than ilmenite		
rutile	TiO_2	(typically niobian)
armalcolite	$(Fe,Mg)Ti_2O_5$	
perovskite	$CaTiO_3$	
sphene	$(Ca,Cr)(Ti,Zr)SiO_5$	
Zr-bearing minerals		
zircon	$(Zr,Hf)SiO_4$	
baddeleyite	$(Zr,Hf)O_2$	
zirconolite	$CaZrTi_2O_7$	
zirkelite	$(Ca,Fe)(Zr,Ti)_2O_5$	
tranquillityite	$Fe_8(Zr,Y)_2Ti_3Si_3O_{24}$	
Others		
cohenite	Fe_3C	
calcite/arag	$CaCO_3$	(tentative, contaminant(?) in 10058)
cordierite	$Al_3(Mg,Fe)_2[Si,AlO_{18}]$	
eskolaite	Cr_2O_3	see Bogatikov et al. (2001)
lawrencite	$FeCl_2$	
schreibersite	$(Fe,Ni,Co)_3P$	
yoshiokaite	$Ca_{8-(x/2)}Al_{16-x}Si_xO_{32}$	see Vaniman & Bish (1990)
yttrobetafite	$(Ca,Y,Fe,REE,Th,U)_2(Ti,Nb,Ta)_2O_7$	

---

[1] Spinel explanation: general formula is $(A^{IV})(B^{VI})_2O_4$; normal spinels have $8R^{2+}$ in A, $16R^{3+}$ in B; inverse spinels have $8R^{3+}$ in A, $8R^{2+}$ in B, $8R^{3+}$ in B (e.g., magnetite is inverse).

thin layers of pigeonite in augite, or vice versa. Papike et al. (1971) attempted to relate these exsolution features to the relative cooling histories of mare basalts. They pointed out that certain parameters of the pyroxene crystal unit cell (the length b and the angle β) could also be used to estimate the composition of the intergrown augite and pigeonite. They also suggested that $\Delta\beta$ (β-pigeonite − β-augite) could be used to indicate the degree of subsolidus exsolution and thus the relative annealing temperatures of the exsolved pyroxenes. Takeda et al. (1975) summarized similar exsolution data for pyroxene grains from Apollo 12 and 15 basalts. They compared the relative cooling rates (determined from exsolution studies) with absolute cooling rates determined from experimental studies. Ross et al. (1973) experimentally determined the 1-atmosphere augite-pigeonite stability relations for pyroxene grains from mare basalt 12021. Grove (1982) used exsolution lamellae in lunar clinopyroxenes as cooling rate indicators, and his results were calibrated experimentally. These studies all indicate that the cooling and subsolidus equilibration of igneous and metamorphic pyroxenes is a slow process; estimated cooling rates range from 1.5–0.2 °C/hr for lava flows 6 m thick for Apollo 15 mare lavas (Takeda et al. 1975). McCallum and O'Brien (1996) studied the width of exsolution lamellae and chemistry of exsolved pyroxenes in lunar highlands rocks to infer the stratigraphy of the highland crust, and the method has been applied to other rock types (e.g., Jolliff et al. 1999).

Shock lamellae can be produced in pyroxenes by the shock waves due to meteoroid impact. However, these features are rarely observed, and they are much less well characterized than the analogous shock lamellae in plagioclase (Schaal and Hörz 1977).

4.1.2. Plagioclase feldspar. The silicate mineral feldspar is the most common mineral in the lunar crust. It has a framework structure of three-dimensionally linked SiO_4 and AlO_4 tetrahedra (reviewed by Papike 1988). The Si:Al ratio varies between 3:1 and 1:1. Ordering of Si and Al in specific tetrahedral sites can lead to complexities such as discontinuities in the crystal structure. Within this three-dimensional framework of tetrahedra containing Si and Al, much larger sites with 8 to 12 coordination occur that accommodate large cations (Ca, Na, K, Fe, Mg, Ba).

Aside from rare K- and Ba-enriched feldspars, most lunar feldspars belong to the plagioclase series, which consists of solid solutions between albite ($NaAlSi_3O_8$) and anorthite ($CaAl_2Si_2O_8$). Lunar plagioclases are also depleted in Na (the albite component) relative to terrestrial plagioclases indicating the alkali depleted nature of the Moon. The maximum chemical variation involves solid solution between albite and anorthite, a variability that can also be described as the coupled substitution between NaSi and CaAl, in which the CaAl component represents anorthite. The Ca abundance in the plagioclase, and therefore mol% anorthite correlate positively with the Ca/Na ratio in the host basalts (e.g., Papike et al. 1976; BVSP 1981).

Plagioclase from impact-melt breccias that are rich in incompatible elements (Section 5.2) has more Na-rich compositions than those in highland plutonic rocks (i.e., lower anorthite content). Plagioclase from coarsely crystalline igneous rocks has more restricted compositions; however, there is a positive correlation between the alkali content of the host rock and that of the plagioclase.

4.1.3. Olivine. The crystal structure of olivine, $(Mg,Fe)_2SiO_4$, consists of serrated chains formed of edge-sharing octahedra, which parallel the crystallographic c-axis. The octahedral chains are cross-linked by isolated SiO_4 tetrahedra. The major cations in the octahedral sites, Fe^{2+} and Mg^{2+}, are distributed randomly over both the M1 and M2 octahedral sites; however, the small amounts of Ca that may occur in olivine occupy only the M2 site (see Papike 1987).

The major compositional variation within olivines is caused by exchange of Fe and Mg; this exchange, and the resulting variations in composition, are represented by the ratio Fe/(Fe+Mg). The Fe end member, Fe_2SiO_4, is fayalite, and the Mg end member, Mg_2SiO_4, is forsterite. The most magnesian mare basalt olivine grains contain only 20 mol% fayalite (Fa), represented by the notation Fa_{20}. Most mare basalt olivines have compositions in the range Fo_{80}-Fo_{30}; however, a number of mare basalts contain very Fe-rich olivine (Fa_{90}-Fa_{100}). These olivines are part of an equilibrium three-phase assemblage (Ca,Fe-pyroxene, Fe-olivine, silica) that crystallized stably from late-stage, Fe-enriched basaltic melts, typically occurring as mesostasis. Some mare basalts that cooled quickly during the late stages of crystallization instead contain either an Fe-rich pyroxene that crystallized metastably relative to the normal three-phase assemblage, or as Fe-rich pyroxenoid, pyroxferroite. The formation of extremely Fe-rich pyroxene violates a so-called "forbidden region" at the Fe-apex of the "pyroxene quadrilateral."

Other significant elements in lunar olivines are Ca, Mn, Cr, Ni, and Al. Calcium varies directly with the Fe content, and it may be an indicator of the cooling rate (Smith 1974). The experimental data of Donaldson et al. (1975) supported this contention. Olivine in mare basalt is significantly enriched in Cr relative to olivine in terrestrial basalts. Cr_2O_3 values, which are commonly below detection limits (~0.1 wt%) in terrestrial olivine (Smith 1974) range up to 0.6 wt% in lunar olivine. Much or all of this Cr may be in the reduced Cr^{2+} valence state, and Haggerty et al. (1970) identified significant Cr^{2+} in lunar olivine using optical absorption techniques. Cr^{2+} is more readily accommodated in the olivine structure than is Cr^{3+}, which is the normal valence state for Cr in terrestrial olivine. The presence of Cr^{2+} is another strong indicator of the low oxygen fugacities that existed during mare-basalt crystallization. Similarly, Cr^{2+} is much more abundant in lunar pyroxenes than in terrestrial pyroxenes (BVSP 1981).

4.1.4. Silica minerals: quartz, cristobalite, and tridymite. Silica minerals include several structurally different minerals, all of which have the simple formula SiO_2. These minerals are generally rare on the Moon. This rarity is one of the major mineralogic differences between the Moon and the Earth, where silica minerals are abundant in such common rocks as granite, sandstone, and chert.

The silica minerals found on the Moon are cristobalite, quartz, and tridymite. In spite of the intense impact cratering of the Moon, it is interesting that the high-pressure polymorphs of SiO_2, coesite and stishovite, which are known from young terrestrial impact craters, have not been found on the Moon. Explanations for their absence include the rarity of silica grains in the original target rocks and volatilization of silica during impact events in the high vacuum at the lunar surface (Papike et al. 1997).

The crystal structures of the lunar silica minerals are distinctly different from each other, but they all consist of frameworks of SiO_4 tetrahedra in which each tetrahedral corner is shared with another tetrahedron. A comparison of silica mineral structures, along with structure diagrams, can be found in Papike and Cameron (1976). All of the silica mineral structures contain little or no room for cations larger that Si^{4+}, hence the relatively pure SiO_2 composition of these minerals. The structures become more open in going from quartz to tridymite and cristobalite, and the general abundance of impurities increases accordingly.

Quartz occurs in a few granite-like (felsite) clasts as needle-shaped crystals that probably represent structural transformation (inversion) of original tridymite (Quick et al. 1981). Some tridymite is preserved in these felsite clasts. The other rock type in which quartz is abundant is coarse-grained lunar granites occurring in rare fragments. The largest lunar granite clast yet found, from Apollo 14 breccia 14321, weighs 1.8 g and contains 40 vol% quartz (Warren et al. 1983). A smaller granite clast, from sample 14303, was estimated to have 23 vol% quartz (Warren et al. 1983). Based on their isotopic work on the large clast, Shih et al. (1985, 1993) suggested that the sample crystallized in a deep-seated plutonic environment about 4.1 Ga. Consistent with the general absence of hydrous minerals on the Moon, the lunar granites do not contain mica or amphibole, as do granites on Earth.

The most common silica mineral in lunar basalts is not quartz but cristobalite, which can constitute up to 7 vol% of some basalts. This situation contrasts with the general absence of all silica minerals in terrestrial basalts. Lunar cristobalite commonly has twinning and curved fractures, indicating that it has inverted from a high-temperature to a low-temperature crystal structure during cooling of the lavas (Dence et al. 1970, Champness et al. 1971). Other mare basalts contain crystals of the silica mineral tridymite that have incompletely inverted from cristobalite, producing rocks that contain both tridymite and cristobalite. Cristobalite tends to occur as irregular grains wedged between other crystals, while tridymite forms lathlike crystals. Klein et al. (1971) observed tridymite laths enclosed by pyroxene and plagioclase and suggested that tridymite was an early crystallizing phase. In a study of Apollo 12 basalts, Sippel (1971) found that the coarser-grained samples contained cristobalite and quartz. Unfortunately, these mineral pairs are stable over fairly large temperature ranges and can also form metastably, outside of their equilibrium stability fields, so they are not useful for inferring the temperatures of lava crystallization.

The paucity of silica minerals in the lunar samples and presumably the Moon as a whole has several implications. For one, the Moon has apparently not evolved chemically beyond the formation of a low-silica, high-alumina anorthositic crust, so that high-silica granitic rocks are rare. For another, the Moon lacks hydrous and hydrothermal systems like those that can crystallize silica on Earth. Despite the scarcity of lunar silica minerals, some lunar geologic features exhibit a morphology that suggests they may have formed from viscous lavas, presumably silica-rich. Some of these locations are spectrally anomalous in their UV-Visible ratio giving them (and other color anomalies) the nickname "red spots." There is no direct evidence that these locations contain silica minerals (or other minerals indicative of a viscous magma composition) but such evidence could be derived from thermal-infrared spectroscopy.

Despite their rarity in the samples, the silica minerals are nevertheless important in classifying and unraveling the origin of some lunar rocks. Furthermore, lunar crustal rocks that contain silica minerals may be more abundant than their meager representation among the returned Apollo and Luna samples suggests. The silica minerals tend to concentrate along with incompatible elements. For these reasons, the lunar silica minerals deserve greater consideration than their rarity would otherwise warrant.

4.2. Oxide minerals

The oxide minerals, although less abundant than silicates in lunar rocks, are of great significance because they retain signatures of critical conditions of formation (e.g., limited availability of oxygen) of the rocks in which they occur. Whereas most of the silicate minerals differ little from those on Earth, the opaque oxide phases indicate the reducing, anhydrous conditions that prevailed during their formation. By combining analyses of lunar oxide minerals with the results of laboratory experiments on their synthetic equivalents, the temperature and oxygen pressure conditions during formation of lunar rocks can be estimated (see Sato et al. 1973; Usselman and Lofgren 1976). Several oxide minerals are important constituents of lunar samples: ilmenite, $FeTiO_3$; spinels with extensive chemical variations: $(Fe,Mg)(Cr,Al,Fe,Ti)_2O_4$; and armalcolite, $(Fe,Mg)Ti_2O_5$. The less abundant lunar oxide minerals include rutile, TiO_2, baddeleyite, ZrO_2, and zirconolite, $(Ca,Fe)(Zr,REE)(Ti,Nb)_2O_7$ (Table 2.2).

Because their oxygen is more weakly bonded than that in silicate minerals, oxide minerals are obvious and important potential feedstocks for future production of lunar oxygen and metals. On Earth, similar oxide minerals commonly occur in economically recoverable quantities called ore deposits. However, most of these deposits have formed from hydrothermal waters (100–300 °C or hotter). The Moon has little, if any, water, and the presence of similar hydrothermal ore deposits on the Moon is improbable. However, there are other means of concentrating oxide minerals into exploitable ores. Crystal settling of dense minerals (e.g., chromite, ilmenite, and minerals containing the platinum-group elements) is possible within silicate magmas, if the magma remains liquid for a long enough time. On Earth, such accumulations are normally found in layered intrusions. These bodies form from large masses of magma that have been emplaced into deep crustal rocks without reaching the Earth's surface. Under such conditions, cooling is slower, and physical separation processes have time to act and include convection as well as settling. Well-known examples of ore deposits resulting from these processes occur in the Stillwater Anorthosite Complex (Montana) and the Bushveld Igneous Complex (South Africa).

The major differences between the oxide minerals in lunar and terrestrial rocks arise from fundamental differences between both the surfaces and the interiors of these two planets. On the Moon, meteoroid impact and shock-metamorphic processes play a major role in altering rocks. These effects are not the same for all minerals. Shock damage and the formation of shock glasses from minerals, e.g., maskelynite from plagioclase feldspar, are observed chiefly in silicate minerals. Oxide minerals also record shock damage, but another effect of impact on oxide (and sulfide) minerals is to produce small amounts of chemical reduction.

4.2.1. Ilmenite. With the ideal formula $FeTiO_3$, ilmenite is the most abundant oxide mineral in lunar rocks. The amount of ilmenite in a rock is a function of the bulk composition of the magma from which the rock crystallized (Campbell et al. 1978; Norman and Ryder 1980; Rutherford et al. 1980); the higher the TiO_2 content of the original magma, the higher the ilmenite content of the rock. Ilmenite forms as much as 15 to 24 vol% of many Apollo 11 and 17 mare basalts (McKay and Williams 1979). However, the volume percentages of ilmenite in mare basalts vary widely across the Moon, as indicated by the range of TiO_2 contents in samples from different lunar missions.

The ilmenite crystal structure is hexagonal and consists of alternating layers of Ti- and Fe-containing octahedra. Most lunar ilmenite contains some Mg substituting for Fe, which arises from the solid solution that exists between ilmenite ($FeTiO_3$) and $MgTiO_3$, the mineral geikielite. Other elements are present only in minor to trace amounts (i.e., <1 wt%); these include Cr, Mn, Al, and V. In addition, ZrO_2 contents of up to 0.6 wt% have been reported from ilmenite in Apollo 14 and 15 basalts (El Goresy et al. 1971a,b; Taylor et al. 1973). In fact, the partitioning of ZrO_2 between ilmenite and coexisting ulvöspinel (Fe_2TiO_4) has been experimentally determined (Taylor and McCallister 1972) and has been used as both a geothermometer (to deduce temperatures during crystallization) and as a cooling-rate indicator (Taylor et al. 1975, 1978; Uhlmann et al. 1979). Although terrestrial ilmenite almost always contains some Fe^{3+}, lunar ilmenite contains none.

Ilmenite commonly occurs in mare basalts as bladed crystals up to a few millimeters long. It typically forms near the middle of the crystallization sequence, where it is closely associated with pyroxene. It also forms later in the sequence and at lower temperatures, where it is associated with native Fe and troilite. In Apollo 17 rocks, ilmenite is frequently associated with armalcolite and occurs as mantles on armalcolite crystals (e.g., Haggerty 1973a; Williams and Taylor 1974). In these instances, ilmenite has possibly formed by the reaction of earlier armalcolite with the melt during crystallization.

The composition of lunar ilmenite plots along the $FeTiO_3$-$MgTiO_3$ join; variation from $FeTiO_3$ is often expressed in wt% of MgO. In general, the ilmenite with the highest Mg contents tends to come from relatively high-Mg rocks; ilmenite composition correlates with the bulk composition of the rock and therefore reflects magmatic chemistry rather than pressure. In detail, the distribution of Mg between ilmenite and coexisting silicate minerals in a magma is related to the timing of ilmenite crystallization relative to the crystallization of the other minerals. This crystallization sequence is itself a function of cooling rate and other factors, most notably the oxygen fugacity (Usselman et al. 1975). However, it is doubtful that the Mg contents in ilmenite all represent equilibrium conditions, because ilmenite compositions can vary significantly, even within distances of a few millimeters, within a single rock.

The stability curve of pure ilmenite as a function of temperature and fO_2 is significantly different from that of ulvöspinel (Taylor et al. 1973), the spinel phase with which it is commonly associated, implying that the two minerals did not crystallize together. The data suggest that, in these mineral assemblages, ilmenite has formed by solid-state reduction of this high-Ti spinel at temperatures below their melting points. Rare grains of ilmenite also contain evidence for subsolidus reduction of ilmenite to rutile (TiO_2) + native Fe; other grains show reduction to chromite ($FeCr_2O_4$) + rutile + native Fe.

4.2.2. Spinels. Spinel is the name for a group of oxide minerals, all with cubic crystal symmetry, that have extensive solid solution within the group. Spinels are the second most abundant opaque mineral on the Moon, second only to ilmenite, and they can make up as much as 10 vol% of certain basalts, most notably those from the Apollo 12 and 15 sites. The general structural formula for these minerals is $^{IV}A^{VI}B_2O_4$, where IV and VI refer to cations with tetrahedral and octahedral coordination, respectively.

The basic spinel structure is a cubic array of oxygen atoms. Within the array, the tetrahedral A-sites are occupied by one-third of the cations, and the octahedral B-sites are occupied by the remaining two-thirds of the cations. In a normal spinel structure, the divalent cation, such as Fe^{2+}, occupies only the tetrahedral sites, and the two different sites each contain only one type of cation (e.g., $FeCr_2O_4$). If the divalent cation occurs in one-half of the B-sites, the mineral is referred to as an inverse spinel [e.g., $Fe(Fe,Ti)_2O_4$]. In lunar spinels, the divalent cations (usually Fe^{2+} or Mg^{2+}) occupy either the A- or both A- and B-sites (i.e., there are both normal and inverse lunar spinels), and higher-charge cations (such as Cr^{3+}, Al^{3+}, Ti^{4+}) are restricted to the B-sites.

The relations of the various members of the spinel group can be displayed in a diagram known as the Johnston compositional prism (e.g., Haggerty 1978a). The end-members represented include chromite, $FeCr_2O_4$; ulvöspinel, $FeFeTiO_4$ (commonly written as Fe_2TiO_4;, but this is an inverse spinel with Fe^{2+} in both A- and B-sites); hercynite, $FeAl_2O_4$; and spinel (*sensu stricto*), $MgAl_2O_4$. Intermediate compositions among these end-members are designated by using appropriate modifiers (e.g., chromian ulvöpsinel or titanian chromite).

Most lunar spinels have compositions generally represented within the three-component system: $FeCr_2O_4$ - $FeFeTiO_4$ - $FeAl_2O_4$, and their compositions can be represented on a simple triangular plot. The addition of Mg as another major component provides a third dimension to this system; the compositions are then represented as points within a limited Johnston compositional prism in which the Mg-rich half (Mg>Fe) is deleted because most lunar spinels are Fe-rich (e.g., Agrell et al. 1970; El Goresy et al. 1971b, 1976; Haggerty 1971a, 1972b,c, 1973b, 1978a; Taylor et al. 1971; Busche et al. 1972; Dalton et al. 1974; Nehru et al. 1974, 1976). Most lunar spinel compositions fall between chromite and ulvöspinel. The principal cation substitutions in these lunar spinels can be represented by $Fe^{2+} + Ti^{4+} = 2(Cr,Al)^{3+}$. Other cations commonly present include V, Mn, and Zr.

Spinels are ubiquitous in mare basalts, where they occur in various textures and associations. The spinels are invariably zoned chemically. Such zoning occurs particularly in Apollo 12 and 15 rocks, in which chromite is typically the first formed mineral. As the chromite crystals grow, their TiO_2 and FeO contents increase and Al_2O_3, MgO, and Cr_2O_3 contents decrease, with the overall composition moving toward ulvöspinel. In most of the basalts that contain both titanian chromite and chromian ulvöspinel, the ulvöspinel occurs as overgrowths and rims surrounding the chromite crystals. Some individual ulvöspinel grains also occur as intermediate to late-stage crystallization products.

In reflected light, the ulvöspinel in these composite crystals appears as tan to brown rims around the bluish chromite. The contact between the two is commonly sharp, indicating a discontinuity in the compositional trend from core to rim. This break probably records a cessation in growth, followed later by renewed crystallization in which the early chromite grains acted as nuclei for continued growth of ulvöspinel (Cameron 1971). Some rocks (e.g., basalt 12018) contain spinel grains with diffuse contacts that reflect gradational changes in the composition of the solid solution. These textures could result from continuous crystallization of the spinel or from later solid-state diffusion within the crystal (Taylor et al. 1971).

Although most abundant in mare basalts, spinels also occur in highland rocks such as anorthosites, anorthositic gabbros, troctolites, and impact mixtures of these rock types (e.g., Haselton and Nash 1975). The spinels in anorthositic (plagioclase-rich) highland rocks tend to be chromite with lesser amounts of MgO, Al_2O_3, and TiO_2. However, certain highland rocks, notably the olivine-feldspar types (troctolites), contain pleonaste spinel. The composition of this spinel is slightly more Fe- and Cr-rich than an ideal composition precisely between the end members $MgAl_2O_4$ and $FeAl_2O_4$. This spinel is not opaque; viewed with a petrographic microscope, it stands out because of its pink color, high index of refraction, and isotropic character in cross-polarized light.

4.3. Phosphate minerals

Phosphates are found as accessory minerals in most lunar rocks, typically as apatite [$Ca_5(PO_4)_3(F,Cl)$] or RE (rare earth)-merrillite [$Ca_{16}(Mg,Fe)_2(REE)_2(PO_4)_{14}$], and commonly these two are found together. Here we use the mineral name RE-merrillite instead of whitlockite because structural and chemical studies indicate a closer affiliation with meteoritic merrillite than with terrestrial whitlockite (Dowty 1977; Jolliff et al. 1993; Rubin 1997). Lunar merrillite is invariably rich in rare-earth elements (REE) because of the lack of structural H, which sets it apart from terrestrial whitlockite (Dowty 1977). In fact, RE-merrillite is the main mineral host for the REE, containing up to 10% or more RE_2O_3, including Y (Jolliff et al. 1993). In crystalline rocks, the phosphates occur in late-stage mesostasis, commonly with K-rich glass, K-feldspar, ilmenite, zircon, fayalite, and cristobalite. The phosphate mineral monazite [$(La,Ce,Nd)PO_4$], which is rich in light REEs (La, Ce, Nd), has been found in lunar rocks, but it is extremely rare and occurs in association with RE-merrillite (Lovering et al. 1974; Jolliff 1993). The Mg-Fe phosphate, farringtonite [$(Mg,Fe)_3(PO_4)_2$], was tentatively identified by Dowty et al. (1974). Phosphate hydrates, which are extremely diverse and numerous on Earth, have not been found in lunar samples, consistent with the lack of other water or hydroxylated minerals; the halogen site of apatite contains essentially stoichiometric F and Cl.

4.4. Iron metal

Native iron metal occurs commonly in lunar rocks and regolith. In pristine igneous rocks, Fe metal forms in trace to minor amounts by indigenous igneous processes (Reid et al. 1970; Goldstein et al. 1974; Ryder et al. 1980; Warren et al. 1987). Such metal typically exists as grains with dimensions of 1–100 μm. Greater concentrations of Fe metal occur in lunar regolith, where it forms by reduction of Fe^{2+} and by addition of metal from impacting meteoroids. Iron contents and sources in lunar materials are summarized in Papike et al. (1991) and Papike et al. (1998). In this section, we focus on metal found in regolith.

Metal grains of meteoritic composition are found in virtually all lunar breccias and throughout the regolith. Because the Moon has no atmosphere, most metal of meteoritic origin in the regolith has either (1) melted and re-solidified as part of an impact-melt breccia or agglutinate or (2) vaporized and been deposited on the surface of regolith grains. Some types of impact-melt breccias contain as much as 2% FeNi metal, on average (Korotev 1994). Metal grains up to several millimeters in size that have solidified from melts of lunar silicates are found in the regolith (Korotev 1987a, 1991, 1997; Korotev and Jolliff 2000). Iron metal also occurs in the regolith from reduction of Fe^{2+} in silicates and oxides during agglutinate formation and vaporization and deposition. A more detailed discussion of metallic iron in the lunar regolith is presented in Section 6.2.1.

4.5. Importance of the ratio of magnesium to iron

When lunar magmas cooled and solidified, the first-formed mafic (Mg- and Fe-bearing) minerals to crystallize, olivine or pyroxene, had a greater Mg/Fe ratio than the magma. By the time the last-formed olivine and pyroxene crystallized, magmas were depleted in Mg, so the late-formed minerals have lower Mg/Fe ratio than the original magma. The first-formed crystals are said to be more *magnesian* (greater Mg/Fe) than the original liquid, and the last-formed crystals are more *ferroan* (lesser Mg/Fe). Similarly, the first-formed plagioclase has a greater Ca/(Na+K) ratio than the original magma and as crystallization proceeds the Ca/(Na+K) ratio of the crystallizing plagioclase decreases. In other words, early formed plagioclase is at the anorthitic end of the range and later formed plagioclase is at the more albitic end. There are important exceptions to these generalizations, but rocks with high Mg/Fe and high Ca/Na are usually older (more primitive) than geologically related rocks that are more ferroan and more albitic. This simple concept is the heart of why the Mg/Fe ratio of lunar rocks is one of the most fundamentally important petrologic parameters.

For mafic minerals such as olivine and pyroxene, the molar or atom ratio of Mg/(Mg+Fe) is a more useful quantity than the simple mass or molar ratio of Mg/Fe or MgO/FeO. To state that olivine has a composition of Fo_{81} is a shorthand way of saying that the forsterite (Mg_2SiO_4) to fayalite (Fe_2SiO_4) ratio of the olivine solid solution series is 81:19 or that the mole percent of Mg/(Mg+Fe) is 81. When discussing the Mg/Fe ratio of rocks it is similarly convenient to use the "magnesium number," which is simply the whole-rock bulk mole percent MgO/(MgO+FeO). Here, we symbolize the whole rock magnesium number as *Mg´* but the quantity is sometimes symbolized as "Mg#." For lunar rocks, if the abundance of ilmenite and metallic iron is low, *Mg´* approximates the mass-weighted average Fo (forsterite) and En (enstatite) proportions of the olivine and pyroxene.

5. LUNAR ROCKS

In this section, we discuss aspects of the major rock types that are important to understanding the Moon's surface mineralogy and geochemistry. In the following paragraphs, each of the major rock types is described briefly. Additional descriptions and details of petrogenesis are in Chapters 3 and 4.

As on Earth, lunar rocks come in igneous, metamorphic, and sedimentary varieties, although the metamorphic and sedimentary varieties are almost entirely impact-related. Mare basalts are the most common igneous rocks in the sample collection. In the more ancient highlands, unbrecciated igneous rocks are rare, at least among the samples, because the original lunar crust has been thoroughly reworked by meteoroid impacts. Much effort has gone into seeking, within breccias and the regolith, fragments of igneous and plutonic rocks of the original lunar crust that are largely unscathed with respect to composition, texture, and mineralogy. Such rocks are commonly called *pristine* rocks (Warren and Wasson 1977).

5.1. Pristine nonmare rocks

Pristine rocks are identified by a combination of texture and composition (Warren and Wasson 1977, 1978, 1979). Distinguishing characteristics include coarse-grained plutonic textures, absence of petrographic or chemical evidence that the rock is a mixture of more than one rock type, and absence of contamination by siderophile elements of meteoritic origin. Warren (1993) compiled a list of 260 "possibly pristine" rocks, of which 89 were confidently pristine. Less than half of these were over 1 gram in mass, and many were small clasts from breccias.

Until recently, petrologists and geochemists commonly distinguished four suites of pristine nonmare igneous rocks: (1) ferroan anorthosite (FAN) or ferroan-anorthositic-suite (FAS), (2) magnesian suite (aka. magnesium suite, Mg-suite, Mg-rich), (3) alkali suite (alkalic suite), and (4) KREEP basalt, including possibly related rocks such as felsite (granite) and quartz monzogabbro. More recently, (2)-(4) have been shown to be related (discussed at length in chapters 3 and 4). Pristine rocks are rarely found with preserved, original plutonic-rock texture (coarsely crystalline); most occur as monomict breccias, i.e., breccias or aggregates of rock clasts, all of the same original rock type, or as cataclastic rocks with original textures thoroughly disrupted by impact processes. Volumetrically, among the Apollo and Luna samples, alkali-suite pristine rocks and KREEP rocks are far less abundant than are FAS and Mg-suite rocks. In early lunar literature the acronym *ANT* was used to refer collectively to anorthosites, norites, and troctolites (e.g., Keil et al. 1972), but subsequent work has shown that the *A* is not closely related to the *N* and *T*. Lunar anorthosites tend to be ferroan, that is, they have low Mg/Fe ratios, whereas the norites and, particularly, troctolites are magnesian – they have high Mg/Fe ratios. More importantly, mineral compositions differ. The ferroan-anorthosite suite is distinct from the magnesian and alkali suites on plots of *Mg´* of mafic silicates against *AN* [mol% Ca/(Ca+Na)] in plagioclase (Fig. 2.4). Other mineralogical differences occur (Papike et al. 1998), and some trace element ratios also tend differ (Norman and Ryder 1980).

5.1.1. Ferroan-anorthositic suite. Two early surprises in the study of Apollo samples were that (1) anorthosite was common in the lunar highlands and (2) lunar anorthosite is highly anorthitic. Plagioclase in rocks from the lunar highlands is typically An_{96} in composition. This is a much higher anorthite content than that typically found in plagioclase in terrestrial rocks and ultimately reflects the Moon's depletion in volatile elements like sodium. For example, the composition of plagioclase in terrestrial massif anorthosites is typically in the An_{35} to An_{65} range. A third surprise was that by terrestrial standards, the *Mg´* of pyroxene and olivine in lunar anorthosite was much more ferroan than in terrestrial rocks of such high Ca/Na ratio and any other nonmare lunar rocks, such as impact-melt breccias and troctolites (range: $En_{44–76}$, mean: $En_{62 \pm 3}$; Fig. 2.4). For these reasons, since the time of Dowty et al. (1974), lunar anorthosite with a plutonic or relic plutonic textures has been called *ferroan anorthosite*.

The term ferroan-anorthositic suite or *FAS* (Warren 1993) encompasses ferroan anorthosites (>90% plagioclase) as well as their more mafic but less common variants, ferroan noritic anorthosite and ferroan anorthositic norite (Fig. 2.5). Some ferroan anorthosites contain olivine, but pyroxene usually predominates. Lunar ferroan anorthosites formed as coarse-grained igneous rocks. The coarse grain size indicates that they are intrusive rocks, formed during slow cooling at some depth below the surface. The high concentration of plagioclase feldspar suggests that they are also cumulate rocks, produced by the separation and accumulation of just-formed crystals (in this case, plagioclase feldspar) from the remaining melt. Although the vast majority of ferroan anorthosites are severely brecciated, the few samples that show vestiges of their former igneous texture tend to be coarse-grained, with large subhedral to euhedral plagioclase crystals surrounded by smaller anhedral pyroxene or olivine. Geochemically, ferroan anorthosites are distinct in having very low concentrations of both FeO and incompatible trace elements, as exemplified by Th, compared to other lunar rocks (Fig. 2.5).

Ferroan anorthosite is a fascinating rock type in that several large Apollo rocks are nearly monomineralic plagioclase (e.g., Warren 1990) and outcrops large enough to be seen telescopically from Earth occur (Hawke et al. 2003). However, its perceived importance to lunar crustal formation may have been enhanced somewhat by historical accidents. One large sample dubbed the "Genesis Rock" (sample 15415, e.g., Ryder 1985) was found at the Apollo 15 site, and ferroan anorthosite is by far the most common type of pristine rock at the Apollo 16 site, although it is uncommon to rare at other sites. Because (1) the Apollo 16 mission was the only Apollo mission to sample the feldspathic highlands distant from a mare basin, (2) highly feldspathic (typically >98% plagioclase) ferroan anorthosite was common at the site, and (3) the first feldspathic lunar meteorite was not discovered until 10 years after the Apollo 16 mission, the notion persists that the lunar highlands, in general, are dominated by ferroan anorthosite and

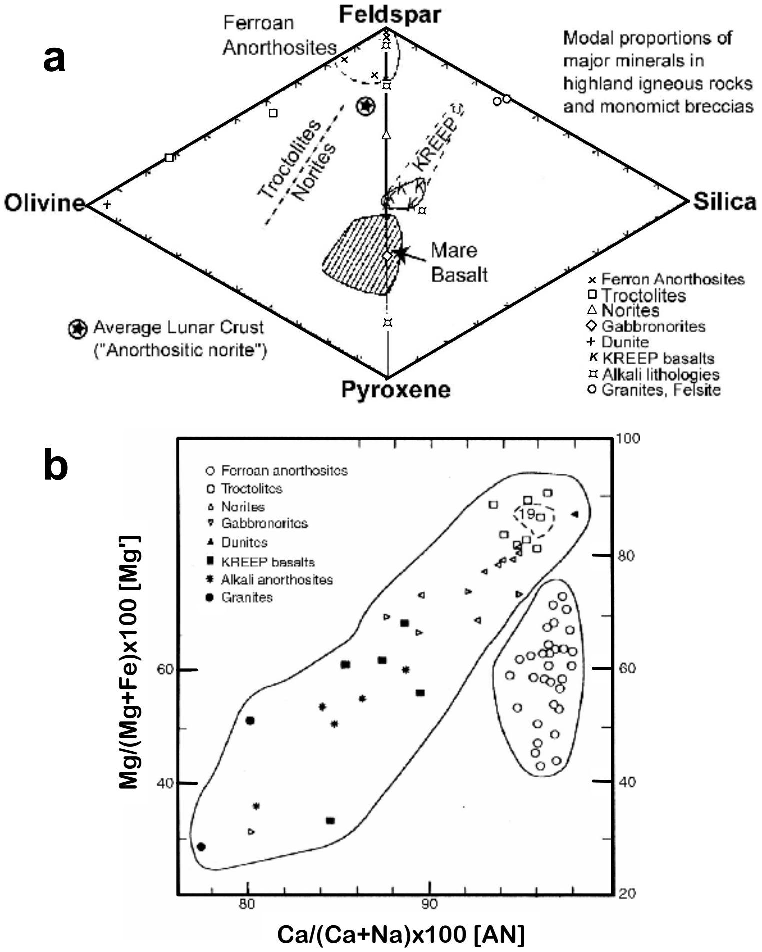

Figure 2.4. (a) Modal (volume) proportions of four lunar minerals in highland pristine igneous rocks and monomict breccias. The KREEP basalts, in general, have higher abundances of feldspar and silica minerals. Part (a) modified after Taylor et al. (1991). (b) Mineral compositions of highland pristine rocks plotted in terms of orthopyroxene Mg/(Mg+Fe) versus plagioclase anorthite content [AN]. The envelope to the right at high AN is the Ferroan Anorthosite (FAN) field. The larger field is for the magnesian-suite rocks.

that the FAS component of the crust is highly feldspathic. However, evidence and arguments based on the feldspathic lunar meteorites, orbital geochemistry, as well as regolith samples from Apollo 16 and Luna 20 suggest a different view. Highly feldspathic ferroan anorthosite is not necessarily typical of the highlands surface, at least, not on the Moon's near side. Most feldspathic lunar meteorites, which are all but devoid of mare volcanic material, are more mafic than the feldspathic material of the Apollo 16 regolith (Korotev 1996, 1997; Korotev et al. 2003). Also, a significant fraction of the plagioclase in the lunar highlands must derive from magnesian feldspathic rocks in order to account for the high *Mg´* of the upper feldspathic crust (70 ± 3), which at the surface is at the high end of the range for FAS rocks (Fig. 2.4; Section 7.1).

5.1.2. Magnesian suite. The precise compositional range of the magnesian suite of pristine nonmare rocks is not well defined (Figs. 2.4, 2.6). Rocks identified as magnesian-suite rocks

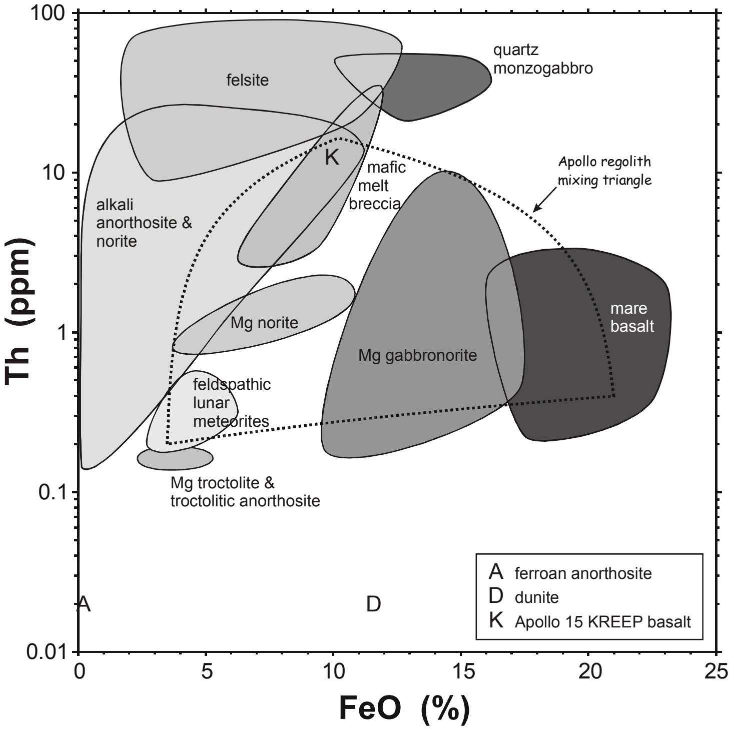

Figure 2.5. Lunar rocks in FeO-Th space. The dotted "triangle" is the Apollo regolith mixing triangle of Figure 2.2, distorted by the logarithmic Th scale. Nearly all regolith compositions from the Apollo and Luna missions plot within the triangle, which is defined by the fields for the feldspathic lunar meteorites, mare basalt, and mafic, KREEP-bearing impact-melt breccias of the Apollo missions. Apollo 15 KREEP basalt (K) plots in the field for the mafic melt breccias and is compositionally similar. Norites and gabbronorites of the magnesian suite mostly plot within the regolith mixing triangle, although they are not mixtures of the rocks represented by the triangle apices. Felsite ("granite") and quartz monzogabbro (alias, quartz monzodiorite) have the greatest concentrations of Th among lunar rocks. Alkali-suite rocks vary greatly in composition. The "A" point represents highly feldspathic ferroan anorthosite sample 15418. Other ferroan anorthosites would plot between "A" and the field for feldspathic lunar meteorites. The "D" point represents the Apollo 17 dunite, sample 72415–7.

are usually substantially more mafic than FAS rocks, although a few plagioclase-rich rocks (magnesian anorthosite) are included. Most samples are norites (*Mg´* = 78 ± 8), troctolites (*Mg´* = 87 ± 5, including anorthositic troctolite and troctolitic anorthosite), or ultramafic rocks (*Mg´* = 88 ± 2). There are also some gabbros and gabbronorites, i.e., rocks with a significant proportion of Ca-rich clinopyroxene. Some of the gabbronorites are not actually magnesian in that they have moderate to low *Mg´* (Fig. 2.4). As originally applied, the term "Mg-rich" rocks covered all coarse-grained nonmare rocks that could be distinguished from the ferroan anorthosites by such chemical indicators as higher *Mg´* or lower *AN* contents (Warner et al. 1976a). Subsequently, many petrologists have come to suspect that there are fundamental genetic distinctions and that different magnesian-suite rocks were produced by separate and dissimilar magmas (e.g., James and Flohr 1983).

Most magnesian-suite rocks were collected at the Apollo 15 and 17 sites. Geochemically, these rocks (norites, troctolites, dunite) mostly appear to have crystallized from magmas rich in incompatible elements. Magnesian-suite rocks among the Apollo 16 collection are restricted

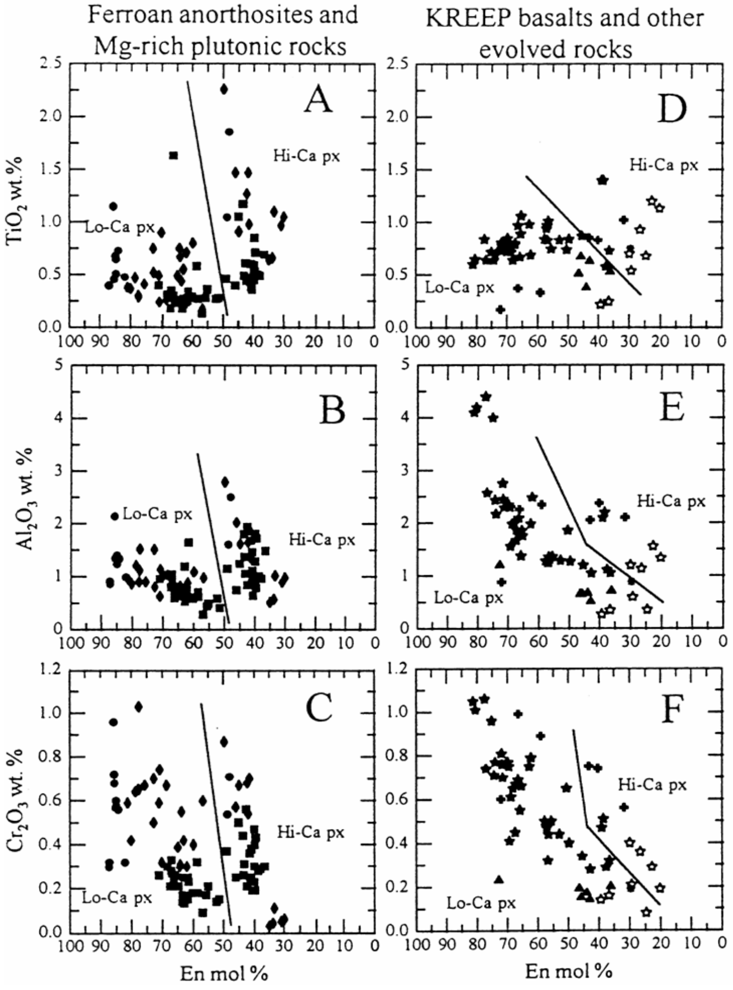

Figure 2.6. Chemistry of pyroxenes in pristine igneous highland rocks. Symbols: ■ = ferroan anorthosites; ● = magnesian plutonic olivine-poor; ◆ = magnesian plutonic olivine-rich; ★ = A15 KREEP Basalts; ☆ = quartz monzodiorites. Figure after Papike et al. (1998).

to a few troctolites and gabbronorites. Mafic, magnesian norites and troctolites are also rare to absent in the feldspathic lunar meteorites. These observations all suggest that many to most of the mafic, magnesian-suite rocks of the Apollo collection are not characteristic of the highlands globally, but instead may derive mainly from parts of the crust where incompatible-element rich materials are inferred to occur on the basis of surface compositions, primarily the Procellarum KREEP Terrane (Korotev 2000; Korotev et al. 2003; see also Chapter 3 and Plate 3.10). Magnesian, but not pristine, rocks occur in the feldspathic highlands (e.g., granulitic breccias, Section 5.2.4), but most are feldspathic and their relationship to the mafic magnesian-suite rocks of the Apollo collection has not been established.

5.1.3. Alkali Suite, KREEP basalt, felsite, and quartz monzogabbro. Alkali-suite rocks range in composition from anorthosite to norite and gabbronorite. They are distinguished by plagioclase that is more sodic ($An_{82\pm8}$) than that of ferroan anorthosite (An_{96}), e.g., Na concentrations are about a factor of 4 greater. Alkali-suite rocks are also tend to be enriched in incompatible elements. Most alkali-suite rocks occur in the Apollo 12 and 14 collection (e.g., Warren and Wasson 1980, 1981; Warren 1993), suggesting that they are petrogenetically related to KREEP (Shervais and McGee 1998). Because alkali-suite rocks are all but nonexistent in the feldspathic lunar meteorites, they are almost certainly a nonmare but also non-highlands lithology. The petrogenesis of alkali-suite rocks is discussed in more detail in Chapters 3 and 4.

Few rocks of KREEP composition occur in pristine form. Nearly all pristine KREEP rocks are basalts from Apollo 15, and the term KREEP basalt usually refers to these rocks (e.g., samples 15382 and 15386). Some workers have advocated that KREEP basalt is crystallized impact melt whereas others regard it as an extruded magma (Taylor 1982; McKay et al. 1986; Dymek 1986; Spudis and Hawke 1986). The Apennine Bench Formation in Mare Imbrium is a candidate site of origin for the Apollo 15 KREEP basalts (Spudis and Ryder 1985; Spudis and Hawke 1986). The main arguments against the impact-melt hypothesis is that KREEP basalt has low concentrations of siderophile elements and essentially no clasts compared impact-melt breccias. However, most rocks of KREEP composition are impact-melt breccias, and the possibility that KREEP basalts are ponded impact melt that extruded onto the surface has not been ruled out. Virtually all KREEP impact-melt breccias in the Apollo collection were ejected from a basin by the impact that formed them whereas KREEP basalts likely formed in a basin. Ejected melt is more likely to be clast rich than ponded melt and iron metal containing siderophile elements may have settled from ponded impact melt (e.g., Delano and Ringwood 1978). The origin of KREEP basalt is an important unanswered question in lunar science.

KREEP basalts typically contain 40–50% plagioclase, 30–40% low-Ca pyroxene, and minor cristobalite, ilmenite, apatite, merrillite, and Si- and K-rich glass (Spudis and Hawke 1986). Concentrations of highly incompatible elements in Apollo 15 KREEP basalts are typically 90 (Lu) to 310 (Th, U) times those of ordinary chondrites. The bulk Mg' is 60 ± 6. KREEP basalt presents a petrogenetic enigma: the Mg' is much too primitive (high) for such an evolved rock (high concentrations of silica and incompatible elements). The enigma is discussed in more detail in Chapter 4 and in the next section on breccias.

Some rare rocks in the Apollo collection are probably related to KREEP in that they appear have differentiated from magmas of KREEP composition. These include felsite (granite), quartz monzogabbro (quartz monzodiorite), and other rocks that occur as clasts in Apollo 14 breccias (Neal et al. 1989; Jolliff 1991; Marvin et al. 1991; Snyder et al. 1992, 1994; Jolliff et al. 1993).

5.2. Breccias

Lunar breccias are rocks composed of materials from older rocks that were disaggregated or melted by meteoroid impacts. Those materials can exist as (a) mineral and lithic (rock) fragments, (b) crystallized impact melt, or (c) glassy impact melt. Large fragments are called *clasts*; the material binding the clasts is called *matrix*. Breccias are lithified (converted to a solid rock) by the heat and shock associated with meteoroid impacts. Most breccias are *polymict*—they contain fragments from many different older rocks. Some are *dimict*—they contain material from only two sources. *Monomict* breccias are rocks that are re-lithified fragments from a single precursor igneous rock. Idealized locations showing where different kinds of breccia would occur in an impact structure are shown in Figure 2.7.

At the time of the Apollo missions, little work had been done on terrestrial impact craters and no generally accepted classification system existed for impact-produced rocks. As a result, the nomenclature for lunar breccias developed and evolved during the Apollo missions on a piecemeal basis. Terms used in most old, and some new, literature is confusing and duplicative. For example, a common breccia that occurs at the Apollo 17 site has been identified by terms emphasizing, variously, mineralogy (*noritic* breccia; Rhodes et al. 1974),

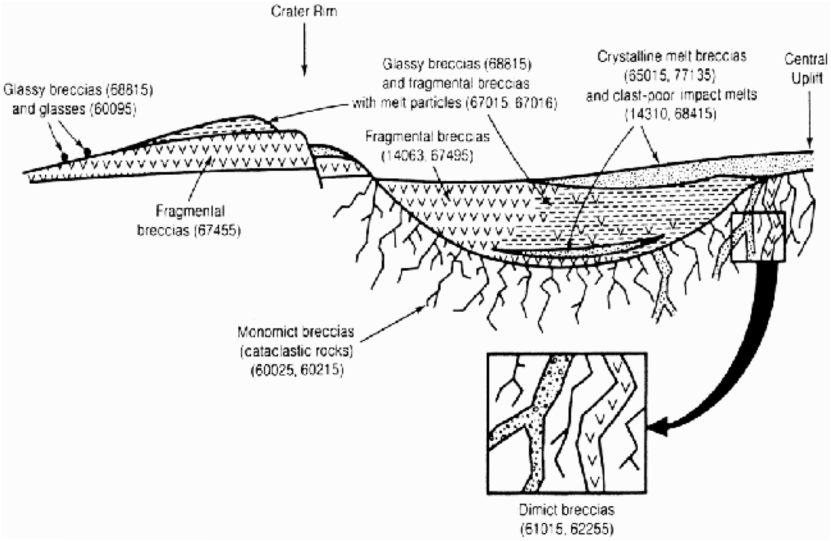

Figure 2.7. Cross-section of an ideal lunar crater showing the relations of different polymict breccia types and possible monomict breccias to the geological environment of the crater (adapted from Stöffler 1981). Numbers indicate actual lunar samples that are examples of the different breccia types. Many lunar polymict breccias may be the result of a series of impacts, such that the target for each new breccia-producing impact is already a polymict breccia.

a chemical composition that is rich, but not too rich, in incompatible elements (*low-K* KREEP; Laul and Papike 1980), texture (*poikilitic breccia*; Spudis and Ryder 1981), implied components (*KREEP-bearing* breccia; Korotev et al. 2003), geographic location of the type specimen (low-K *Fra Mauro*; Vaniman and Papike 1980), and mode of formation (*impact melt* breccia; Stöffler et al. 1980). Such inconsistency provides a hurdle to the newcomer and still confuses the old-timers. Stöffler et al. (1980) produced a consistent, unified classification and nomenclature for lunar highland rocks, including breccias. This is the classification that is followed by most subsequent workers and is given in Table 2.3.

5.2.1. Glassy melt breccias and impact glasses. Glassy materials produced by meteoroid impacts vary widely in texture, depending on the amount of glass present. These materials range from extremely clast-rich breccias with glassy matrices (glassy melt breccias) to glass-rich bodies that are clast-poor or clast-free (impact glasses). Shapes of samples of glassy melt breccias are irregular. Many glassy breccias are ovoid, some are ropy or hollow, and others occur as splashes on rocks (Fruland et al. 1977; Morris et al. 1983; Borchardt et al. 1986; Wentworth et al. 1994). Glassy melt breccias are polymict; they show a wide range of fragment types and there may be more than one generation of glass involved in their formation and lithification. Impact glasses appear to have formed and cooled in single impacts. A distinctive feature of most impact glasses is the presence of a free melt surface, in contrast with most breccias, including glassy melt breccias, which have mechanically broken surfaces. Small impacts lead to glassy melt breccias, and most glassy breccias are younger in solidification age than crystalline melt breccias (Borchardt et al. 1986).

5.2.2. Crystalline melt breccias and impact-melt breccias. A large impact produces a large volume of melt that cools more slowly than melt formed in a small crater. Thus, large impacts produce crystalline melt breccias. Crystalline melt breccias can be formed from impact melt pooled in craters as small as a few kilometers in diameter (Deutsch and

Table 2.3. Classification, characteristics, and examples of nonmare polymict breccias (adapted from Stöffler et al. 1980)

Class	*Main Characteristics*	*Examples*
Fragmental Breccia	Angular clasts in porous, clastic matrix of rock, mineral, and rare glass debris. Some melt clasts may be cogenetic with assembly (suevite). Most are friable.	14063 67015 67455
Glassy Melt Breccia	Coherent glassy or devitrified glass matrix with clasts (melt breccia) or without clasts (impact glass).	60115 68815 60095 79175
Crystalline Melt Breccia (Impact-Melt Breccia)	Rock or mineral clasts or both in an igneous (extrusive)-textured matrix (ophitic, subophitic, poikilitic, dendritic, etc.) May be fine-grained or coarse-grained, and clast-poor to clast-rich.	15455 62295 76015
Clast-Poor Impact Melt	Igneous (extrusive)-textured rock containing meteoritic siderophile-element contamination. Textures can be slightly more heterogeneous than igneous rocks, and rare clasts may be present. Compositions can be unlike those generated by igneous processes.	14310 68415
Granulitic Breccia and Granulite	Rock and/or mineral clasts in an equilibrated granoblastic to poikiloblastic matrix. Clasts may not be obvious, and poikilitic textures may mimic those of, or be transitional to, plutonic rocks. Compositions reflect siderophile-element contamination.	79215 77017 67955 78155
Dimict Breccia	Veined texture of intrusive, dark, fine-grained crystalline melt breccia with coarser-grained light-colored breccia consisting of plutonic or metamorphic fragments or both. In some cases, the dark-light relationship appears mutually intrusive.	61015 62255 64475
Regolith (Soil) Breccia	Lithified regolith. Regolith fragments including impact glass and volcanic glass and volcanic debris with a glassy matrix. Commonly retains some solar wind gases through the lithification process. See also the lunar meteorite regolith breccias listed in Table 2.1.	14318 15299 60019

Stöffler 1987). Crystalline impact-melt breccias resemble rocks crystallized from a magma, with clast proportions ranging from a few percent to more than half the rock. As the amount of clastic debris increases, the matrix tends to be more glassy, thus crystalline melt breccias grade into the glassy melt breccia group. Many of the clasts show evidence of shock metamorphism or resorption by the melt. Melt breccias in the Apollo collection typically have high concentrations of siderophile elements resulting from contamination by the impacting meteoroid. The siderophile elements are carried in FeNi metal from the impactor, which has melted and re-crystallized along with the silicate and oxide minerals. Vesicles are abundant in some samples, and there is evidence that vesicle abundance correlates with clast load, i.e., vesicles are more likely to be frozen into melt that cooled rapidly as a result of a high clast/melt (Korotev 1994).

Crystalline melt breccias from the Apollo missions are composed of nonmare material. Crystalline impact-melt breccias composed mainly of mare material are not known; most mare breccias are glassy. Crystalline impact-melt breccias composed mainly of mare material likely exist on the Moon, but for impacts into the maria large enough to produce a significant volume of crystalline melt, the zone of impact melting lies mainly beneath the surficial layer of mare basalt. Crystalline melt breccias are common at all the Apollo highland sites and they also occur in the regolith of the mare-basalt-dominated Apollo 11 and 12 sites (e.g., Simon et al. 1983; Simon and Papike 1985).

The chemical compositions of crystalline melt breccias span nearly the entire range of compositions observed in nonmare samples, from 2% to 11% FeO (33–14% Al_2O_3; Fig. 2.2). Breccias at the Fe-poor end of the range were clearly formed by impacts into the feldspathic highlands. It is the melt breccias on the mafic (high-Fe) end of the trend that are enigmatic. Virtually all mafic impact-melt breccias are rich in incompatible elements and those from Apollo 12 and 14 are essentially identified with KREEP. Early studies reasonably concluded that (1) given that mafic impact-melt breccias are more mafic and richer in KREEP than the surface of the feldspathic crust (FHT of Fig. 2.2) and (2) the breccias are found in basin ejecta deposits, the crust must become more mafic with depth and KREEP is concentrated beneath the feldspathic crust (Ryder and Wood 1977). However, one of the most significant new views provided by Lunar Prospector is that KREEP is concentrated at the surface in and only in the Procellarum KREEP Terrane and that, except perhaps for South Pole-Aitken, basins distant from the Procellarum KREEP Terrane show no hint of having exhumed KREEP. These observations lead to an alternate hypothesis, that all mafic, KREEP-rich impact-melt breccias were formed by impacts into the Procellarum KREEP Terrane, most likely the impacts forming the Imbrium and, perhaps, Serenitatis basins (Haskin et al. 1998).

To a first approximation, the composition of all of the mafic impact-melt breccias of the Apollo collection can be modeled as mixtures of (1) a KREEP-norite component similar to KREEP basalt of the Apollo 15 site, (2) an olivine or dunite (Fo_{90}) component (possibly a troctolite), and (3) material of the feldspathic highlands (Fig. 2.8). The KREEP component is the dominant component of the mixture (40–95%). Proportions of the three component vary among mafic melt breccias found at a given site and among different Apollo sites. The feldspathic component of the breccias (4–46%) is mainly clastic and is more abundant in breccias from sites distant from the Procellarum KREEP Terrane (Apollo 16 and 17; Fig. 2.8). Melt breccias with greater concentrations of incompatible elements tend to be less diluted with the olivine and feldspathic components. Overall, the compositional variation among mafic impact-melt breccias is consistent with mixing between the Procellarum KREEP Terrane and Feldspathic Highlands Terrane.

The mafic impact-melt breccias of the Apollo missions tell us that the melt zone of the impactor(s) that formed them was dominated by KREEP, in some form, but that there was also a substantial amount of non-uniformly distributed, highly magnesian olivine in the target area (0–30%; Fig. 2.8). Mass balance allows that the actual KREEP component of the breccias can have a more primitive composition, one corresponding to Apollo 15 KREEP basalt minus a normative component of Fo_{90} olivine (Fig. 2.8). This observation may account in part for the KREEP enigma (Section 3.4.2)—perhaps all KREEP sampled by the Apollo missions is an impact mixture of a low-Mg' magma ocean residuum, the urKREEP of Warren and Wasson (1979), and a mantle-derived, olivine-rich component (Korotev 2000).

Most of the crystallization ages of about 3.9 Gy that have been obtained on lunar rocks have been obtained on mafic, KREEP-rich impact-melt breccias. Compared to crystalline breccias formed from feldspathic highlands material, mafic breccias have high concentrations of all of the radioactive elements used in geochronology. Among the mafic breccias discussed here, only the group-A breccias of Apollo 15 (on Fig. 2.8, represented by the point lying closest to the KREEP apex) may to have a substantially different age, 1–1.5 Gy [see discussion of Ryder (1985) for sample 15405].

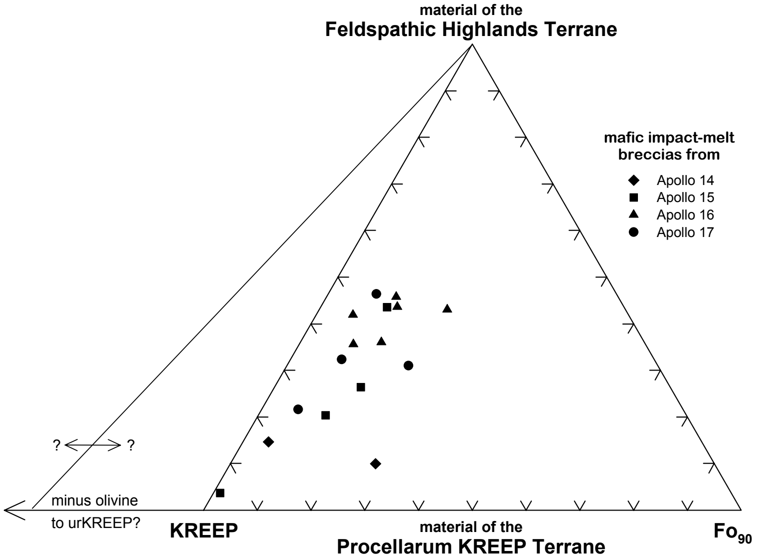

Figure 2.8. Mafic impact-melt breccias from the Apollo missions vary in composition, but compositional groupings occur (e.g., Apollo 15 type D), each represented by a point. The bulk composition of each breccia group corresponds to a mixture of a (1) KREEP component generally similar to Apollo 15 KREEP basalt, (2) a dunite or olivine component of Fo_{90} composition, and (3) feldspathic material of the highlands (Korotev 2000). Variation in the proportions of the three components accounts for the compositional variation among the breccias (e.g., Al/Fe, Mg/Fe, and Th/Fe ratios).

5.2.3. Clast-poor impact melts. Crystalline melt breccias that have so few clasts that they have textures similar to igneous rocks are *clast-poor impact melt breccias* or, in the total absence of clasts, *impact-melt rocks*. In many cases it is difficult to distinguish between such impact-produced rocks and pristine lunar igneous rocks, particularly on the basis of small thin sections typical of lunar samples. Much research and discussion has been directed to distinguishing between clast-poor impact melts and extrusive igneous rocks. High concentrations of siderophile elements in proportions characteristic of meteorites are typically used as a criterion of impact-melt origin. Another test is whether a rock has a bulk composition that is representative of a melt. On this basis, KREEP-like rocks from Apollo 14, which have more plagioclase than a corresponding low-pressure lunar lava (constrained to the pyroxene-plagioclase cotectic) have been classified as clast-poor or clast-free impact melts, as opposed to volcanic KREEP basalts (as found at Apollo 15).

5.2.4. Granulitic breccias and granulites. Granulitic breccias were formed during the alteration and recrystallization of older breccias that have been subjected to high temperatures (~1000°C) since they were formed. Under these conditions the original textures have been obliterated during recrystallization and replaced by an even-grained granulitic texture. A completely recrystallized rock that retains none of its original texture is a granulite. The recrystallization textures are characterized by rounded or *equant* polyhedral grain shapes with triple-junction grain boundaries common (i.e., granoblastic texture) or the presence of small bead-like crystals enclosed within larger crystals (poikiloblastic texture), and by an absence of typical volcanic textures (Bickel et al. 1977; James and Hammarstrom 1977; Warner et al. 1977; Stöffler et al. 1980; Cushing et al. 1999).

Granulitic breccias contain mineral or lithic clasts or relicts of clasts, whereas granulites do not. Granulites are less abundant than granulitic breccias. Both rock types commonly consist of a mosaic of grains whose boundaries meet at angles of about 120°, a texture produced by thorough recrystallization (Stewart 1975). Mineral compositions are also uniform and equilibrated. All samples are aluminous (25–29% Al_2O_3) with wide a range of *Mg´* (56–77; Lindstrom and Lindstrom 1986) and low abundances of the incompatible elements. All granulitic breccias and granulites are contaminated with siderophile elements of meteoritic origin, indicating that they were produced in meteoroid impact melts before they were recrystallized. Ferroan granulitic breccias have compositions consistent with derivation from igneous rocks of the ferroan-anorthositic suite. However, the composition of magnesian granulitic breccias (*Mg´* > 70) are not consistent with any mixture of known pristine rocks (Korotev and Jolliff 2001; Korotev et al. 2003). The magnesian precursor of magnesian granulitic breccias appears to be a feldspathic lithology largely unrecognized in pristine form in the Apollo collection. Most granulitic breccias were found in the Apollo 16 and 17 collection, but they are also common as clasts in the feldspathic lunar meteorites (Korotev et al. 2003b).

5.2.5. Dimict breccias. Dimict breccias are relatively rare among the lunar samples. They consist of two distinct lithologies combined into a single rock. In most examples, the two lithologies are mutually intrusive, i.e., neither one can be defined as the host rock. The samples generally resemble complex veins or dikes of dark and light components. The dark material is a fine-grained crystalline melt breccia or a nearly clast-free impact melt rock. The light-colored material is, in most cases, an anorthositic breccia whose main constituents are crushed and shattered (cataclastic) anorthosite fragments. Dimict breccias cannot be recognized in samples less than a few centimeters across, because the scale of mutual intrusion is on that order.

All of the few recognized dimict breccias are from the Apollo 16 site. (In an older classification as "black-and-white rocks," some similar Apollo 15 samples were included with them.) The dark crystalline melt breccia is similar in all samples. It has about 21% Al_2O_3, it is moderately enriched in incompatible elements (James et al. 1984; McKinley et al. 1984), and it has among the highest concentrations of meteoritic siderophile elements of any lunar rock type (Korotev 1994, 1997). The impact melt phase of the Apollo 16 dimict breccias is one of the least mafic of mafic impact-melt breccias of Figure 2.8. The white portion of the breccias varies from nearly pure cataclastic ferroan anorthosite to less feldspathic breccias (but nearly all containing more than 30% Al_2O_3; James et al. 1984; McKinley et al. 1984). Dimict breccias are believed to have been produced in the shattered rocks injected by and mixed with impact melt below an impact crater (Stöffler et al. 1980; James et al. 1984). In large impact events the melt could have been created and the older anorthositic breccia could have been shattered and remobilized at the same time.

5.2.6. Fragmental breccias. Fragmental breccias are composed of fragments of rocks, commonly including earlier-formed breccias, that have been lithified by shock compaction during a meteoroid impact. The matrix consists of finer-grained fragments of the same material; there is no chemical cementing agent. Brecciation and lithification occurs only by impact processes, thus the degree of coherency is a function of shock pressure, which in turn is a function of location within the impact target region and amount of intergranular melt produced, if any. Fragmental breccias can be composed of any rock type, and some consist entirely of feldspathic highlands material and others consist mainly of mare material. Several of the lunar meteorites are fragmental breccias.

5.2.7. Regolith breccias. Regolith breccias are rocks composed of regolith that was lithified by shock compaction or heating. Regolith breccias differ from fragmental breccias in containing lithologies such as glass spherules and agglutinates that can only be produced or acquired at or above the lunar surface. The distinction between regolith breccias and fragmental breccias is not always clear because regolith lithologies may be rare or not present in every thin section of a regolith breccia. Another characteristic of regolith breccias is that they are rich in solar-wind implanted gases compared to other types of breccias because they contain a high proportion of fine-grained material (high surface to volume ratio) that was exposed at the lunar surface (Section 8). Some regolith breccia are glassy, but many are not. Regolith breccias range from friable clods to highly coherent rocks. For example, some Apollo regolith breccias largely disaggregated between collection on the Moon and arrival at the NASA curatorial facility in Houston (e.g., sample 73131; Korotev and Kremser 1992). In contrast, many of the lunar meteorites are regolith breccias, and these rocks survived being blasted off the Moon, the stress of passing through Earth's atmosphere, and a hard landing on Earth (Warren 1994, 2001). Vesicles in glassy regolith breccias are abundant and can result from escaping solar wind-volatiles; in fact, highly vesicular fusion crusts on regolith-breccia lunar meteorites likely form in this way. Regolith breccias have a wide range of compositions because they can be formed in any regolith.

Regolith breccias are important for at least three reasons. First, they are fossil regoliths that at some point became closed to further input of material. Consequently, some regolith breccias represent very ancient regoliths and thus provide information about conditions in the past (McKay et al. 1986). For example, the Apollo 16 regolith developed upon the ejecta deposit of the Imbrium basin. The ancient regolith breccias of Apollo 16 contain virtually no mare volcanic material whereas the present Apollo 16 regolith does (McKay et al. 1986; Korotev 1996). This difference implies that the mare component of the Apollo 16 regolith results from post-Imbrium redistribution of material. Second, some regolith breccias represent regoliths from places that are distant from where the breccias were collected. For example, the Apollo 12 and 14 sites are in the Procellarum KREEP Terrane and their regoliths are dominated by mafic, KREEP-rich impact-melt breccias and mare basalt (Apollo 12). Yet, a few feldspathic and KREEP-poor regolith breccias that surely formed in the Feldspathic Highlands Terrane have been found among samples collected at both sites (Simon et al. 1985; Jerde et al. 1990). These breccias were delivered to the Apollo 12 and 14 sites by impacts in the feldspathic highlands. The ultimate examples, of course, are the numerous lunar meteorites found on Earth that are regolith breccias from the Moon. Some regolith breccias are dissimilar in detail to any sample of the Apollo or Luna regolith fines (e.g., Jerde et al. 1987; Jolliff et al. 2003), and these breccias provide information about otherwise unsampled places on the Moon. Third, because a regolith breccia is a thoroughly polymict rock consisting of soil, its composition is more likely to represent the average composition of the surface of the area at which it formed than is any more primary rock type such as mare basalt or anorthosite. This aspect is particularly important for the lunar meteorites because, although we do not know where on the Moon any of them originate, we can be reasonably certain their compositions represent the regolith at their points of origin (e.g., Section 7).

5.3. Mare volcanics

The mare basaltic lavas formed by melting of the solid interior (mantle) of the Moon, probably at depths of 100-500 km, followed by the buoyant rise of molten rock through the mantle and eruption to the lunar surface as a result of overpressurization. Two types of volcanic materials have been erupted at the lunar surface:

(1) Basaltic lavas/flows. Lunar lava flows erupted from fissures in the lunar surface. Because lunar basalts contain more Fe and less Si and Al than terrestrial basalts and were much hotter because of a lack of water, the lavas possessed low viscosities and readily formed thin, widespread flows. The lavas cooled at different rates, dependent on the thickness of individual flows, to produce a variety of mineral textures. Many lava flows accumulated in thick stacks that partly filled many of the mare basins.

(2) Pyroclastic deposits. Gases, probably CO, contained within rising magmas, were explosively released when the magmas approached the surface of the Moon (e.g., Nicholis and Rutherford 2005). As lavas poured from a fissure vent, gases were released that effectively expelled a fountain of molten droplets. Such a "fire fountain" produces volcanic droplets,

subsequently found as glass beads of various compositions and colors (e.g., the well known Apollo 17 'orange' soil).

On the Moon, the lava fountains associated with eruptions of basalt formed small, submillimeter glassy beads. Deposits of these beads are widely dispersed around lunar volcanic vents because of low gravity and eruption into a vacuum. Such pyroclastic deposits are similar to the volcanic ash deposited around lava fountains on Earth. Two striking examples of lunar pyroclastic rocks are the orange soils (although they really are not soils, but rather volcanic ash deposits) from the Apollo 17 landing site and the green glass from the Apollo 15 landing site. Green-glass "clod" sample 15426 contains variable proportions of glass beads in different subsamples, but a thin section of green glass-rich sample 15427 regolith breccia consists of 90% green glass shards and spherules (Ryder 1985). The "orange soil" from Shorty crater – 74220 – is >90% glass beads with an average size of 44 μm. The "black soil" just below the orange soil contains the same proportion of glass beads, but they appear black because they cooled a bit slower and contain skeletal crystals of olivine and ilmenite. In the 74001/2 drill core, the deposit is >99% pyroclastic material. Orbital photographs of the lunar surface reveal dark-mantle deposits, many surrounding apparent volcanic vents, which have been interpreted as representing such volcanic ash and glass of pyroclastic origin.

Lunar basalts have been classified, to a first approximation, by their TiO_2 contents (Fig. 2.9**)**, with additional divisions based upon Al_2O_3, and further subdivided by K_2O contents (Neal and Taylor 1992). Six of the nine missions to the Moon that retrieved samples returned mainly mare basalts and fragmented, consolidated basaltic breccias. A useful plot of the various basalt and volcanic glass compositional data is shown in Figure 2.10, which addresses the subdivisions of these extrusive materials within the context of elements that can be detected by remote sensing (Fe, Ti, K). On this plot, samples of basalt types have compositions that form clusters, making this a useful classification scheme.

5.3.1. Mare basalts. Mare basalts are exposed over 17% of the lunar surface area and are thought to make up less than 1% of the lunar crustal volume (Head 1976, Head and Wilson 1992). They primarily fill multi-ringed basins and irregular depressions on the Earth-facing hemisphere of the Moon. On the lunar far side, limited patches of mare basalts occur in younger craters (e.g., Tsiolkovsky) and in some basins, such as Ingenii and Apollo (see Fig. 1.21, Chapter 1). This preponderance of mare basalts on the Earth-facing hemisphere of the Moon has been attributed to the thicker highland crust on the far side of the Moon and the gravitational attraction of the Earth (Kaula et al. 1972, 1974; Toksoz et al. 1974). More recently, Haskin et al. (2000) suggested the possibility that this distribution is broadly related to non-uniform distribution of heat-producing residua relating to early lunar differentiation and thermal evolution (see Chapter 4). The general style of volcanic activity was the eruption of large volumes of magma from relatively deep sources (not shallow crustal reservoirs) with high effusion rates (Head and Wilson 1992). The mare basalts and pyroclastic glasses vary considerably in terms of their compositions, textures, and distribution across the Moon. A wide range of variation in terms of TiO_2 concentrations is seen both in the samples and in remote sensing. A key question, to be addressed in a later section, is this: do the samples fairly represent the diversity of basalt and pyroclastic glasses on the Moon? In some ways, the diversity in the samples far exceeds what can be discerned with remote sensing, and certainly, the diversity observed among the samples provides a key to interpreting variations in the remotely sensed data. This is one of the fundamental lessons to be learned with regard to the exploration of Mars and other planetary objects.

Below, an overview is given of the major basalt types. Interested readers are referred to more thorough treatments in several review articles (e.g., Neal and Taylor 1992; Papike et al. 1998). A tabulation of some 500 chemical analyses of the basalts and volcanic glasses is given on the electronic archive associated with this book.

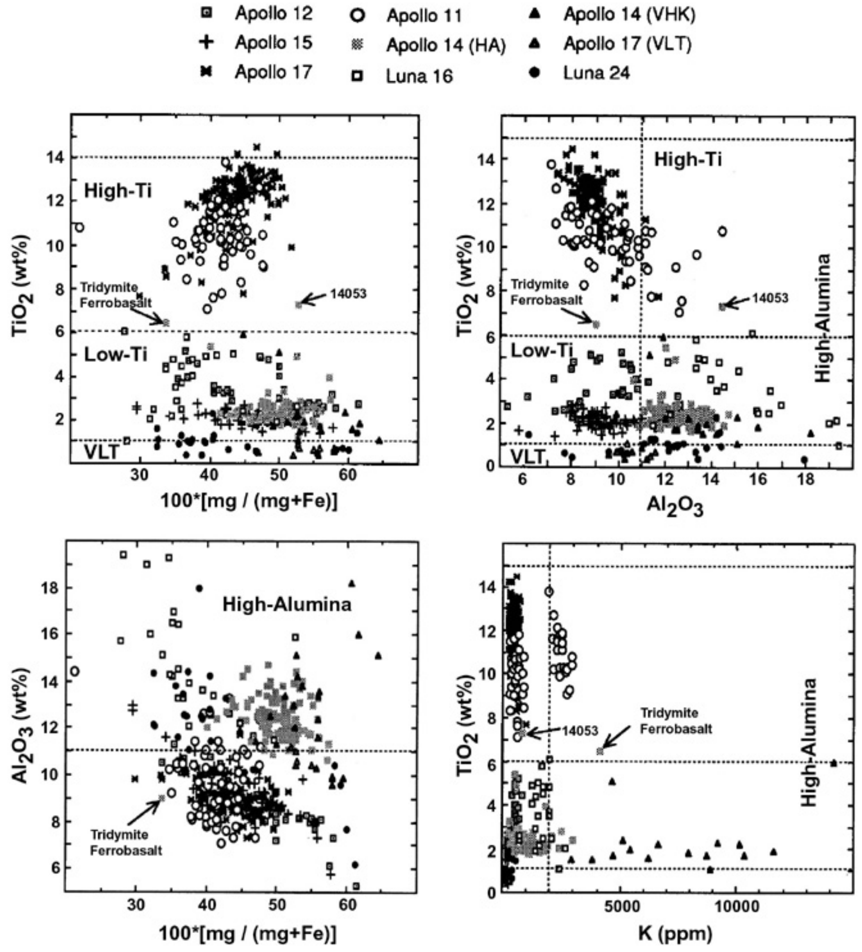

Figure 2.9. Plot of 500 basalt compositions illustrating the lunar classification (data and figures after Neal and Taylor 1992). Notice the distinctions between the different classes of basalt as based initially on TiO_2, secondarily on Al_2O_3, and lastly on K_2O.

High-Ti mare basalts. Basalts collected from the Apollo 11 and 17 sites are mainly high-Ti mare basalts (Figs. 2.8, 2.9). The Apollo 11 high-Ti basalts have been subdivided into two main groups, low-K and high-K. The Apollo 17 high-Ti basalts include one group that is much like Apollo 11 low-K basalts, as well as another high-Ti group, which is more abundant, that contains even more TiO_2 and more of the opaque mineral ilmenite (Table 2.4). Even within these groups, the compositions of high-Ti basalts vary significantly from sample to sample. Explanations for these differences are complicated by the fact that all mare basalt samples were collected as loose blocks in the regolith and no identifiable lava flows were sampled directly on the lunar surface. Nevertheless, studies of terrestrial lava flows suggest that the observed variations from sample to sample reflect variation both within and between individual lava flows.

Low-Ti mare basalts. A wide variety of low-Ti mare basalts were collected at the Apollo 12, Apollo 15, and Luna 16 landing sites on various maria, as well as at the Apollo 14 landing site (Figs. 2.9, 2.10). The Apollo 12 and 15 varieties each consist of two main basalt types,

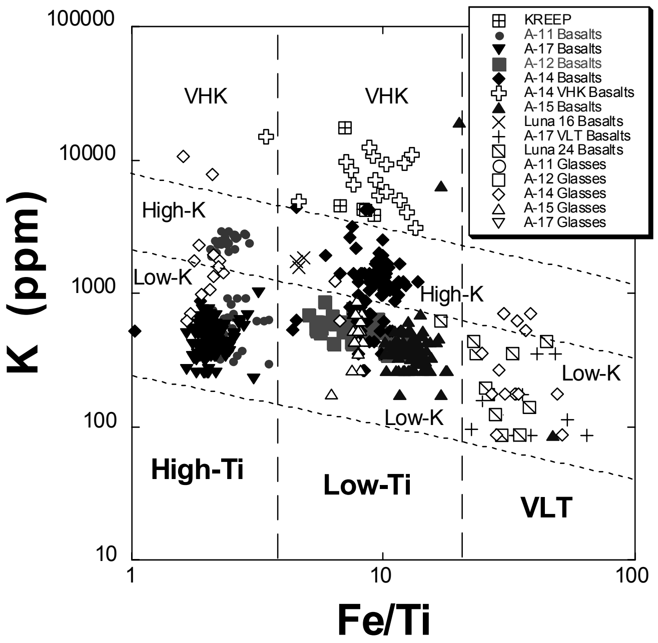

Figure 2.10. Plot of K vs. Fe/Ti shows the major types of basalts and volcanic glasses is terms of chemical components that can be determined remotely (database from Neal and Taylor 1992). A similar pattern exists for Fe/Ti vs. Th, but the database is much smaller.

olivine basalts and pigeonite (low-Ca pyroxene) basalts. In general, the olivine basalts have more MgO and less CaO, Al_2O_3, and TiO_2, than do the pigeonite basalts at the same site. Like the high-Ti mare basalts, none of these low-Ti basalts crystallize plagioclase feldspar early as they cool. Both types show clear evidence for the early separation of olivine or pigeonite, but not of ilmenite. The resulting trends of chemical composition show increasing TiO_2 and Al_2O_3 with decreasing MgO (Fig. 2.9). In addition to these basalts, some of the low-Ti basalts collected at the Apollo 12 site are noticeably richer in ilmenite than the others; these have been designated ilmenite basalts. In general, the REE abundances in low-Ti basalts are lower than in the high-Ti basalts, although both groups have the same bow-shaped pattern and both have negative Eu anomalies. Concentrations of other incompatible elements (i.e., those elements that tend to stay in the melt rather than in the early crystallizing minerals), such as Sr and U, are also lower in the low-Ti basalts than in the high-Ti basalts.

Aluminous, low-Ti mare basalts contain more $A1_2O_3$ than do those from the Apollo 12 and 15 sites (Fig. 2.9). Three major categories of aluminous mare basalts can be distinguished on the basis of their location and chemistry: those from the Luna 16 site and two types from the Apollo 14 site. Although the petrologic record has been obscured by the early catastrophic impact history of the Moon, a record of pre-mare volcanics retained in highland high-Al soils and breccias as clasts (e.g., Taylor et al. 1983; Dickinson et al. 1985, Neal et al. 1988). In addition, there are very-high-K, low-Ti basalts associated with the high-alumina basalts at the Apollo 14 site (Fig. 2.10). Although this 2000-12,000 ppm K_2O range is “very-high” for the Moon, it is not to be confused with values from terrestrial rocks many times higher. The Luna 16 mare basalts contain the most TiO_2 of any of the aluminous low-Ti basalts, averaging about 5 wt%. They also have distinctive REE patterns that are characterized by higher concentrations of the light REE (La through Sm) than the heavier REE. The Luna 16 basalts do, however, display the

Table 2.4. Summary of average modal data for the mare basalts (modified after Papike and Vaniman 1978)

Basalt type	***Opaques***	***Pyroxene***	***Feldspar***	***Olivine***
A-17 high-Ti	24.4	47.7	23.4	4.6
A-11 high-K/high-Ti	20.6	57.5	21.7	0.1
A-17 low-K/high Ti	15.1	51.6	33.3	--
A-11 low-K/high Ti	14.6	50.9	32.2	2.3
A-12 ilmenite	9.3	61.1	25.9	3.6
A-12 pigeonite	9.1	68.4	21.1	1.4
A-12 olivine	7.1	53.5	19.2	20.2
A-15 olivine-normative	5.5	63.3	24.1	7.0
A-15 quartz-normative	3.7	62.5	33.8	--
Luna 16 high-Al	7.1	51.5	41.2	0.1
A-14 high-Al	9.0	37.1	43.9	10.0
A-14 VHK/high-Al	8.0	33.2	46.8	12.0
Luna 24 “VLT”	1.8	48.6	39.1	10.4
A-17 “VLT”	1.0	61.7	31.9	5.4

Apollo 14 data from Neal et al. (1988a, 1989). The opaque minerals do not transmit light as viewed with a microscope. The major opaque mineral in lunar basalts is ilmenite (up to 25 vol%), with lesser abundances of spinel phases (chromite, ulvöspinel), troilite, and native FeNi metal.

same typical bow-shaped pattern, with a negative Eu anomaly, that is characteristic of almost all mare basalts.

Very-low-Ti (VLT) mare basalts. VLT basalts were first discovered as tiny fragments in the Apollo 17 drill core (Vaniman and Papike 1977). The basalt particles collected by Luna 24 from Mare Crisium were also VLT mare basalts (Figs. 2.9, 2.10). Besides containing lower concentrations of TiO_2 (<1.5) than other mare basalts, these basalts are distinctive in having low concentrations of REE and other incompatible elements; they also have REE patterns that are not bow-shaped. Instead, the REE contents rise continuously from La to Lu. All but one fragment of the Luna 24 basalts have small negative Eu anomalies. A similar basaltic composition, the Apollo 15 green-glass pyroclastic material, has comparable chemical characteristics.

5.3.2. Pyroclastic deposits. Glass beads and fragments are a common component in the lunar soil; they are found at all the Apollo sites, in several of the Luna samples, and in lunar meteorites. The glasses have a broad range in both composition and texture**.** Lunar glasses have been produced by two very different processes, meteoroid impacts (impact melting) and volcanic eruptions. Glasses formed by impact melting can generally be recognized by their heterogeneous textures (e.g., swirls and schlieren, and incompletely melted clasts) and compositions. The volcanic glasses formed in a fundamentally different way, in gas-driven “fire-fountain” eruptions that leave deposits made up of glass droplets that have chilled from the spray of molten lava. The volcanic glasses have volatile coatings produced during fire-fountaining (Meyer et al. 1975). Except for Apollo 17 orange glass, which was most likely collected in place, i.e., where the glass droplets landed, no field or stratigraphic evidence exists to show that any other sample of lunar glass is volcanic, but investigators have developed other criteria for distinguishing between these two types of glasses. These criteria are discussed in detail by Delano (1986).

Evidence of lunar fire-fountaining is preserved not only as spherical glass beads, but also as dark mantling deposits (Wilhelms and McCauley 1971, Head 1974, 1976; Head and Wilson 1992). Remote-sensing data indicate that deposits of volcanic glasses are fairly abundant on the Moon. The dark-mantle deposits include the one sampled in the form of orange and black glass by the Apollo 17 mission. Such pyroclastic deposits often occur on the edges of the maria and overlap onto the adjacent highland regions. As their name implies, these deposits have low albedo (they are poor reflectors of visible light) and so appear dark. Gaddis et al. (1985) have shown that not all pyroclastic deposits are necessarily dark. Some thick dark-mantle deposits exhibit low intensities on depolarized 3.8-cm radar maps, indicating the absence of surface scatterers. Gaddis et al. (1985) suggest that numerous other areas are likely to contain pyroclastic deposits. Some of these other pyroclastic units may be as large as the observed dark mantle deposits. If the dark mantle deposits and similar units are indeed pyroclastic, then they should be composed of relatively homogeneous glasses with concentrations of volatile elements on their surfaces, similar to Apollo 15 green glass and the Apollo 17 orange glass.

In these dark-mantle deposits, there is abundant evidence of basaltic volcanism that predated formation of the younger basins (i.e., pre-Nectarian). These have been identified through remote sensing as “cryptomaria” (e.g., Hawke et al. 1990; Head and Wilson 1992; Head et al. 1997; Antonenko et al. 1995). However, numerous studies imply that large volumes of these basaltic magmas (“cryptomaria”) were erupted (Metzger and Parker 1979; Davis and Spudis 1985, 1987; Head and Wilson 1992; Antonenko et al. 1995). Head and Wilson (1992) have suggested that perhaps up to a third of the erupted basalts at the lunar surface were such cryptomaria, now buried by later-formed impact-ejecta deposits.

6. REGOLITH COMPOSITION

This section reviews aspects of regolith composition, as it is known from samples, that are relevant to interpreting data obtained remotely from the lunar surface. The discussion focuses on chemical elements for which the surface concentrations can be determined directly or indirectly from orbit.

6.1. Chemical composition data for regolith samples

Data on the chemical composition of lunar regolith are abundant. Most of these data are available in the annual *Proceedings of the Lunar [and Planetary] Science Conference* published from 1970 through 1992. Although compilations of averages are also available (McKay et al. 1991; Haskin and Warren 1991; Korotev and Gillis 2001 [Apollo 11]; Korotev 1996, 1997 [Apollo 16]; Korotev and Kremser 1992 [Apollo 17]), there are many problems and pitfalls associated with obtaining “the composition” of a lunar soil sample (and some of these problems are even worse for rocks). Problems include: (1) There is no Apollo or Luna soil sample for which data are available for all chemical elements. For many samples, no data are available for some important elements, e.g., MgO. (2) Most laboratories that have analyzed lunar samples have used only one or two analytical techniques and, consequently, have determined the concentrations of only some elements; some labs determined only a few. Some important element pairs (e.g., Ti and Fe, Fe and Mg, K and Th, Gd and Sm) were not always precisely measured together on a single subsample. (3) For any given element, some techniques are more precise and reliable than others and some laboratories consistently provided better data than others. Even for data from a given laboratory, some elements were measured more precisely than others. It is not always easy to identify the precise and imprecise data. (4) Some available data are systematically erroneous. (5) A common test of the veracity of data reported for the major elements is whether the sums-of-oxides is close to 100%. SiO_2 accounts for almost half the mass of any sample, thus SiO_2 data are essential for checking the oxide sum. However, SiO_2 data are often not available or are imprecise. (6) Analyzed subsample masses are highly variable and often not reported. (7) Finally, data for lunar samples suffer from sampling error, which acknowledges that no two subsamples of any given sample have exactly the same composition. Sampling error occurs because lunar samples are not homogenized prior to allocation, analyzed subsample masses are small, typically 10–500 mg for lunar soils, and any given subsample contains only a finite number of particles or mineral grains, some of which are large or have unusual compositions. Elements typically affected by sampling error include Ti (in ilmenite), Zr, Hf, Th, and U (in zircon), REEs (rare earth elements), Th, and U (in RE-merrillite), K, Rb, Cs, Ba, Th, U (in minerals associated with felsite), Na, Sr, and Eu (in alkali feldspar), and Fe, Ni, Co, Ir, Au, etc. (in metal of meteoritic origin). Sampling error is common in the lunar-sample literature and cannot be overlooked when compiling data.

For these various reasons, calculation of simple means from all available data can lead to systematic errors that are unacceptable for some purposes. For example, if in a given source of data the reported concentration of FeO or La is anomalously high because of sampling error (an excess of olivine or RE-merrillite), other elements will be affected because of the various mineral-controlled interelement correlations discussed in Section 6.2. If the report does not also include data for MgO or Sm, inclusion of the FeO or La data in the average will lead to systematic errors in calculated mean ratios of correlated elements (e.g., FeO/MgO or La/Sm).

Sparse data for a sample can lead to other types of errors as well. For example, the reported I_s/FeO (Section 9.2.2) value of sample 64501 is 61 (Morris 1976). The value is based on an FeO concentration of 5.2%, which is the mean of pre-1976 data from three sources. However, the value of one of those sources is highly anomalous. Assuming the anomalous datum is the result of analytical or computational error, an assumption confirmed by post-1976 data, the FeO concentration of 64501 is more nearly 4.45%, which leads to I_s/FeO of 71, not 61. This difference is a significant error associated with a erroneous data from a single laboratory.

With these various caveats in mind, we present selected averages of concentrations of a number chemical elements in surface and trench soils from the Apollo and Luna missions in Table 2.5. For the simple missions in which only one or two regolith samples were taken (e.g., Apollo 11 and all Luna missions), the values presented are based on all available data. For the more complex missions (the later Apollo missions), the compositional extremes are listed.

6.2. Mineral and rock control of regolith composition

6.2.1. FeO and metallic iron. Most analytical techniques that have been used to determine the bulk concentration of iron in lunar samples (mainly X-ray fluorescence and neutron activation) provide the total concentration of iron regardless of its oxidation state. By geochemical convention, this concentration (and that of other major elements) is usually expressed as the percent oxide (e.g., Table 2.5). Because essentially no Fe on the Moon exists as Fe^{3+}, iron concentrations in lunar samples are commonly reported as percent FeO. In lunar breccias and soil, however, particularly those from the feldspathic highlands, a significant fraction of the Fe exists as metal (Fe^0). Some studies have measured the concentration of metallic Fe in the regolith directly by magnetic techniques. These studies conclude that the lunar regolith contains, on average, 5.4 ± 1.8 mg/g of Fe metal ("~0.5 equivalent wt%" as Fe^0; Morris 1980). This mean and standard deviation corresponds to 0.69 ± 0.23% as FeO. Because most of the metallic iron in feldspathic soils derives from meteorites, a greater fraction of the total iron exists in the metallic state for feldspathic soils than for mare soils. For example, approximately 10% of the (total) iron in the feldspathic lunar meteorites, which represent typical surface material of the highlands (Section 7), is of extralunar origin (asteroidal meteorites; Korotev et al. 2003b) and most of this iron likely occurs as metal. For example, in mature Apollo 16 soil, which contains a high proportion of metal-rich, mafic impact-melt breccia, about 15% of the iron is metal derived from meteorites (Korotev 1997, 2000) and another 3% is nanophase iron (Morris 1980).

Although no quantitative data are available, it is likely that only a small fraction of the metallic iron in the lunar regolith is indigenous to igneous and plutonic rocks. Most metallic iron in the regolith derives from four other sources.

Table 2.5. Compositions of soils from the Apollo (A) and Luna (L) missions

mission	type	location or station no.	note	SiO_2 %	TiO_2 %	Al_2O_3 %	FeO %	MnO %	MgO %	CaO %	Na_2O %	K_2O %	Cr_2O_3 %	P_2O_5 %	S %	Σ %	*Mg´* %	Li ppm	Na ppm	P ppm
A11	only sample	lunar module	1	42.0	7.5	13.5	15.8	0.21	7.9	12.0	0.44	0.14	0.30	0.10	0.11	100.1	47	12.	3200	400
A12	typical	most of site	2	46.1	2.7	12.6	16.5	0.21	10.2	10.3	0.46	0.24	0.38	0.30	0.08	100.0	52	17.	3400	1300
A12	atypical	Head Crater	3	47.0	2.5	14.3	14.6	0.20	9.1	10.6	0.64	0.39	0.33	0.39	0.07	100.1	53	23.	4800	1700
A14	typical	most of site	4	47.7	1.7	17.4	10.5	0.14	9.4	10.9	0.70	0.52	0.20	0.49	0.10	99.8	61	27.	5200	2100
A14	atypical	Cone Crater	5	n.a.	1.6	16.8	10.0	0.13	9.8	10.6	0.81	0.64	0.20	0.51	0.08	–	64	n.a.	6000	2200
A15	highest Fe	9a, edge of rille	6	46.2	2.0	10.4	19.8	0.25	11.1	9.6	0.30	0.094	0.53	0.11	0.06	100.4	50	10.	2200	500
A15	highest Mg	7, Apennine Front	7	46.3	1.3	15.6	13.0	0.17	11.9	10.4	0.41	0.16	0.36	0.16	0.07	99.8	62	n.a.	3000	700
A15	highest Th	6, Apennine Front	8	46.7	1.5	16.4	12.2	0.16	10.4	11.2	0.46	0.21	0.34	0.22	0.08	99.8	60	9.	3400	1000
A15	lowest Fe	2, Apennine Front	9	46.5	1.3	17.6	11.6	0.16	10.4	11.5	0.42	0.18	0.31	0.16	0.07	100.1	62	10.	3100	700
A16	typical mature	all Cayley	10	44.9	0.59	26.7	5.44	0.07	6.0	15.3	0.46	0.121	0.111	0.12	0.07	99.9	66	8.	3400	540
A16	highest Fe	5 & 6	11	45.0	0.66	26.2	5.85	0.07	6.3	15.1	0.46	0.131	0.119	0.14	0.08	100.1	66	8.	3400	600
A16	lowest Fe	1	12	45.3	0.50	28.3	4.36	0.06	5.0	15.9	0.48	0.083	0.084	0.10	n.a.	100.1	67	7.	3600	420
A16	lowest Fe	4	13	45.3	0.47	28.0	4.45	0.06	5.4	16.4	0.46	0.107	0.086	0.11	0.05	100.8	68	7.	3400	480
A16	atypical	11, North Ray Crater	14	44.7	0.39	28.7	4.14	0.05	4.6	16.3	0.53	0.084	0.080	0.08	0.03	99.6	66	6.	3900	300
A17	orange glass	4, Shorty Crater	15	38.7	8.8	6.5	22.3	0.29	14.5	7.5	0.37	0.077	0.70	0.06	0.05	99.8	54	11.	2800	300
A17	highest-Fe	1 & 5, valley floor	16	39.9	9.6	10.9	17.7	0.24	9.5	10.7	0.38	0.078	0.46	0.07	0.12	99.8	49	9.	2800	300
A17	lowest-Fe	6, North Massif	17	43.5	3.3	18.2	10.7	0.15	10.8	12.2	0.40	0.116	0.28	0.09	0.08	99.8	64	10.	3000	400
A17	lowest-Fe	2A, South Massif	18	45.1	1.3	21.3	8.3	0.11	9.8	12.9	0.43	0.144	0.22	0.13	0.06	99.9	68	10.	3200	600
L16	only sample	lander	19	44.3	3.4	15.6	16.3	0.21	8.4	11.9	0.39	0.11	0.30	0.05	0.21	101.2	48	7.	2900	200
L20	only sample	lander	20	45.2	0.49	22.8	7.3	0.11	9.5	14.4	0.35	0.07	0.19	0.12		100.5	70	6.	2600	500
L24	only sample	lander	21	44.8	1.1	11.8	19.7	0.26	9.7	11.3	0.28	0.03	0.46	0.04	0.14	99.6	47	6.	2100	200

table continued on following page

Table 2.5. continued

mission	sample type or location	K ppm	Sc ppm	V ppm	Cr ppm	Mn ppm	Co ppm	Ni ppm	Zn ppm	Ga ppm	Rb ppm	Sr ppm	Y ppm	Zr ppm	Nb ppm	Cs ppm	Ba ppm	La ppm	Ce ppm	Pr ppm
A11	only	1100	63.	65.	2100	1600	29.	200	24.	4.5	2.8	163	115	300	19.	0.11	170	16.	47.	7.
A12	typical	2000	39.	110.	2600	1700	43.	200	7.	4.2	6.2	137	131	480	29.	0.30	390	34.	89.	12.
A12	atypical	3200	35.	100.	2300	1500	32.	110	7.	4.7	9.1	164	180	720	42.	0.41	560	49.	128.	17.
A14	typical	4300	22.	55.	1400	1100	35.	370	25.	6.0	15.	179	242	880	55.	0.65	800	67.	176.	24.
A14	atypical	5300	22.	45.	1300	1000	27.	250			20.	182	248	860	n.a.	0.70	910	69.	186.	25.
A15	highest Fe	800	38.	190.	3600	1900	50.	180	~6.	3.3	2.7	114	46	240	13.	0.22	150	11.	31.	4.
A15	highest Mg	1300	25.	100.	2500	1300	46.	210	29.	4.4	3.9	117	69	270	17.	0.20	210	19.	49.	7.
A15	highest Th	1700	24.	85.	2300	1300	41.	260	25.	4.2	5.8	140	90	380	23.	0.26	280	25.	68.	9.
A15	lowest Fe	1500	21.	85.	2100	1200	38.	280	19.	3.1	5.1	157	75	290	16.	0.22	280	22.	54.	7.
A16	typical mature	1010	9.5	25.	760	540	31.	440	26.	3.6	2.9	176	46	180	13.	0.14	140	13.0	34.	4.5
A16	highest Fe, station 5	1090	10.3	26.	820	580	33.	480	23.	3.5	3.2	176	51	190	14.	0.15	150	14.4	38.	5.
A16	lowest Fe, station 1	690	7.3	20.	570	460	17.	220	22.	4.6	2.0	177	31	120	9.	0.10	100	8.7	23.	3.
A16	lowest Fe, station 4	890	7.5	20.	580	470	32.	440	20.	4.5	2.4	173	40	170	11.	0.12	120	11.1	29.	4.
A16	atypical, NRC	700	7.2	20.	550	410	15.	170	13.	4.1	2.0	194	25	90	6.	0.09	85	6.6	18.	2.3
A17	orange glass, station 4	640	49.	130.	4800	2200	62.	90	250.		1.1	209	49	190	15.	0.12	80	6.4	19.	3.
A17	highest-Fe, stations 1 & 5	640	67.	91.	3200	1900	32.	120	36.	10.	1.2	151	78	230	22.	0.12	100	7.4	23.	4.
A17	lowest-Fe, NM station 6	1000	29.	55.	1900	1100	32.	210	22.	5.1	2.7	159	52	190	13.	0.13	130	10.	28.	4.
A17	lowest-Fe, SM station 2A	1200	17.	40.	1500	900	32.	270	15.	2.8	3.4	152	58	220	13.	0.18	170	15.	39.	5.
L16	only	900	51.	80.	2000	1600	31.	180	23.	n.a.	1.8	276	62	240	n.a.	0.07	170	11.	35.	5.
L20	only	600	16.	45.	1300	900	30.	230	~50.	n.a.	1.6	139	26	110	n.a.	0.09	90	6.9	17.	2.4
L24	only	200	43.	145.	3100	2000	50.	140	15.	1.1	0.5	91	18	50	n.a.	0.06	38	3.0	8.	1.2

table contined on following page

Table 2.5. continued

mission	sample type or location	Nd ppm	Sm ppm	Eu ppm	Gd ppm	Tb ppm	Dy ppm	Ho ppm	Er ppm	Tm ppm	Yb ppm	Lu ppm	Hf ppm	Ta ppm	W ppm	Ir ppb	Au ppb	Th ppm	U ppm	I_s/FeO
A11	only	38.	13.	1.77	17.	2.9	19.	4.6	11.	1.7	10.6	1.54	10.	1.3	0.2	7.	2.9	2.0	0.51	78
A12	typical	55.	16.	1.75	20.	3.5	22.	4.8	13.	1.9	12.3	1.74	13.	1.5	0.7	7.	3.5	5.8	1.5	55
A12	atypical	82.	22.	2.3	27.	4.6	30.	6.6	18.	2.7	17.	2.4	18.	2.2	n.a.	3.	2.2	9.2	2.6	8
A14	typical	105.	30.	2.5	35.	6.2	39.	8.7	23.	3.5	22.	3.1	23.	3.0	1.7	13.	7.	13.	3.5	65
A14	atypical	106.	31.	2.6	36.	6.5	42.	9.1	25.	3.6	23.	3.2	24.	3.1	1.8	6.	7.	14.	3.8	6
A15	highest Fe	22.	5.8	0.98	8.	1.3	8.	1.7	5.	0.7	4.3	0.66	4.	0.6	0.5	4.	1.6	1.5	0.45	28
A15	highest Mg	30.	8.8	1.15	10.	1.7	11.	2.5	7.	1.0	6.5	1.01	7.	0.9	n.a.	4.	3.	3.4	0.9	43
A15	highest Th	39.	12.	1.45	13.	2.3	15.	3.4	9.	1.3	8.5	1.24	10.	1.1	1.2	7.	4.	4.2	1.2	65
A15	lowest Fe	34.	10.	1.28	12.	2.0	13.	2.9	8.	1.1	6.9	0.96	8.	0.9	n.a.	8.	2.2	3.4	0.90	64
A16	typical mature	21.	6.0	1.20	8.	1.2	8.	1.7	5.	0.7	4.3	0.61	4.5	0.55	<0.5	15.	10.	2.2	0.62	82
A16	highest Fe, station 5	23.	6.7	1.22	8.	1.3	9.	1.9	5.	0.7	4.8	0.68	5.0	0.63	n.a.	16.	11.	2.4	0.68	83
A16	lowest Fe, station 1	14.	4.2	1.19	5.	0.9	6.	1.2	3.	0.5	3.0	0.42	2.9	0.38	n.a.	6.	4.	1.6	0.35	9
A16	lowest Fe, station 4	19.	5.1	1.11	6.	1.0	7.	1.5	4.	0.6	3.6	0.50	3.9	0.46	n.a.	15.	19.	1.9	0.50	61
A16	atypical, NRC	11.	3.1	1.24	4.	0.63	4.	0.9	2.	0.4	2.3	0.33	2.2	0.30	<0.3	6.	3.	1.1	0.34	25
A17	orange glass, station 4	18.	6.6	1.84	9.	1.5	9.	1.8	5.	0.7	4.2	0.61	5.	1.0	n.a.	0.8	0.3	0.5	0.16	1
A17	highest-Fe, stations 1 & 5	22.	8.3	1.71	11.	2.1	13.	2.9	8.	1.2	7.6	1.06	7.	1.3	<0.3	6.	2.	0.7	0.21	31
A17	lowest-Fe, NM station 6	20.	6.2	1.33	8.	1.4	9.	1.9	5.	0.8	5.0	0.70	5.	0.8	n.a.	8.	3.	1.6	0.45	63
A17	lowest-Fe, SM station 2A	26.	7.3	1.24	9.	1.5	10.	2.1	6.	0.9	5.5	0.78	6.	0.7	n.a.	12.	5.	2.6	0.73	65
L16	only	26.	8.2	2.3	11.	1.6	11.	2.3	6.	0.9	5.6	0.82	7.	0.6	45.	10.	2.6	1.3	0.31	n.a.
L20	only	11.	3.1	0.91	4.	0.64	4.2	0.9	2.7	0.4	2.5	0.38	2.5	0.3	64.	10.	3.4	1.3	0.33	n.a.
L24	only	6.	1.9	0.65	2.6	0.46	3.0	0.7	1.9	0.3	1.8	0.27	1.5	0.2	n.a.	5.	7.	0.4	0.11	n.a.

table continued on following page

Table 2.5 continued:

Concentration values in the table are selected means based on literature data too numerous to cite and some unpublished data from Washington University (Korotev). The table presents typical compositions and extreme compositions. The Apollo data are based only on samples of surface and trench soils. Some soils in cores and drive tubes are more extreme in composition, but less well characterized. The Luna samples were taken with coring equipment and are contaminated with W, presumably from tungsten carbide. Concentrations of some elements for which no data exist, e.g., Y, Pr, Gd and Er, have been estimated on the basis of interelement correlations. Oxide concentrations represent the total concentration of the element expressed as the oxide. All units are mass ratios, e.g., % = cg oxide per g of sample and ppm = µg element per g of sample. I_s/FeO values are values or means of values from Morris et al. (1983). *Mg´* = mole percent MgO/(MgO+FeO). Compositionally atypical samples tend to be less mature (lower I_s/FeO).

Notes:

1 Apollo 11: Based on many data for sample 10084 and a few data for samples 10085 and 10010, which are both essentially identical to 10084 (Korotev and Gillis, 2001).

2 Apollo 12: Based on data for typical samples 12001, 12023, 12029, 12041, 12042, 12044, 12057, and 12070, which are all very similar in composition (e.g., FeO range: 15.9% to 17.1%; Th range: 5.3 ppm to 6.3 ppm). Some Apollo 12 samples (12003, 12030, 12037, 12060) are contaminated with fines abraded from mare basalts carried in the same container; data for these samples are not included.

3 Apollo 12: Based on data for atypical samples 12032 and 12033 from Head Crater.

4 Apollo 14: Based on data for all samples except 14141. Except for 14141, Apollo 14 soil samples are virtually identical in composition (e.g., FeO range: 10.1% to 10.9%; Th range: 12.3 ppm to 13.6 ppm).

5 Apollo 14: Data for sample 14141 from Cone Crater, which appears to have a greater proportion of felsite (K, Ba, Th) and alkali anorthosite (Na) than the typical soils.

6 Apollo 15: Based on data for samples 15531 & 15601 from station 9a at the edge of Hadley Rille. These samples contain the greatest proportion of mare volcanic material and are consequently richest in FeO.

7 Apollo 15: Based on data for all samples from station 7 (*N*=4) on the Apennine Front. Most data are from samples 15301 and 15411. The station 7 regolith contains the greatest proportion of 15426-type green picritic glass and is consequently the richest in MgO.

8 Apollo 15: Based on data for all samples from station 6 (*N*=6). The station 6 regolith contains the greatest proportion of KREEP-rich lithologies and consequently has the greatest concentrations of incompatible elements.

9 Apollo 15: Based on data for all samples (*N*=6) from station 2. The station 2 regolith contains the greatest proportion of nonmare lithologies and consequently has the lowest concentration of FeO. All other surface and trench soils from Apollo 15 are intermediate in composition to the four extremes listed here.

10 Apollo 16: Mean of data for all 24 samples of mature soil from Apollo 16. This composition probably best represents the surface of the Cayley Plains (Korotev, 1997). The compositional range of mature soils is moderate (e.g., FeO: 4.4% to 6.0 %; Th: 1.6 ppm to 2.5 ppm) and mainly represents variation in the relative abundance of anorthosite.

11 Apollo 16: Based on data for all samples (*N*=7) from stations 5 and 6. The soils of these stations are all similar in composition and are at the high-Fe extreme of the range of Apollo 16 soils because they contain the lowest proportion of anorthosite.

12 Apollo 16: Based on data for sample 61121 from station 1 on the Cayley Plains. This sample is the most feldspathic (lowest FeO) of the surface and trench soils from the central part of the site (stations LM, 1, & 2). Some soils at depth in the cores of the central area are more feldspathic, however (Korotev and Morris, 1993).

13 Apollo 16: Based on data for sample 64601 from station 4 on Stone Mountain. This sample is the most feldspathic (lowest FeO) of the surface and trench soils from the southern part of the site (stations 4, 5, 6, 8, & 9).

14 Apollo 16: Based on data for all true soil samples (*N*=8) from station 11 at North Ray Crater (some 67xx0 and 67xx1 samples are not true soils; see Korotev, 1996). This is the only set of means presented here for which the samples upon which they are based vary considerably in composition (e.g., FeO range: 2.9% to 4.6%; Th range: 0.5 ppm to 2.0 ppm) and *Mg´* (range: 62 to 70). Soils from station 13 (63xx1) about a kilometer from North Ray Crater are intermediate in composition between the station-11 soils and the mature soils.

15 Apollo 17: Based on many data for the “orange glass” soil, sample 74220, taken near Shorty Crater at station 4. This soil is the most anomalous in the Apollo collection because it consists nearly entirely of pyroclastic glass beads, with some minor contamination by “normal” soil. (Soil from the double drive tube 74001/2 taken at the same location is less contaminated, but fewer data are available.)

16 Apollo 17: Based on data for all samples (*N*=6) from stations 1, 1A, and 5 on the valley floor. These samples are all similar in composition and represent the most Fe-rich extreme (excluding 74220) of soils found at the Apollo 17 site in that they contain the highest proportion of mare basalt.

17 Apollo 17: Based on data for all samples (*N*=6) from station 6 at the base of the North Massif. The station-6 soils are the least contaminated with mare material of nominally nonmare soils collected from the north side of the site, although the degree of contamination is still substantial (about one 27%, Korotev and Kremser, 1992).

18 Apollo 17: Based on data for all samples (*N*=3) from station 2A (LRV stop 4) on the light mantle deposit at the base of the South Massif. The station-2A soils are the least contaminated with mare material of any soils collected at the Apollo 17 site (about 6%, Korotev and Kremser, 1992). Other soils from Apollo 17 are intermediate in composition to the four extremes listed here.

19-21 Based on all available data for Luna soils.

(1) Ancient impact-melt breccias. A peculiar and fascinating feature of nearly all of the Th-rich, mafic impact-melt breccias of the Apollo collection (Section 5.2.2) is that they contain FeNi metal of meteoritic origin in moderately high abundances, 0.2–1.7% Fe^0 by mass, depending upon the type of breccia (Korotev 2000). The composition of the metal (typically 6 ± 2% Ni and Ni/Co $\approx$ 15) is not like that in ordinary chondrites but resembles that in some iron meteorites (Hewins and Goldstein 1975; Korotev 1987a,b; James 1995, 1996). Nearly all of the breccias are ancient, ~3.9 Gy, and all or most are products of impacts that formed basins or large craters. Like the metal in the igneous and plutonic rocks, this metal is very old. In the melt breccias, the metal grains range in size from micrometers or less to a few millimeters. Because some regoliths contain a high proportion of such breccias, this ancient metal is a major source of metallic Fe in some Apollo soils, most notably those of Apollo 14 and 16. Grains of metal that exceeding 1 mm in size have been found as fragments in the Apollo 16 soil samples (Goldstein et al. 1972; Reed and Taylor 1974; Ali and Ehmann 1977; Korotev and Jolliff 2000). Most large metal grains in lunar soil appear to derive mainly from disaggregation of melt breccias, not directly as meteorites (Korotev 1987a; Korotev 1991, 1997; Korotev and Jolliff 2000). Metal derived from ancient melt breccias is identifiable because it is compositionally distinct in having high concentrations of W, compared to metal in meteorites, as a result of having solidified from W-rich, mainly-silicate impact melt (Wlotzka et al. 1973; Korotev et al. 2003a). These large metal nuggets are a common source of anomalously high Fe concentrations in small subsamples of lunar soils (Korotev 1987a).

In lunar soils, metal contained in igneous rocks and ancient impact-melt breccias together correspond to the Fe^0_{SM} (source material) component of Morris (1980), that is, the metal component which is uncorrelated with the magnitude of surface exposure. On average, this component accounts for a few tenths of a percent of the mass of Apollo soils (0.17 ± 0.08 "equivalent wt %" as Fe^0, mean and standard deviation; Morris 1980). For some regoliths it is higher. Based on siderophile-element abundances, the soils of the Apollo 14 and 16 sites each contain 0.5% "FeO" as metal derived from ancient impact-melt breccias. These concentrations correspond, respectively, to 5% and 9% of the total iron in the regoliths and a large fraction of the metallic iron.

(2) Macrometeoroids. Most of the craters produced since the time of basin formation have been caused by impacts of ordinary chondrites and iron meteorites, all of which contain FeNi metal. The amount of metal in the regolith derived from post-basin macrometeorites is not known. At the Apollo 16 site, glass from the South Ray crater impact 2 Ma ago is commonly found as spherules in the regolith and as glass coatings and splashes on rocks (Morris et al. 1986; Eugster 1999). The glass is rich in siderophile elements (mean Ni: 800 µg/g; Morris et al. 1986) and Ni/Co and Ir/Au ratios of the glass are consistent with a chondritic impactor. The glass contains "minute" metal spherules (James et al. 1984). Metal spherules in glass "bombs" found in the North Ray Crater ejecta range up to at least 50 µm in diameter (Fig. 3 of Borchardt et al. 1986).

(3) Micrometeoroids. Morris (1980) noted that the concentration of some Fe metal that exists in the regolith as grains >33 nm in diameter increases with regolith maturity and concluded that this maturity-correlated, multiple-domain metal component, designated Fe^0_{MM}, derived from micrometeorites. This conclusion is consistent with the observation that FeNi metal occurs in the glass of 0.1–1 mm craters formed by impacts of interplanetary dust particles (Brownlee et al. 1991, 1992). It is also likely that a portion of the nominal micrometeorite component is actually metal from macrometeorites because metal-bearing glass spherules, such as those produced when South Ray Crater was formed, accumulate at the surface and thus increase in concentration with time.

Morris (1980) concluded that on average, the regolith contains 0.17 ± 0.08 "equivalent wt%" Fe^0 as the micrometeorite component. In samples of submature and mature soils, Ni concentrations in excess of that portion likely carried by source rocks is typically 120–200 μg/g, which corresponds to 0.21–0.35% Fe or 0.27–0.45% FeO, using CI chondrite abundance ratios (Anders and Grevesse 1989). Thus, half to most of the Fe that is contributed by meteorites associated with surface exposure occurs in metallic form in the regolith. In the Apollo 16 regolith (5.5% Fe as FeO), 13–17% of the Fe is carried by metal and another 4–9% is carried by ilmenite, leaving only 73–83% in silicate minerals and glass. Clearly, not all the Fe contained in lunar soil leads to UV-VIS spectral absorption bands.

(4) Nanophase iron. "Nanophase" or "single-domain" iron occurs as very small (submicrometer) grains, usually in agglutinates and coatings on regolith grains. Some nanophase Fe is pure iron that is produced by reduction of Fe^{2+} in lunar minerals as a consequence of exposure of the mineral grains at the lunar surface (Morris 1980). Other nanophase Fe is produced when vapors formed during micrometeorite impacts condense on the surface of regolith materials (Keller and McKay 1997). Because micrometeorites totally vaporize upon impact, some nanophase iron must be of meteoritic origin. There are no studies, however, that quantify the relative importance of the two possible sources of nanophase iron, *in situ* reduction, and vapor deposition. The relative abundance of nanophase iron correlates both with the iron concentration of the regolith and with regolith maturity, as determined by other parameters. Morris (1980) concluded that, on average, 40% of the metallic Fe in the lunar regolith occurs as nanophase iron (0.20 ± 0.10 "equivalent wt%" as Fe^0). Nanophase iron is discussed in more detail below (Section 9), because it is main cause of spectral reddening of lunar regolith with increased surface exposure.

6.2.2. The regolith as a mixture. Despite the wide variety of materials in the lunar regolith, the compositions of soils from the Apollo and Luna landing sites correspond to mixtures of only three compositional classes of material: (1) rocks and breccias of the feldspathic highlands ("anorthosites," including rocks with compositions corresponding to noritic and troctolitic anorthosite and anorthositic norite and troctolite; Fig. 2.3), (2) some form of KREEP, usually impact-melt breccia of basaltic, noritic, or troctolitic composition or (rarely) KREEP basalt, and (3) mare basalt and volcanic glass (Fig. 2.2). Thus on many 2-element plots of regolith composition, regolith samples define a triangular array (Figs. 2.11, 2.12d, 2.13). The lithologies representing the three classes typically differ in composition from site to site (e.g., different types of melt breccia or mare basalt) and several different compositionally distinct lithologies may represent a given class at a given landing site (e.g., several types of mare basalt at Apollo 11 or several kinds of impact-melt breccia at Apollo 17). Thus, the apices of the triangle are not discrete points but are "fuzzy" (e.g., Garrison and Taylor 1980).

Regolith samples collected on the Apollo and Luna missions cover much of the range of the mixing triangle. Certain possible mixtures, however, do not occur among the Apollo and Luna samples. For example, Apollo collection does not contain soils composed subequally of mare basalt and feldspathic material with negligible KREEP but such soils might be expected to occur elsewhere. The QUE 94281 and Yamato-793274 lunar meteorites apparently derive from such a regolith (Jolliff et al. 1998a; Arai and Warren 1999). At points distant from the Apollo landing sites, e.g., the South Pole-Aitken area, other classes of material may exist, although there is no strong reason to suspect that anomalous regoliths occur elsewhere. At the Apollo and Luna sites, soils that consist mainly (>90%) of a single lithology or of rocks of a single compositional class are rare. The orange-glass soil at station 4 of Apollo 17 would be an example of such a rare regolith. Most soil samples contain at least a few percent of material from all three compositional classes. For example, all mare soils contain nonmare material (Luna 24 soil appears to be the "cleanest" in this regard) and mare material is rare but present to varying degrees even in the feldspathic lunar meteorites.

At Apollo and Luna landing sites that are geologically simple or where only one or a few samples were collected, soil compositions tend to occupy only a small portion of the mixing

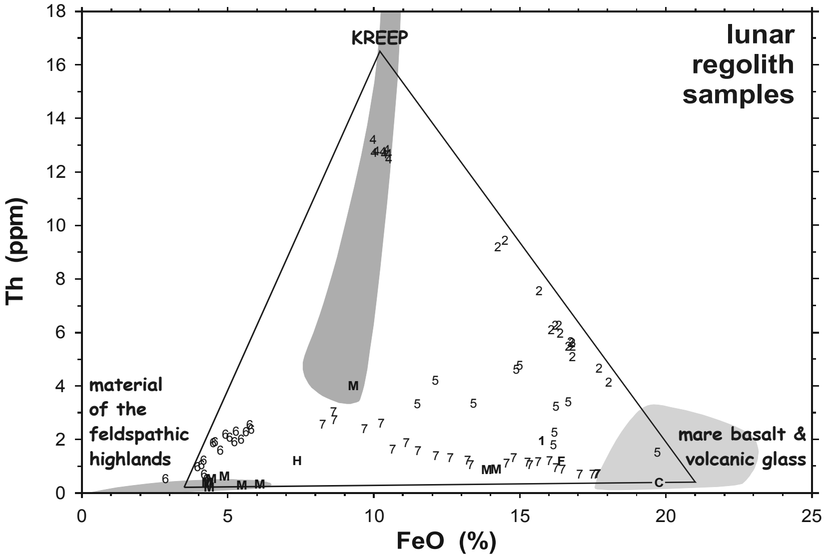

Figure 2.11. The Apollo regolith mixing triangle in terms of FeO (total Fe as FeO) and Th concentrations (adopted from Jolliff et al. 2000). Regolith samples from the Apollo missions are mainly mixtures of the three classes of material represented by the apices of the triangle. Mean FeO and Th concentrations of the actual rocks representing the three classes differ from site to site, but for any given site the apices lie within the shaded fields. For example, in Apollo soils, KREEP is carried by mafic impact-melt breccias; those from the Apollo 16 and 17 sites have low Th concentrations (4–8 ppm) whereas those from the Apollo 12 and 14 sites have high concentrations (16–22 ppm). Symbols are as in Figure 2.3, except that all lunar meteorites that are plotted (M). For Apollo 12 (2) and 14 (4), each point represents a numbered surface or trench soil sample (e.g., 12070 and 14163). For Apollo 15 (5), 16 (6), and 17 (7), each point represents the mean of all surface and trench soils from a sampling station (e.g., station 2), except that all samples from station 11 (North Ray Crater) at Apollo 16 are plotted.

triangle. In contrast, soils from the Apollo 15 and 17 missions cover a large range because the landing sites were at highlands-mare interfaces, the ratio of mare to nonmare material in the regolith varies from place to place, and the astronauts collected samples over a wide area. Although material of all three compositional classes occurs in the regoliths of all sites (Fig. 2.14), soil compositions from a given site do not scatter all over the mixing triangle. This simple observation indicates that the material of the regolith is so well mixed that even the tiny samples used for chemical analysis are remarkably uniform in composition from sample to sample. We might expect that for larger samples sizes, e.g., the area of a Clementine pixel, the degree of sample-to-sample (pixel-to-pixel) uniformity would be even greater.

At landing sites where regolith compositions are not uniform, the variation is systematic, typically leading to linear trends on plots of element Y vs. element X. For example, Apollo 12 soils are largely binary mixtures of mare basalt and KREEP impact-melt breccias. The basalt/KREEP ratio varies among different regolith samples, leading to a linear trend on 2-element plots (Fig. 2.11). Such trends can be used to infer information about local geology. For example, a plot of the concentration of any lithophile element against that of FeO for Apollo 17 soils yields a linear trend such as that of Figure 2.11. Extrapolation of the trend to high FeO concentration provides the mean composition of the mare components, essentially the Apollo 17 high-Ti basalts and orange volcanic glass. Extrapolation to low FeO provides the mean composition of the nonmare components. That composition does not, in fact, correspond to any single rock type that occurs at the Apollo 17 site but to a mixture of various nonmare li-

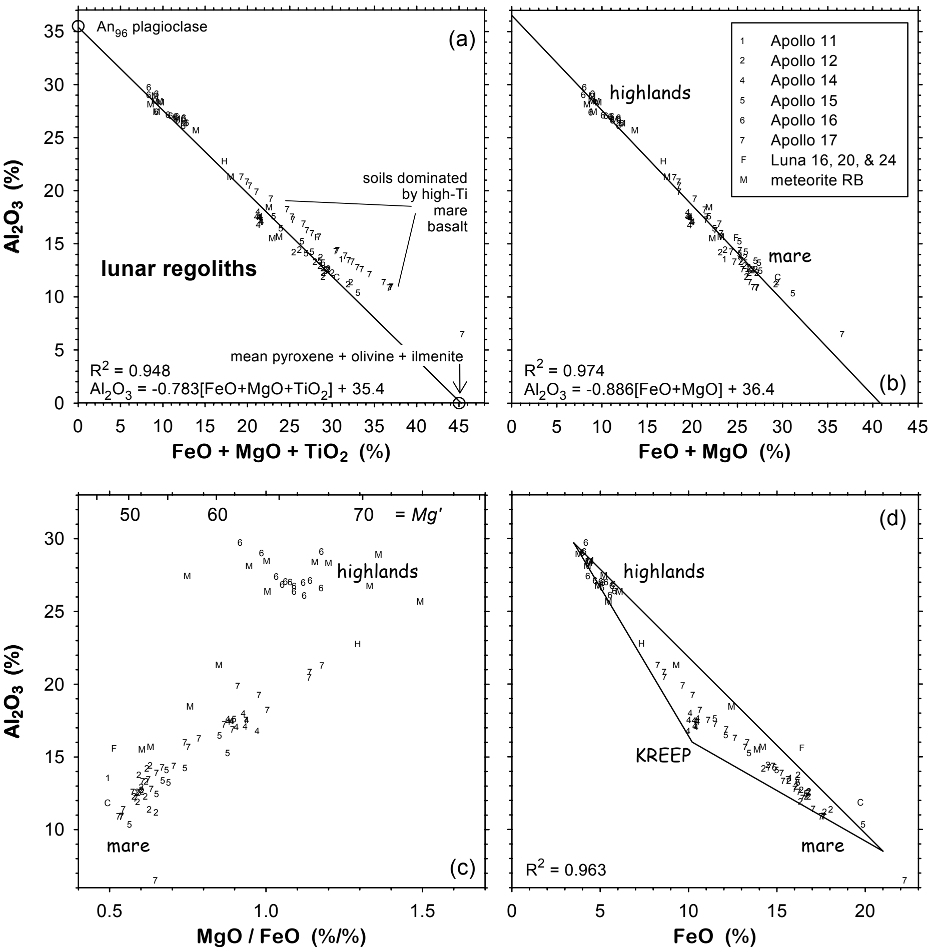

Figure 2.12. In the lunar crust, nearly all Al is carried by plagioclase whereas Fe, Mg, and Ti are carried by pyroxene, olivine, and ilmenite. Thus, to a first approximation, all regolith samples plot on or about a mixing line between the composition of plagioclase and a point corresponding to the mean composition of the three Fe-bearing minerals, which varies from site to site. Soils from the feldspathic highlands plot at the high-Al_2O_3 end of the trend, those dominated by mare basalt plot at the low-Al_2O_3 end, and soils dominated by KREEP (Apollo 14) plot in the middle (Fig. 2.11). Symbols are as in Figure 2.3. (a) Soils from Apollo 11 and 17, which are dominated by high-Ti mare basalt, deviate from the trend defined by the low-Ti samples because of the excess of Ti. The equation is that for the line, which excludes the Apollo 11 and 17 data; R^2 is for all data. (b) The correlation is best between Al_2O_3 and FeO+MgO. (c) MgO/FeO ratios for highland soils have a wide range while those for mare soils are uniformly low. *Mg´* = bulk mole percent MgO/(MgO+FeO) (d) The nonlinearity of the trend occurs because the Apollo 14 soils in the middle of the array are not mixtures of feldspathic highlands material and mare basalt (Fig. 2.11) and because mare basalts have higher FeO/MgO ratios than the nonmare materials (c). The triangle represents the mixing triangle of Figure 2.11; in (a) and (b) the mixing triangle is compressed to a line. See also Figure 8 of Fischer and Pieters (1995).

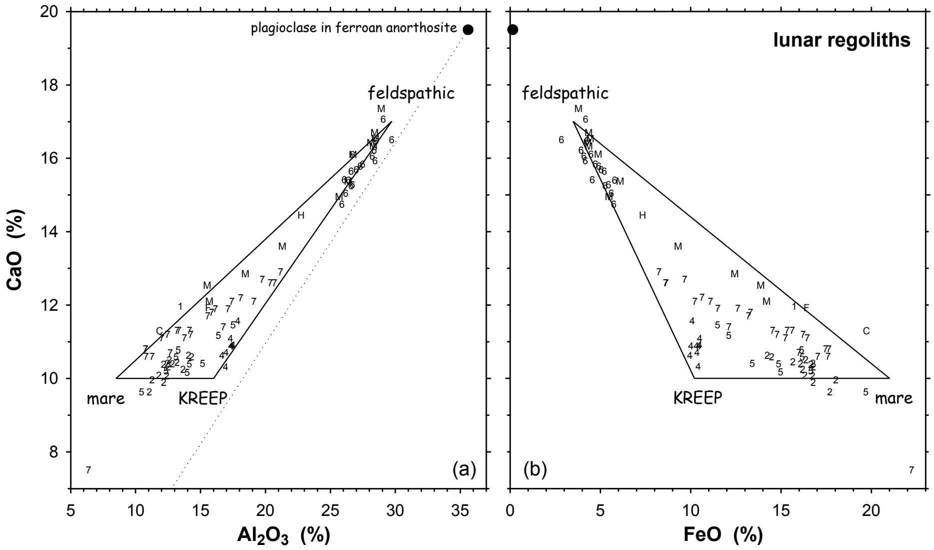

Figure 2.13. Variation of CaO with Al_2O_3 and FeO in lunar regolith (total Fe as FeO). The triangles are the Apollo regolith mixing triangle of Figure 2.11. In (a), the CaO/Al_2O_3 ratio of plagioclase in ferroan anorthosite (●) is shown by the dotted line. Mare basalts have high CaO/Al_2O_3 ratios compared to plagioclase in ferroan anorthosite and KREEP because in mare basalts some CaO is carried by Ca-rich pyroxene (clinopyroxene) whereas the pyroxenes of feldspathic and KREEP-rich samples are low-Ca pyroxenes.

thologies. This observation indicates that the nonmare lithologies were moderately well mixed before the admixture of the mare component. We can expect similar trends on a regional basis in data taken from orbit.

The mixing triangle of Figure 2.11 does not contain apices for magnesian-suite or alkali-suite nonmare rocks (e.g., Spudis and Davis 1986) because, with two possible exceptions, in Apollo and Luna regoliths such rocks are volumetrically minor subcomponents of the KREEP or, possibly, feldspathic highlands components. The exceptions are that soils from the North Massif at Apollo 17 appear to contain as much as a few tens of percent troctolite or troctolitic anorthosite for which the abundance is not correlated with the abundance of the other nonmare components (Korotev and Kremser 1992; Jolliff et al. 1996). Much of the Luna 20 regolith also contains anorthositic norite, troctolitic anorthosite, and spinel troctolite with moderately high Mg concentrations. Some of these compositions would plot outside the field of "material of the feldspathic highlands" on Figure 2.11.

One implication of Figure 2.11 requires some words of clarification and caution. In terms of the KREEP concept, the figure implies, for example, that the Luna 20 regolith contains 5–10% of a high-Th KREEP lithology that was mixed into the regolith. This inference is probably incorrect or, at least, misleading for Luna 20 and perhaps for other regoliths of the figure as well. The Luna 20 regolith, which is not well understood, may instead derive ultimately from early crustal rocks that never differentiated to the point where they developed high concentrations of incompatible elements (Korotev et al. 2003b). The components of the Luna 20 regolith are moderately low-Th rocks that happen to have concentrations of incompatible elements that occur in the same ratios as KREEP because early crustal rocks formed from a global magma ocean and they contain some trapped residual liquid of KREEP-like composition (Jolliff and Haskin 1995; Jolliff 1998). This example highlights one the ambiguities associated with the

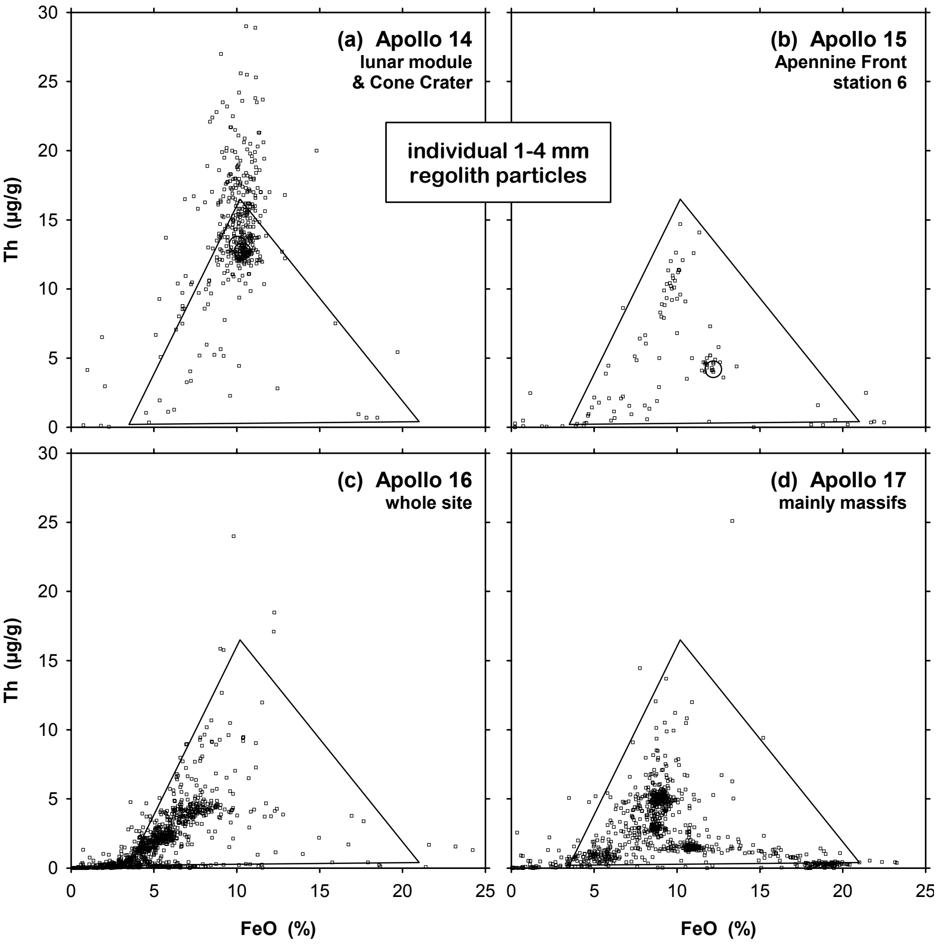

Figure 2.14. Concentrations of FeO (total Fe as FeO) and Th in individual rock particles from the 1–2 mm and 2–4 mm fractions of lunar soils shown with the Apollo regolith mixing triangle of Figure 2.11. (a) Data are mainly for 14161, a surface scoop sample taken near the lunar module; the rest are for 14142 and 14143 taken near Cone Crater (Jolliff et al. 1991, and unpublished data). Large circles obscured by the main cluster of points represent the composition of the <1-mm grain-size fractions of the two soils (14163 and 14141). Apollo 14 soils are dominated by impact-melt, fragmental, and regolith breccias of KREEP composition (i.e., most points with >10 µg/g Th). Feldspathic lithologies and mare basalt are rare. Six particles in this data set contain >30 µg/g Th. (b) Data for 15272 and 15273 from station 6 on the Apennine Front (Korotev 1987c, and unpublished data). The station-6 soils of Apollo 15 consist of subequal amounts of rock types representing all three apices of the mixing triangle. The large circle represents the composition of the <1-mm grain-size fraction of 15271; the cluster of points near the circle are for regolith breccias of bulk-soil composition. Points with >8 µg/g Th mainly represent KREEP basalts, with some impact-melt breccias. (c) Data for particles from all over the Apollo 16 site (Korotev 1983a,b; Jolliff and Haskin 1995; Korotev et al. 1997b). Some of the points with >18% FeO represent gabbronorites (James and Flohr 1983), not mare basalts. (d) Most of the points are for 2–4 mm particles from the North and South Massifs of Apollo 17, so mare basalts are underrepresented (Jolliff et al. 1996, 1998). Nearly every point with >3 µg/g Th in (c) and (d) represents a KREEP-bearing impact-melt breccia.

KREEP concept. The term is used to refer to a discrete high-K, high-Th lithologic component of polymict materials such as regoliths and breccias (e.g., Simon et al. 1986), as a compositional component that may or may not represent a lithologic component (e.g., Schonfeld 1974), and as the residual liquid phase of a crystallizing igneous system (Warren and Wasson 1979) that may or may not have been separated from rock in which it occurs.

6.2.3. Compositional variation with depth in the regolith. A several locations where regolith core samples were taken, the range of compositional variation with depth over tens of centimeters is equivalent to the range among surface samples taken over a few kilometers of lateral distance (Fig. 2.15). Compositional variation with depth reflects less-than-ideal vertical mixing of the components of which the soil is composed. Regolith stratigraphy results from overlapping ejecta deposits from many craters, big and small. Compositionally anomalous layers almost always contain an excess of some specific lithology of which the soil is composed compared to the average for the whole core (Fig. 2.16). Such layers probably have only limited lateral extent. Apollo 16 cores 60001–7, 60009/10, and 60013/14 were taken at apices of a triangle 40–50 m apart (Fig. 2.15). Each of the cores contains a layer a few centimeters thick that is richer in anorthosite that surface soils, but there is no way to know whether these layers are part of a continuous deposit. Core 60009/10 shows the widest variation in composition with depth of any lunar core (Figs. 2.15, 2.16).

It is not uncommon for soil in the upper 0.5–1 cm to have concentrations of several elements that are 10 or more percent different from the average for the upper half meter or meter. For example, the FeO concentration of the upper centimeter of the Apollo 17 deep drill core is 9% greater than the mean for the whole 3 m core (Fig. 2.15). However any such effects probably cancel over a large areal extent unless there is some large scale stratigraphy. In the absence of such stratigraphy there is no reason to believe that the upper millimeter, centimeter, or meter, that is, the portion of the regolith observed by orbiting spectrometers, is a systematic biased sample of the material of the upper 10 m with respect to concentrations of lithophile elements. Siderophile (iron-metal loving) and volatile elements, on the other hand, are concentrated toward the surface because they derive mainly from micrometeorites.

6.2.4. Correlations among major elements resulting from mineralogy. More than 98% of the crystalline material of the lunar crust consists of only four minerals: plagioclase feldspar, pyroxenes, olivine, and ilmenite. Thus, seven chemical elements, O, Mg, Al, Si, Ca, Ti, and Fe, account for >98% of the mass of the lunar crust. Ilmenite is minor, <5% in most rocks, except for mare basalts which may contain up to 25% by mass ("high-Ti basalts") of ilmenite plus other Fe-Ti oxides. In soils, the three remaining minerals, all silicates, each contain average concentrations of Si and O that are similar to each other, thus there is little variation in these two elements among regolith samples (Fig. 2.17). For example, total Si as SiO_2 ranges from 42% in the ilmenite-rich Apollo 11 and 17 soils to 48% in KREEP-rich Apollo 14 soils. This range narrow range compares with essentially 0% to 100% in terrestrial sediments (e.g., carbonates to sandstones). Because of the narrow range of Si variation in lunar soils, Al/Si and Mg/Si ratios obtained by the Apollo 15 and 16 orbiting X-ray spectrometers (Section 10.3) provided accurate estimates of absolute Al and Mg concentrations. Total oxygen ranges from 42% in the ilmenite-rich Apollo 11 and 17 soils (40.6% in the anomalous Apollo 17 orange-glass soil) to 45% in plagioclase-rich highlands regoliths (Fig. 2.18). This leaves only five major elements that vary significantly in concentration: Mg, Al, Ca, Ti, and Fe.

In terms of the Apollo mixing triangle, feldspathic highlands materials are rich in plagioclase (70–99%) and consequently poor in pyroxene, olivine, and ilmenite. Thus highlands materials are rich in Al and Ca and poor in Fe, Mg, and Ti (Figs. 2.13, 2.19). At the other extreme, mare basalts are rich in pyroxene, olivine, and sometimes ilmenite ($\Sigma \approx 80 \pm 10\%$ by mass, leaving 20 ± 10% plagioclase) and are consequently rich in Fe, Mg, and Ti. KREEP-rich impact-melt breccias and basalt are intermediate (40–70% plagioclase by mass), which leads

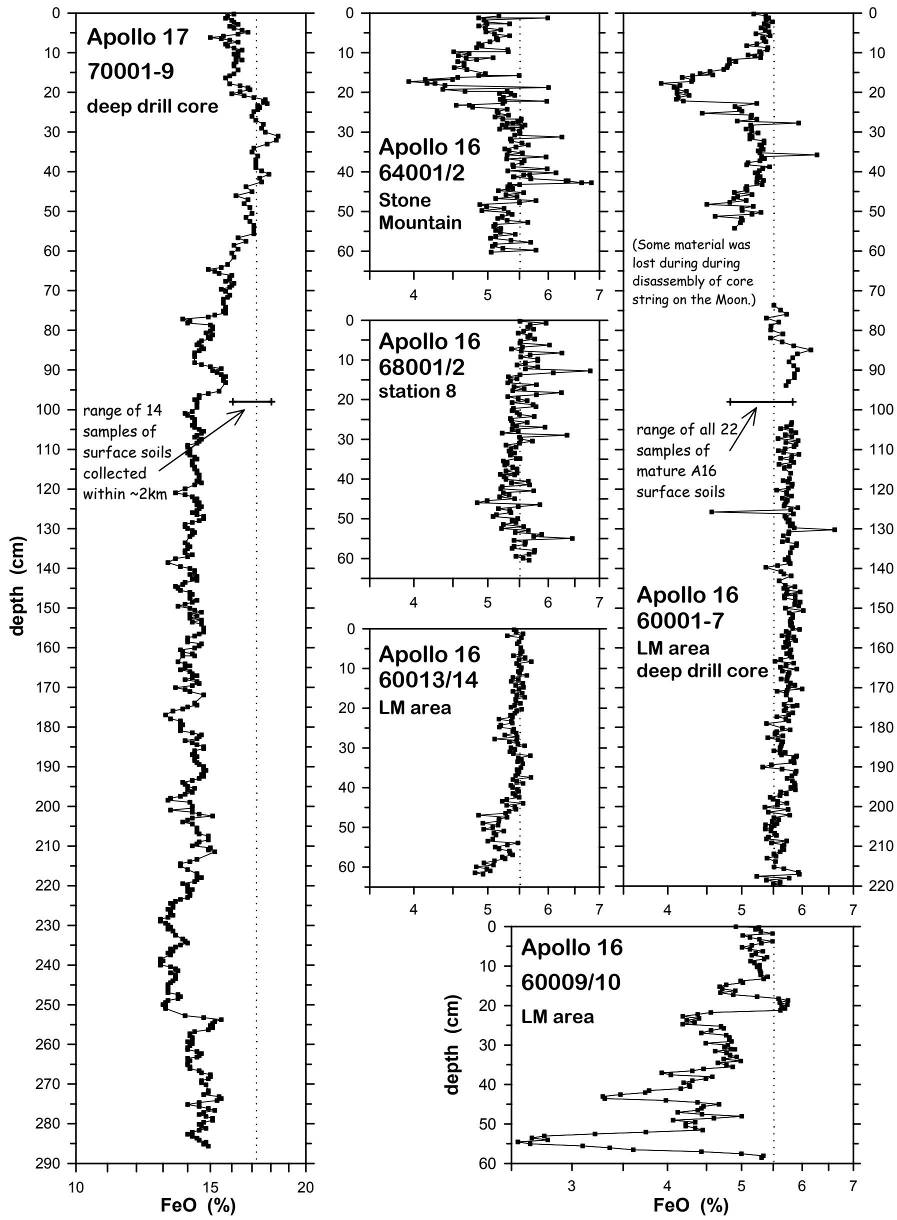

Figure 2.15. Variation in FeO concentrations with depth in the Apollo 16 and 17 deep drill cores and four Apollo 16 double drive tubes. For Apollo 17, the vertical dotted line represents the mean concentration of 14 samples of surface and trench soils collected within 2 km of the core location; the range is also shown (the soil from LRV stop 9, which has 14.6% FeO is excluded). For Apollo 16, the vertical dotted line is the mean FeO concentration of all 22 mature surface and trench soils from the site; the range is shown in the 60001-7 plot. The FeO axes are logarithmic and, e.g., a 10% change is represented by the same horizontal distance on all plots. Data sources: Morris et al. (1979), Korotev et al. (1984), Korotev (1991), Korotev and Morris (1993), and Korotev et al. (1997a).

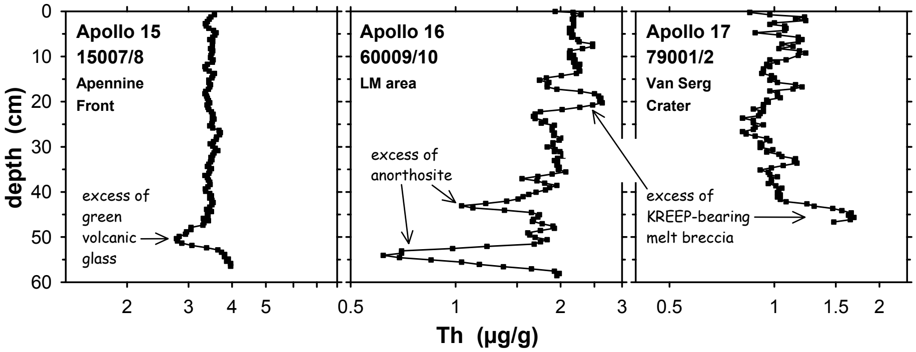

Figure 2.16. Variation in Th concentration with depth in three Apollo double drive tubes. Compositionally anomalous layers usually contain an excess of one of the lithologies of which the regolith is composed. Each of the lithologies causing the anomalies illustrated here corresponds to one of the apices of the mixing triangle of Figure 2.11. Data are from Korotev (1995), Korotev (1991), and Morris et al. (1989).

to FeO concentrations (~10%) that are about half those of mare basalt (~20%) yet considerably greater than those of rocks of the feldspathic highlands (<6%; Figs. 2.11, 2.19). Thus although soils typically contain material of all three compositional classes, most compositional variation ultimately involves variation in the ratio of plagioclase to the three Fe-bearing minerals (Fig. 2.10). Closure leads to a tight anticorrelation between Al or Ca with Fe+Mg+Ti (Fig. 2.12, Fig. 2.13) and many regions of compositional space are disallowed, e.g., high Al coupled with high Fe (Fig. 2.12) or high Ti coupled with low Fe (Fig. 2.19a). Most correlations among major, minor, and trace elements in lunar materials ultimately result from two factors: (1) the simplicity of lunar mineralogy and (2) the fact that there is only one apparent significant carrier of incompatible elements, KREEP, which in addition to having much higher concentrations of incompatible elements is more mafic (i.e., richer in olivine, pyroxene, and ilmenite) than feldspathic highlands rocks and less mafic than mare basalts.

There are at least three second-order effects that lead to imperfect correlations among elements: (1) the high abundance of ilmenite in some mare basalts but not others (Figs. 2.12a, 2.19), (2) variation in the MgO/FeO ratios of pyroxenes and olivine, with low ratios characteristic of mare basalts and volcanic glass and high ratios characteristic of nonmare rocks (Figs. 2.12c, 2.19), and (3) the presence of significant Ca in the clinopyroxene of mare basalts and its low abundance in the pyroxenes of most nonmare samples (Fig. 2.13). Nonmare regoliths and breccias vary considerably in MgO/FeO, from ferroan (low MgO/FeO) to magnesian (high MgO/FeO) extremes (Fig. 2.12c).

6.2.4. Correlations among incompatible elements. To a first approximation, ratios of any two incompatible elements are constant among Apollo regolith samples (Taylor 1975; Haskin and Warren 1991) because KREEP lithologies (Section 3.4.2) such as impact-melt breccias are the major carriers of incompatible elements. To a second approximation, important differences exist and the reasons are well understood. There are two causes.

(1) Among rocks and breccias that do not contain KREEP or that contain only a small proportion of KREEP, ratios of incompatible elements vary because of differences in compositions of magmas from which the rocks ultimately derived and the crystallization history of the magmas. For example, Gd/Sm and Th/Sm ratios are quite variable among different types of mare basalt (next sections) and ratios of light to heavy REE vary among the various feldspathic lunar meteorites (Korotev et al. 2003b). Although these differences can be measured in the laboratory where high analytical precision can be achieved, they are difficult to detect

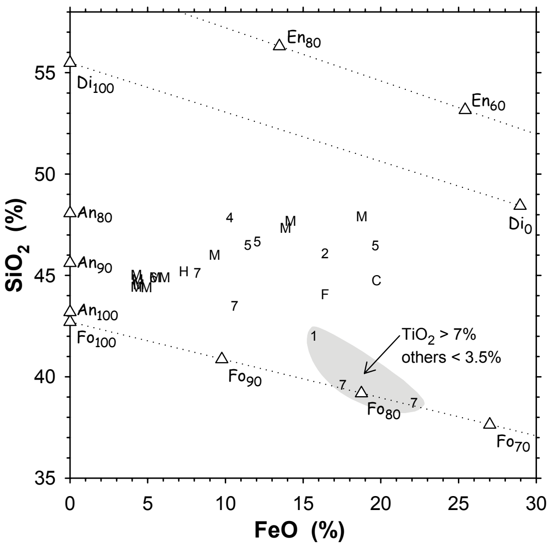

Figure 2.17. Variation of SiO_2 with FeO (total Fe as FeO) in lunar regolith (symbols as in Fig. 2.3) and comparison to stoichiometric concentrations in some minerals (△). High TiO_2 soils (Apollo 11 and 17) have low SiO_2 concentrations because the main carrier of Ti, ilmenite, contains essentially zero SiO_2. SiO_2 concentrations are nearly constant in Ti-poor soils, but increase somewhat with FeO because (1) FeO is carried mainly by pyroxenes in low-Ti soils (Fig. 2.3) and pyroxenes have a greater SiO_2 concentrations than the plagioclase (~An_{96}) typical of Fe-poor soils and (2) average anorthite (An) content of plagioclase from Fe-rich rocks tends to be less than that of Fe-poor rocks and SiO_2 increases with decreasing An content of plagioclase. Mineral abbreviations: An, anorthite; Fo, forsterite; En, enstatite; and Di, diopside.

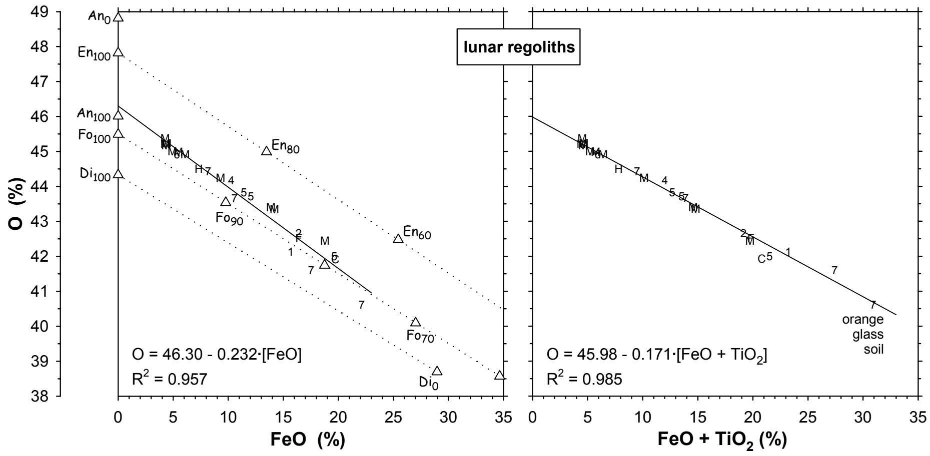

Figure 2.18. Variation of oxygen (O) with FeO and FeO plus TiO_2 (total Fe as FeO) in lunar regolith and comparison to stoichiometric concentrations in some minerals (see Fig. 2.17).

from orbit by remote techniques because in low-KREEP samples the absolute concentrations of incompatible elements are usually low and the relative precision is consequently poor.

(2) Although largely excluded from the major rock-forming minerals, when the concentrations of incompatible elements become sufficiently high in a cooling magma, they are incorporated into specific minor or accessory minerals, e.g., K and Ba into alkali feldspar, REE into RE-merrillite, and Th into zircon. In an igneous system where concentrations of incompatible elements are high, such as when crystallization of a liquid is nearly complete, minor minerals form and magmatic processes can separate one type of mineral from another. Feldspar may rise buoyantly in a magma chamber, concentrating alkali elements like Na and K toward the top. (This is a hypothetical example, one not actually demonstrated to be the cause

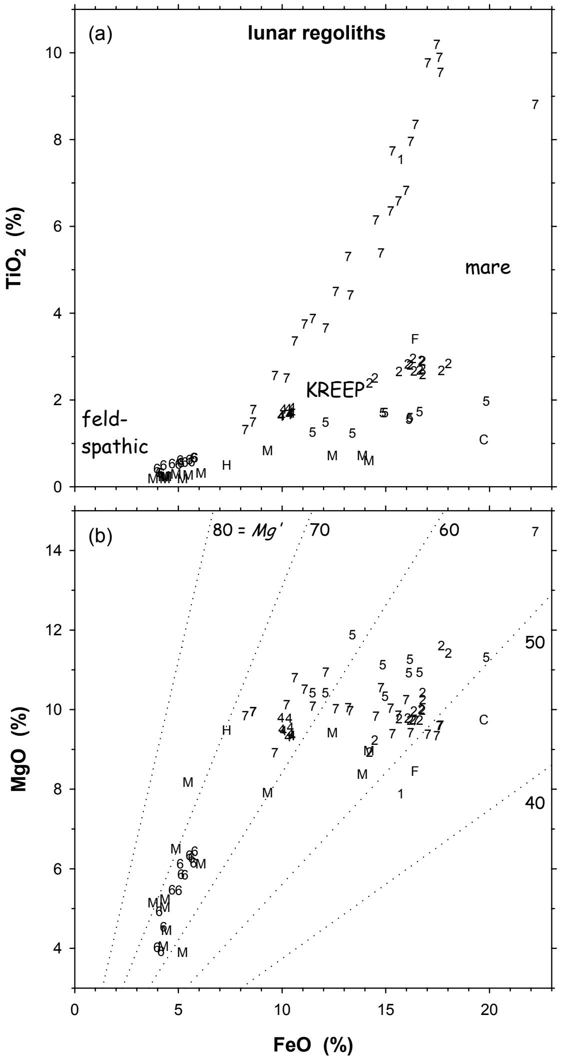

Figure 2.19. Variation of TiO_2 and MgO with FeO (total Fe as FeO) in lunar regolith samples. *Mg'*= mole percent Mg/[Mg+Fe]. (a) TiO_2 is uncorrelated with FeO in mare basalts, so high-FeO soils have highly variable TiO_2 abundances. TiO_2 concentrations in feldspathic regolith are consistently low. (b) MgO is only poorly correlated with FeO in lunar soils. Nonmare soils tend to have greater MgO/FeO (and *Mg'*) than mare soils (see also Fig. 2.12c).

of formation of alkali anorthosites.) In highly differentiated lunar magmas, two immiscible silicate liquids can form, one rich in Fe, Ti, P, and REE and the other rich in K and Si. This mechanism has been suggested to be the one leading to formation of lunar granite or felsite (Quick et al. 1977; Taylor et al. 1980; Neal and Taylor 1989; Jolliff 1991, 1998; Jolliff et al. 1999). If separation, for example, of K feldspar from RE-rich phosphate minerals occurs, the resulting rocks will not have KREEP-like K/REE ratios. Although on the basis of the Apollo and Luna samples, such separations are known to occur, all incompatible-element-rich rocks with non-KREEP-like ratios of incompatible elements are very small rocks, usually less than a gram. A small felsite clast in a breccia or a small felsite fragment in the regolith may represent a segregation and separation on the order of centimeters or kilometers. That such segregations occur on a small scale is clear; however, it is not known if they occur in lunar magmatic systems on a large scale. In principle, the chemical effects of large-scale separations might be observed with detectors on orbiting spacecraft. Any such anomalies in ratios of incompatible elements are of special importance because they ultimately relate to whether there was a global magma ocean and, if so, how it evolved.

Samarium and Gadolinium. Two incompatible elements of special interest are the rare earth elements Sm and Gd because, like Th, their concentrations provide a measure of the relative abundance of KREEP (Section 1.3.2) and the sum of their concentrations can be estimated from the Lunar Prospector neutron spectrometer (LP-NS) data (e.g., Elphic et al. 2000). Because the geochemical behavior of the two elements is very similar, Gd/Sm ratios in lunar rocks span a narrow range, about a factor of 2, and soils show an even narrower range, less than a factor of 1.4 (Figs. 2.20, 2.21). Samples with high concentrations of REEs, that is, samples with a large component of KREEP, consistently have a Gd/Sm ratios of about 1.18. Gd/Sm ratios in mare basalts are greater than in KREEP and they cover a broader range, 1.3–1.6. The most extreme Gd/Sm ratios occur in samples with very low concentrations of REE.

For the purpose of comparing data obtained remotely for Gd and Sm with samples, one problem is the lack of data for samples. Concentrations of Sm in lunar samples are widely available because Sm concentrations have been determined by INAA (instrumental neutron activation analysis), mass spectrometry, and other techniques. The most precise data for Gd and Th in lunar samples have been obtained by mass spectrometry, a technique that has been rarely used for these elements since the 1970’s. Most data for the REEs and Th have been

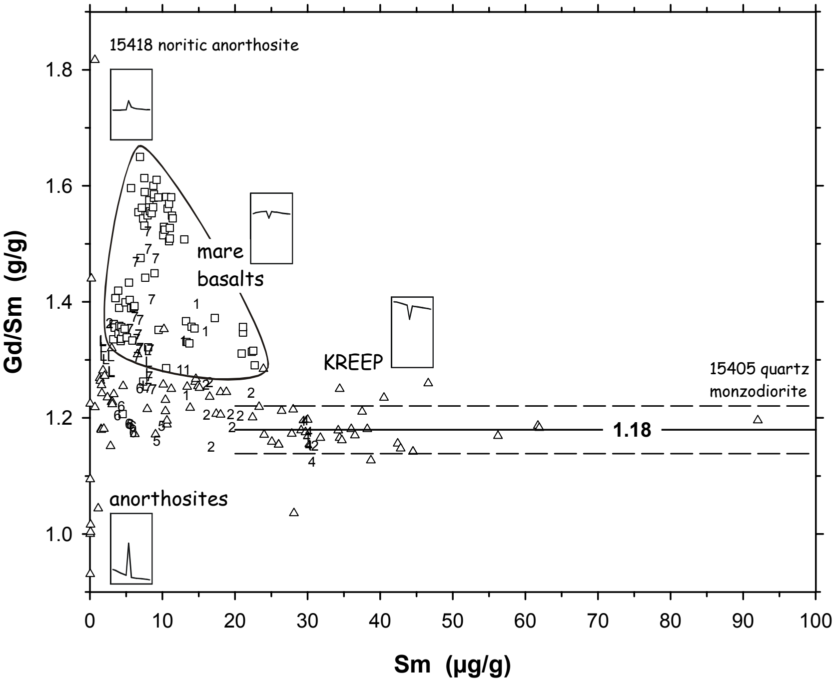

Figure 2.20. Data for Sm and Gd obtained by mass-spectrometric isotope dilution in lunar samples. Letters and numbers represent soils (e.g., Fig. 2.11, squares represent mare basalts, and triangles represent nonmare rocks. Mare basalts have Gd/Sm ratios that range from 1.3–1.6. For nonmare samples with high concentrations of rare earth elements (Sm >20 μg/g), that is, those with a large proportion of KREEP component, Gd/Sm ratios are essentially constant at 1.18 ± 0.04 (mean ± standard deviation). For nonmare samples with very low concentrations of Sm, Gd/Sm ratios are highly variable. Idealized chondrite-normalized REE patterns (e.g., Fig. 2.21) are shown for different portions of the plot.

obtained by INAA, a technique that determines Sm with high precision and Th with poor precision at low concentration and moderate precision at high concentration but which does not determine Gd accurately. As a consequence, there are no Gd data for most lunar samples. However, for any given sample or rock type, the Gd concentrations can be estimated from other trivalent REEs with high accuracy because of the strong interelement correlations among the trivalent REE. For nonmare soils and breccias with moderate to high concentrations of Sm, the Gd concentration can be estimated well by multiplying the Sm concentration by 1.18 (Fig. 2.20). Gd concentrations can also be estimated graphically in any sample using plots of chondrite-normalized concentrations of other REE against atomic number (e.g., Fig. 2.21). From INAA data for Ce, Sm, Tb, and Yb, the concentration of Gd can be estimated well in any

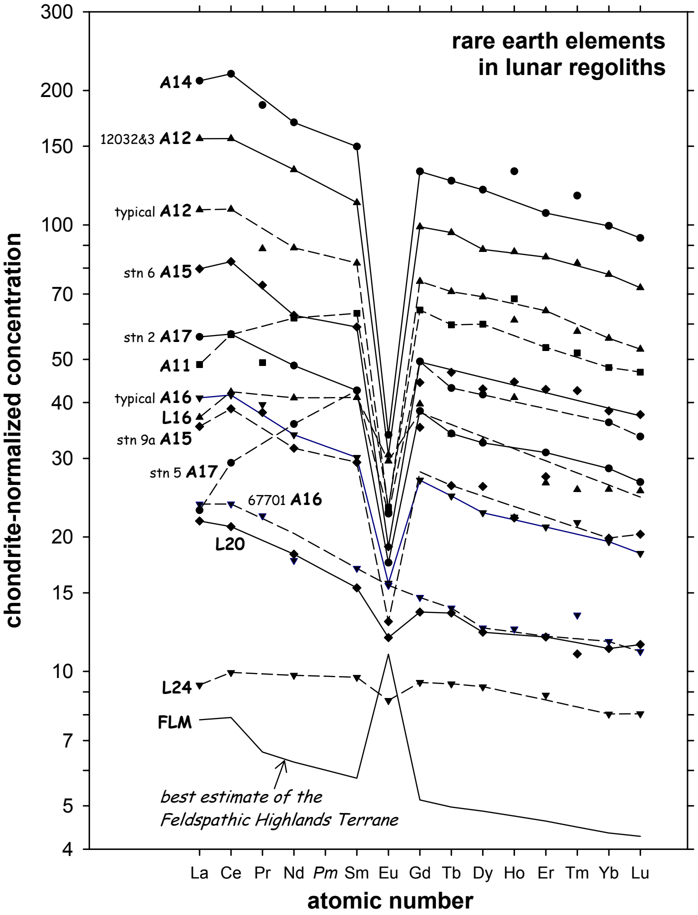

Figure 2.21. Chondrite-normalized concentrations of rare earth elements in lunar regolith as a function of REE atomic number (e.g., Haskin, 1985). Each regolith pattern represents averages of all data for that regolith. Data for Pr, Ho, and Tm are rare and imprecise. Dashed lines represent soils dominated by mare basalt. Samples 12032 and 12033 are the two most Th rich soil samples from Apollo 12 (Fig. 2.11). At Apollo 15, the soil from station 9a is the richest in Fe and that from station 6 is poor in FeO (Fig. 2.11). Sample 67701 is a soil from North Ray Crater at Apollo 16. At Apollo 17, soil from station 5 is the most Fe rich and that from station 2 is among the most Fe poor (Fig. 2.11). The feldspathic lunar meteorites (FLM), provide our best estimate of the surface composition of the Feldspathic Highlands Terrane (Table 2.6). Normalization values: 1.36*C*, where *C* represents the "Mean C1 Chondr." values of Table 1 of Anders and Grevesse (1989).

lunar sample by formulas based on logarithmic plots of chondrite-normalized concentrations using the CI chondrite values of Anders and Grevesse (1989):

$$Gd = 0.267\ \ln[(A+B+C)/3] \qquad \text{(mean)}$$

$$A = \exp[3\ \ln(Sm/0.2) - 0.5\ \ln(Ce/0.82)] \qquad \text{(Ce-Sm extrapolation)}$$

$$B = \exp[(\ln(Sm/0.2) + 2\ \ln(Tb/0.0493))/3] \qquad \text{(Sm-Tb interpolation)}$$

$$C = \exp[(6\ \ln(Tb/0.047) - \ln(Yb/0.221))/5] \qquad \text{(Tb-Yb extrapolation)}$$

where Gd, Ce, Sm, Tb, and Yb are element concentrations in µg/g (ppm). The accuracy of the estimate depends strongly on the accuracy of the Tb concentration, an element that is determined with poor to moderate precision by INAA and for which systematic errors occur in some data sets. (The Ce-Sm extrapolation could be formulated with Nd instead of Ce, but Nd is determined with lower precision by INAA.)

Correlations with Thorium. In all lunar regolith, Th and U are highly correlated, with a mean U/Th ratio of 0.28 (Fig. 2.22). The correlation is strong because both elements are carried by the same few minerals, mainly zircon and RE-merrillite, the latter also being the main carrier of the REEs.

In nonmare regoliths, REEs such as Sm correlate well with Th, and Sm/Th ratios are typically about 2.8 (Fig. 2.23). Because the Apollo 14 rocks and regolith contain felsite (granite), a rare evolved lithology that has high concentrations of Th and low Sm/Th ratios (highly variable, but 0.9 ± 0.3 is typical) compared to KREEP (Jolliff 1998), the Sm/Th ratio of the Apollo 14 regolith is lower, 2.36. This difference is consistent with the observation that the ratio of RE-merrillite to zircon is less in felsite than in generic KREEP and zircon is not an important carrier of Sm. In contrast, the RE-merrillite to zircon ratio is high in alkali anorthosite compared to KREEP, leading to high Sm/Th ratios (6 ± 3). Although the Apollo 14 regolith also contains a high proportion of alkali anorthosite compared to other nonmare regoliths, Sm concentrations are not usually so high in alkali anorthosites that their presence modifies the Sm/Th ratio. Regoliths from mare sites also have high Sm/Th ratios, particularly

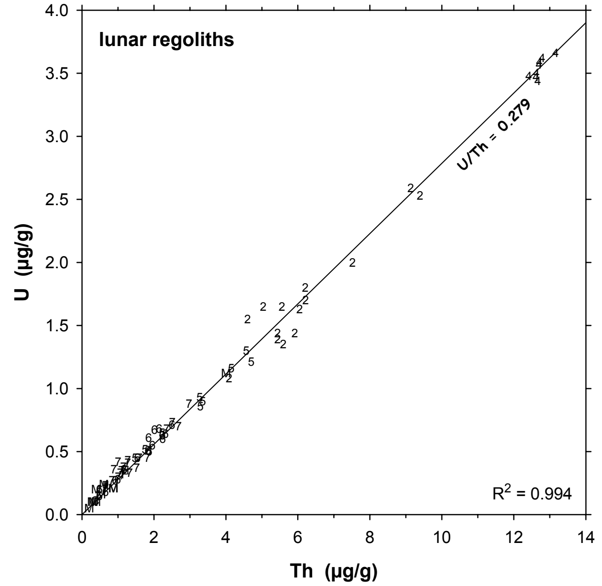

Figure 2.22. Th and U are highly correlated in lunar regolith. The line is defined by the origin and the mean Th and U concentration of the plotted points. Most of the scatter results from analytical uncertainty.

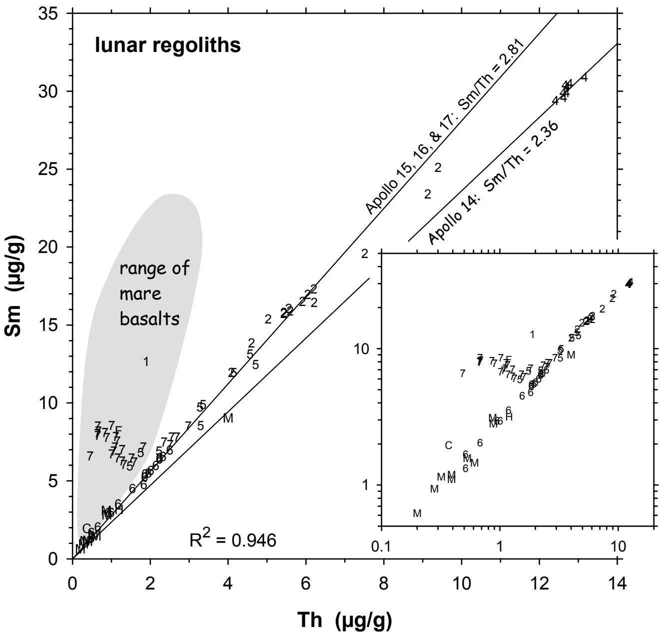

Figure 2.23. Variation of Sm with Th in lunar regolith (same symbol key as Fig. 2.12). Soils with high concentrations of Th are dominated by KREEP (Fig. 2.11). All KREEP-rich soils have similar Sm/Th ratios, although breccias and soils from Apollo 14 have somewhat lower ratios (2.36 ± 0.04) than those from other sites (2.81 ± 0.10; see text). Mare basalts have greater Sm/Th ratios than KREEP, thus soils dominated by mare basalt (Apollo 11, 15, and 17) plot off the KREEP mixing lines. The inset shows the same data on logarithmic scales.

those formed from high-Ti mare basalts (Figs. 2.23, 2.24). For example, the Sm/Th ratio of the Apollo 11 regolith is 6.5 and for the mare soils of Apollo 17 the Sm/Th ratio is 12.

Although also an elemental characteristic of KREEP, K does not correlate perfectly with Th in lunar regolith (Fig. 2.25). K/Th ratios in KREEP-rich samples are variable because K and Th are carried by different phases (K is in potassium feldspar) that are not exactly in the same proportions in all rocks of nominal KREEP composition. Mare basalts and KREEP-poor nonmare samples also have variable K/Th ratios. Anomalous regolith samples typically have greater K/Th ratios than Apollo 14-type KREEP.

7. FELDSPATHIC LUNAR METEORITES AS REGOLITH

Most of the information provided in this section is summarized from Korotev et al. (2003b) without further citation.

7.1. Composition of the feldspathic upper crust

Remarkably, a large fraction of the lunar meteorites are either regolith or fragmental breccias that are composed of fine-grained material that occurred within a few meters of the lunar surface (Warren 1994, 2001). Most lunar meteorites have compositions that are consistent only with an origin in the feldspathic highlands (Fig. 2.26). All of the feldspathic lunar meteorites have lower concentrations of the elements associated with KREEP (e.g., 0.2–0.5 µg/g Th; Table 2.1 and Fig. 2.27) than does typical regolith of the Apollo 16 site

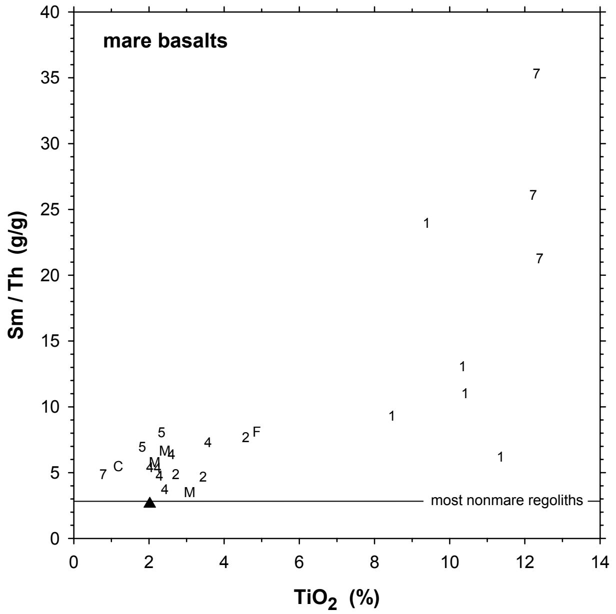

Figure 2.24. Among mare basalts there is a tendency for high-Ti basalts (Apollo 11 and 17) to have greater Sm/Th ratios than low-Ti basalts (2 = Apollo 12, etc., F = Luna 16, C = Luna 24, and M = lunar meteorite). Sm/Th ratios are greater in mare basalts than in KREEP basalt (triangle) and nonmare regolith (Fig. 2.23). Each symbol represents the mean composition of a type of mare basalt or a mare basalt meteorite.

(1.9–2.5 µg/g Th; Fig. 2.27), suggesting that the meteorites all originate from points more distant from the Procellarum KREEP Terrane than the Apollo 16 site. There are no reasons to suspect that the source craters of the meteorites are not randomly distributed about the Moon. Thus, ironically, the feldspathic lunar meteorites provide the best estimate of the composition of the surface of the Feldspathic Highlands Terrane (Table 2.6) even though their point of origin on the lunar surface is not known. Among the brecciated lunar meteorites, only Sayh al Uhaymir 169 and, possibly, Calcalong Creek have concentrations of incompatible elements great enough to have an origin in the Procellarum KREEP Terrane.

On the basis of the feldspathic lunar meteorites, the surface of the Feldspathic Highlands Terrane has the following composition: 0.22 ± 0.04% TiO_2, 28.2 ± 1.0% Al_2O_3, 4.4 ± 0.5% FeO (total Fe as FeO), 5.4 ± 1.4% MgO, and 0.37 ± 0.11 µg/g Th (Table 2.6). These estimates apply strictly to the lunar surface because the meteorites are surface samples. Consequently they include about 1.6% meteoritic material as CI chondrite, based on the mean concentrations of Ni, Ir, and Au in the meteorites. If we estimate the mean composition of, say, the upper kilometer of regolith by removal of the meteoritic component (Sections 2.1 and 6.2.1), concentrations of FeO and MgO are distinctly lower (4.0% and 5.3%) and that of Al_2O_3 is a bit greater (28.5%). This composition corresponds to 78% plagioclase by mass or about 82% by volume and is equivalent to that of a noritic anorthosite (Fig. 2.3).

7.2. Lunar meteorites as ground truth

Lunar meteorites are important to remote sensing because they provide a form of ground truth. For example, the distribution of FeO concentrations on the lunar surface as derived from Clementine spectral reflectance data compares well with the distribution of FeO among the lunar meteorites (Fig. 2.26). This concurrence provides support that the algorithm used to derive FeO concentrations from spectral reflectance parameters (Lucey et al. 2000) is accurate to first order. Conversely, it provides support to the assumption that estimates of the composition of the upper crust of the Feldspathic Highlands Terrane as derived from lunar meteorites are reasonable.

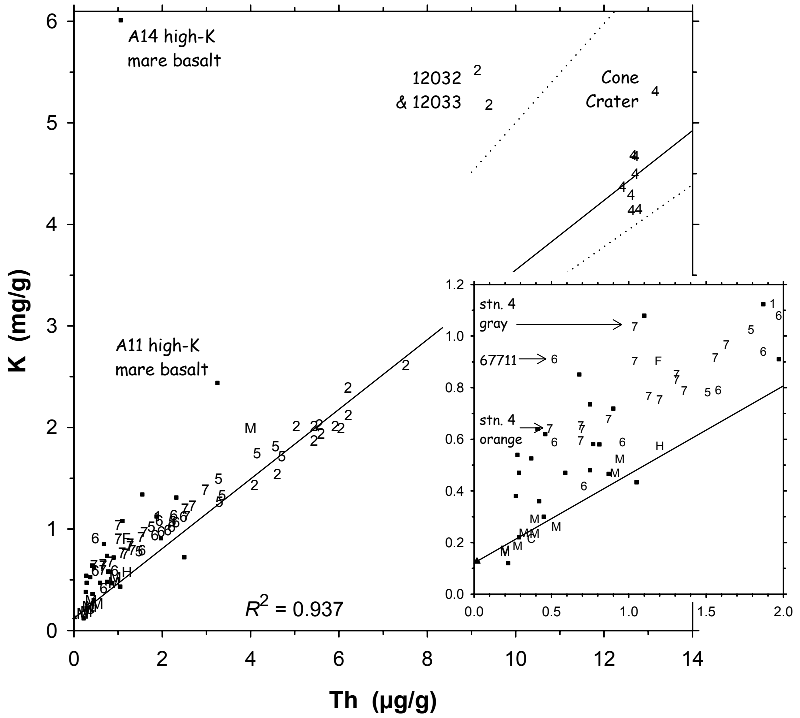

Figure 2.25. Variation of K with Th in lunar regolith (symbols as in Fig. 2.11) and all known types of mare basalt (small squares). The solid diagonal line (K = 120 + 343•Th) is defined by highly feldspathic ferroan anorthosite (sample 15415, triangle) and Apollo 14 KREEP-rich impact-melt breccias (off scale at 16.1 µg/g Th and K/Th = 350; Korotev 2000). R^2 refers to the regolith points only. The dotted lines represent the range of K/Th ratios in KREEP basalt and KREEP-rich impact-melt breccias from the Apollo sites (310 < K/Th < 500). Most mare basalts have K/Th ratios greater than that of KREEP and the feldspathic lunar meteorites (M's at low Th), with the high-K basalts of Apollo 11 and 14 being the most anomalous. Some regolith samples have anomalously high K/Th ratios compared other regolith samples collected at the same site. These include the ropy glass soils of Apollo 12 (samples 12032 and 12032, Korotev et al. 2000) and Apollo 17 (gray soils of station 4; Korotev and Kremser 1992), the orange glass soil of Apollo 17 (74220), the soil from Cone Crater at Apollo 14 (14141), and the alkali-rich immature soil, 67711, of North Ray Crater at Apollo 16 (Korotev 1983b, 1996).

A similar comparison of Th between the feldspathic lunar meteorites and data from the Lunar Prospector GRS suggests that at low Th concentration, the LP-derived concentration values (Lawrence et al. 2000) are too high (Fig. 2.27; Gillis et al. 2004; Warren 2005). Similarly, all feldspathic lunar meteorites have TiO_2 concentrations in the range of 0.2–0.3% (Table 2.1), much lower than the average of 1.5% TiO_2 derived for farside highlands from the Apollo GRS (Metzger and Parker 1979; Davis 1980). This discrepancy confirms the existence of a systematic error in the Apollo-derived data. Within the large uncertainties, Clementine-derived TiO_2 concentrations (Lucey et al. 2000; Section 10.4.6) are consistent with the feldspathic lunar meteorites.

7.3. The magnesium to iron ratio of the feldspathic crust

The numerous feldspathic lunar meteorites have the following interesting combination of properties: (1) With 72–86 wt% plagioclase (approximately 76–89 vol%, they are highly feldspathic, but not as feldspathic as ferroan anorthosites of the Apollo collection,

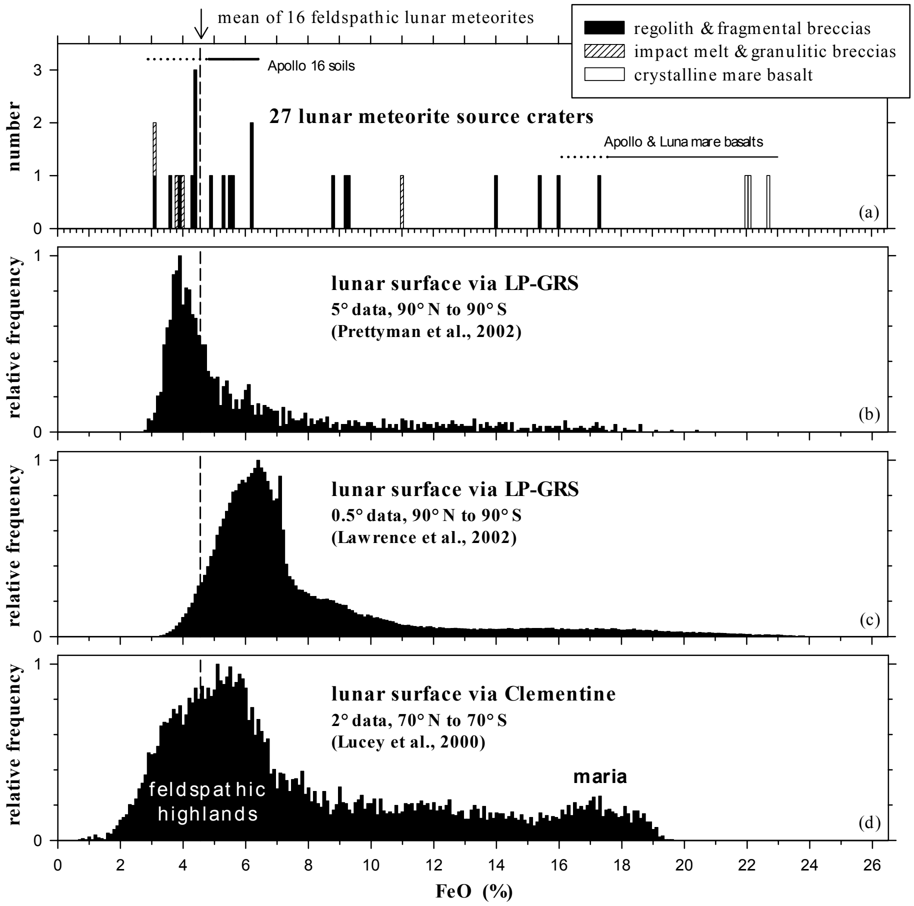

Figure 2.26. Comparison of estimates and measurements of the distribution of FeO on the lunar surface (updated from Korotev et al. 2003b). (a) Distribution of FeO concentrations (total iron as FeO) in source regions of lunar meteorites. The range of compositions of mature surface and trench soils from Apollo 16 is shown by the solid horizontal line at low FeO; the dotted line represents the range of immature and submature soils from North Ray Crater (Korotev 1996, 1997). The solid horizontal line at high FeO represents the range of most mare basalts from the Apollo and Luna missions; the dotted portion corresponds to the aluminous basalts of Apollo 14 (Dickinson et al. 1985). (b–d) Concentrations derived from data acquired from orbit. The LP (Lunar Prospector) GRS (gamma-ray spectrometer) results are those of Prettyman et al. (2002a; June 2002 data) and Lawrence et al. (2002; January 2002 data). For the Clementine results of Lucey et al. (2000), 94% of the lunar surface lies between 70° S and 70° N. The peak at low-FeO concentration corresponds mainly to farside, northern highlands.

which average 92 wt% plagioclase, (8.1 ± 8.6 wt% mafic silicates; Warren 1990). (2) To a first approximation the meteorites are all similar in composition in that they all have low concentrations of incompatible elements and a moderately narrow range of Al_2O_3 concentrations (25–31%) but they differ in having a wide range of MgO to FeO ratios (Fig. 2.12). The MgO/FeO variation leads to a wide range for *Mg´* of 57 to 77 (Fig. 2.19). (If only those meteorites for which compositional data have been published in peer-reviewed literature are considered, the range is reduced to 60–73.) (3) The MgO/FeO ratio of feldspathic lunar meteorites correlates with the proportion of normative olivine and high *Mg´* meteorites are rich

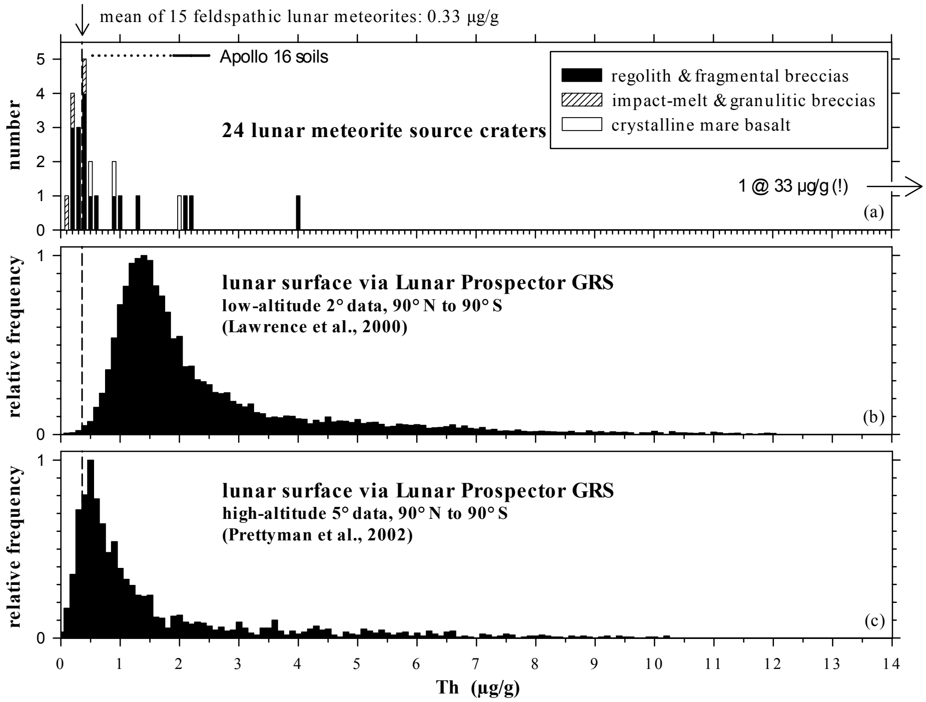

Figure 2.27. Like Figure 2.26, but for Th (updated from Korotev et al. 2003b). All feldspathic lunar meteorites have ≤0.6 µg/g Th. (a) One lunar meteorite, Sayh al Uhaymir 169 with 33 µg/g Th (Gnos et al. 2004), plots far off scale. No Th data are yet available for two meteorites of Figure 2.26. (b) Th concentrations derived from LP-GRS (gamma-ray spectrometer) data by Lawrence et al. (2000; with June 2001 update of data) using a simple peak-over-background technique are systematically high, at least at low Th concentration, compared the lunar meteorites. The mode (1.4 µg/g) exceeds the mean of the feldspathic lunar meteorites (0.36 µg/g) by a factor of 3.6. (c) The distribution of Th concentrations derived by Prettyman et al. (2002a; data of June 2002), using a library least-squares technique, more closely match the distribution of the brecciated lunar meteorites and yields a highlands mode (0.5 µg/g) only a bit greater than the mean of the feldspathic lunar meteorites.

in modal forsterite. (4) The mean *Mg´* of the feldspathic lunar meteorites (~69) is greater than the mean of ferroan anorthosite (~60) and the most magnesian lunar meteorites are outside the range for ferroan anorthosite (Fig. 2.4).

These observations have important implications if one accepts the premise that the meteorites represent the upper crust of the Moon, at least with respect to composition, and that they derive from numerous random locations. For example, they support the hypothesis that a significant fraction of the Mg and Fe in the feldspathic lunar crust does not derive from the ferroan-anorthositic suite of lunar plutonic rocks (Korotev and Haskin 1988). Qualitatively, the various observations are consistent with models that the early crust of the Moon was a flotation cumulate of ferroan anorthosite into which magnesian-suite magmas intruded. In terms of such models, the feldspathic lunar meteorites are mainly mixtures of FAS rocks and Mg-suite rocks such as those at the high-*Mg´* end of the trend of Figure 2.4 because most of the high-*Mg´* rocks of the figure are olivine-rich, i.e., troctolite and dunite. In detail, however, this simple model does not account for the feldspathic lunar meteorites and certain other observations. Problems include the following. (1) In feldspathic lunar meteorites, mafic, high-*Mg´* rocks such as troctolite and dunite are all but absent as clasts. (2) The actual lithologic

Table 2.6. Estimates of the concentrations some mostly lithophile elements in the upper few meters (Surface) and upper few kilometers (FUpCr) of typical feldspathic crust based on feldspathic lunar meteorites (from Korotev et al. 2003b)

	Unit	*Surface*	±	*FUpCr*		*Unit*	*Surface*	±	*FUpCr*
SiO_2	%	44.7	0.3	44.9	Zr	ppm	35	11	35
TiO_2	%	0.22	0.04	0.22	Ba	ppm	33	10	33
Al_2O_3	%	28.2	1.0	28.5	La	ppm	2.3	0.6	2.4
Cr_2O_3	%	0.096	0.014	0.092	Ce	ppm	6.0	1.6	6.0
FeO	%	4.4	0.5	4.0	Pr	ppm	0.8	0.2	0.8
MnO	%	0.063	0.004	0.060	Nd	ppm	3.6	0.9	3.7
MgO	%	5.4	1.4	5.3	Sm	ppm	1.1	0.3	1.1
CaO	%	16.3	0.9	16.4	Eu	ppm	0.78	0.05	0.79
Na_2O	%	0.35	0.03	0.34	Gd	ppm	1.3	0.3	1.3
K_2O	%	0.027	0.008	0.026	Tb	ppm	0.23	0.05	0.23
P_2O_5	%	0.027	0.009	0.023	Dy	ppm	1.5	0.4	1.5
Σ	%	99.8		99.9	Ho	ppm	0.33	0.08	0.33
Mg´	%	69	3	70	Er	ppm	0.9	0.2	0.9
K	ppm	220	60	210	Tm	ppm	0.14	0.03	0.14
Sc	ppm	8.0	1.0	8.0	Yb	ppm	0.89	0.2	0.90
Cr	ppm	660	90	630	Lu	ppm	0.13	0.03	0.13
Mn	ppm	490	40	460	Hf	ppm	0.8	0.2	0.8
Co	ppm	17	3	10	Ta	ppm	0.11	0.02	0.11
Ni	ppm	185	45	~16	Ir	ppb	7.5	2.8	=0
Rb	ppm	0.7	0.3	0.7	Au	ppb	2.8	1.0	~0.6
Sr	ppm	150	12	151	Th	ppm	0.37	0.11	0.38
Y	ppm	9	2	9	U	ppm	0.16	0.10	0.16

"Surface" is essentially the mean composition of lunar meteorites ALHA 81005, MAC 88105, QUE 93069, Yamato 86032, Dar al Gani 262, Dar al Gani 400, Dhofar 025, and NWA 482 based all literature data (Table 1), except that estimated concentration values were used for data suspected to be compromised by terrestrial contamination (K, Ca, Rb, Sr, Ba, and Au). Values for Y, Pr, Gd, Dy, Ho, Er, and Tm were estimated from the other REE. The uncertainty (±) is the 95% confidence limit on the mean values. "FUpCr" (feldspathic upper crust) is an estimate of the composition of the upper few kilometers of the crust and differs from the surface composition only in the absence of a component of CI chondrite (1.58%; values of Anders and Grevesse, 1989, or 1.16% on a volatile-free basis).

carriers of Mg are feldspathic lithologies, mainly magnesian granulitic breccias (Section 5.2.4). (3) Compositions of the magnesian granulitic breccias are not consistent with mixtures of ferroan anorthosite and mafic Mg-suite rocks such as the norites, troctolites, and dunites of the Apollo collection. (4) Among the Apollo samples, mafic Mg-suite rocks were found mainly at the Apollo 15 and 17 sites, which are in or near the Procellarum KREEP Terrane; they were not found at the Apollo 16 site, which is in the Feldspathic Highlands Terrane.

Compositions of the feldspathic lunar meteorites suggest that *Mg´* varies considerably from place to place at the surface of the feldspathic highlands, even in regions largely devoid if Imbrium ejecta. There is little information on the nature of scale and distribution of the variation because the Mg concentration of the feldspathic highlands is low (3–8% MgO) and has, as of this writing, not been determined precisely by orbital spacecraft. Obtaining such information is a high priority goal of future orbiting missions because the data would provide an important constraint for models of formation of the lunar crust. For example, the Luna 20 regolith (23% Al_2O_3) is more mafic than the feldspathic lunar meteorites and has a moderately high *Mg´* (70). Does the unusual composition reflect that the regolith consists mostly of ejecta from Crisium, a basin that penetrated deeper into the crust than most? Are the ejecta of other basins in the Feldspathic Highlands Terrane more magnesian than regions distant from basins? Is the lower crust more magnesian than the upper crust?

In order to constrain *Mg´* to the ± 2 units (e.g., 69 ± 2), which would provide truly useful information, Fe and Mg concentrations need be determined to within 2–3% of their values, e.g., 4.4 ± 0.11% FeO and 5.4 ± 0.14% MgO for typical feldspathic highlands (Table 2.6). Alternatively, the Mg/Fe ratio would need to be determined to within 4%. Such precision would be a challenge to any presently available technology. If the uncertainty in Fe and Mg concentrations are each 10% and not correlated with each other, then the uncertainty in *Mg´* is 8 units (e.g., 69 ± 8) for typical highlands compositions. For certain types of questions, for example, "Is proximal basin ejecta more magnesian than distal ejecta?," this level of precision would be adequate if the spatial resolution were small enough such that numerous measurements could be obtained on the proximal deposit.

8. REGOLITH EVOLUTION: MICROMETEORITES AND ENERGETIC PARTICLE INTERACTIONS

The Moon's surface is a hostile environment. Unprotected by a planetary magnetic field and atmosphere, it is assailed by meteoroids and energetic particles. These influences constitute the lunar weathering agents. Unlike on Earth where water and wind are major weathering forces, the forces of weathering on the Moon originate external to the planet. Thus the term *space weathering* is often used to denote the *in situ* modification of lunar surface material by external forces. The result of space weathering of lunar soil is *maturation*, the accumulated effects of space weathering. Space weathering denotes processes at the finest scales, of grains or a few grains. The process that operates at larger scales, impacts of objects larger than dust particles, produce the lunar soil upon which space weathering operates. These effects include disaggregation, lithification, melting, and vaporization of material from meteoroid impacts, implantation of ions from solar and galactic cosmic rays and the solar wind, sputtering of surface atoms from interaction of cosmic rays, condensation of sputtered and impact-vaporized material, accumulation of meteoritic material and agglutinates. Micrometeorite impact also produces "nanophase," "single-domain," or "submicroscopic" iron grains not of meteoritic origin that are very small, typically 4–33 nm in diameter, thought to consist of essentially pure iron that is produced by reduction of Fe^{2+}.

Many of the effects of maturation can be quantified, e.g., the concentrations of solar-wind derived gases or the relative abundance of agglutinates, and these quantities are used as a measure of maturity. This section discusses progress in understanding regolith evolution and maturation from a sample perspective. Space weathering products, principally the production of nanophase Fe, have major effects on the optical properties of lunar soil. Optical effects of space weathering are discussed in Section 10.4.3.

8.1. The Moon's micrometeorite and energetic-particle environment

The scientific significance of the energetic particles in lunar science is two-fold. First, these particles alter the composition of the lunar surface physically and chemically and these influences are used to make inferences about the history of the lunar surface. Second, the immediate effects of these particles enable gamma-ray and neutron spectroscopic remote sensing (Sections 10.1, 10.2). Micrometeorite impact causes effects not found in larger impacts owing to very short timescales. These effects are central to many space-weathering effects.

There are a variety of energetic particles in the Moon's environment. Because the Moon has essentially no atmosphere and no or very weak magnetic fields, these particles interact with the lunar surface and often leave a characteristic and measurable record of their interactions. Some interaction products, such as energy-rich defects and stable cosmogenic nuclides, may be preserved over the entire history of the Moon and provide windows into the distant past of the Moon and of these particles. Other products, such as cosmogenic radionuclides, can be used to study specific time periods.

The most numerous energetic particles in the lunar environment are those in the solar wind, in the solar energetic particles, and in the galactic cosmic rays (for details on these particles and their lunar interactions, see, e.g., Reedy et al. 1983; Sonett et al. 1991; Vaniman et al. 1991). These particles are either implanted or induce nuclear reactions in lunar materials.

The solar wind is a plasma continuously emitted from the Sun and contains an equal number of ions and electrons. At 1 A.U. from the Sun, the solar wind ions are moving away from the Sun at velocities of ~300-800 km/s and have energies of ~1 keV/nucleon. Solar wind ions penetrate only a few tens of nanometers into lunar material before stopping. Many solar wind-implanted species diffuse out of the surface and escape back into space. Some, however, remain implanted indefinitely.

Solar energetic particles, sometimes called solar cosmic rays, are particles emitted from the Sun that have been accelerated to energies of ~1-100 MeV/nucleon either at the Sun (small impulsive events) or by shock processes in the interplanetary medium (large gradual events). Occasionally, solar particles can be accelerated to GeV and higher energies. Solar energetic particles occur very irregularly and for most of the time are not present in the solar system. Solar particle events last a few days to a week or so. Most solar-particle events occur two or more years away from the time of minimum solar activity. Modern solar energetic particles have been studied since 1956, and are usually about 98% protons with a proton/alpha-particle ratio of ~50. There is also a small fraction of heavier ions. Solar protons penetrate up to ~1 cm in lunar material. Lunar surface materials contain noble-gas isotopes implanted deeper into grains than those isotopes in the solar wind. Although these more-energetic implanted particles are referred to as solar energetic particles, they appear to be different from those that make up modern solar energetic particles (Wieler 1998).

The galactic-cosmic-ray particles come from outside the solar system and typically have energies of ~0.1-10 GeV/nucleon. They are about 87% protons, 12% alpha particles, and 1% heavier ions. The flux of galactic cosmic-ray particles vary by factors of ~2 over a typical 11-year solar-activity cycle. Galactic cosmic-ray particles can penetrate meters into the Moon and produce a large cascade of secondary energetic particles, including many neutrons.

Energetic charged particles are slowed down in material by ionization energy losses. While ionizing matter, they can induce radiation damage that can be observed as tracks or as thermoluminescence. Most solar energetic particles and galactic cosmic-ray particles are energetic enough to induce nuclear reactions. The nuclear reactions that are produced by these primary and secondary energetic particles make a variety of stable and radioactive nuclides. Some of these product nuclides can be identified as having been made by such nuclear reactions, including rare noble-gas isotopes such as ^{21}Ne and radionuclides such as ^{26}Al. Recent reviews on cosmogenic nuclides and their applications include Vogt et al. (1990), Herzog (1994), Tuniz et al. (1998), and Michel (1999).

The impact of micrometeoroids, essentially interplanetary material ("dust") of less than a millimeter in diameter, has strongly affected the lunar surface. On the basis of estimates for the Earth (Love and Brownlee 1993), approximately 80 g/km^2 of micrometeoroids accrete to the Moon each year. Assuming, for convenience, that they each have the typical diameter of 0.22 mm (Love and Brownlee 1993), a typical square meter of lunar surface will be hit 5 to 10 times per year by a micrometeoroid. Each impact delivers on the order of a Joule of energy. The micrometeoroid vaporizes, but the lunar regolith both melts and vaporizes. This impact flux also causes erosion of rocks. The rates that micrometeoroid impacts (and sputtering reactions) erode the surfaces of lunar rocks have been inferred from profiles for solar cosmic-ray-produced nuclides. The erosion rates of ~1–2 mm/Ma inferred by recent measurements generally agree with previous erosion rates. The erosion rate determined for the hard layer on the surface of rock 64455 (Nishiizumi et al. 1995) was less than that for 74275 (Fink et al. 1998).

8.2. Recent developments in the detection and studies of these interaction products

The products from the interactions of energetic particles with the Moon are measured by counting the atoms themselves or, for some radionuclides, by counting their decay radiations. New and improved techniques have been developed over the last decade that have improved the ability to detect and study these products in lunar samples. For long-lived radionuclides, the use of accelerator mass spectrometry (AMS) has greatly improved detection sensitivities, accuracies, and precision (e.g., Tuniz et al. 1998). The measurements of atoms in gaseous and solid samples have improved, such as better methods for making and extracting ions into mass spectrometers. New techniques have also been developed to get these ions from a sample, such as using closed-system stepped etching (Wieler and Baur 1995). Some measurements of implanted isotopes are now being done with ion microprobes (e.g., Hashizume et al. 2000).

New auxiliary data that are critical for interpreting the measurements have become available, especially for cosmogenic nuclides. Many cross sections have recently been measured for nuclear reactions that make cosmogenic nuclides (e.g., Michel et al. 1997; Sisterson et al. 1997; Jull et al. 1998). Much better computer codes are now available to numerically simulate the propagation of cosmic-ray particles in the Moon and the attendant production of cosmogenic nuclides (e.g., Reedy 2000; Leya et al. 2001; Masarik et al. 2001). Experimental simulations have been performed to test these models (Leya et al. 2000a). The calculated production rates for making cosmogenic nuclides are now much better than they were previously and have been extended to unusual compositions and irradiation geometries (such as very deep in the Moon).

8.3. Implanted solar-wind gases

Mature lunar soils are rich in gas, and the abundance of this gas correlates well with other maturity indices. Many of the noble-gas isotopes found in lunar samples were implanted. Such isotopes can be used to study the history of the lunar sample in which they are found. Samples now buried up to several meters deep in the regolith and some grains inside breccias record such implantations, indicating that they once were on the very surface of the Moon.

Some isotopes have been identified that escaped from the Moon, became ionized, were accelerated in the interplanetary medium, and were then implanted in the Moon. Many atoms of ^{40}Ar made by the decay of ^{40}K escape and are later implanted in the Moon. The amount of this "parentless" ^{40}Ar relative to solar wind-implanted ^{36}Ar changed with time and has been used to study the antiquity of the samples into which they were implanted (Eugster et al. 2001). Some lunar samples had their parentless ^{40}Ar implanted at about 4 Ga.

The record of noble-gas isotopes implanted in the Moon has been well studied. By using samples with known dates for their surface exposures, it has been shown that the relative abundances of noble-gas isotopes from the Sun have changed little during the last 4 Ga (Wieler and Baur 1995; Wieler 1998). Elemental ratios of heavy noble gases have also provided some evidence on how atoms in the solar wind are ionized at the Sun (Wieler 1998).

Some of the nitrogen observed in lunar samples, especially near the very surface of lunar grains, is implanted (e.g., Hashizume et al. 2000). The isotope ratio for this implanted nitrogen in the past has varied by ~30%. The source of this variation is still in question (e.g., Kerridge 2001; Hashizume et al. 2001; Mathew and Marti 2001).

Excesses of 5730-year ^{14}C and 1.5-Ma ^{10}Be have been observed in the surface of lunar samples (e.g., Jull et al. 2000; Nishiizumi and Caffee 2001). These radionuclides are believed to have been made at the Sun and can serve as tracers as nuclear processes occurring in the outer regions of the Sun and for the escape of isotopes from the Sun into the solar wind.

8.4. Solar cosmic rays

8.4.1. Recent measurements. Several depth-versus-concentration profiles have been measured for nuclides made by solar energetic particles. Thin layers were ground from rock 64455 to give a detailed profile near the very surface where most SCR nuclides are produced (Nishiizumi et al. 1995). Better profiles have been measured using AMS for ^{10}Be,^{14}C, and ^{26}Al in several lunar rocks (e.g., Nishiizumi et al. 1995; Fink et al. 1998; Jull et al. 1998). Because ^{10}Be is mainly made by higher-energy solar protons, its measurement with other SCR-produced radionuclides such as ^{26}Al helps to constrain the spectral shape of the solar protons. Profiles have also been measured by AMS for radionuclides that previously were very hard to measure, ^{36}Cl, ^{41}Ca, and ^{59}Ni (Fink et al. 1998; Reedy and Nishiizumi 1998; Schnabel et al. 2000). Near-surface depth profiles for cosmogenic ^{3}He and Ne isotopes were also measured and used to study the records of the solar cosmic rays over the last 2 Ma (Rao et al. 1994).

8.4.2. SCR fluxes in the past. These new and some older profiles of cosmogenic nuclides in the top ~1 cm of lunar samples have been used to determined average fluxes of solar protons during the past ~10 Ma. The profile for ^{59}Ni was used to study the fluxes of solar alpha particles averaged over the last ~0.1 Ma (Schnabel et al. 2000). Measured profiles for solar-proton-produced nuclides have been interpreted by using newly measured cross sections and improved models for GCR production of these nuclides. These new and better average fluxes of solar protons during the last few Ma appear to be less than those for more recent periods (~10-500 kyr) and for SEP measurements since 1956 (Reedy 1998).

8.5. Products of galactic-cosmic-ray interactions

8.5.1. Neutron-capture reactions. Several profiles for neutron-capture reactions as a function of depth have recently been reported in Apollo deep-drill cores. The measurements done by AMS for the 0.1-kyr radionuclide ^{41}Ca agreed well with theoretical calculations (Nishiizumi et al. 1997). Regular mass spectrometry was used to study Sm and Gd isotopic anomalies induced by thermal-neutron-capture reactions as a function of depth (Hidaka et al. 2000). The depth profile for such neutron-capture reactions is quite different from those for most cosmogenic nuclides, which are made by high-energy spallation reactions. Having cosmogenic nuclides with very different depth profiles helps in determining the depth at which a sample, such as a lunar meteorite, was exposed. Other isotopic anomalies have been observed due to reactions on Eu (Hidaka et al. 2000) and cadmium (Sands et al. 2001). Leya et al. (2000b) reported that neutron-capture reactions on ^{181}Ta can affect the isotopic ratios of tungsten isotopes and could affect the use of W in the Hf-W cosmochronometer.

8.5.2. Spallation reactions. Cosmogenic ^{15}N was measured by Mathew and Marti (2001) in nitrogen released at high temperatures from lunar samples. These data were used to infer its production rate near the lunar surface, which was then compared with previously inferred or calculated production rates.

New numerical simulations of the production of spallogenic nuclides have been used to calculate production rates for many cosmogenic nuclides in the Moon. These calculated production rates have been used to unfold the irradiation histories of lunar meteorites and to predict effects not yet seen. Leya et al. (2001) reported depth-versus-production rate profiles for several spallogenic radionuclides and for ^{21}Ne and ^{22}Ne. Masarik et al. (2001) reported calculated production rates as a function of lunar depth for ^{3}He, ^{21}Ne, and ^{22}Ne and noted that the ^{22}Ne/^{21}Ne ratio starts to increase at great depths after decreasing with depth, an effect not yet seen experimentally in lunar samples.

8.5.3. Regolith gardening. SCR-produced radionuclides can be used to study the top ~1 cm of lunar cores. Rates for the mixing of grains due to micrometeoroid impacts, called "gardening," are of the order of a few centimeters per million years (e.g., Reedy et al. 1983). Jull et al. (1996) reported that the top few centimeters of core 76001 was disturbed very recently, probably less than 1 kyr ago by a nearby cratering event. Stable cosmogenic nuclides can be used to estimate gardening effects to lunar depths of meters on time scales of billions of years. The measured profiles of Hidaka et al. (2000) for Sm and Gd isotopic anomalies confirm earlier results that the Apollo 15 deep-drill core has been relatively undisturbed over a very long part of the Moon's history.

8.5.4. Rock erosion. The rates that micrometeoroid impacts and sputtering reactions erode the surfaces of lunar rocks have been inferred from profiles for SCR-produced nuclides. The erosion rates of ~1-2 mm/Ma inferred by recent measurements generally agree with previous erosion rates. The erosion rate determined for the hard layer on the surface of rock 64455 (Nishiizumi et al. 1995) was less than that for 74275 (Fink et al. 1998).

8.5.5. Crater ages. Cosmogenic nuclides have been used to determine when many craters were formed. New measurements by Eugster (1999) confirm the previously reported 2 Ma age for the Apollo 16 South Ray crater.

8.6. Exposure records of lunar meteorites

8.6.1. Ages. By measuring several cosmogenic nuclides with a range of half-lives, the various ages of lunar meteorites can be determined (e.g., Nishiizumi et al. 1996; Polnau and Eugster 1998). Lunar meteorites are finds. The length of time that they were on the Earth's surface and shielded from cosmic rays can be determined from the decay of the shorter-lived radionuclides such as ^{14}C. Most lunar meteorites have terrestrial ages of less than 100 kyr. The length of time that the meteorite was exposed to the omnidirectional (4π) cosmic rays in space while in transit from the Moon to the Earth can usually be distinguished from any cosmogenic-nuclide production while the meteorite was in the lunar surface (a 2π irradiation). The sum of the meteorite's terrestrial age and its 4π-exposure age in space gives the time that the meteorite was ejected from the Moon. Many cratering events on the Moon ejected lunar meteorites.

8.6.2. Lunar exposure depths. Not only can the exposure ages for lunar meteorites in the Moon's surface be determined, but also the depth at which that exposure took place usually can be determined. Measurements for several cosmogenic nuclides are needed to determine this lunar exposure depth and the various ages for a lunar meteorite (e.g., Nishiizumi et al. 1999). The exposure depths for eight lunar meteorites are summarized in Warren (1994), with six of them having been exposed at depths in the Moon of less than about 600 g/cm^2 (less than ~ 3 meters). Warren (1994) noted that none of the 10 martian meteorites then studied had a record of a 2π exposure in their parent body.

9. REGOLITH EVOLUTION: MIXING, SPACE WEATHERING, AND MATURITY

9.1. Reworking and mixing

In addition to energetic particle interactions at the very top surface, major physical changes are induced by the interaction of micrometeorite impacts. Two major physical changes that occur with regolith maturation are (1) comminution, the disaggregation or breaking of rocks and minerals into smaller fragments, and (2) agglutination, the formation of agglutinates (Section 2.1). The two processes compete to decrease and increase, respectively, the mean grain size of soil particles at the very surface. Beginning with a fresh deposit of mare basalt or impact ejecta from a crater, maturation leads to a decrease in the mean grain size of the surface material with time because comminution by micrometeorite impacts dominates at first. As the soil matures *in situ* and more fine-grained material is produced, agglutination converts fine material to coarser-grained material. This process was termed *soil evolution path 1* ("reworking dominates mixing") by McKay et al. (1974). In principle, in an undisturbed area a steady state might be reached where the agglutination rate equals the comminution rate. However, the mean grain size of lunar regolith increases with distance below the surface, thus on average large impacts deposit material at the surface that has a coarser mean grain size than the material that was there before the impact. The mixing of rock fragments with soil, or soil with soil, was called *soil evolution path 2* ("mixing dominates reworking") by McKay et al. (1974). In effect, the grain size distribution of a lunar soil is controlled by three processes: comminution, agglutination, and mixing. On average, mature soils, that is, soils with a high percentage of agglutinates, a high density of energetic particle tracks, and high concentrations of solar-wind-implanted ions, are finer grained than immature soils (McKay et al. 1974; Morris et al. 1978b; Fig. 2.28).

Although maturation effects occur only at the very surface, the turnover of the regolith by small impacts, a process termed *in situ reworking*, mixes and buries mature soil, thus units of mature soil exist to depths of at least a few meters (Morris 1978a). Data for Apollo cores show that any of a number of parameters, such as maturity or chemical composition, vary unsystematically with depth at any given location. The cores do not represent continuous slow-deposition, as in a terrestrial ocean environment, but sporadic impact events intermixed with periods of quiescent soil development. Stratigraphic units in the cores (Figs. 2.15, 2.16) represent discontinuous pods, rather than layers with horizontal extent and time significance (e.g., Korotev and Morris 1993). On average, however, maturity decreases by a factor of two within the upper half meter (Fig. 2.29; see also Plate 2.2).

9.2. Space weathering products

9.2.1. Nanophase iron and agglutinates. An important observation made on the first Apollo samples to be studied was that the intensity of the ferromagnetic resonance (FMR) signal from the lunar soil samples was almost an order of magnitude greater than that from rock samples (e.g., Manatt et al. 1970; Tsay et al. 1971a,b). Tsay et al. (1971a,b) demonstrated that the FMR signal was due to small particles of metallic Fe. The FMR signal is dominated

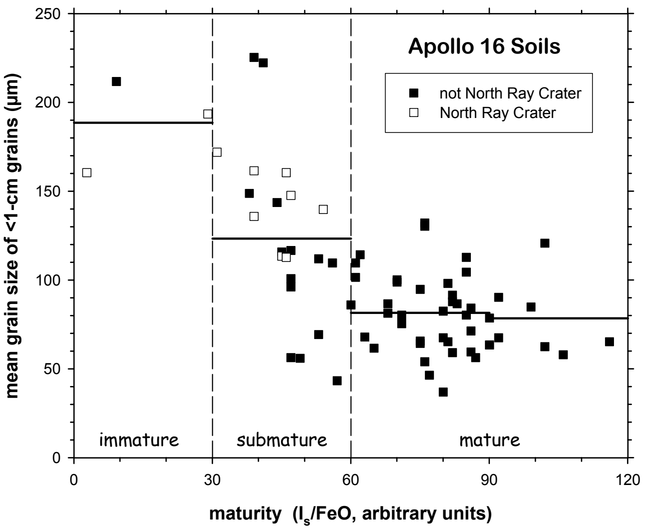

Figure 2.28. Variation in the mean grain size of the <1-cm grain-size fraction of Apollo 16 regolith samples (Graf 1993) with regolith maturity as measured by I_s/FeO (Morris 1978b). Open squares represent surface and trench soils developed on the ejecta deposit of North Ray crater, a fresh crater formed 50 Ma ago; closed squares represent all other surface and trench soils. The immature, submature, and mature divisions are those of Morris (1976, 1978b). The horizontal lines represent the mean concentration of all points within the range of I_s/FeO that they span. The plot demonstrates that mature soils tend to be finer grained than immature soils (McKay et al. 1974).

by single-domain grains of Fe^0 in the size range of 4 to 33 nm, grains that today are usually called nanophase Fe. Housley et al. (1974) and Cirlin et al. (1974, 1975) showed that for soil particles, the characteristic resonance is predominantly associated with agglutinates and regolith breccias. Agglutinates are the carriers of much of the nanophase iron in lunar soil and that most of the iron grains are in the 10–20 nm range. FMR Curie-point measurements show that these grains are essentially pure metallic Fe in composition (Morris et al. 1975). These tiny blebs of Fe^0 are found as a surface-correlated feature in the rims of grains, and also incorporated throughout agglutinates (Keller and McKay 1997).

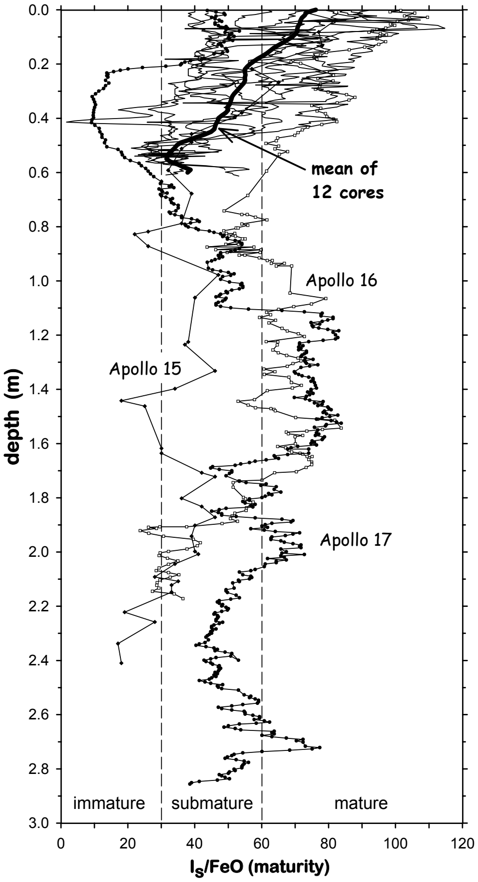

Figure 2.29. Variation in the regolith maturity parameter I_s/FeO with depth in 12 Apollo regolith cores. "Deep drill cores," which penetrated to 2–3 m, were collected on the last three Apollo missions. Other data derive from drive tubes of ~30 or ~60 cm length. It takes about 500 m.y. to garden to a depth of ~50 cm and ~100 m.y. integrated surface time to produce a mature regolith on the surface (Morris 1978a). All data are from R.V. Morris (Heiken et al. 1976; Morris and Gose 1976; Gose et al. 1977; Morris et al. 1979, 1989; Bogard et al. 1980, 1982; Korotev and Morris 1993; Korotev et al. 1997a; and unpublished data). See Plate 2.2 for color version.

Recent discoveries have been made of another major reservoir of nanophase iron in lunar soils (Keller and McKay 1993, 1997). This Fe^0 is present in thin patinas (~0.1 µm thick) on the surfaces of most soil particles (Wentworth et al. 1999). Several high-resolution TEM and EMP studies have described and documented the significant contributions from vapor-deposited, nanophase iron present in the patinas of most lunar soil grains (e.g., Keller and McKay 1997; Keller et al. 1999, 2000; Pieters et al. 2000; Taylor et al. 2000a,b, 2001a,b). Figure 2.30 shows BSE and X-ray images produced from both mature and immature mare soils, where even plagioclase grains contain thin rims with appreciable Fe contents, and silica-rich patinas are developed on ilmenite and olivine. These last two minerals also contain Fe-rich rims, as confirmed by high resolution transmission-electron-microscopic examination. Figure 2.30 also shows TEM photos from Keller et al. (2000) where the thin patinas on plagioclase and agglutinate grains show numerous nanophase iron particles. The spheres of Fe^0 found in agglutinates are roughly twice as large as those found in amorphous rims, averaging ~7 nm in diameter vs. ~3 nm for the rims (Fig. 2.30). The image shows layers of patinas on the agglutinate as well as the finer-grain size of the nanophase iron relative to that in the interior of the agglutinate. The major portion of this nanophase iron formed by deposition of vapor produced by abundant micrometeorite impacts, as documented by the presence of multiple and overlapping patinas. A smaller portion seems to have formed by radiation sputtering (Bernatowicz et al. 1994). The exact mechanism of formation of this surface-correlated Fe^0 is not well understood (Keller and McKay 1997), but

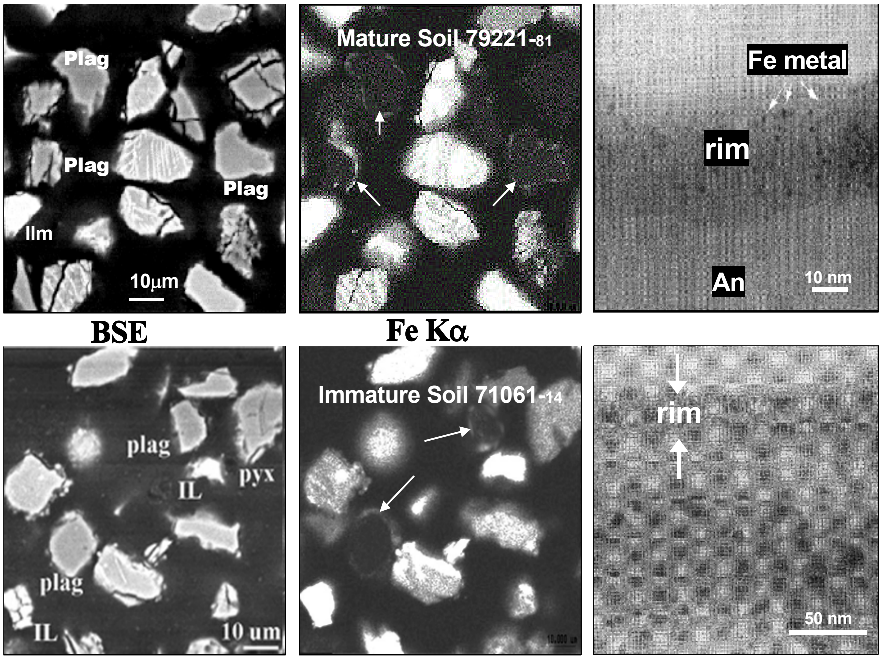

Figure 2.30. Plagioclase grains in lunar soil. Note the plagioclase grains ($CaAl_2Si_2O_8$) in the Back-Scattered Electron (BSE) image (left). In the Fe X-ray map (center), a thin Fe rim is present on these plagioclase grains, giving them a significant bulk magnetic susceptibility. Both mature (79221; top row) and immature (71061; bottom row) soils have vapor-deposited coatings on rims of most grains. The TEM images (right) show the fine-grained nature of the nanophase Fe^0 on the plagioclase (An) grains. Modified after Keller et al. (2000), Pieters et al. (2000), and Taylor et al. (2001a).

its presence was predicted by Hapke et al. (1975), but largely overlooked for over 20 years. Recent work (e.g., Basu et al. 2001) suggests that the nanophase iron in agglutinates was originally formed in vapor-deposited rims. The grain size of the metal in agglutinates is typically larger than in the rims, consistent with aggregation of the metal particles in the melt phase.

The relative importance of patinas vs. agglutinates as carriers of nanophase iron was addressed by Taylor et al. (2001b), who presented a comparison of the FMR values for each size fraction of nine mare soils versus agglutinitic glass abundances for these same soil splits, as shown in Figure 2.31. The numbers above each data point represent the percentage increase in the value with reference to the next coarsest size. For example for 79221, the FMR value for the <10 µm fraction is 117% greater than that for the 10-20 µm size, while the agglutinitic glass content has only increased by 15%. The large increases in the FMR values with decreasing grain size contrast with the small increases in the agglutinitic glass abundances for the same grain-size change.

Assuming spherical particles, for the same masses of two soil-size fractions, the surface area of the size fraction increases by a factor of 4, as the average grain size decreases by only 50%. If the increase in FMR signal that is attributable to the increase in agglutinitic glass is accounted for in each change in grain size, the "residual" is the surface-correlated FMR contribution. On average, there is about a 100% increase in FMR signal value between the finest two size fractions (Fig. 2.31). Therefore to a first approximation, the increase of 2× in FMR correlates well with the predicted 4 times increase in particle surface area. The contribution to the

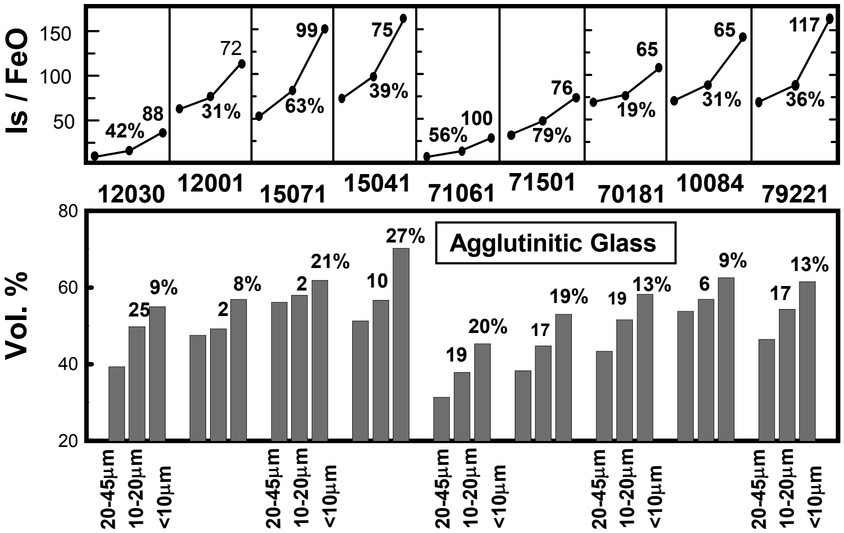

Figure 2.31. Comparisons of the I_s/FeO values for the finest fractions of mare soils with changes in agglutinitic-glass abundances between grain-size fractions. The numbers above each data point represent the stepwise percentage increase in the value on going from each coarser to finer grain size.

FMR from surface-correlated nanophase iron in the <10 µm fraction may be even greater than that made by the nanophase iron in the agglutinitic glass (Taylor et al. 2001b). This surface-correlated nanophase iron can account for the additional contribution to the FMR values of the finest fractions of lunar soils. Taylor et al. (2005) showed that this greatly increased nanophase Fe in the finest fractions yields an increase in magnetic susceptibility that virtually all grains <20 µm can be picked up by a simple hand-held magnet. This magnetic property has direct applications to dust mitigation during future lunar missions.

9.2.2. Nanophase iron and the maturity index I_s/FeO. Cirlin et al. (1974), Housley et al. (1975), and Pearce et al. (1974) suggested that the FMR signal intensity, I_s, normalized to the total concentration of iron expressed as percent FeO, is a measure of the relative surface exposure ages of lunar soils. The normalization to FeO concentration was proposed because more Fe^{2+} is available for reduction in a high-FeO soil than a low-FeO soil. The parameter I_s/FeO, usually taken to be dimensionless, conveniently ranges from essentially zero in rocks and soils with no surface exposure to about 100 in highly mature lunar regolith. I_s/FeO correlates reasonably well with other maturity indices such as the modal abundance of agglutinates in the 90–150 grain-size fraction and the concentration of solar-wind-implanted gasses (Pillinger et al. 1974; Morris 1976; Morris et al. 1989). I_s/FeO has become the standard measure of regolith maturity because it is much easier and quicker to measure than other indices of maturity, and data for nearly all Apollo soil samples have been generated (Cirlin et al. 1975; Housley et al. 1976; Heiken et al. 1976; Morris 1976, 1977, 1978a,b, 1979, 1980, 1989; Morris and Gose 1976, 1977; Gose and Morris 1977; McKay et al. 1977, 1978a,b, 1979, 1980; Morris et al. 1979; Morris and Lauer 1979, 1980; Korotev et al. 1984, 1997a; Korotev and Morris 1993; Taylor et al. 2001a,b). From definitions originally established on the basis of agglutinate abundance (McKay et al. 1974), the categories *immature*, *submature*, and *mature* now correspond to I_s/FeO ranges of <30, 30–60, and >60 (e.g., Fig. 2.28).

Although I_s/FeO is a convenient and common measure of soil maturity, there are several factors that should be considered with respect to this measure.

Sampling. Most I_s/FeO data have been obtained on very small subsamples of material with a nominal grain size of <0.25 mm or, in some cases, 90–150 µm (Morris 1976, 1978b). More precisely, the ferromagnetic resonance intensity, I_s, was obtained from ~2 mg of material from the <1-mm fines that fit into a tube with a nominal inside diameter of 0.5 mm, whereas in most cases the FeO concentration was obtained from literature data for <1-mm fines. In other words, the numerator and denominator were obtained from different subsamples of different mean grain size. For submature and mature soils, 84 ± 8% of the mass of the <1-mm grain-size fraction also passes through a 0.25-mm sieve (Graf 1993), so this difference is a likely source of error only for samples for which there is a strong variation in composition with grain size (Section 9.7).

Analysis. For most samples, published data for I_s/FeO are based on a single FMR determination. For some core samples, the denominator, the total FeO concentration, is obtained by imprecise magnetic methods, not by chemical analysis. Even when the FeO concentration is determined by chemical analysis, the value determined may not necessarily be representative of the soil. For this reason, published I_s/FeO data for some samples may be in error by as many as 10 units.

Grain Size. Some maturation effects are not strongly related to grain size. For example, neutron capture and galactic-cosmic-ray effects are volume correlated, not surface correlated. Many maturation effects, however, occur only at a surface of a soil grain, e.g., condensation of volatiles or implantation of solar wind ions. As a consequence, some space-weathering effects are a strong function of grain size (e.g., Fig 2.28) and others are not. Even among those effects that are surface correlated, the depth of each effect within a given grain differs. The process of agglutinate formation, which converts finer-grained material to coarser-grained material, may release or erase some effects (solar-wind-derived gases, energetic particle tracks) and concentrate others into coarser particles (nanophase iron). Thus, there is no particular reason to expect that the pattern of variation of any given maturity parameter with grain size will match that of another.

Resetting. There is one known case where a layer of soil in a core is submature on the basis of agglutinate abundance and siderophile-element concentrations yet I_s/FeO is very low (i.e., <<30; Korotev et al. 1997a). The FMR signal was apparently reset by a heating event that agglomerated nanophase iron particles into larger, multi-domain particles that gave no single-domain range FMR signal.

Vector paths. A path-1 soil (*in situ* reworking) will have a different exposure history than a path-2 soil (mixing), yet the two soils can have identical values of I_s/FeO or any other maturity parameter. In particular, a path-2 soil that is a mixture of regoliths with differing I_s/FeO values and different FeO concentrations can have misleading and non-intuitive value of I_s/FeO, one that does not reflect its history if it is interpreted as a path-1 soil (Fig. 2.32).

Despite the various problems discussed here, maturity parameters such as nitrogen abundance and agglutinate abundance correlate reasonably well with I_s/FeO among soil samples of varying maturity (e.g., Morris et al. 1989; Fig. 2 in Lucey et al. 2000). Imperfect intercorrelations among maturity parameters ultimately reflects that every grain in the regolith has a different exposure history, no two maturation parameters record that history in exactly the same way, and the concept of "the maturity" of a soil or surface is an average characteristic.

9.3. Compositional variation with maturity in path-1 soils

Two types of changes in bulk composition occur in regolith that matures *in situ*, that is, regolith that follows soil evolution path 1 of McKay et al. (1974). First, concentrations of those solar-wind elements that are all but nonexistent in lunar igneous rocks (H, He, C, N, and other light elements), as well as isotopes produced by cosmic-ray interactions, increase dramatically (McKay et al. 1991). Second, impacts of micrometeorites cause concentrations of siderophile elements (Ni, Ir, Au) and some volatile elements (Zn, Ga) to increase because these

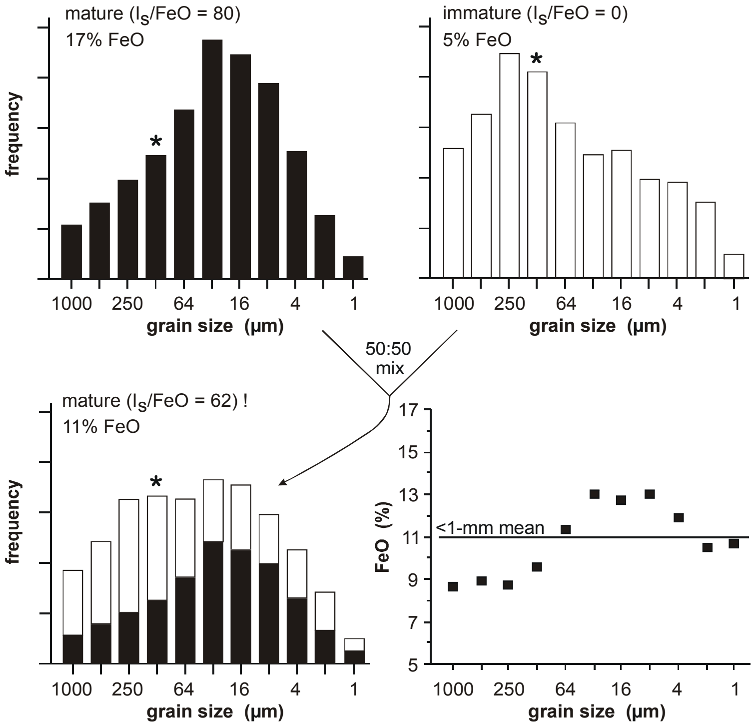

Figure 2.32. Schematic diagram showing how mixing of two compositionally distinct regoliths with different grain-size distributions leads to variation in composition with grain size (after Fig. 6 of McKay et al. 1974) as well as a non-intuitive final value of I_s/FeO. Although exaggerated, the example corresponds to mixing mature, fine-grained mare regolith with a totally immature, coarse-grained highlands regolith. Note that although half the material in the mixture has never had any surface exposure, the mixed soil would still be classified as mature on the basis of the I_s/FeO scale of Morris (1976, 1978b) (I_s/FeO = [17(80)0.5 + 5(0)0.5]/11 = 62 > 60). Conversely, mixing a highly mature feldspathic soil with freshly disaggregated mare basalt will yield an immature I_s/FeO even though other measures of maturity may still be high. That other maturity indices (e.g., nitrogen and agglutinate abundances) correlate well with I_s/FeO (e.g., Fig. 2 of Morris et al. 1989) for many soils indicates that these extreme examples are rare. The asterisk represents the grain-size range for which most modal petrography data are available.

elements are more highly concentrated in meteorites than in lunar igneous rocks (Wasson et al. 1975; Haskin and Warren 1991; Korotev and Morris 1993). In highly feldspathic soils, maturation can lead to nontrivial increases in concentrations of some lithophile elements by the same mechanism because chondritic meteorites have high concentrations of certain elements compared to feldspathic lunar rocks. For example, lunar meteorite QUE 93069 is a feldspathic regolith breccia (4.4% FeO) formed from a mature regolith (Thalmann et al. 1996). Siderophile-element concentrations (Spettel et al. 1995; Korotev et al. 1996; Lindstrom et al. 1996) are high and equivalent to 2.9% CI chondrite. Thus, about 14% of the Fe and 10% of the Mg and Cr in the regolith breccia derives from meteorites. Much of the meteoritic material was delivered as micrometeoroids associated with the soil maturation process. This component probably exists in agglutinates or as vapor-deposited coatings on soil grains. The rest is carried in glassy and crystalline breccias of which the regolith is in part composed. The latter were formed during crater-forming impacts that were not related to the maturation process. Some to most of the meteoritic Fe occurs as metal (Sections 4.4 and 6.2.1).

9.4. Compositional variation with maturity in path-2 soils

Impacts that form craters with diameters in the decameter to kilometer size range will mix less mature regolith with more mature surface regolith. Soils formed in this manner, that is, regolith that follows soil evolution path 2 of McKay et al. (1974), will typically have intermediate or low values for soil maturity parameters such as I_s/FeO. Freshly exhumed rock debris or buried regoliths with little surface exposure are not likely to have the same composition as mature surface soils because they have not been as thoroughly mixed with other local materials. Thus, at the Apollo sites, soils of low maturity (e.g., samples 12032, 15531, 61221, 67511) are commonly compositionally distinct from mature soils collected nearby, and all mature soils at some sites (Apollo 12 and 16) tend to be compositionally similar to each other.

Mixing by impacts can lead to correlations between a regolith maturity parameter such as I_s/FeO and some other property such as bulk composition. These correlations, which result from mixing (soil evolution path 2), can be erroneously attributed to effects of the *in situ* maturation process (path 1). For example, Apollo 16 soils are mixtures dominated by feldspathic lithologies but also contain mafic, KREEP-rich impact-melt breccias (Fig. 2.11). Prior to the Imbrium impact, the site was likely entirely dominated by KREEP-poor, feldspathic lithologies. The Imbrium impact emplaced an ejecta deposit at the site that was a mixture of KREEP-rich breccias from the Imbrium area and KREEP-poor anorthositic rocks of local origin. Immature soils of Apollo 16 consistently contain a higher proportion of feldspathic material having little surface exposure than do the mature soils. As a result, Apollo 16 soil compositions vary systematically with maturity (Fig. 2.33). The variation is not caused by the maturation process because there is no mechanism by which the soils can become richer in Fe and Th by up to a factor of 2 simply as a result of *in situ* maturation. As there are no outcrops of feldspathic rocks at the site, the feldspathic material must derive from beneath the surface. Impacts that are sufficiently large to penetrate the regolith, such as that which formed North Ray crater, encounter rocks at depth that are more feldspathic (lower FeO, Fig. 2.33a) than the typical mature surface soil (Stöffler et al. 1985; Korotev 1991, 1997). None of the soils collected near North Ray crater are mature because the time elapsed since the crater was formed (50 m.y.) is not long enough for the crater ejecta to have become mature (Morris 1978a). Soils collected at station 13, about one crater-diameter from the crater (Fig. 2.33b), are intermediate in both composition and maturity (submature, as measured by I_s/FeO) to soils collected on the rim of the crater and to the soils collected more distant because they are mixtures of the two types of material. However, submature soils with Th concentrations greater than that of the main trend of Figure 2.33b (all from station 5 and from 18–21 cm depth in the 60009/10 core) cannot be simple mixtures of the two end-member regolith types; they may instead be products of *in situ* maturation.

9.5. Compositional variation with grain size

Many early studies of lunar soil showed that the composition of the regolith changed with grain size. Because optical and infrared remote sensing is sensitive to particle size, such changes are important for interpreting data from these techniques. One consistent finding is that the finest grain-size fractions of soils developed on the maria are consistently richer in elements associated with plagioclase (Al, Na) and late-crystallizing minerals (incompatible elements) and depleted in elements associated with ferromagnesian minerals (Fe, Mg, Ti, Sc, V, Cr, etc.) compared to coarser grain-size fractions and the bulk (<1-mm) soil (Evensen et al. 1974; Korotev 1976; Laul et al. 1978, 1979, 1980, 1988; Papike et al. 1981, 1982; Taylor et al. 2001a,b). The effect is not often apparent among grain-size fractions of >45-µm material but becomes pronounced with decreasing grain size for <45 µm grain-size fractions (e.g., Laul et al. 1988; Taylor et al. 2001a,b). For example, in soil from the Apollo 17 deep drill core, which is composed of about 50 ± 20% high-Ti mare basalt, Fe and Ti are 7–8% lower, and Al is 12% higher in the <20 µm grain-size fractions compared to the <1-mm fractions; incompatible elements Sm and Th are enriched by 6% and 36% in the <20 µm fractions (Table 2.7). There

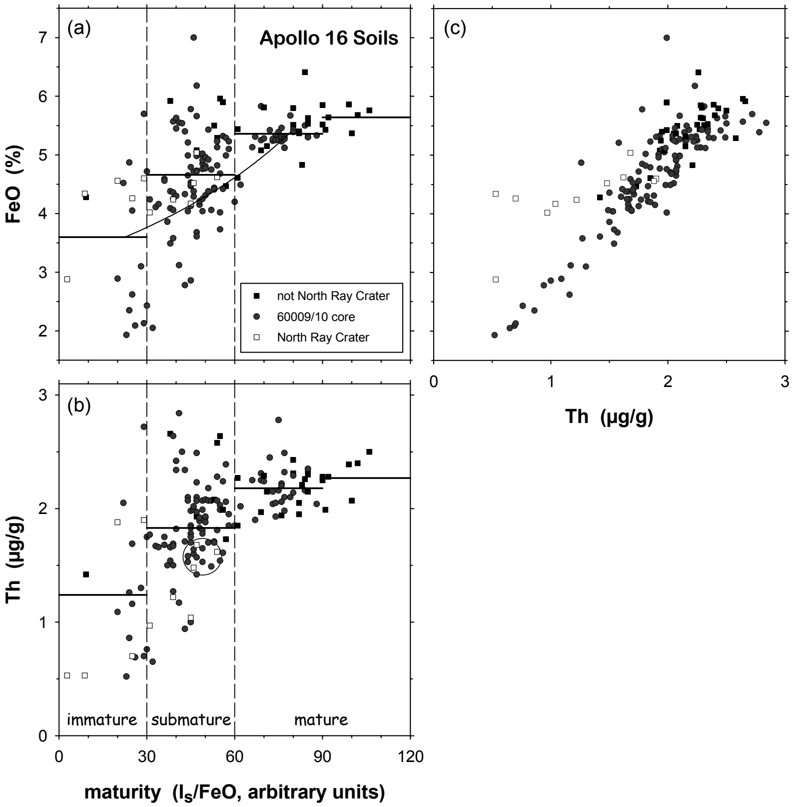

Figure 2.33. (a,b) Concentrations of FeO and Th as a function of the maturity parameter I_s/FeO in Apollo 16 soils. Open squares represent surface and trench soils from station 11 on the rim of North Ray crater and station 13 about a kilometer from the crater, closed squares represent all other surface and trench soils, and circles represent samples from the 60009/10 double drive tube. The immature, submature, and mature divisions are those of Morris (1976, 1978b). The horizontal lines represent the mean concentration of all points within the range of I_s/FeO that they span. (c) The correlations between composition and maturity of (a) and (b) are not caused by maturation of regolith, they are mainly the result of mixing mature surface regolith that is rich in FeO and Th with immature subsurface material that is poorer in FeO and Th. For example, many submature soils, such as those from station 13 [represented by the three North Ray Crater points inside the circle in (b)], are mixtures of mature surface soil and immature North Ray crater ejecta. The curved line in (a) is the mixing line between mean immature and mean mature soil. In (a), most points with I_s/FeO >30 and which have anomalously high FeO also have anomalously high concentrations of Ni and other siderophile elements because they contain nuggets of Fe-Ni metal (Korotev 1987a, 1997). FeO and Th data are from Korotev (1991, 1996, 1997); I_s/FeO data are from Morris (1978b) and Morris and Gose (1976).

is some evidence that the degree of enrichment or depletion may be somewhat greater for immature soils, but the effect is still strong in mature soils.

What causes such variations? Four processes have been proposed for why the composition of the lunar regolith varies with grain size (Korotev 1976).

(1) Surface processes. As the grain-size decreases, the concentrations of highly volatile elements such as Cd, Zn, In, and Ga increase. Some of the surface-correlated volatiles derive from volcanic-gas condensates, whereas others derive mainly from vaporization of micrometeorites (Boynton et al. 1976). Similarly, concentrations of solar-wind implanted gases

Table 2.7. Mean concentration of some elements in two grain-size fractions of 16 samples from the Apollo 17 deep drill core.

	unit	<1000 µm mean	<20 µm mean	<20/<1000	
				mean	±
TiO_2	%	6.32	5.79	0.92	0.03
Al_2O_3	%	13.41	14.97	1.118	0.015
FeO	%	16.27	15.14	0.931	0.017
Sm	µg/g	7.78	8.24	1.06	0.06
Th	µg/g	1.40	1.83	1.36	0.11

The uncertainties (±) on the mean ratios are 95% confidence limits. Data are from Laul et al. (1978, 1979) and Laul and Papike (1980).

(Eberhardt et al. 1970; Bernatowicz et al. 1979) and nanophase iron (I_s/FeO) increase with decreasing grain-size (Taylor et al. 2001a,b; Fig. 2.34) because of the increase in surface-to-volume ratio. Among mainly-lithophile elements, surface processes are probably not the cause of any detectable compositional variations with grain size, except perhaps in part for Na.

(2) Mixing processes. As noted in the previous section, some soils are mixtures of fine-grained, mature soil of one composition with coarse-grained, immature material of another. The mixing of compositionally distinct materials with different grain-size distributions is one important cause of variation in regolith composition with grain size (e.g., Fig. 2.32). One extreme example is the orange and black volcanic glass spherules of the Apollo 17 site. All samples of soil collected at the Apollo 17 site contain volcanic glass spherules. The mean grain size of the spherules (~44 m for 74220 “orange soil”) is less than that of nearly any mature soil (Fig. 2.28) and the spherules have higher concentrations of Fe and Cr than any other component of the soil. Thus, among the various submillimeter grain-size fractions of Apollo 17 soils analyzed by Laul and coworkers, the 20–90-µm fractions consistently had the greatest concentrations of Fe and Cr (Laul and Papike 1980; Laul et al. 1978, 1979, 1981) because they contained the greatest relative abundances of volcanic spherules. This effect is particularly evident in the nominally nonmare soils, those of the South and North Massifs.

As noted above, in mare soils, the finer grain-size fractions tend to be richer in Al and incompatible elements than the coarser fractions or the bulk soil. Given that all nominally mare soils from the Apollo sites contain considerable nonmare material, which consists of high-Al feldspathic lithologies or high-Th impact-melt breccias (Fig. 2.11), a reasonable explanation for the data is that the proportion of nonmare material increases with decreasing grain size (Korotev 1976; Laul et al. 1979; Pieters and Taylor 2003). This explanation is particularly appealing at the Apollo 15 and 17 sites, which are on the boundary between maria and Al- and Th-rich highlands and where Th-rich lithologic components are local, not exotic (Papike et al. 1981).

(3) Mineral property processes. An hypothesis that also accounts for the observations about mare soils is that a greater proportion of plagioclase and mesostasis from disaggregated mare basalt is concentrated in the finer grain-size fraction (Korotev 1976; Papike et al. 1982; Laul et al. 1987). Mesostasis is the last material to crystallize and commonly occurs between grains of the major mineral phases in igneous rocks. It consists of accessory minerals and glass with high concentrations of incompatible elements. In laboratory studies, during the disaggregation of basaltic rocks by impacts, there is preferential enrichment of plagioclase in the finest grain-size fractions and mesostasis phases (Haskin and Korotev 1977; Hörz et al. 1984; Cintala and Hörz 1992). For mesostasis phases, the enrichment occurs because the

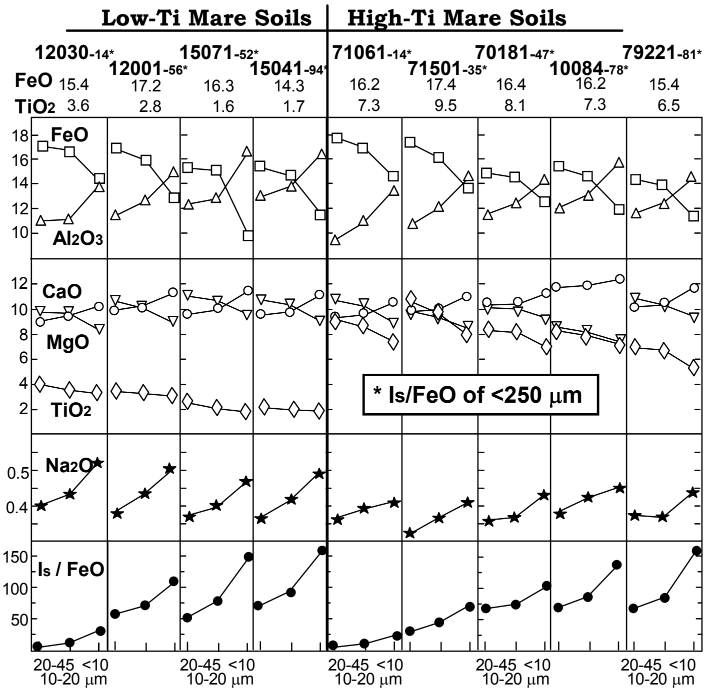

Figure 2.34. Chemistry of the finest size fractions of lunar mare soils, from Taylor et al. (2001b). The soils are divided into high- and low-Ti soils for this figure and further arranged in left to right order from least to most mature. The small number after the sample number (e.g., 12030-14) is the I_s/FeO value of the <250 μm fraction (Morris 1978). The data for a given soil are presented from left to right for decreasing grain size of the soil fractions. With decreasing grain size, there is a systematic increase in plagioclase components (CaO, $A1_20_3$, Na_2O) and decrease in ferromagnesian-mineral components (FeO, MgO, TiO_2). Also, there is a increase in I_s/FeO with decreasing grain size.

intrinsic grain size of the minerals is small. For plagioclase, the enrichment occurs because the mineral shatters to a finer grain size with shock than does pyroxene (Hörz et al. 1984).

X-ray imaging of soils has been used to better understand relationships between mineralogy of soil grain-size fractions and chemical composition, and on variations as a function of grain size. As part of the characterization of lunar soils for remote-sensing purposes, detailed chemical and modal analyses were made of the fine-size fractions of a set of soils of contrasting chemistry and maturity (9 mare and 10 nonmare) (Taylor et al. 2001b). The modal percentages of mineral and glass components for all the 45-20 μm, 20-10 μm, and <10 μm size fractions of the nine mare soils are shown graphically in Figure 2.35**.** The bulk soil maturities, expressed as I_s/FeO values for the <250 μm portion of each soil (Morris 1978), are given for comparison, in addition to bulk-soil FeO and TiO_2 contents.

Examining the properties of the size fractions for individual soils reveals systematic changes. Impact-produced agglutinitic-glass content increases with decreasing grain size. The modal abundances of crystalline plagioclase are relatively constant to slightly increasing, with decreasing grain size of the fractions. However, the abundances of all other components (pyroxene, oxides, volcanic glass, and olivine) decrease with particle size. This decrease for pyroxene is pronounced and very significant since pyroxene is probably the most optically active of the lunar minerals.

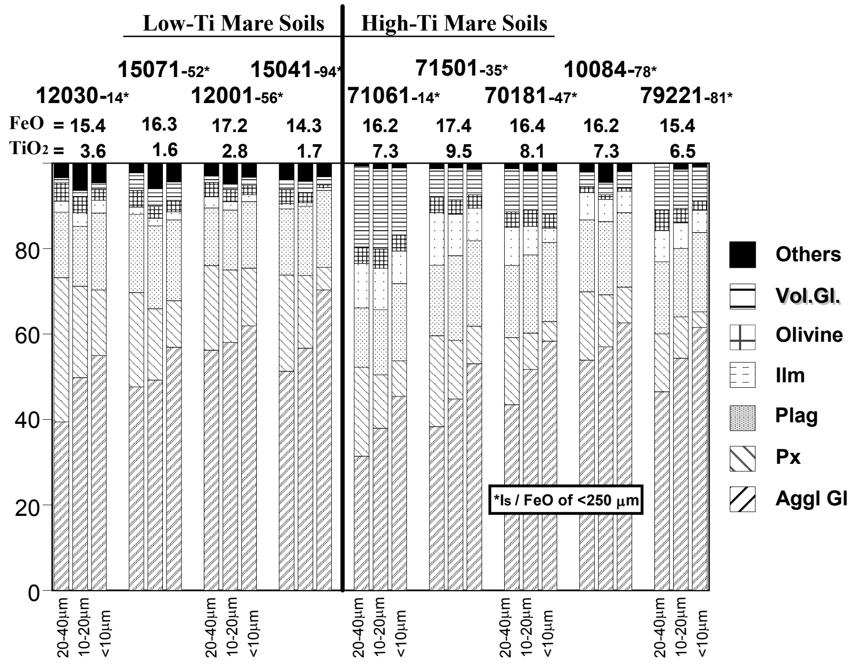

Figure 2.35. Modal analyses of the finest size fractions of Mare Soils, from Taylor et al. (2001b). The soils are divided into high- and low-Ti soils for this presentation and further arranged left to right within these two groups from least to most mature. The small number after the sample number (e.g., 12030-14) is the I_s/FeO value of the <250 µm fraction (Morris 1978), commonly referenced as the maturity value for the soil in general. The FeO and TiO_2 contents of the soils are shown for comparison. These soils were selected to have similar compositions, as well as contrasting maturities. Note the general increase in agglutinitic-glass and decrease in pyroxene contents as maturity increases *between* soils, as well as the same trends *within* a given soil with decrease in grain size.

Data for lunar soils are dependent upon the nature of the location. For example, the modal data of Taylor et al. (2003) for mare soils show that although the plagioclase abundance remains nearly constant with decreasing grain size, the pyroxene abundance decreases significantly (Fig. 2.35), with a net result that the plagioclase concentration in the finest fractions increases. From the detailed analyses for a suite of soils from Apollo 14 and 16, Taylor et al. (2003a,b) reported that the feldspathic component also increases significantly with decreasing particle size, consistent with the expected differential comminution of plagioclase during soil formation (e.g., Hörz et al. 1984). However, the mean composition of the agglutinitic glass from these highland soils is clearly not associated with the composition of the finest fraction. It would appear that the F^3 Model (Papike et al. 1981) does not apply to the highland samples. Instead, the data are interpreted to indicate that lateral mare-highland mixing and selective melting of soil phases are both significant parts of the lunar soil formation and evolution (Pieters and Taylor 2003).

Qualitatively the two processes, mixing and preferential comminution, lead to the same effect in mare soils—increasing plagioclase and incompatible element-rich phases and decreasing pyroxene with decreasing grain size. On the basis of a compositional mass-balance modeling, Korotev (1976) concluded that both processes were important in Apollo 17 soils. The effect is also strong, however, in the Luna 24 regolith (Laul et al. 1988), which contains only minimal nonmare material and which is not likely to contain any appreciable component of KREEP-rich impact-melt breccia or other form of KREEP on the basis of data from Lunar Prospector. Similarly, Al is enriched in the finest grain-size fractions of Apollo 12 soils (Papike et al. 1982; Taylor 2001b) and feldspathic lithologies are rare at the Apollo 12 site. Thus in general, enrichment of the finest grain-size fractions with basalt-derived mesostasis and plagioclase is probably the main cause of variation in composition with grain size in mare soils. A similar effect (Al, Ca, and incompatible-element enrichment, Fe and Mg depletion in the finest grain-size fraction; Laul and Papike 1980) is even seen in the Apollo 14 soil, which is dominated by KREEP-rich impact-melt breccias. At the Apollo 16 site, mixing effects may be more important than mineral effects.

(4) Agglutinate fractionation processes. In the 1970's, several papers addressed the issue of whether agglutinates or the glass in agglutinates differ in composition from the soils in which they were formed. If, for example, some fractionation occurs during the melting associated with a micrometeorite impact such that an agglutinate particle is systematically enriched in Fe, for example, compared to the bulk soil, then formation of an agglutinate would cause the concentration of Fe to decrease imperceptibly in finer grain-size fractions and increase in a coarser fraction. If such a process were important and the other three processes discussed here were not, then we would expect differences in Fe concentrations between fine and coarse grain-size fractions to increase as a soil matures.

In the first of the 1970's papers, Adams et al. (1975) and Rhodes et al. (1975) made magnetic separates of soils and identified these as "agglutinate fractions." The implicit assumption was that most of the metal in the soil was or had been nanophase Fe associated with agglutinate formation. They observed that the "agglutinate fractions" were consistently richer in incompatible elements and elements associated with mafic minerals and depleted in elements associated with plagioclase compared to the bulk soil. The effect was particularly strong among the Apollo 16 soils. Adams et al. (1975) and Rhodes et al. (1975) interpreted the result in terms of chemical fractionation associated with the formation of agglutinates by micrometeorite impacts. Various later works showed that the composition of glass in agglutinates, although variable in composition, does not differ significantly, on average, from the composition of the soil in which the agglutinates are formed (Marvin et al. 1971; Gibbons et al. 1976; Via and Taylor 1976; Hu and Taylor 1977). The explanation is that much of the Fe metal in lunar soils, particularly soils from Apollo 16, is not associated with maturation but instead derives from the ancient KREEP-bearing impact-melt breccias which constitute part of the soil. The magnetic separates may have been richer in agglutinates than the nonmagnetic separates, but they were also richer in the melt-breccia component (high Fe, high Th) and poorer in metal-poor anorthosite than the bulk soils.

Although the initial work on "agglutinate fractions" was a "red herring," it led to subsequent work on understanding agglutinate formation. For example, there is evidence that the glass in agglutinates more closely reflects the composition of the <10 μm grain-size fraction than the <1-mm fraction (Walker and Papike 1981; Taylor et al. 2001a,b). One explanation is that the finest material preferentially melts during micrometeorite impacts (Papike et al. 1981). However, an agglutinate particle can only be composed of material that was smaller than itself prior to the impact that formed it, so a 100-μm agglutinate will necessarily have a composition more similar to the <100-μm material in the regolith than to the >100-μm material. Large agglutinates in the 1–2 mm and 2–4 mm grain-size fractions of lunar soils have compositions, on average, indistinguishable from the soils (<1-mm) in which they form (Blanchard et al. 1975; Jolliff et al. 1991a, 1996). Little work has been done on the bulk composition of submillimeter agglutinates, where we might expect the largest differences between the compositions of agglutinate and the <1-mm soil. One such work, that of Taylor et al. (1978) on ~100-μm agglutinates, does, in fact, demonstrate that the average composition of agglutinates can differ from that of the soil (<1-mm) in which they are *found*. This work concludes that agglutinates move and that they do record the composition of the soil in which they are *formed*. However, it is likely that the six sets of average agglutinate compositions reported by G. J. Taylor et al. (1978) do, in fact, match the <100-μm grain-size fractions of the soils in which they were found much better than they do the <1-mm fraction. The high Fe and Ti concentrations of agglutinates from the South Massif compared to <1-mm soils almost certainly reflects that the agglutinates were formed from fine-grained material in which the mass proportion of pyroclastic ash ("orange glass") was much greater than in the <1-mm soil used for comparison.

The pattern and magnitude of compositional differences among grain-size fractions is not a strong function of soil maturity. The lack of dependence on maturity is particularly evident in results for Apollo 17 soils for which I_s/FeO varies considerably (Korotev 1976; Taylor et al. 2001a; Fig. 2.34). This observation suggests that the formation of agglutinates is probably not a significant cause of differences in composition with grain-size in lunar soils and, in fact, probably acts to diminish the magnitude of differences caused by other processes.

The bulk chemistry of the nine mare soils studied by Taylor et al. (2001b), representing both high-Ti and low-Ti compositions, have systematic differences relative to each other, as well as among the different grain-size fractions of a given soil (Fig. 2.34). These differences permit comparisons of their chemistries, both as individuals and collectively, as a function of different maturities. With decreasing grain size, FeO, MgO, and TiO_2 concentrations decrease, and CaO, Na_2O, and Al_2O_3 (plagioclase components) increase for all soils. By comparison with the modal values in Figure 2.35, these chemical variations parallel increases in agglutinitic glass and decreases in the oxide minerals (mainly ilmenite), pyroxene, olivine, and volcanic glass. There is also a large increase (i.e., >100%) in the agglutinitic glass contents between the 90-150 μm and the 10-20 μm size fractions (Taylor et al. 1996, 1999). The I_s/FeO values for each soil increase significantly as the grain size decreases, which is another effect of space weathering (see below).

The glass that forms the binder in an agglutinate particle is a product of several complex processes. Primarily the glass is a melt from the very small volume of soil that was directly impacted by a micrometeoroid. As mentioned above, small compositional changes must have occurred during melting, such as the escape (at least in part) of volatile elements, or the extraction of metallic Fe^0 from silicate melt, leaving the melt slightly depleted in Fe. Additional effects could have been produced by the character of the mineral grains involved. Close examination of the composition of individual agglutinates suggests that the composition of the agglutinate glass is determined by the initial shock-induced melting and is not modified by incorporation (assimilation) of unmelted grains into the glass. Seemingly pure glass is actually riddled with many submicrometer-sized vesicles and clasts. Analyses by Basu and McKay (1985) of the "pure" glass, both adjacent to and away from such clasts, both large and small, show no differences in chemical composition between different areas. This observation suggests that assimilation of the clasts by the primary impact melt has not been a major process modifying the final composition of the glass in different areas.

As determined by Taylor et al. (2001a,b), chemical compositions of individual mineral and glass phases within a soil are relatively constant for <45 μm sizes and independent of grain size. The agglutinitic glass compositions remain relatively constant with changes in grain size and soil maturity. In fact, changes in the chemical compositions of the soil size fractions are caused mainly by the abundances of the phases (e.g., pyroxene, agglutinitic glass), not by distinct changes in the chemistry of the individual minerals and/or glasses. It was originally suggested by Hu and Taylor (1977) that the composition of agglutinitic glass in a soil mimics, to large extent, the chemistry of the bulk soil. However, the compositions of the agglutinitic glasses presented here, at least for the grain sizes <45 μm, are more feldspathic than the overall bulk chemistry of the soil. Thus the composition of the agglutinitic glass is a fair representation of the bulk chemistry plus a feldspathic component.

Figure 2.36 compares the bulk chemistry of each size fraction and the composition of the corresponding agglutinitic glass for the high-Ti mare soils. The systematic changes in

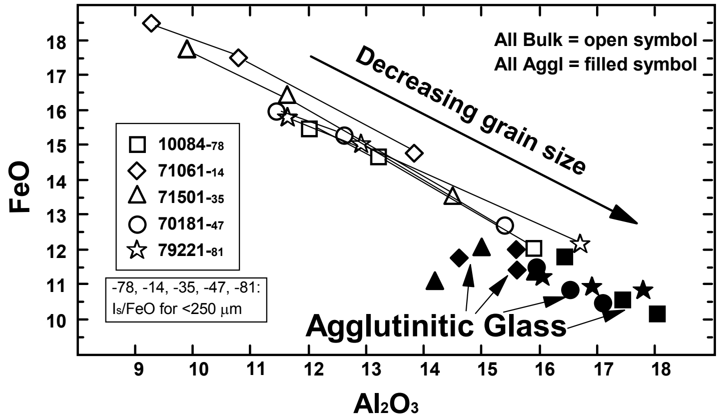

Figure 2.36. Comparisons of changes in the bulk chemistry of the three finest size fractions for the high-Ti soils versus the compositions of their agglutinitic glasses. The small number after the sample number (e.g., 10084-78) is the I_s/FeO value of the <250 μm fraction (Morris 1978). Note that the bulk compositions of decreasing-size fractions within a given soil converge on the composition of the agglutinitic glass by decreasing FeO and increasing $A1_2O_3$ contents.

soil composition with decreasing grain size show that the bulk chemistry of each size fraction becomes more feldspathic with increasing maturity, with the effect being most pronounced in the finest fractions (Fig. 2.34. The composition of the agglutinitic glass is relatively invariant and even more feldspathic (i.e., rich in $A1_2O_3$) than even the <10 μm fraction, largely a function of the "Fusion of the Finest Fraction" (F^3) model (Papike et al. 1981). However, the selective impact-produced vaporization of FeO may also play a role. Thus, it would appear that the differences in bulk compositions of the mare soil fractions, with decreasing grain size, approach the composition of the agglutinitic glasses (Taylor et al. 2001a,b).

10. REMOTE SENSING OF LUNAR SURFACE COMPOSITION

Remote sensing is the determination of the physical or compositional state of a surface without physical contact. While the parameters derived remotely are extremely limited compared to analyses that can be conducted in the laboratory, remote sensing offers a synoptic view inaccessible in any other way. Compositional remote sensing of the Moon is broadly divided in two on the basis of physical technique and spatial resolution: mineralogical remote sensing utilizes spectral analysis of reflected (and potentially, emitted) light from the lunar surface to determine mineralogical parameters with existing data at the 10's to 100's of meters scale, and elemental remote sensing exploits energy dependent variations in neutron, X-ray or gamma-ray flux to determine elemental compositions 10's to 100's of kilometers scale. The signal available to mineralogical remote sensing is very strong and enables high spatial resolution to be obtained, even from Earth. Ground-based astronomy established the requirements for spectral observations of the Moon, and the Clementine mission obtained multispectral imaging data for nearly the entire lunar surface at wavelengths sensitive to lunar mineralogy. The elemental signals are far weaker and require that spatially resolved measurements be obtained from lunar orbit. Apollo carried the first elemental sensors to the Moon that provided data for important elements over a significant portion of the lunar surface and set a baseline for future missions. Lunar Prospector collected gamma-ray and neutron flux data for the entire Moon and returned data for many important elements.

Many missions are planned for remote sensing of the Moon in the first decade of the 21st century, with the ESA SMART-1 mission underway at this writing, and the Japanese SELENE mission in an advanced state of development, the Indian mission Chandrayan and the US Lunar Reconnaissance Orbiter in development. Undoubtedly these missions will yield a new bounty of information on the Moon, but these missions rest on the lessons of Clementine and Lunar Prospector, and the brief pause the lunar science community has enjoyed to contemplate the new results.

In this section we review the major remote-sensing measurements made by the two missions Clementine and Lunar Prospector, but do not neglect the important contributions of ground-based spectroscopy, Apollo geochemical measurements, and the potential of radar and thermal infrared spectroscopy for understanding the composition of the Moon in the future.

10.1. Gamma-ray spectroscopy

The concentrations of many elements can be determined for spatially resolved portions of the lunar surface by measuring the characteristic gamma-ray line emissions of specific elements produced by either nuclear spallation reactions or radioactive decay reactions. Figure 2.37 shows a spectrum of gamma-rays coming from the lunar surface as measured by the Lunar Prospector gamma-ray spectrometer. The nuclear spallation reactions are initiated by high-energy galactic cosmic rays that continually hit the lunar surface. There are two dominant nuclear spallation reactions: neutron inelastic scatter and thermal neutron capture. Inelastic scatter reactions occur when high energy neutrons initially produced by spallation reactions lose energy to a target nucleus, leaving the nucleus in an excited state. The nucleus can then de-excite by producing a gamma-ray having an energy characteristic of that particular element. Thermal neutron capture occurs when low-energy neutrons (again the product of galactic-cosmic-ray spallation reactions) are absorbed by a target nucleus, which again leaves the nucleus in an excited state. As with the inelastic scatter reaction, the nucleus can de-excite by producing one or more gamma rays,

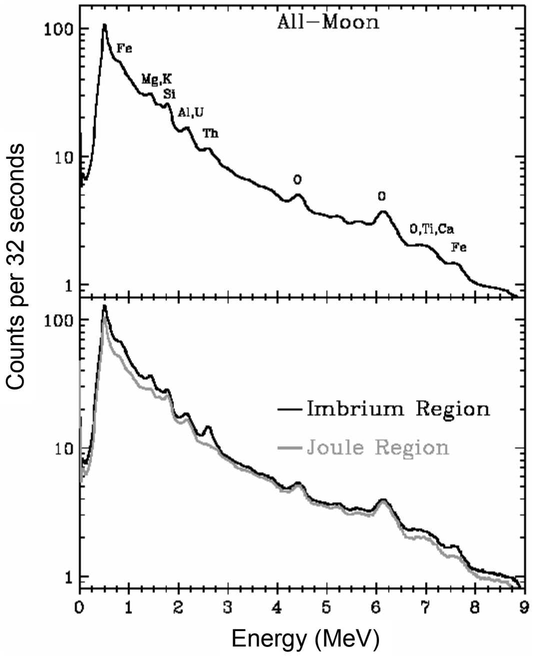

Figure 2-37. Gamma-ray spectra measured from the lunar surface using the LP-GRS. The top panel shows gamma-ray spectra from the entire Moon. The bottom panel shows spectra from two regions that have substantially different gamma-ray responses and surface compositions.

which have energies characteristic of the particular element. Finally, there are a few naturally radioactive elements (Th, U, K) that produce gamma rays having fluxes large enough such that their lunar abundances can be measured from orbit. A comprehensive description of gamma-ray spectroscopy is given by Evans et al. (1993). The most complete tabulation of gamma-ray fluxes coming from the lunar surface is given by Reedy (1978). Table 2.8 gives a summary of various gamma-ray spectroscopy observational parameters. Table 2.9 lists the most prominent gamma-ray lines that can be used for orbital elemental-composition measurements.

There have been two experiments that have carried out orbital gamma-ray measurements of the lunar surface: the Apollo Gamma-ray Spectrometer (AGRS) and the Lunar Prospector Gamma-ray Spectrometer (LP-GRS). Table 2.10 lists some of the important measurement parameters for each experiment. Further details about these experiments can be found in Metzger et al. (1993); Feldman et al. (1999), and Lawrence et al. (2004). Both experiments used scintillator-based gamma-ray detectors adequate for identifying the major gamma-ray lines seen from the lunar surface. Three of the major differences between the AGRS and LP-GRS experiments are the mission duration, coverage of the lunar surface, and direct measurement of the neutron flux. The AGRS measurements were taken from an equatorial orbit over the Apollo 15 and 16 missions, and resulted in a measurement coverage of ~18% of the lunar surface. In contrast, the LP-GRS measurements were taken from a polar orbit and resulted in global coverage from two different average altitudes of 30 and 100 km (Lawrence et al. 2000). Because the measured spatial resolution is proportional to the instrument height above the lunar surface, the two average altitudes had two different average spatial resolutions. The high altitude data has an average spatial resolution of 150–200 km^2; the low altitude data has an average spatial resolution of 60–80 km^2 (Lawrence et al. 2003) (though efforts can be made to carry out a spatial deconvolution if the gamma-ray angular emission and detection can be sufficiently well understood (Etchegaray-Ramirez et al. 1983)). The ultimate size of an analysis region, however, depends on the particular element being analyzed. For example, Th and Fe lines (Sections 10.1.1 and 10.1.2) are sufficiently resolved in the gamma-ray spectra and have a sufficiently high flux so that the intrinsic spatial resolution dominates the measured spatial resolution However, for other elements, such as Mg, the spatial resolution is more likely to be determined by the need to have a large enough region to reduce statistical uncertainties to an acceptable level.

Gamma-ray spectroscopy has unique measurement properties that distinguish it from other methods, such as multispectral imaging. Gamma-ray spectroscopy, like X-ray spectroscopy, measures elemental abundances independent of the molecular or mineralogical state of a given element. There are, however, some composition effects that need to be accounted for when deriving elemental abundances from gamma rays produced by neutron capture and inelastic scatter reactions, and which distinguish the AGRS from the LP-GRS experiment. For example, when abundances are measured using neutron-capture gamma rays, variations in thermal-neutron number density, which has a dynamic range of over a factor of three across the lunar surface, need to be taken into account (Lawrence et al. 2002). For inelastic-scatter gamma rays, variations in the fast-neutron flux need to be accounted for before deriving elemental abundances (Prettyman et al. 2002a,b). One of the distinguishing features of the LP-GRS experiment compared to the AGRS experiment is that Lunar Prospector had onboard neutron measurements that were used to make these neutron corrections.

Another characteristic of gamma-ray spectroscopy, compared to techniques such as optical, infrared and X-ray methods, is that the measured gamma-ray signal comes from an average depth of 30 cm beneath the lunar surface that avoids very superficial deposits such as small crater ray systems. A strength of gamma-ray spectroscopy is that absolute elemental abundances can be measured that are to a first approximation independent of ground-truth data (Metzger et al. 1977; Lawrence et al. 1999, 2000). This capability is important because the footprint of gamma-ray spectroscopy data is large (~60–200 km) compared to the sample-return sites and

Table 2.8. Summary of observational measurement parameters for different remote sensing techniques.

Technique	*spatial resolution*	*depth of signal*	*surface effects*	*mineral effects*	*measurement specificity*	*absolute abund.*	*collection times*
multispectral imaging	~100 m	~1 µm	Yes	Yes	Fe, Ti	Yes[1]	minutes
thermal imaging							
radar							
gamma-ray spectroscopy	50 – 200 km	30 cm	Minimal	No	Th, K, U, Fe, Ti, Al, Mg, Si, Ca, O	Yes[2]	minutes to hours
thermal neutrons	50 – 200 km	100 cm	Minimal	Not likely	Combinations of Fe, Ti, Gd, Sm	Yes[3]	minutes to hours
epithermal neutrons	50 – 200 km	50 cm	Minimal	No	H, Gd+Sm	Yes[3]	minutes to hours
fast neutrons	50 – 200 km	50 cm	Minimal	No	Fe, Ti, <A>	Yes[3]	minutes to hours
X-ray spectroscopy	20 – 100 km	10 µm	Cannot see through dust layer	No	Si, Mg, Al, Fe[4], Ti[4]	No[5]	minutes to hours

[1] Absolute abundances require ground truth calibration. [2] Absolute abundances have been obtained using both ground truth calibration and independent of ground truth calibration. [3] Information about ground truth abundances and/or other remotely sensed data needed to obtain absolute abundances. [4] No lunar surface measurements for Fe and Ti using XRF have been reported. Fe and Ti abundances can only be obtained using XRF during times of high solar activity. [5] Absolute abundances have not been reported using XRF.

Table 2.10. Comparison of the Apollo and Lunar Prospector gamma-ray spectrometer measurements.

Parameter	*Apollo GRS*	*Lunar Prospector GRS*
type of instrument	NaI scintillator	BGO scintillator
energy resolution	10% @ 662 keV	10.5% at 662 keV
mission duration	dates of Apollo 15 and 16	16 Jan 1998 – 31 July 1999
collection time over a 150 × 150 km^2 area	0.21 hours	4.7 hours at equator, 228 hours at poles
coverage of lunar surface	~18% coverage from an equatorial orbit	100% coverage from a polar orbit
spatial resolution	~200 km at 100 km altitude	~200 km at 100 km altitude, ~60 km at 30 km altitude
reported elemental measurements	Th, K, Fe, Ti	Th, K, U, Fe, Ti, Mg, Al, Si, Ca, O,

Table 2.9. List of strongest gamma-ray lines for the ten elements that have been measured using orbital gamma-ray spectroscopy (after Reedy 1978).

Element	*Assumed Abundance*	*Energy (MeV)*	*Estimated Flux*[1]	*Reaction Type*
O	43.5 wt%	2.741	5.98×10^{-3}	inelastic scatter
		3.086	4.72×10^{-3}	inelastic scatter
		3.684	1.15×10^{-2}	inelastic scatter
		3.854	6.20×10^{-3}	inelastic scatter
		4.438	2.02×10^{-2}	inelastic scatter
		6.129	4.78×10^{-2}	inelastic scatter
		6.917	1.23×10^{-3}	inelastic scatter
		7.117	1.35×10^{-2}	inelastic scatter
Mg	4 wt%	1.369	1.33×10^{-2}	inelastic scatter
Al	11 wt%	2.210	1.13×10^{-2}	inelastic scatter
		7.724	2.88×10^{-2}	neutron capture
Si	20 wt%	1.779	6.54×10^{-2}	inelastic scatter
K	1200 µg/g	1.461	3.92×10^{-2}	radioactive decay
Ca	10 wt%	1.943	3.42×10^{-3}	neutron capture
		3.737	5.77×10^{-3}	inelastic scatter
		3.904	3.87×10^{-3}	inelastic scatter
		6.420	4.02×10^{-3}	neutron capture
Ti	1.4 wt%	1.382	4.48×10^{-3}	neutron capture
		6.419	4.67×10^{-3}	neutron capture
		6.762	6.87×10^{-3}	neutron capture
Fe	9 wt%	0.847	1.92×10^{-2}	inelastic scatter
		7.631	1.00×10^{-2}	neutron capture
		7.646	9.20×10^{-3}	neutron capture
Th	1.9 µg/g	0.911	1.76×10^{-2}	radioactive decay
		0.965	3.37×10^{-2}	radioactive decay
		0.969	1.09×10^{-2}	radioactive decay
		2.615	3.66×10^{-2}	radioactive decay
U	0.5 µg/g	1.120	8.02×10^{-2}	radioactive decay
		1.765	1.06×10^{-2}	radioactive decay
		2.204	3.73×10^{-3}	radioactive decay

[1] The estimated flux is given in gamma-rays per second and assumes the abundances given in the second column. Other assumptions and details about the modeled gamma-ray fluxes are given in Reedy (1978).

the abundances sampled over the small-area landing sites may not be representative of the large areas sampled by the gamma-ray spectrometer. The ability to independently obtain absolute abundances, however, requires a detailed understanding of the gamma-ray and neutron detectors as well as the gamma-ray and neutron production processes on the lunar surface (Prettyman et al. 2002a). Finally, gamma-ray spectroscopy provides the ability to measure some key elements that cannot be measured by any other remote technique, such as Th, K, U, O, and Ca.

10.1.1. Gamma-ray spectroscopy measurements of Th and K. There are three naturally radioactive elements – Th, K, and U (Table 2.9) – that produce gamma-ray fluxes high enough to be measured from a gamma-ray detector in lunar orbit. Each of these elements are "incompatible" and are therefore expected to show similar abundance distributions (Section 3.4.2).

Of the three elements, the easiest to measure is Th. Th produces a very strong gamma-ray signal. According to the gamma-ray tabulation of Reedy (1978), the 2.61 MeV Th gamma ray is the second strongest elemental gamma ray coming from the lunar surface (the 1.46 MeV K gamma-ray is the strongest). Second, the 2.61 MeV gamma ray is one of the best separated gamma rays in the measured lunar gamma-ray spectra, which is particularly important for gamma-ray spectra measured using scintillator detectors that have low energy resolution. Finally, because the 2.61 MeV Th line has the highest energy of the radioactive and incompatible elements, it is located in a region of relatively low gamma-ray background. In contrast, the lower energy lines are contaminated by the Compton continuum background from the 2.6 MeV Th line, which makes the determination of their fluxes more difficult.

The gamma ray line with the largest flux in lunar spectra is the 1.46 MeV gamma-ray produced by ^{40}K. In spite of this large flux, however, several difficulties arise in using this line to measure K abundances. First, compared to the 2.61 MeV Th line, the 1.46 MeV K line is not as well separated in the measured gamma-ray spectra (see Fig. 2.37). It is close to a number of other large-flux gamma rays such as the 1.38 MeV Mg line. Second, since it has a relatively low energy, it sits atop a large gamma-ray background that consists in part of Compton continuum gamma rays originating from the 2.61 MeV Th line. On most of the lunar surface, the background component that originates from the 2.61 MeV Th line varies in the same way as the 1.46 MeV full-energy K line. One of the goals for measuring K abundances, however, is to find where they deviate from Th abundances, which for nonmare regions would indicate the occurrence of materials with non-KREEP-like K/Th (Section 6.2.4).

Finally, U produces a number of gamma-ray lines having energies less than 3 MeV. Because the expected fluxes of these lines are lower than either the large Th or K line and because there is a high degree of correlation between U and the elements Th and K, it is difficult to cleanly separate out the effect of the U lines from the rest of the spectrum. Because of these effects, there are no reported measurements of U independent of Th and K.

Since the gamma rays from Th and K are produced by radioactive decay reactions, it is relatively straightforward to determine absolute abundances to first order, independent of ground-truth measurements. This is because no neutron corrections need to be made to the measured gamma-ray fluxes, and the parameters that describe the radioactive decay reactions are very well known.

The first remotely measured Th abundances on the lunar surface used data from the AGRS (e.g., Bielefeld et al. 1976; Metzger et al. 1977). Maps of these data on the lunar surface are given by Spudis and Pieters (1991) and Metzger (1993). Metzger et al. (1977) used an energy band analysis ($0.55 \leq E \leq 2.75$) combined with information about the gamma-ray background and detector efficiency to determine absolute Th abundances independent of ground truth. While these data only covered 18% of the lunar surface, many features of the global Th distribution were identified. These include the near-side/far-side composition dichotomy, elevated Th abundances around Aristarchus crater, the Fra Mauro region, the Apennine mountains SE of Imbrium basin, and near Van de Graff crater in SPA basin.

The first global maps of Th abundances on the lunar surface used high-altitude LP-GRS data to derive relative abundances on 150 km × 150 km pixels (Lawrence et al. 1998). Further studies derived absolute abundances using low-altitude (Lawrence et al. 1999) and both high- and low-altitude LP-GRS data (Lawrence et al. 2000) on 60 km × 60 km pixels. Finally, the spatial resolution and information content of the low-altitude data were optimized by Lawrence et al. (2003) to produce a map (Plate 2.3) having an intrinsic spatial resolution of $\sim(80\text{ km})^2$ mapped onto $0.5° \times 0.5°$ pixels. The absolute abundances in Lawrence et al. (2003) were derived from Prettyman et al. (2002a,b), who determined absolute Th abundances using a full modeling and spectral analysis of the gamma-ray spectra. The Lawrence et al. studies used an energy band analysis ($2.5 \leq E \leq 2.7$ MeV) to determine the relative number of counts in the 2.61 MeV Th peak. Other studies have used alternate forms of determining absolute abundances using either ground truth information (Gillis et al. 2004) or a more detailed analysis of the intrinsic uncertainties and background determination (Warren 2001a, 2005). Although neither of these analyses changed the abundance determinations by more than 20% for most of the abundance range, they argued that for abundances less than 2 ppm, the Lawrence et al. and Prettyman et al. concentrations may be high by up to a factor of two. The Warren studies used a combination of statistical analysis of LP-GRS and sample data to adjust the absolute Th concentrations, and the Gillis et al. studies used a combination of lunar samples, including lunar meteorite data, and AGRS regional data to make an empirical correction.

Upon inspection, the global distribution of Plate 2.3 is consistent with the partial coverage map made with AGRS data. The general features that are seen include high Th concentrations (up to 12 µg/g) on the lunar near side in and around Imbrium basin and western Oceanus Procellarum. There are also Th enhancements at a number of large craters that appear to have penetrated a mare basalt layer and exposed underlying material with high Th concentrations. These craters include Aristarchus, Mairan, Aristillus, and Kepler. Detailed descriptions of the Th abundances around some of these craters are given in a number of studies (e.g., Blewett et al. 2001; Gillis et al. 2004). Plate 2.3 also shows moderately elevated Th concentrations across much of the SPA basin.

Despite the fact that most of the lunar highlands have very low Th abundances, a few locations exist in the lunar highlands that have elevated Th abundances. One of these locations is a Th enrichment near the craters Compton and Belkovich (60°N, 100°E) that appears to be co-located with a bright albedo feature having a size of 15 × 30 km (Gillis et al. 2002). This Th enrichment likely has surface Th concentration in the range of 40–55 ppm (Lawrence et al. 2003), which suggests this region is dominated by an evolved lithology such as alkali anorthosite (Elphic et al. 2000; Lawrence et al. 2000, 2003; Gillis et al. 2002).

Measurements of K abundances were first obtained using AGRS data (Bielefeld et al. 1976; Metzger et al. 1977). As described by Metzger et al. (1977), K/Th in the western and eastern mare regions were shown to be roughly the same as for KREEP-like materials (~400, Korotev 2000). However, in the Th-poor farside regions, K/Th ranged up to 1800, which is much higher than the near-side values. While these large farside values were attributed, in part, to the low abundances causing large scatter in the data, Metzger et al. (1977) stated that some of the variation was attributable to real compositional variations.

With LP-GRS data, a preliminary global map of K abundances was reported by Lawrence et al. (1998). Using the analysis that is described in Section 10.1.4, Prettyman et al. (2002a,b) reported global maps of the absolute abundances of K. These data show a strong correlation between Th and K, with a correlation trend that is similar to what is seen in the sample data.

10.1.2. Gamma-ray spectroscopy measurements of Fe. Two dominant gamma-ray lines can be used to measure Fe abundances: the 7.6 MeV line produced by neutron-capture reactions and the 0.846 MeV line produced by inelastic-scatter reactions. With current data sets, the 7.6 MeV line is easier to analyze because (1) it is largely separated in measured gamma-ray spectra (see Figs. 2.37 and 2.38); (2) of the identified lines, it has a relatively large dynamic range (again see Fig. 2.37); and (3) because it occurs at a high energy, it sits on top of a relatively low background of gamma rays scattered from higher energies. In contrast, despite its comparable flux (Reedy 1978), the 0.846 MeV line is difficult to analyze with existing data because it is not well separated in the measured gamma-ray spectra and it sits on top of a large and variable background. In particular, variations in the Compton continuum from the higher energy Th, K, and U lines dominate the background.

Several different studies have used data from both the 7.6 and 0.846 MeV lines to derive Fe abundances on the lunar surface. The first comprehensive map of Fe abundances using the 7.6 MeV gamma-ray line was produced by Davis (1980) using AGRS data. In that study, approximately 18% of the lunar surface was mapped with a spatial resolution of ~200 km. Maps of these data can also be found in Spudis and Pieters (1991). To derive these abundances, Davis measured the total counting rate within an energy window ($6.99 \quad E \leq 8.99$ MeV) around

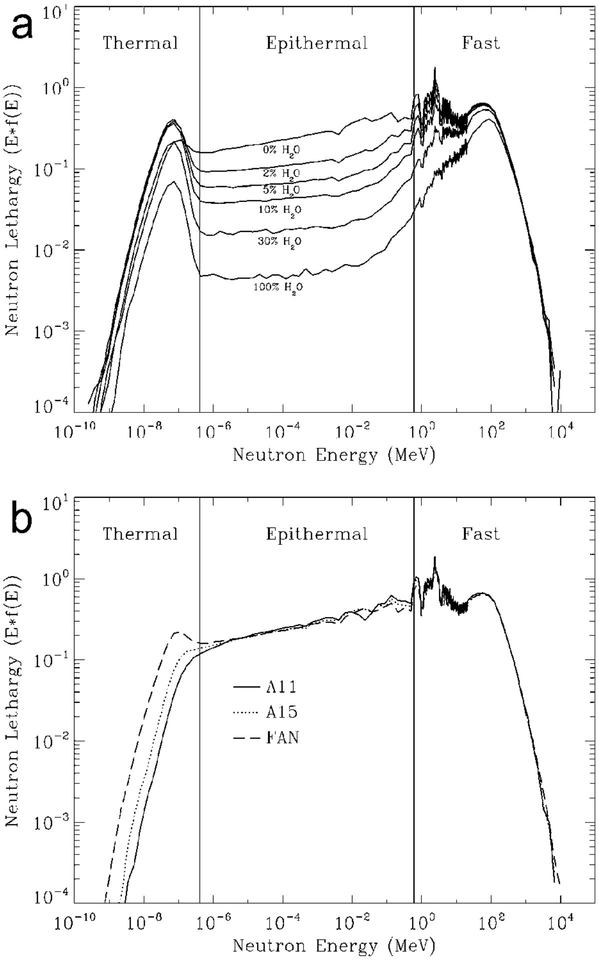

Figure 2.38. Simulated neutron flux spectra for different lunar soil compositions. Top panel shows the simulated neutron flux (or lethargy, which is flux times energy) for three different lunar soils: Apollo 11, Apollo 15, and ferroan anorthosite. Bottom panel shows simulated spectra for a ferroan anorthosite soil combined with varying amounts of water from 0 wt% to 100 wt%.

the 7.6 MeV line. Absolute abundances were obtained by normalizing the measured counting rate with ground truth abundances at the sample sites.

In a subsequent study, Davis and Bielefeld (1981) reported Fe abundances derived from variations in the 0.846 MeV gamma-ray line using AGRS data. The background from Th, K, and U was accounted for using a semi-empirical model derived from measured counting rates and assumed Th/U and Th/K abundance ratios. When the AGRS data were averaged over large regions, a good correlation was found between the inelastic scatter and the AGRS neutron-capture data of Davis (1980).

The first global map (Plate 2.4) of gamma-ray-derived Fe abundances using low-altitude LP-GRS data measured the counting-rate variations of the 7.6 MeV line (Lawrence et al. 2002). In a manner similar to the study of Davis (1980), the total counting rate within an energy window ($7.35 \leq E \leq 7.92$) was measured to derive the Fe abundances. These counting rates were binned onto 0.5° × 0.5° pixels on the lunar surface and smoothed using a two-dimensional, equal-area Gaussian function in order to maximize the compositional contrast and minimize the scatter in the data. Finally, absolute abundances were obtained by normalizing to landing site abundances via the Clementine spectral-reflectance-derived FeO concentrations of Lucey et al. (2000). For this normalization, the Clementine spectral reflectance data were smoothed to match the LP-GRS footprint. The validity of this normalization is founded upon the assumption that the Clementine-derived data give a good representation of the true FeO concentrations within ~150 km of the landing sites (see Section 10.4.7).

Prettyman et al. (2002a,b) did a comprehensive analysis of high- and low-altitude LP-GRS data to derive abundances for ten different elements (Th, K, U, Fe, Ti, Mg, Ca, Al, Si, and O). In this study, absolute abundances were determined largely independent of ground truth; modeling and experimental verification of the gamma-ray production and detection process enabled absolute abundances to be derived from the measured LP-GRS and LP-NS data alone. Figure 2.39 shows the resulting fits from the analysis of Prettyman et al. (2002b) to measured gamma-ray spectra for a few selected regions. As part of this analysis, FeO abundances were determined on (150 km × 150 km) and (60 km × 60 km) equal area pixels using variations of both the 7.6 and 0.846 MeV lines.

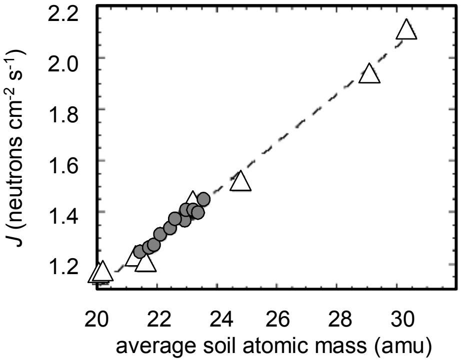

Figure 2.39. Simulated integrated neutron leakage flux from the lunar surface for typical lunar minerals (triangles) and typical lunar compositions (circles). The integration is between 600 keV and 8 MeV (taken from Gasnault et al. 2001).

When inter-comparisons are made among the various gamma-ray-derived Fe datasets, reasonably good agreement is found for all measurements. For example, the correlation coefficient between the Fe dataset of Davis (1980) and Lawrence et al. (2002) is 0.85. The correlation coefficient between the two LP-GRS datasets is 0.98.

Upon close inspection, however, significant differences occur between the datasets. For example, when the analysis of AGRS data (Davis 1980; Clark and McFadden 2000) is compared to the analysis of LP-GRS data (Lawrence et al. 2002), there are systematic differences in both mare and highlands regions. Specifically, the AGRS data tend to show higher Fe abundances in the highlands compared to the LP-GRS data, and the AGRS data tend to show lower Fe abundances in the mare regions compared to the LP-GRS data. These differences are almost certainly due to the fact that a neutron-number-density correction was done on the LP-GRS data and not on the AGRS data (Lawrence et al. 2002). Such a correction is needed because the total number of thermal neutrons in a given location dictates the number of neutron-capture gamma rays that can be produced (Lawrence et al. 2002). Because the number of thermal neutrons varies by over a factor of three across the lunar surface (see Plate 2.5), this correction is non-negligible. When a detailed comparison is made between the two LP-GRS datasets (Lawrence et al. 2002; Prettyman et al. 2002a,b), discrepancies appear to be related in part to differences in how latitude-dependent detection asymmetries were treated.

10.1.3. Gamma-ray spectroscopy measurements of Ti. The strongest grouping of Ti gamma-ray lines are neutron-capture lines that occur at 6.42, 6.56, and 6.76 MeV. In contrast to the Fe neutron-capture line at 7.6 MeV, these Ti lines are not cleanly separated in either the AGRS or LP-GRS spectra (e.g., Fig. 2.37). In particular, interferences from gamma-ray lines are produced by O (6.92 MeV), Si (6.88 MeV), and Ca (6.42 MeV). Furthermore, these lines are located on the Compton continuum background produced by the higher-energy Fe lines.

Despite these complications, Ti abundances have been reported using data from both the AGRS and LP-GRS experiments. Davis (1980) reported the first gamma-ray derived map of Ti abundances using AGRS data. As with the Fe data, the reported Ti data covered approximately 18% of the lunar surface. Davis derived absolute Ti abundances using a combination of an energy-window counting-rate technique ($4.78 < E < 6.99$) and normalization to ground-truth abundances. Furthermore, an Fe- and Al-dependent background was subtracted from the window counting rate to account for the Fe-dependent Compton-continuum-background gamma rays. A global Ti map using high-altitude LP-GRS data was reported by Prettyman et al. (2002a,b). The Ti map was derived using the same analysis used to determine Fe and other elemental abundances (Section 10.1.4).

10.1.4. Gamma-ray spectroscopy measurements of Mg, Al, Ca, Si and O. In addition to the abundances for Th, K, Fe, and Ti, preliminary results for the global, absolute abundances of Mg, Al, Ca, Si, and O were reported by Prettyman et al. (2002a,b). Prettyman et al. (2002a,b) did a comprehensive analysis of the entire gamma-ray production and detection process. Included in this analysis was detailed modeling of the gamma-ray production process, the surface-to-spacecraft gamma-ray transport process, and the instrument gamma-ray detection process. A linear least-squares fitting procedure of the gamma-ray energy spectra was used to determine the absolute elemental abundances. Finally, absolute concentrations were obtained by normalizing the gamma-ray flux to the composition of feldspathic lunar meteorites for selected highlands regions. For all elements, data from the high-altitude portion of the LP mission were used and data were mapped using pixels having a size of ~ 150 km × 150 km (or 5°×5° at the equator).

The general behavior of the elemental abundance maps shows trends that are to first order consistent with sample studies. The near-side mare basalt regions have relatively high Mg abundances and relatively low Al, Ca, and Si abundances. In contrast, the far-side highlands regions have relatively low Mg abundances and relatively high Al, Ca, and Si abundances. The O abundances fall within a narrow range near 44 wt% as is expected from sample studies (Section 6.2.4; Fig. 2.18).

It should be noted that these data are preliminary and work continues as of this writing to refine and improve the analysis of Prettyman et al. (2002a,b). Specific issues include the gamma-ray production cross sections for a number of key elements (e.g., O, Ti, Mg), the high-energy physics models that describe the proton-to-neutron (and hence gamma-ray) production, and the source, magnitude, and energy dependence of the non-lunar background gamma-rays.

10.2. Neutron spectroscopy

The technique of orbital neutron spectroscopy can measure the composition of the lunar surface by measuring broad energy ranges of neutrons produced by nuclear spallation reactions. Specifically, these neutrons are generated by interactions between galactic cosmic rays and their secondary particles, and the nuclear constituents of surface material. After production, an equilibrium velocity distribution forms as a result of multiple elastic and non-elastic collisions between the neutrons and nuclei in the surface. The intensity and velocity-space structure of resulting spectra depend on the elemental composition of surface material. Figure 2.38 shows a plot of simulated neutron energy spectra for various assumed lunar compositions (Feldman et al. 1998a).

In practice, there are three broad ranges of neutron energies that contain compositional information about the lunar surface (see Fig. 2.38). The neutrons within these energy ranges are referred to as fast neutrons (0.6–3 MeV), epithermal neutrons (0.4 eV $< E <$ 0.6 MeV), and thermal neutrons ($E <$ 0.4 eV). In general, the flux of fast neutron is related to average atomic mass of the surface material (Section 10.2.1**;** Gasnault et al. 2001). Since variations in the atomic mass of lunar material is dominated by variations in Fe and Ti abundances, a global map of fast neutrons looks similar to a combination of the observed Fe and Ti abundances (Maurice et al. 2000). The flux of epithermal neutrons reflects primarily the abundance of H (Lingenfelter et al. 1961; Feldman et al. 1998b, 2000a, 2001). However, epithermal neutrons are also observed to be sensitive to Gd and Sm because of a few very large (n,γ) resonances between 0.4 eV and 10 eV. Finally, because the neutron absorption cross sections for Fe, Ti, Gd, and Sm are quite large, the flux of thermal neutrons is highly sensitive to abundance variations of these elements across the lunar surface (Elphic et al. 1998; 2000; Feldman et al. 1998a; 2000b).

The only mission to conduct orbital neutron spectroscopy measurements of the lunar surface has been the Lunar Prospector mission (Binder 1998). The Lunar Prospector spacecraft carried the neutron spectrometer (LP-NS) that measured the fluxes of thermal and epithermal neutrons using two ^{3}He gas proportional counters (Feldman et al. 1999, 2004; Maurice et al. 2004). Fast neutrons and a broad energy range of epithermal neutrons (Genetay et al. 2003) were measured using signals from the scintillator anti-coincidence shield of the LP-GRS (Feldman et al. 1999, 2004).

As demonstrated by the LP-NS, there are a number of strengths to the orbital neutron spectroscopy technique. First, the signal from both epithermal and fast neutrons provides one of the only ways to measure the H content of the lunar surface (see Section 10.9). Second, the dynamic range of the fast and thermal neutron flux measurements is relatively large and provides a very sensitive measure of composition parameters across the lunar surface. Neutron measurements also provide critical corrections for a the analysis of the gamma-ray spectroscopy data (Lawrence et al. 2002; Prettyman et al. 2002a,b).

Some of the limitations of orbital neutron spectroscopy are the same as gamma-ray spectroscopy. For example, the spatial resolution of the epithermal neutron measurements is between 1 and 1.5 × the spacecraft altitude above the lunar surface (Feldman et al. 2001). In addition, with the exception of the strong sensitivity to H, orbital neutron spectroscopy measurements do not by themselves provide specific elemental abundance measurements. Other data must supplement the orbital neutron spectroscopy measurements to provide information about specific elemental abundances. Nevertheless, even with this limitation, orbital neutron spectroscopy measurements can still provide valuable constraints for the composition of the lunar surface.

10.2.1. Average atomic mass of the lunar surface. In a study of fast-neutron data from Lunar Prospector, Gasnault et al. (2001) showed that a direct relation between the fast neutron flux and the average atomic mass of the soil is generally valid for planetary surfaces having very low H abundances. The correspondence between average atomic mass and fast neutrons results from neutron production processes and the subsequent interactions of neutrons with the surrounding materials. This relationship has been characterized using numerical calculations supported by laboratory experiments of the irradiation of thick targets (materials like Be, Pb, W, and Sn) with high-energy protons.

As described by Gasnault et al. (2001), the average atomic mass is related to the fast neutron flux according to the following relation:

$$< A > = \alpha J + \beta \tag{2.1}$$

where $<A>$ is the average soil atomic mass (amu), J is the neutron flux at the surface (neutrons cm^{-2} s^{-1}), $\alpha = 10.6 \pm 0.3$, and $\beta = 8.3 \pm 0.4$. The presence of light elements in the soil may induce modifications of this relation. However, except for H, these modifications will be small. Fast neutron spectroscopy can therefore be used to provide a measure of the average soil atomic mass of planetary surfaces through use of Equation (2.1) when the soil has typical low lunar abundances of hydrogen.

Because the Moon is mostly devoid of H, Equation (2.1) is valid for the Moon. Gasnault et al. (2001) correlated Lunar Prospector measurements with <*A*> of the various lunar soil samples. Although there are mixing effects due to the relatively low spatial resolution of the data, Figure 2.39 shows that the correlation is very good (0.917) and compatible with Equation (2.1). That result leads to the construction of a map of the average atomic mass for the lunar surface from measurements of Lunar Prospector (Plate 2.6). The lowest <*A*> values (about 21 amu) are scattered over the highlands, whereas the highest <*A*> values (about 24 amu) are concentrated at the west and south of the Aristarchus plateau. The uncertainties lead to a standard deviation in <*A*> for this map of between 15% and 20%. Finally, we note that since the abundances of Fe and Ti dominate the variation of <*A*> across the Moon, fast neutrons are alternatively a good indicator of the abundance and location of Fe and Ti (Maurice et al. 2000).

10.2.2. Thermal and epithermal neutron measurements of Fe , Ti, Gd, and Sm. Monte Carlo simulations of cosmic ray-induced neutron production in lunar soils and rocks indicate that the leakage flux of thermal neutrons out of the lunar surface depends strongly on the soil composition. Materials that are abundant in thermal-neutron absorbing elements, such as Fe, will have a markedly lower leakage flux than those lacking these absorbers. This is clearly seen in orbital neutron spectrometer measurements from the Moon. For example, the thermal-neutron leakage flux is much lower over the Fe-rich maria than over the Fe-poor highlands (Maurice et al. 2004, Plate 2.5). The epithermal neutron flux is much less affected by the presence of such absorbers, and simulations show that there is a linear relationship between the ratio of epithermal to thermal fluxes (or count rates) and the macroscopic absorption cross section of materials with typical lunar compositions. The macroscopic absorption cross section Σ_a is a measure of the net thermal-neutron-absorbing effect due to all elements making up the material:

$$\sum_a = \sum_i \sigma_{ai} f_i \frac{N_A}{A_i} \tag{2.2}$$

where σ_{ai} is the thermal neutron absorption cross section at 0.025 eV (usually expressed in barns, where 1 barn = 10^{-28} cm^2), f_i is the weight fraction, A_i is the atomic mass of element *i*, and N_A is Avogadro's number. For the known range of lunar soil and rock compositions, Σ_a is strongly dominated by Fe, Ti and the REEs Gd and Sm. These trace elements can have a profound effect on thermal-neutron absorption because certain of their isotopes have very large thermal-neutron-absorption cross sections.

Because the relationship between the epithermal-to-thermal flux ratio and Σ_a depends almost entirely on three constituents, Fe, Ti, and the REEs, it is in principle possible to obtain the abundance of one of these constituents if the other two can be somehow constrained. For example, if Fe abundance can be determined by either gamma-ray spectroscopy or optical spectral-reflectance techniques, and if the REEs can be constrained by a close relationship with Th as measured by gamma-ray spectroscopy, then the Ti abundance can be inferred using the neutron data. This Ti-detection technique complements that of optical spectral reflectance and gamma-ray spectroscopy. The effect in thermal neutrons is very strong for the high-Ti mare basalts, and much more readily distinguished than the (n,γ) capture line of Ti in the BGO gamma-ray spectra obtained by the LP-GRS. In contrast, given estimates of Fe and Ti abundances, the combined REE concentrations of Gd and Sm can be extracted using this technique. Finally, in feldspathic highlands regions where both REE and Ti concentrations are very low, thermal neutrons can be used to estimate Fe concentrations.

The technique suffers in two areas: first, it necessarily has the broad spatial resolution of the gamma-ray and neutron-spectrometer footprints, and second, it depends on having well-determined concentration values for Fe and the REEs, Gd and Sm, or Ti. The former issue limits the technique's effectiveness in prospecting for ilmenite-rich regions, whereas optical techniques can provide this information down to arbitrarily small scales. However there is evidence that the optical technique may respond to more than just ilmenite (see Section 10.4.6). The latter issue is a serious drawback, since uncertainties in Fe or REE determinations add to the uncertainty in inferred Ti abundance. Likewise, using Th as a proxy for REEs may be problematic, since more highly-evolved lithologies such as alkali anorthosite, monzogabbro, or granite fractionate Th and REEs differently. Finally, uncertainties in the determination of Ti cause uncertainty in the determination of REE abundances using thermal neutrons.

Regarding quantitative abundance determinations, various analyses have presented results for Fe, Ti, and the REE. An analysis of the thermal-to-epithermal neutron counting rates in feldspathic highlands materials where Ti and REE abundances are low (and therefore should make almost no contributions to the observed thermal-neutron flux) show that the weight fraction of FeO must be between 2% and 5% (Feldman et al. 2000b). Elphic et al. (2002) presented the first neutron-derived abundances of Ti on the Moon. The results disagree with the abundance estimates provided by UVVIS spectral reflectance techniques (Lucey et al. 2000; see Section 10.4.6); the neutron abundance is on average about half that of the optical estimates (see also Section 10.5.3). The disagreement between the two data sets is likely to shed light on lunar mare basalt opaque mineral abundances and compositions as can be determined from orbit. Preliminary Ti abundance estimates from the Lunar Prospector GRS support the neutron numbers, but there are spatial discrepancies (Prettyman et al. 2002b) (see above).

Finally, the first qualitative maps of REE abundance (Gd and Sm) were shown by Elphic et al. (1998). Quantitative estimates were produced using both preliminary Lunar Prospector global FeO abundance estimates based on GRS data, and TiO_2 abundance estimates derived from Clementine UVVIS spectral reflectance data (Plate 2.7, Elphic et al. 2000). In general the correlation with LP-GRS Th distributions is very good. However, the TiO_2 abundance estimates appeared to be a factor of two too high, which had the effect of reducing the REE contribution in some high-Ti mare basalts (Elphic et al. 2000; 2002).

One strength of these REE measurements is that they are an independent measure of incompatible trace elements, specifically the rare earth elements Gd and Sm. The REE abundances can then be compared with that of Th to determine the Th/REE ratio, one indicator of the degree to which igneous evolution has caused incompatible-element fractionation, insofar as it may occur on a large scale. So in principle it is possible to separate KREEP, alkali anorthosite, and granitic compositions. It may be possible to investigate this ratio in mare basalts as well. The effect of the REEs in the neutron data is profound, and can be comparable to that of Fe and Ti in mare basalts.

It should be noted that the technique described here depends on knowing Fe and Ti abundance; uncertainties in these values produce uncertainties in the inferred REE abundance. Finally, there is some debate about the values of "effective" thermal-neutron capture cross sections for Gd and Sm, which are critical to determining the elemental abundance of the REEs.

10.2.3. Epithermal neutron measurements of Gd and Sm. The REEs Gd and Sm can also be detected using epithermal neutrons (Maurice et al. 2004). In contrast to the Gd and Sm measurement with thermal neutrons, the measurement of Gd and Sm concentrations with epithermal neutrons requires fewer assumptions about the surface composition. In general, epithermal-neutron data from the LP-NS yield a map (Plate 2.8) that comprises three levels of information relevant to the surface composition. The first signal is related to the production rate of fast neutrons that generate the epithermal neutrons. The second signal is due to solar-wind-implanted H at mid latitudes and water deposits at the poles (Section 10.8; Feldman et al. 2000a; Johnson et al. 2002). The third signal is caused by a combination of Gd and Sm (Maurice et al. 2004). With appropriate corrections, maps of Sm and Gd concentrations can be derived with values that correlate well in non-mare regions with the measured Th concentrations (see Fig. 2.40 and Plate

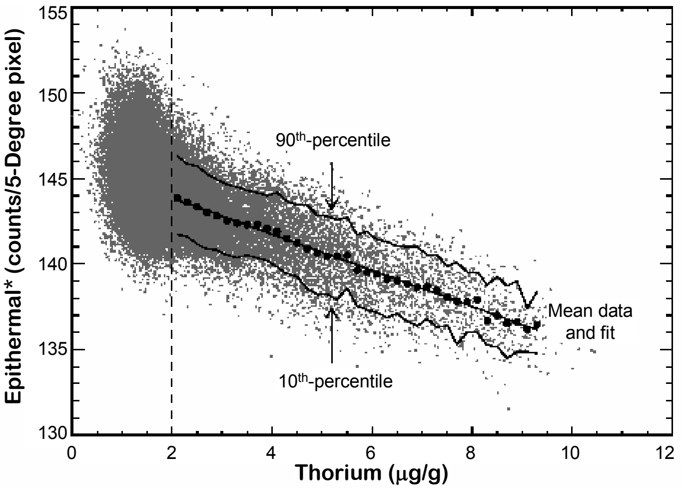

Figure 2.40. Comparison of Gd+Sm abundances measured using epithermal neutrons with thorium concentrations as measured with the LP-GRS.

2.7). In terms of Sm concentration, epithermal-neutron measurements have a 10 ppm threshold sensitivity, a 6.4 ppm precision, and a maximum value of ~35 ppm.

10.3. X-ray spectroscopy

The technique of planetary X-ray fluorescence (XRF) spectroscopy can measure the chemical composition of an airless planetary body by measuring the characteristic X-ray line emission that is excited on the planetary surface by solar X-rays. During solar quiet times, the spectral shape and intensity of the solar X-ray flux limit the available elemental measurements to the geophysically important elements Mg (1.254 keV), Al (1.487 keV), and Si (1.740 keV). During times of enhanced solar activity, it is possible to measure the higher energy X-rays from Ca (3.691 keV) and Fe (6.403 keV). Yin et al. (1993) give a detailed description of the technique of planetary XRF spectroscopy.

Prior to the present time, the only XRF spectroscopy measurements to successfully measure the composition of the lunar surface were the Apollo 15 and 16 XRF instruments. As described in a variety of studies (Adler et al. 1973; Clark and Adler 1978; Adler and Trombka 1980; Clark and Hawke 1981; Spudis and Pieters 1991; Yin et al. 1993), the Apollo 15 and 16 XRF instruments measured the elemental ratios of Mg/Si and Al/Si over 9% of the near-side surface. To simplify the data analysis procedures, the results were reported as elemental ratios instead of absolute elemental abundances. Abundance maps and summaries of these measurements are given by Andre et al. (1977), Spudis and Pieters (1991), and Yin et al. (1993).

The strengths of the XRF technique include the ability to measure elemental ratios and absolute elemental abundances such as Mg , Al, and Si that may be difficult to measure with other techniques. In addition, with the XRF technique, the measured elemental abundances are measured independently of the molecular or mineralogical state of the given elements. Furthermore, with suitable data processing, the spatial resolution of XRF measurements has been shown to be better (~30 km) than unprocessed gamma-ray and neutron data taken from a similar altitude above the lunar surface (~150–200 km). The spatial resolution of XRF measurements, however, is still quite broad compared to imaging data. The depth sensitivity in the lunar regolith of the XRF technique is on the order of tens of microns (Yin et al. 1993). Consequently, any thin deposit of excavated material can be identified with the XRF technique. Because of the shallow depth sensitivity, the XRF technique is complementary to the gamma-ray and neutron techniques that measure compositions down to about half a meter in the regolith. One of the drawbacks of XRF is that because solar X-rays provide the incident X-ray illumination, composition measurements can only be made on the sunlit side of the Moon. This limits the duty cycle and potential surface coverage for any XRF mission.

Finally, there are two missions, one in progress and one in planning, to fly XRF instruments to measure the composition of the lunar surface (Grande et al. 2001; Okada et al. 1999). These include the European Space Agency's SMART-1 mission (presently in orbit) and the Japanese-sponsored SELENE mission. It is anticipated that both these instruments will provide larger surface coverage and have better X-ray energy resolution than the Apollo 15 and 16 instruments.

10.4. Spectral reflectance remote sensing of lunar surface composition

Optical, ultraviolet and infrared remote sensing of the Moon has a venerable history, beginning with Wood (1912) who discovered significant variations in the visible and ultraviolet characteristics of the lunar surface. A host of techniques has been applied using ground-based telescopes; the most scientifically fruitful of these for compositional mapping have been spectroscopy and multispectral imaging in the region of solar reflectance from 0.4 to 2.5 microns. Spectral reflectance measurements of the lunar surface are sensitive to the mineralogy, mineral chemistry, and physical state of the regolith, including the important optical effects of space weathering.

The foundation for remote compositional analysis lies in optical absorption physics (Burns 1993) and the linking of spectral properties of materials measured in the laboratory to well-understood mineral species and their mixtures. The pioneering work by Burns (1970), Hapke et al. (1970), McCord and Adams (1973), McCord et al. (1981), and others amply demonstrated the potential of spectral reflectance measurements for understanding lunar materials. Following this initial era, a diverse set of remote-sensing investigations made significant progress in understanding the distribution of mare and highland materials. Mare studies using spectroscopy and multispectral imaging produced maps of a diverse suite of mare basalts, including unsampled types, pyroclastic deposits and the abundance of Ti. Spectroscopy of the lunar highlands uncovered a spectral diversity that mirrors the diversity found in the pristine rock collection, but occurs in vast exposures that the tiny fragments found in the Apollo collection did not anticipate (Pieters 1986). The state of lunar spectroscopic remote sensing just prior to the new spacecraft results is summarized by Pieters (1993).

Techniques and methodologies developed during the 1970's and 1980's for lunar spectral analysis provided the foundation for understanding of the new mission data, such as using observations of craters of all sizes to probe beneath the regolith, and inferring the abundance of Ti from lunar color. These and similar approaches benefit from three key characteristics of the Clementine data set: global reach, high spatial resolution, optimal band passes, and data uniformity. The value of global data is obvious; studies previously confined to the lunar near side can now be conducted globally. High spatial resolution enables entirely new studies, such as examination of compositional properties of individual lava flows. The Clementine band passes were chosen to characterize the major features in the spectra of lunar rock-forming minerals (Fig. 2.41). Data uniformity in terms of calibration and photometric correction enable confident comparison of radiometric and derived compositional information Moon-wide and provide access to new quantities such as albedo to be applied more confidently. Continuing studies of lunar samples, especially the regolith, have provided new understanding of lunar soil formation processes and effects that strongly influence the ability to glean information from the Moon remotely.

10.4.1. Spectral properties of major lunar materials.

Pyroxene and olivine. Of the major lunar minerals, the mafic silicates pyroxene and olivine are the most readily detected using near-infrared spectroscopy. They exhibit strong and unam-

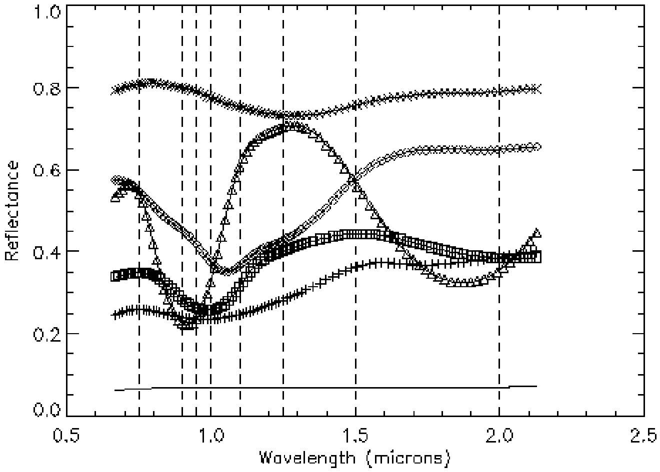

Figure 2.41. Spectra of individual lunar mineral phases: Ilmenite (solid line), glass (+), Orthopyroxene (Δ), clinopyroxene (□), olivine (◊), plagioclase (×). Wavelengths of Clementine band passes for the UVVIS and NIR cameras (vertical dashed lines) are superimposed for comparison.

biguously diagnostic spectral features near 1-2 μm due to electronic transitions in ferrous iron (Burns 1970); the vast majority of lunar spectra obtained—remotely or in the laboratory—show evidence of pyroxene or olivine. Only spectra of regions essentially lacking these minerals can show clear evidence of the presence of other phases by casual inspection, such as areas identified as anorthosites (Spudis et al. 1984) and glass-rich pyroclastic deposits (Adams et al. 1974). The dependence of key spectral properties of these minerals on mineral chemistry has been well documented; the number, centers and widths of the absorption features due to ferrous iron in the mafic silicates are strong indicators of their compositions, enabling not only distinctions between minerals, but constraints on the composition within mineral classes (Fig. 2.42) (Adams 1974; Adams and Goulaud 1978; Hazen et al. 1977; Hazen et al. 1978; King and Ridley 1987; Cloutis and Gaffey 1991; Sunshine and Pieters 1998).

The strong spectral properties of pyroxene led to the first remote detection of a lunar mineral as reported in McCord and Johnson (1970). New measurement capability led to the detection of regions differing in pyroxene chemistry (McCord et al. 1981). Although many lunar highland regions show evidence for abundant low-Ca pyroxene, consistent with the sample collection, highland areas with high abundances of high-Ca pyroxene were also detected (McCord et al. 1981; Lucey et al. 1986; Pieters 1986; Lucey and Hawke 1987). In a survey of central-peak compositions, Pieters (1986) found that the frequency of occurrence of central peaks showing strong evidence of abundant high-Ca pyroxene was relatively high (18 of 77 locations, or 22%), which is in strong contrast to the scarcity of such rocks in the sample collection.

Olivine was the first unambiguously detected mineral other than pyroxene. Pieters (1982) reported that the central-peak complex of the large crater Copernicus exhibited a spectrum indicating the presence of a mineral assemblage with abundant olivine, but little or no pyroxene. Using geologic arguments, (Pieters and Wilhelms 1985) concluded that this spectrum represented troctolite, a mixture of olivine and plagioclase. Spacecraft observations would show that olivine-rich/pyroxene-poor locations occur elsewhere on the Moon (see below, and Pieters and Tompkins 1999; Tompkins and Pieters 1999; Pieters et al. 2001a,b).

Feldspar. Iron-bearing plagioclase feldspar also exhibits a diagnostic absorption feature, albeit weak, and the wavelength position of the feature is sensitive to the sodium content of the feldspar (Adams and Goulaud 1978). Subtle features in spectra of lunar materials appearing on the wings of pyroxene features are sometimes attributed to feldspar, but pyroxenes can also inherently exhibit such a feature (Sunshine and Pieters 1993), and in the absence of detailed analysis or high spectral resolution, olivine can also plausibly mimic feldspar in this respect. The plagioclase iron feature is also known to be susceptible to shock at levels frequently experienced by lunar rocks (Adams et al. 1979; Bruckenthal and Pieters 1984). Despite weakness and fragility of this feature the inherent high albedo of feldspar owing to its low ferrous iron content enhances its detectability.

Feldspar was the last of the major silicates to be unambiguously detected remotely. Spudis et al. (1984) reported the presence of anorthosite in the Inner Rook rings of the Orientale multiringed impact basin. In the strictest sense, that and subsequent similar detections of anorthite are not in themselves unambiguous. Spectra attributed to anorthite (or anorthosite) are characterized by the apparent lack of a measurable spectral feature due to ferrous iron; the spectra are featureless except for a spectrally red slope and a break in this slope near 1.5 microns (Fig. 2.43). Excepting the break in slope, the characteristics are consistent with a number of Fe-free minerals (e.g., enstatite), but of minerals and rocks present in the lunar sample collection, anorthite and anorthosite are the only plausible candidates that can account for the detected spectral properties. The remote spectra themselves are unusual in the sense that Fe-bearing lunar anorthite and anorthosite do exhibit weak ferrous-iron absorptions near 1.25 μm that the remotely-obtained data lack. The lack of this feature in the remote spectra has been attributed to the effect of shock (Spudis et al. 1984), thus these regions have been interpreted to be composed of maskelynite. However, recent modeling (Lucey 2002) has shown that space-weathering effects even on immature anorthosite surfaces can obscure the weak band and cause the observed break in slope without any shock effects (Fig. 2.43).

Figure 2.42. Spectra of orthopyroxene (a), clinopyroxene (b), and olivine (c) as a function of Mg-number at four Clementine wavelengths. Spectra are scaled to their mean reflectance and computed from the optical constants of Lucey 1998 at a grain size of 15 microns. The range of Mg-number in each case is 50-95, and intervals of 5 are shown, with increasing symbol size indicating increasing Mg-number. Both pyroxenes show strong variations in spectral properties with change in Mg-number (or iron content) suggesting that the chemistry of the minerals may be detectable remotely, even with the sparse spectral sampling of Clementine data. In each case the reflectance also a strong function of Mg-number and iron content.

Ilmenite. Ilmenite, $FeTiO_3$, is the most abundant oxide mineral found in lunar rocks, varying between 0 and 24 vol% (Papike et al. 1982). Spectrally, ilmenite is dark and neutral,

Figure 2.43. Spectra of Orientale Massif from Spudis et al. 1984 and model spectra from Lucey 2000 with straight line continua removed. Space weathered shocked anorthosite is generally consistent with the spectrum of the Orientale anorthosite, but does not account for the break in slope found in anorthosite spectra. Models containing crystalline material reproduce the shape of the lunar spectrum better, so the presence of shocked material is not required.

but not entirely featureless, exhibiting broad absorptions centered near 500 nm and 1200 nm (Adams 1975; Burns 1985). As with feldspar, the effect of the distinctive reflectance of ilmenite is arguably more diagnostic of its presence than its spectral properties. The presence of ilmenite is inferred in mare regions on the basis of its strong optical effects on both immature and mature mare soils. Mare soils with lower TiO_2 tend to exhibit steeper and "redder" UVVIS slopes than mare soils with relatively more TiO_2, which appear spectrally bluer (Section 1.5.3).

Glass. Technically not a mineral, glass is important geologically on the Moon, both as a product of space weathering and in pyroclastic deposits. Glass shows spectral features at 1 and 2 microns due to ferrous iron and these features are broad, which indicate a lack of long-range order. Laboratory experiments show the reflectance and intensity of glass absorptions is a strong function of Fe content beyond 700 nm; shortward of 700 nm the reflectance is controlled by the sum of Fe and Ti which interact by means of a charge transfer absorption (Bell and Mao 1972; Lucey et al. 1998). Iron-bearing glass has been unambiguously detected in regional pyroclastic deposits (Gaddis et al. 1985, 2003) and in the form of impact melt glass in the dark halo around Tycho (Smrekar and Pieters 1985).

Coarse-grained metallic iron. The presence of significant amounts of iron metal in some rocks has been neglected by the remote-sensing community. However, its abundance is generally below stated performance goals for uncertainties in determining modal abundance (~10%). Experiments aimed at understanding the spectral properties of metal on asteroids show that Fe metal is moderate in reflectance relative to other minerals, and spectrally red, characteristics that may confound its detection. In some rocks it is the major carrier of Fe, so its spectrally stealthy nature may be an important source of uncertainty in Fe estimation using spectral techniques in low-Fe terrains.

10.4.2. Characterization of soil modal mineralogy: validation of remote sensing. Since the return of the first lunar samples, standard operating procedure for soil petrography has been to characterize a lunar soil by "particle counting" (e.g., Simon et al. 1981; Heiken and McKay 1974). Such analyses provide detailed information about the abundances of mineral and rock fragments, volcanic glasses, impact-produced glasses, and glass-bonded aggregates, called agglutinates. Particle counting simply involves classifying a soil fragment with a title (e.g., pyroxene, basalt, breccia, agglutinate). These particle count data, however, do not provide information on the real percentages of minerals (modes) locked in rock fragments and fused-soil particles (e.g., agglutinates).

With studies of lunar-soil formational processes (e.g., Simon et al. 1981; Fischer and Pieters 1995), particle abundances are commonly reported, and each agglutinate contains 30-80% glass that binds these soil aggregates together. However, it is the absolute abundance of individual mineral phases and the agglutinitic glass that is important for chemical considerations (Hu and Taylor 1978), as well as spectral reflectance modeling, and these data do not exist in the literature. Modal analyses of the phases in the soils also permit us to address the abundances of nanophase Fe^0-bearing agglutinitic glass, as a function of grain size.

The actual amounts of the various minerals and glasses in the soil that interact with solar radiation are the important input data for the remote compositional analysis and space-weathering studies. Modal analysis, *sensu stricto*, is defined as the volume percentage (or calculated mass %) of the mineral constituents, not the particle type. It is essential that accurate quantitative modal analyses of the components of lunar soils be obtained, particularly of the <45 μm grain sizes, where the characteristics of the individual agglutinates are lost. This is accomplished using the techniques described and illustrated by Taylor et al. (1993, 1996), Chambers et al. (1995), and Higgins et al. (1996). Accurate modal analyses were performed with X-ray digital-imaging analyses on grain mounts of lunar soils as detailed by Taylor et al. (1996). In addition to the modes, the average chemical composition of each phase is determined (e.g., different types of pyroxene, plagioclase, high-Ti volcanic glass, high-Al agglutinitic glass), as related in Taylor et al. (2000, 2001a,b).

This methodology, applied to a statistical sample of lunar soils of varying composition, is essential to validate many of the results that have begun to emerge from spectral remote sensing of the Moon. Such a sample does not yet exist, but these crucial data could be obtained from the existing lunar-sample collection.

10.4.3. Optical effects of space weathering. Even before the Apollo missions, a darkening process was thought to act on the lunar surface (Gold 1955). With the return of lunar samples, it was immediately apparent that the optical properties of lunar soils are very different from those of lunar rocks powdered in the laboratory (McCord and Johnson 1970; McCord and Adams 1973). As noted by McCord and Adams (1973) and described by Fischer and Pieters (1994), the three principal manifestations of space weathering on optical properties of lunar materials are: 1) overall reduction of reflectance; 2) general attenuation of diagnostic absorption bands; and 3) development of a red-sloped continuum. These effects increase with soil maturity (i.e., surface exposure). Cassidy and Hapke (1975) first suggested that the red slope might be due to tiny inclusions of nanophase iron ($npFe^0$). Experimental (Allen et al. 1995, 1996), observational (Noble et al. 2001), and modeling (Lucey et al. 1995; Pieters et al. 2000; Hapke 2001) results have demonstrated the systematic effects of increasing amounts of small particles of $npFe^0$ (Fig. 2.44). Experimentally-produced coatings of nanophase iron cause strong reddening and darkening of samples (Allen et al. 1995, 1996). The observations of generally similar coatings rich in nanophase iron on most soil particles (Wentworth et al. 1999) confirms the Cassidy and Hapke hypothesis that lunar reddening and darkening are caused by submicroscopic metal.

The effects of nanophase iron can be broken into four stages (Noble et al. 2001): (1) Miniscule amounts of nanophase Fe^0 result in a large curvature in visible wavelengths, while leaving the longer wavelengths largely unaffected. (2) As nanophase Fe^0 accumulates, the continuum becomes less curved and significantly redder, reaching peak redness somewhere between 0.15 and 0.35 wt% Fe^0. (3) Additional nanophase Fe^0 results in an increasingly linear continuum that starts to lose redness in the visible. (4) From the experimental and modeling results, it is clear

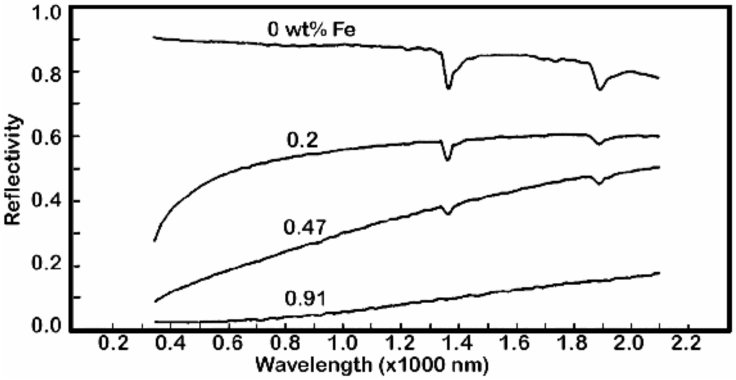

Figure 2.44. Visible-NIR reflectance spectra of silica gel particles (35-74 μm in diameter) with various amounts of nanophase Fe^0 filling pores 6 nm in diameter (Allen et al. 1996).

that if significantly more nanophase Fe^0 could be added to the soil, eventually the continuum would become dark and featureless. However, even the most mature Fe-rich <10 μm mare sample studied to date (15041) still has a significantly red slope. The natural soils achieve an equilibrium state where there is a balance between the creation and destruction of weathered rims and the influx of new material. Mature mare soils reach this equilibrium state at stage 3. Mature highland soils, having less iron available to them, reach steady state around stage 2. Soils of intermediate iron content, either inherently or due to mixing, show intermediate properties.

In addition to the demonstrated importance of nanophase iron, radiative-transfer modeling suggests that lunar soil spectral properties also require a dark neutral component to match the red slope and the low reflectance: extremely fine-grained nanophase metal does not darken sufficiently as it reddens to match both these characteristics of soils (Pieters et al. 2000; Hapke 2001). This dark component is undoubtedly the dark agglutinate glass that is so abundant in lunar soils.

Separated agglutinates are dark, but not extremely red despite being riddled with fine-grained iron (Pieters et al. 1993). However, this is consistent with observations that the nanophase metal in agglutinate glass is generally larger than coating metal (Keller and Clement 2001). Larger nanophase Fe^0 particles (those greater than ~10 nm in diameter) result in darkening of the soil (Britt and Pieters 1994; Keller et al. 1998), whereas the smaller particles (<5 nm in diameter) are largely responsible for the reddening effect. It is of note that the size range of nanophase iron particles sensed by FMR and represented in I_s/FeO measurements is much narrower than those that cause optical effects (Hapke 2001). In the optical literature the nanophase iron is commonly referred to as "submicroscopic iron" abbreviated as SMFE. The correlation between the size range sensed by FMR ($npFe^0$) and larger, but optically active sizes (SMFE), is only modest (Morris 1976, 1977; Lucey et al. 2000) so that I_s/FeO cannot even in principle be a precise predictor of optical effects of space weathering, and vice versa.

Historically, both micro-meteoroid impacts and solar-wind ion bombardment have been considered as contributors to the production of nanophase iron metal on grain surfaces that lead to the observed maturation (Keller et al. 1999; Hapke 2001). In the case of the ion bombardment, the resulting implantation of solar-wind H may act as an effective reducing agent that enhances the rate of production of nanophase metal from pre-existing silicates during micrometeoroid impacts (Taylor 1988). In addition, solar-wind ion sputtering may contribute to vapor deposition of lunar patinas, which are coatings or discolorations caused by space weathering (Wentworth et al. 1999).

It has been suggested that lunar orbital magnetic field data may afford a macroscopic means of investigating the importance of the solar-wind ion bombardment in producing the optical maturation of the lunar surface (Hood and Schubert 1980; Hood and Williams 1989). Specifically, some lunar crustal field anomalies may be sufficiently strong to shield portions of the surface from the ion bombardment (Lin et al. 1998). Ideally, by comparing the optical properties of shielded surfaces with those of unshielded surfaces, one might expect to be able to estimate the relative contributions of the ion bombardment and micrometeoroid impacts in the maturation of the surface with time.

In this regard, it is of interest that the strongest local lunar magnetic field anomalies have been found to correlate in location with unusual, curvilinear albedo markings (Hood et al. 1979, 2001). For example, Figure 2.45 shows a correlation of a magnetic anomaly over western Oceanus Procellarum with unusual albedo markings northwest of the crater Reiner (6.7 N, 54.7 W). These markings are classified by lunar geologists as the "Reiner Gamma Formation" (e.g., Schultz 1976) and are also found elsewhere on the Moon in association with strong crustal fields. The higher albedos and curvilinear shapes of these markings have been suggested to be, at least partly, a consequence of deflection of the ion bombardment by strong local magnetic fields (Hood and Schubert 1980). The sources of the magnetic anomalies are

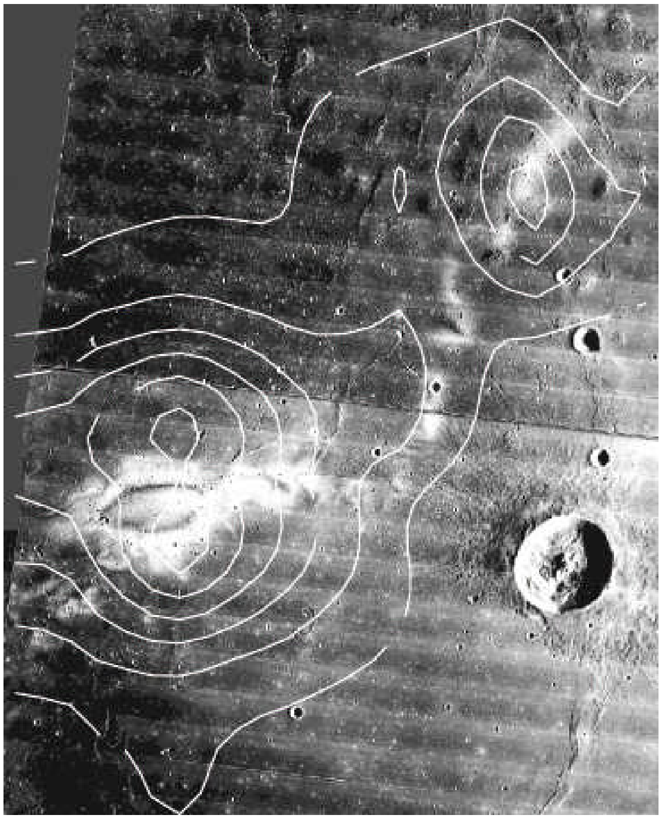

Figure 2.45. Contour map of the magnetic field magnitude over the Reiner Gamma region on western Oceanus Procellarum. The image was constructed from Lunar Prospector magnetometer data using a series of closely spaced orbit passes at altitudes ranging from 18 to 20 km. The contour interval is 3 nT and the 30-km crater Reiner is at the lower right. (after Hood et al. 2001)

proposed to be basin ejecta materials beneath the visible mare surface (Hood et al. 2001). However, there are several unresolved problems with this interpretation. First, it has not been demonstrated conclusively that lunar crustal field anomalies are sufficiently strong to completely shield portions of the surface from the solar wind. Second, the geologic origin of the Reiner Gamma Formation remains poorly understood. The alternate suggestion has been made, for example, that these albedo markings represent regions of surface scouring by a recent (<100 m.y.) cometary impact (Schultz and Srnka 1980).

In spite of remaining difficulties, the correlation of strong, local lunar magnetic-field anomalies with unusual albedo markings must be regarded as circumstantial evidence for a role of the solar-wind ion bombardment in the optical maturation of the lunar surface. Future combined orbital and surface measurements, together with returned samples from possible shielded surfaces, may therefore be very useful in establishing the precise contributions of ion and micrometeoroid bombardments to the lunar space-weathering process.

10.4.4. Grain-size effects. The presence of nanophase iron-rich coatings explains the surprising relative insensitivity of lunar soil spectra to variations in particle size. It is well known that spectra of transparent material normally brighten as particle size decreases (e.g., Adams and Filice 1967; Pieters 1983). This characteristic is not observed in particle-size separates of naturally formed lunar soils. While some increase in the albedo with decreasing particle size is observed in the near infrared along with reddening of the continuum, reflectance in the visible range (near 0.4 μm) typically has very little, if any, change as a function of particle size. Synthetic particle size separates of lunar fractions produced by crushing larger fractions of lunar soils follow the normal pattern of brightening with decreasing particle size throughout and do not duplicate the optical effects of natural particle separates of lunar soils (Pieters et al. 1993). This difference suggests that the structure of the natural surface is destroyed in the grinding process as fresh surfaces are exposed. Thus, the optical properties of the finest fractions must be due largely to surface correlated weathering products rather than simply to particle size effects.

A related property of lunar soils is that the spectral properties of bulk soil appear to be dominated by a very narrow grain size distribution. Fischer and Pieters (1996) demonstrated that the 10–20 μm and 20–45 μm sizes are optically the most similar to the bulk soil (Fig. 2.46). Larger size fractions resemble less altered material and are not representative of bulk soil optical properties (Pieters et al. 1993) whereas the <10 μm fractions appear to be highly unusual (Fischer and Pieters 1995). The dominance of the fine (but not finest) size fractions has been attributed to two factors: 1) fine particles coat larger particles, whereas, photons that enter large particles are unlikely to escape; and 2) although the <45 μm portions of lunar soils make up almost 50 wt% of the soils, this fraction constitutes over 75% of the surface area of the soil (Taylor et al. 1998). This observation has an important implication. The effect of grain size has marked effects on the spectral properties of minerals and glasses in a manner that can mimic compositional variations. The dominance of lunar soils by a narrow size fraction minimizes grain-size effects, enhancing the ability to map composition with confidence. When this spectral dominance of the fine particles begins during the evolution from rock to regolith is unstudied, so caution should be applied in assessing analyses of very immature surfaces; nevertheless, this observation supports a significant simplification in spectral analysis. A companion issue is that if spectral reflectance perceives a narrow grain size range, it is important to understand the relationship between the composition of this range and the bulk soil. In Section 9.5, it was shown that compositions of soils do change with grain size, so this effect must be borne in mind when interpreting spectral-reflectance data.

10.4.5. Mapping major mineralogy. The Clementine mission carried two multispectral imaging cameras that covered the spectral range from 0.4 to 1 μm in 5 bands (the UVVIS camera) and 1.1 to 2.7 μm in 6 bands (the NIR camera) (Fig. 2.47). The wavelengths were selected to characterize the major spectral properties of the lunar surface as understood from

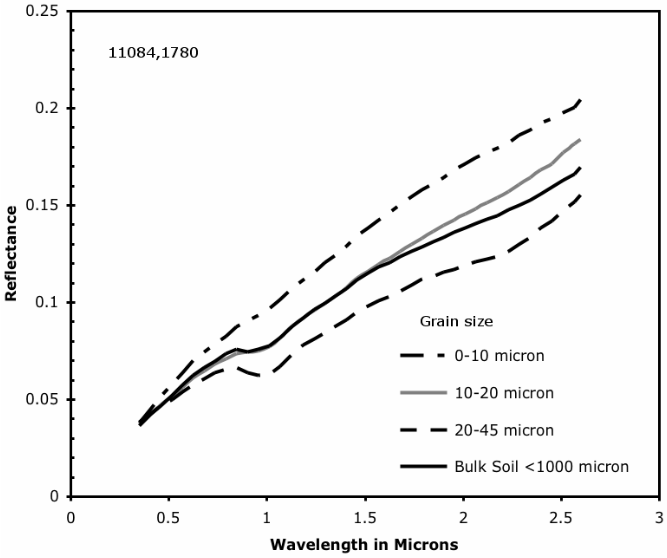

Figure 2.46. Reflectance spectra of 10084 size separates and bulk soil.

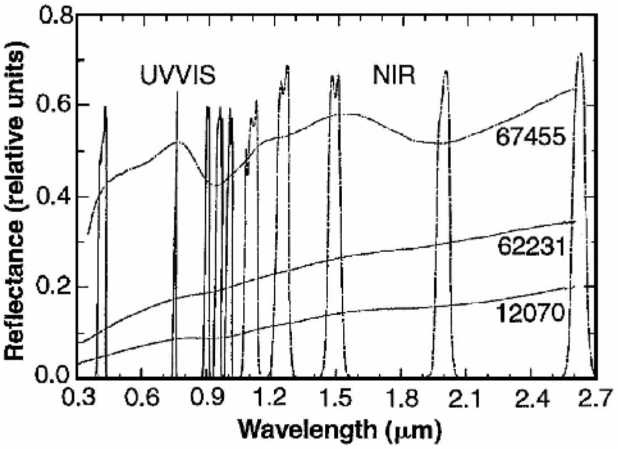

Figure 2.47. Laboratory Reflectance spectra of lunar samples superimposed on bandpasses of Clementine filters for the UVVIS and NIR cameras. Sample 67455 is a feldspathic breccia with low-calcium pyroxene, sample 62231 is a mature feldspathic soil that served as a ground-truth spectral standard for the Clementine data, and 12070 is a mature basaltic soil typical of the Apollo 12 landing site.

telescopic spectroscopy of the Moon and spectral characteristics of lunar samples. The UVVIS and NIR cameras were similar in spatial resolution and field of view and would ultimately achieve essentially 100% coverage of the lunar surface at resolutions higher than 500-m per pixel (Nozette et al. 1994; McEwen and Robinson 1997). Data from the UVVIS camera have been available for some ten years at this writing (see Plate 2.9); pilot projects have been carried out using NIR data and the global mosaic was available for analysis as of January 2004.

The spectral distinctions among lunar minerals are subtle over the wavelengths covered by the UVVIS camera, but Tompkins and Pieters (1999) developed a method to distinguish and identify spectrally dominant mineralogies from UVVIS camera data and applied this method to Clementine data of 109 globally distributed central peaks (Pieters et al. 1997, 2001;

Pieters and Tompkins 1999). They detected all the major silicates in portions of their sample of crater central peaks and in that study were able to reveal mineralogies of the lunar farside. They found evidence for both shocked and unshocked plagioclase, high- and low-Ca pyroxene, and olivine in craters on the near side where these minerals had already been detected, and they extended these discoveries to the far side. Because lunar space-weathering processes rapidly weaken spectral features, Tompkins and Pieters (1999) took care to select study areas with steep topographic slopes (clearly common in central peaks). In these locations space-weathering products are shed by mass wasting, leaving behind highly immature material that exhibits high spectral contrast, simplifying analysis. Using the high resolution of Clementine data, they were also able to illustrate spatial relationships previously unreported. Pieters and Tompkins (1999) made a detailed case study of the central peak of Tsiolkovsky.

The first publication exploiting NIR data was McEwen et al. (1994), who assembled a mosaic of an orbital swath through a portion of Aristarchus crater and surroundings, and used ground-based spectral data to calibrate the orbital swath. They found evidence for exposures of crystalline anorthite and olivine within Aristarchus crater. More extensive work with the NIR data was performed by LeMouelic et al. (1999, 2000) who further investigated Aristarchus crater and also the craters Aristillus and Kepler. They found clear evidence of variations in orthopyroxene-clinopyroxene ratio in the central peak of Aristillus and confirmed the presence of olivine on the rim and wall of Aristarchus. Their analysis showed evidence of about 25% pyroxene in the Aristarchus olivine locations and indicated that these olivine-rich locations would not have been detectable using UVVIS data alone.

In their demonstration that that mineralogy could be extracted from Clementine data, Tompkins and Pieters (1999) used a non-linear mixing model based on the work of Bruce Hapke to guide their interpretations of the spectral data. Lucey (2004) automated this analysis to produce global maps of the abundance of plagioclase, olivine, and clinopyroxene, and orthopyroxene (e.g., Fig. 2.48; see also Plates 2.9 and 2.10). Following the approach of Tompkins and Pieters, this analysis was confined to the most immature surfaces on the basis of a combination of reflectance and NIR-visible ratio, so only about 5% of the lunar surface was analyzed. Global maps of olivine, orthopyroxene, clinopyroxene, and plagioclase were produced from these sparse analyses by interpolating between the data points in a manner similar to production gridded data from sparse laser-altimeter profiles.

10.4.6. Mapping titanium. Prior to the global remote-sensing missions, many groups studied the relationship between lunar color in the ultra-violet and visible (UVVIS) and Ti content. Full-disk color photography was processed to reveal strong color differences on the lunar disk (McCord 1969; McCord and Johnson 1969; Pieters and McCord 1976; Whitaker 1972). These images show strong variations in color between the UV and visible, especially in the mare. Whitaker (1972) cited R. Strom as being the first to suggest that the strong color variations were due to the principal compositional variable in mare basalt samples, namely Ti. Shortly thereafter, Charette et al. (1974) showed that Ti content is correlated with telescopic measurements of UVVIS ratio in mature (agglutinate-rich) basaltic regolith, whereby samples with high TiO_2 concentrations (e.g., derived from Mare Tranquillitatis) exhibit relatively flatter and "bluer" UVVIS slopes than basalts with lower concentrations of TiO_2 (e.g., central Mare Serenitatis), which are spectrally redder. The Charette Relation provided quantitative comparisons of TiO_2 for sites in the near-side mare for the first time.

Failure to predict the low-Ti content of Luna 24 basalts returned from Mare Crisium indicated that a more complex relation exists between the two parameters. Subsequent revisions to the Charette Relation were made to increase the predictability of TiO_2 concentrations by improving spectral contrast (Johnson et al. 1991, 1977), and spatial resolution (Melendrez et al. 1994).

New algorithms for TiO_2 mapping were developed using Clementine and Galileo multispectral data. These algorithms included the ability to estimate TiO_2 for highland and

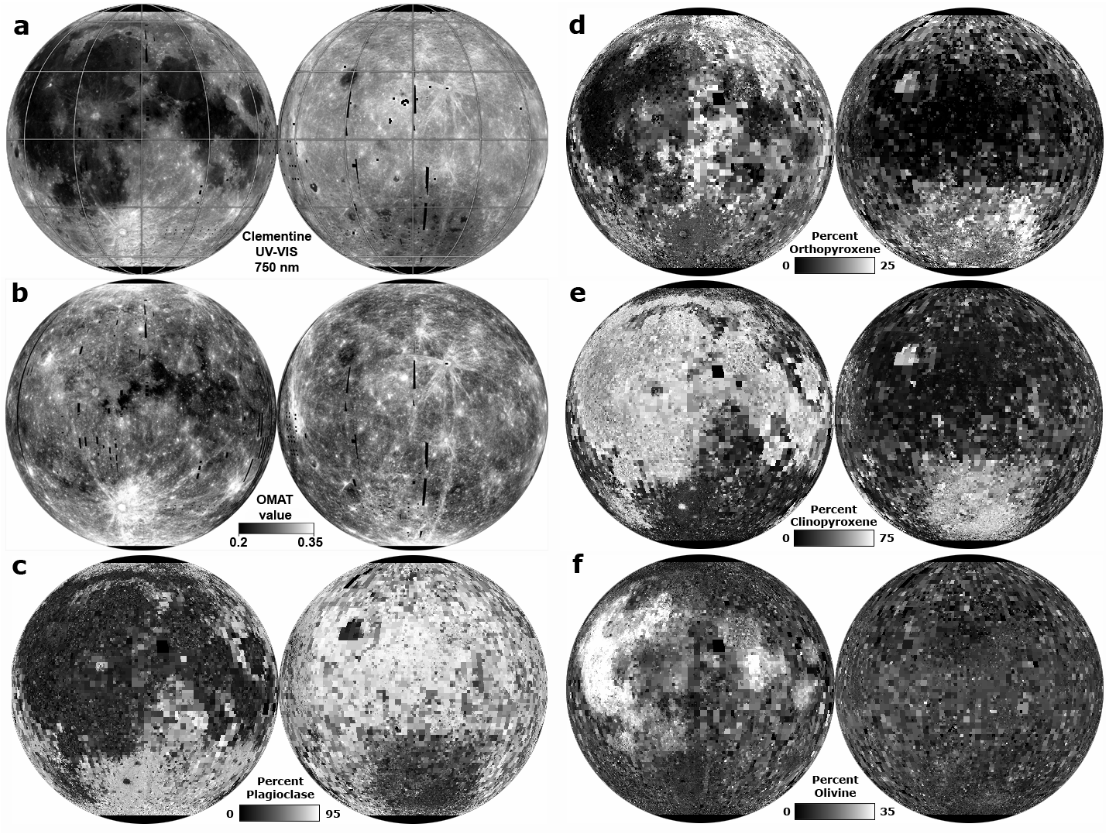

Figure 2.48 Global mineral maps and optical maturity derived from Clementine multispectral data in orthographic projection, with near side on left and far side on right of each pair. (a) Clementine 750 nm filter image with 30 degree latitude-longitude grid for reference; (b) optical maturity; (c) plagioclase; (d) orthopyroxene (low-Ca), (e) clinopyroxene (high-Ca); and (f) olivine. The mineral maps were made from 4-component nonlinear mixing model analysis of each immature spectrum in the global Clementine data set at 1 km spatial resolution (Lucey 2002). The four components are plagioclase, orthopyroxene, clinopyroxene and olivine. The maturity cutoff was based on the OMAT parameter (see Plates 2.9 and 2.10) with a value of 0.3 or greater. Only about 5% of the lunar surface is this optically immature, so the analyzed data feature large spatial gaps, especially in the highlands where immature exposures are infrequent. The data were then interpolated using algorithm similar to kriging. An artifact of the interpolation is that mare compositions tend to be over-reported, even in the highlands, as these more recent lava flows can provide abundant fresh material. The high abundance of clinopyroxene observed in South Pole-Aitken is likely due to the presence of frequent small mare ponds and cryptomare.

immature mare surfaces (Blewett et al. 1997; Lucey et al. 1998, 2000). Results using these algorithms support that the apparent gap between high- and low-Ti basalt samples is observed at the remote-sensing level for all of the Apollo and Luna landing sites (Gillis et al. 2003) (Fig 2.49). On a global scale, however, a continuum of TiO_2 concentrations exist for mare basalt regions (Giguere et al. 2000; Gillis et al. 2003).

Ti maps derived from multispectral imaging, however, have been shown to exhibit low precision and accuracy, on the order of 5 wt% in Ti, using sample analyses (Gillis et al. 2003) and Lunar Prospector neutron-spectrometer estimates of TiO_2 (Elphic et al. 1998, 2002). A complex relation between the UV/VIS ratio and TiO_2 was further shown to exist by comparing Lunar Prospector neutron TiO_2 concentrations and the UV/VIS ratio for mare regions of uniform color (Gillis et al. 2005). Data from these regions of interest reveal an apparent sigmoidal trend in the UV/VIS-TiO_2 relationship (Fig. 2.50) in which mare areas with <1.5 wt% TiO_2 trend along a shallower slope than basalts with higher TiO_2 contents. Also, the high-Ti trend is redder than predicted on the basis of the low-Ti trend alone by inferring that the UV/VIS values for basalts of the lower trend would extend linearly to higher values if they were to contain >3 wt% TiO_2.

The sigmoidal relation is notably different than the single curvilinear trend of Charette (1974), but reminiscent of large variation in color at low-Ti values (<2 wt%) that indicate higher uncertainty at low-Ti, as previous workers have noted Pieters (1993). In contrast to previous observations with sparser data, it appears that color values for high-Ti soils (>5 wt%) are also quite variable and that the lowest scatter in color is at intermediate Ti values (2-4 wt%).

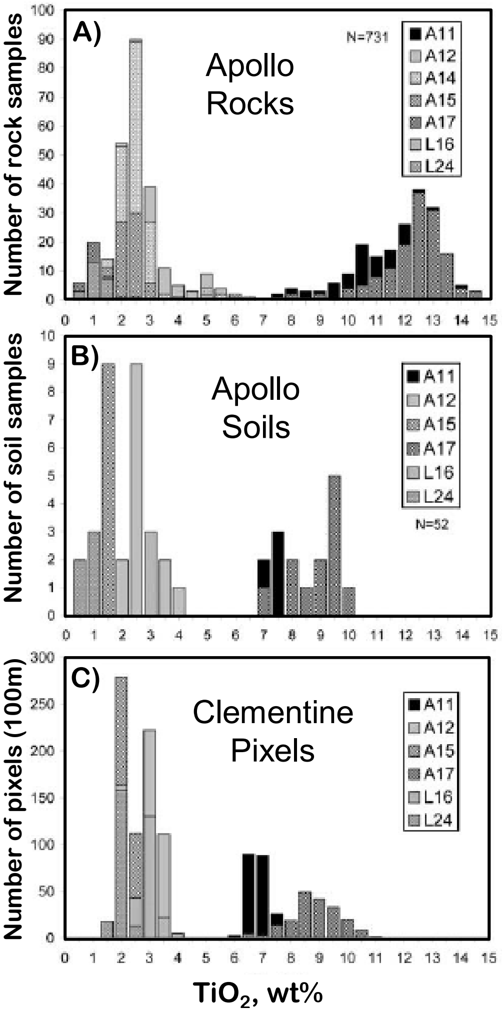

Figure 2.49. A) Histogram of TiO_2 concentrations for Apollo and Luna mare basalt samples. Note the "gap" in TiO_2 concentration between 5.5 and 9 wt% TiO_2: data from (BVSP 1981; Papike et al. 1998). B) Histogram of TiO_2 concentrations determined for representative basaltic soils from individual Apollo (A) and Luna (L) sampling sites. C) Frequency of Clementine UVVIS-based TiO_2 estimates determine using the modified regression for a 20×20 pixel image (100 m/pixel) that contains the respective landing site.

Focusing on predictability yields new insights regarding the utility of the spectral data. The utility of the multispectral data is in the prediction of Ti from color, rather than the spectroscopically interesting color effects at a given Ti content. At the lowest color values, (UV/VIS <0.58)

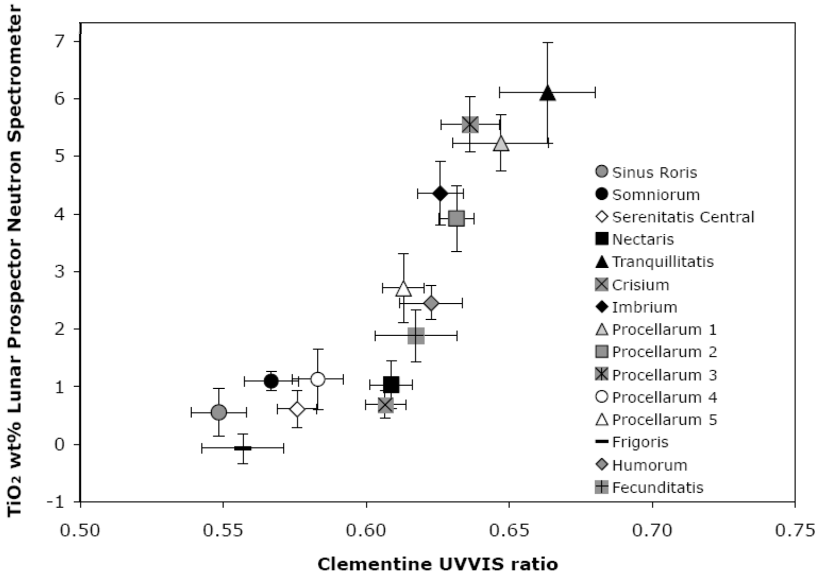

Figure 2.50. Average TiO_2 concentrations (Lunar Prospector neutron spectrometer) and UVVIS ratio data (Clementine) for 15 regions of interest. These data reveal an apparent non-linear, sigmoidal shape to the UVVIS-TiO_2 correlation. Regions of interest were selected on the basis of uniform color and composition in an effort to reduce error as a result of physical and spectral mixing. Error bars represent 1σ deviation.

all Ti values are <2 wt% (Fig. 2.50), so very low color values do indicate low Ti, however, all low Ti surfaces do not have low color values. For instance, UV/VIS ratios as high as 0.64 exist for some low-Ti basalts, <2 wt% TiO_2. Similarly, at high color values (UV/VIS >0.66) all Ti values are uniformly high, >5 wt%, but again high-Ti surfaces exist with lower color values. At intermediate UV/VIS ratios, Ti varies across nearly its entire range of values (Fig. 2.50). Figure 2.51 maps the distribution of surfaces with varying confidence. High confidence is assigned to UV/VIS values <0.58 or >0.66. On the basis of these arguments, one might conclude that no useful TiO_2 concentrations can be obtained where UVVIS values occur between 0.58 and 0.66. In this UV/VIS range, TiO_2 can vary unpredictably from 0 to 7.4 wt%, with a mean of 2.2 and a standard deviation of ±1.6. Perhaps UVVIS color can place a lower limit on the distribution of high- and low-Ti basalts, but it may not capture all basalts of these compositions, and little can be said with confidence about the basalts that have intermediate color values, which cover a vast majority of the maria (75%). This large area of uncertainty is in agreement with the finding of Gillis et al. (2003) who showed that TiO_2 concentrations for over two-thirds of maria were over- or underestimated by algorithms of Lucey et al. (2000). This result would affect the conclusion of Giguere et al. (2000) that intermediate Ti basalts (4.5–7.5 wt% TiO_2) are common. Basalts with intermediate color, previously interpreted as intermediate Ti, are now recognized to have poorly constrained Ti contents. The absolute mode of TiO_2 concentrations and/or the width of the mode might change, but it is unlikely that there is a bimodal distribution for basalt Ti contents globally (Fig. 2.52) because the Lunar Prospector neutron and gamma-ray spectrometer data (Elphic et al. 2002; Prettyman et al. 2002) do not exhibit a bimodal distribution.

Two qualitative models may explain the relationship between UVVIS color and TiO_2. One model, summarized by Pieters (1993), suggests that predictability in high Ti terrains should be good because the low albedo of soil components allows surface scattering to dominate; thus masking the optical properties of components. At low Ti contents, however, the complexity

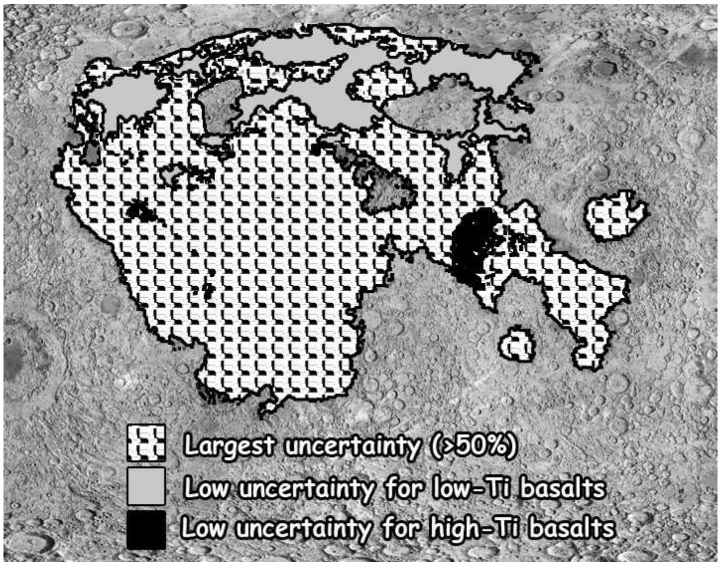

Figure 2.51. The distribution of TiO_2 uncertainty values based on the prediction of TiO_2 from color.

associated with mineralogy is increasingly perceived, breaking down the UVVIS-TiO_2 correlation.

Rava and Hapke (1987) emphasized the role of spectrally neutral opaques in controlling the Ti-color relationship. Ilmenite is dark and spectrally neutral relative to the spectrally red mature lunar mare soils, and must contribute to lunar UVVIS color as its volume proportion varies from essentially zero to as much as 25% (Section 4.2.1). Other oxides such as chromite, ulvöspinel, and armalcolite, however, are spectrally similar to ilmenite and thus their presence contributes to deviations from the UVVIS-TiO_2 correlation. In addition, Ti partitioned into non-opaque silicates (e.g., pyroxene) would also contribute to deviations from the correlation.

Recent results on the composition of agglutinate glasses (Taylor et al. 2001) show that Ti is only weakly enriched in the glasses of high-Ti basalts, reducing the effectiveness of Ti-Fe charge transfer absorptions in lowering reflectance of high-Ti soils. This finding suggests that opaques are more important than was previously assumed. The Fe content of silicate minerals and glasses in basaltic soils has a strong control on the visible reflectance that can also contribute to variations in the UVVIS ratio (Gillis et al. 2005).

Mare units show strong and consistent variations in UVVIS color that can be used to map geologic units; however, to what extent the variations in any individual mare deposit depend on Ti or other compositional parameter is not known. Clementine 2.7-µm data may help improve the accuracy of mapping TiO_2 because it correlates well with the UVVIS ratio, but the 2.7-µm data show a greater range in values with fewer effects from maturity than the UVVIS ratio and are not affected by Fe-Ti charge transfer as in the case of the UVVIS (Gillis et al. 2005). A full understanding the relationship between Ti and lunar color can be addressed by a focused study of lunar soils and a quantitative understanding of the optical properties of their components, but such a study has not yet been done.

10.4.7. Mapping iron. Efforts to map Fe using multispectral methods prior to Clementine were limited, but suggested that an algorithm might be derived analogous to Ti mapping algorithms (Charette et al. 1977; Fischer and Pieters 1994). Iron dominates the reflectance

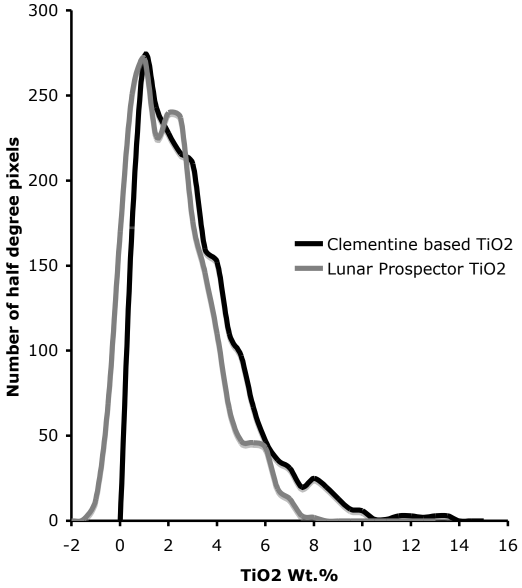

Figure 2.52. Comparison of Clementine derived TiO_2 and Lunar Prospector neutron spectrometer TiO_2 results. Differences between the two histograms highlight the uncertainty in TiO_2 distribution predicted from UVVIS color data.

properties of the Moon in three ways: (1) the reflectance and absorption properties of mafic silicates and glass are proportional to Fe content; (2) the major and locally abundant opaque mineral phase, ilmenite, is Fe rich; and (3) nanophase Fe, the principal actor in space-weathering optical effects, strongly effects the lunar reflectance and is proportional to Fe content. In rocks and minerals, increasing Fe makes them darker and if the carrier of Fe is a silicate, the absorption features near 1 and 2 µm are strong, leading to a decreased ratio of near-IR to visible reflectance (Burns 1993). Nanophase Fe imparts a different behavior. Reflectance decreases with increasing nanophase Fe (and hence maturity), but the ratio of near-IR to visible reflectance increases (Fischer and Pieters 1994). A series of algorithms exploiting these observations were developed for predicting Fe contents from visible reflectance and near-IR to visible ratio of lunar soils. Correlations between derived Fe-sensitive spectral parameters and known FeO contents were shown to be high in several studies, with few outliers, in contrast to similar studies of Ti mapping (Lucey et al. 1995, 1998, 2000; Blewett et al. 1997; Lawrence et al. 2002; Gillis et al. 2004).

As with mapping of Ti, there are mineralogical effects that contaminate the Fe estimates (Staid and Pieters 2000). The spectral properties of silicates alter at different rates as a function of Fe content (Lawrence et al. 2002). Comparison of Lunar Prospector Fe abundances to multispectral Fe shows three major regional anomalies: Western Oceanus Procellarum, South Pole-Aitken Basin, and Mare Tranquillitatis. Western Procellarum is now thought to be olivine-rich (Staid and Pieters 2001). The absorbance of olivine is weaker than pyroxene at Clementine wavelengths for equivalent Fe (Lawrence et al. 2002). This leads to systematic underestimates of the Fe content at high olivine contents using calibration curves dominated by soils rich in pyroxene. In contrast to the FeO overestimate of the olivine-rich mare, the South Pole-Aitken (and Apollo 14) FeO abundances are overestimated. Current global mineral maps (Section 10.4.5) suggest that South Pole-Aitken basin is anomalously low in olivine relative to the rest of the Moon, which seems to carry a background olivine component of a few weight percent. If this is correct, the absence of regional olivine explains the systematic overestimate of Fe by spectral reflectance methods at South Pole-Aitken basin. Multispectral estimates of Fe content at Mare Tranquillitatis are anomalously high relative to Lunar Prospector by a few weight percent, indicating the effect of opaque ilmenite on the Fe estimates. In practice, few mare surfaces show high Ti or high olivine contents, so for mare deposits low in these components, Fe estimates are probably valid to the degree the calibration curves suggest, namely 1–2 wt% (Lucey et al. 1995). On the basis of the measured error of Tranquillitatis relative to LP-GRS Fe, even moderate Ti basalts would cause only a 1–2 wt% systematic underestimate if the error is proportional to opaque mineral content. In the highlands, no opaque rich deposits are known, and olivine contents can be estimated, suggesting that either a correction could be developed, or problematic areas could be avoided.

Much of the value of the multispectral Fe (and Ti) maps is in their ability to be applied at high spatial resolution not achievable using geochemical (e.g., GRS, XRF) methods. However, for much of the Clementine data, Fe estimates based on the method introduced by Lucey et al. (1995) are compromised by variations of shading due to variable topography observed under oblique lighting conditions, conditions that hold for most of the Clementine data set (e.g., Robinson and Jolliff 2002). Le Mouélic et al. (2000) developed a method for calculating the Fe in silicates based on the correlation of Fe with the 1 μm band depth and the visible-NIR continuum slope. Because the method uses only spectral ratios, it eliminates the influence of topography. It is likely that the Le Mouelic method shares the mineralogic overprints possessed by the Lucey et al. (1995) method, but these have yet to be evaluated.

10.4.8. Mapping maturity. Because the optical effects of space weathering and Fe variations are inversely correlated, these components can be separated. Fischer and Pieters (1996) showed that I_s/FeO correlates with the 1-μm band depth and could be estimated with multispectral images. Lucey et al. (1996) presented lunar soil and remote measurements of optical maturity and showed that compositional effects (especially mare vs. highland) can be largely suppressed, leaving optical maturity as the principal parameter (Fig. 2.48b; Plate 2.9). The range of values in this optical-maturity parameter is almost ten times the residual compositional effects that can be observed in the background, such as variations in the mare and among pyroclastic deposits. Grier et al. (2001) used this parameter to study age relationship among large Copernican and Eratosthenian craters. Like Fe estimates, this method is subject to contamination by topographic shading at high phase angles, but Le Mouélic et al. (2002) also derived a method using NIR data that does not suffer from these effects.

10.4.9. Hydrated minerals. The returned (Apollo) samples are extremely dry and in fact no indigenous lunar water has been unambiguously identified in the sample collection. However, the Moon has been impacted by comets regularly over its history so it is possible that evidence of interaction of the Moon with cometary water might be preserved. Considerable attention has been paid to water which might have accumulated in lunar cold traps (see Chapter 6) but evidence of water might be present elsewhere on the Moon.

Telescopic and space-based searches for evidence of water or hydrated minerals have been conducted. Roush and Lucey (1988) searched for evidence of a water-of-hydration band at 3 μm at the Reiner Gamma Formation, a region proposed to be the result of interaction of a comet with the lunar surface. The Near Infrared Mapping Spectrometer on Galileo obtained spectra of a portion of the Moon through the 3-μm region as well and detected no evidence of a 3-micron absorption band. Vilas et al. (1999) suggested that anomalous features in Galileo multispectral imaging of portions of the Moon in the lunar south showed evidence of phyllosilicates (Galileo used somewhat different bands than Clementine). Finally, McConnochie et al. (2002) used Clementine NIR data obtained in polar regions with no direct illumination but indirectly illuminated by reflections off crater walls to search for evidence of a 2.0-μm band, with no reported detection.

The Clementine NIR data are actually well suited to a search for water as the 2.7-micron band is centered on the strongest portion of the hydroxyl absorption. Any searches using these data must cope with the very significant thermal-emission component inherent at 2.6 and 2.7 microns, but while this component will tend to reduce spectral contrast, reflected solar radiation still dominates, so a search of the data for spectral anomalies consistent with water or other hydroxyl-bearing phase could be useful. A preliminary survey of the data at 500-m resolution between latitudes of 70°S and 70°N revealed no obvious anomalies in 2.7-μm reflectance, or ratios of 2.7 μm to 2.6 or 2.0 μm that might have indicated the presence of hydrated minerals. For example, there is no population of craters exhibiting hydration anomalies that might indicate the impacts of a cometary population, nor did inspection of the Reiner Gamma formation of other lunar swirls exhibit 2.7-μm anomalies. This survey probably was not sensitive to anomalies less than 5-10% in depth owing to the ubiquitous effect of maturity near small craters. More sensitive methods or investigations in the polar regions might bear more fruit (Pieters et al. 1988; Gillis and Lucey 2004).

10.5. Spectral remote sensing in the thermal IR

Spectroscopy in the region of thermal emission (7–14 μm) has the potential to make important contributions to lunar science (Nash et al. 1993). This technique is sensitive to silicate polymerization so in principal it should be more sensitive to the presence of feldspar than near-IR spectroscopy, and also to variations in feldspar chemistry, as well as enable searches for quartz that might be present in outcrop in rare locations on the Moon. There have been a handful of telescopic observations of the Moon in the thermal region (e.g., Sprague et al. 1992). Although none of these observations have contributed substantially to understanding the composition of the lunar surface, they are valuable in determining performance requirements for future experiments. Laboratory measurements of lunar soils by Salisbury et al. (1997) showed that spectral variations among lunar soils in the thermal IR are extremely subtle, and a successful telescopic experiment will likely require extremely high signal to noise ratios, on the order of 1000 or greater. Because of the extreme sensitivity of this technique to grain size, a possible future application might be to detect the presence of bare rock for other types of remote sensing to exploit.

10.6. Remote sensing of lunar thermal properties

10.6.1. Clementine LWIR. The long-wave infrared (LWIR) camera on Clementine measured lunar surface emission between 8 and 9.5 μm. The LWIR spatial resolution ranged from 200 m/pixel near the poles to 55 m/pixel at the equator. Contiguous pole-to-pole imaging strips were obtained with ~10% overlap between adjacent frames; however, significant longitudinal gaps exist between successive orbital passes. The LWIR local lunar noontime thermal-emission observations are unique in many ways. The high resolution of the LWIR images surpasses all other lunar temperature observations and provides substantial information on the spatial variations in temperature. The LWIR nadir-looking observations offer a unique thermal emission perspective on the lunar surface, and the measurements allow observations of variations with local incidence and emission angles that are not available to Earth-based observers. The global nature of the measurements, including the lunar farside, is unprecedented.

The LWIR global dataset demonstrates that the Lambertian temperature model of $\cos^{1/4}(i)$, where i is the solar incidence angle, is a fair approximation for nadir-looking temperatures, rather than the $\cos^{1/6}(i)$ behavior observed for ground-based measurements of the full Moon where both incidence and emission angle vary (Lawson et al. 2000). Deviations from the Lambertian model are likely due to surface roughness effects.

LWIR temperature information can also be combined with other data sets to investigate lunar surface thermophysical properties. Albedo, large-scale surface roughness, and small-scale (subresolution) surface roughness each may affect the lunar surface temperature. An ideal way to explore the effects of these properties is to compare the reflectance and the emission of an area, since they are closely connected. Each thermophysical property will result in a different relationship between reflectance and temperature, and investigating the trends as they vary with terrain and phase angle can help to determine which processes dominate the lunar surface response under varying conditions.

The lunar surface response in different highland and mare locations has been explored as a function of varying phase angle (Lawson and Jakosky 2001). An example can be seen in the Aristarchus Plateau images of Figure 2.53. The continuous LWIR mosaic is bounded

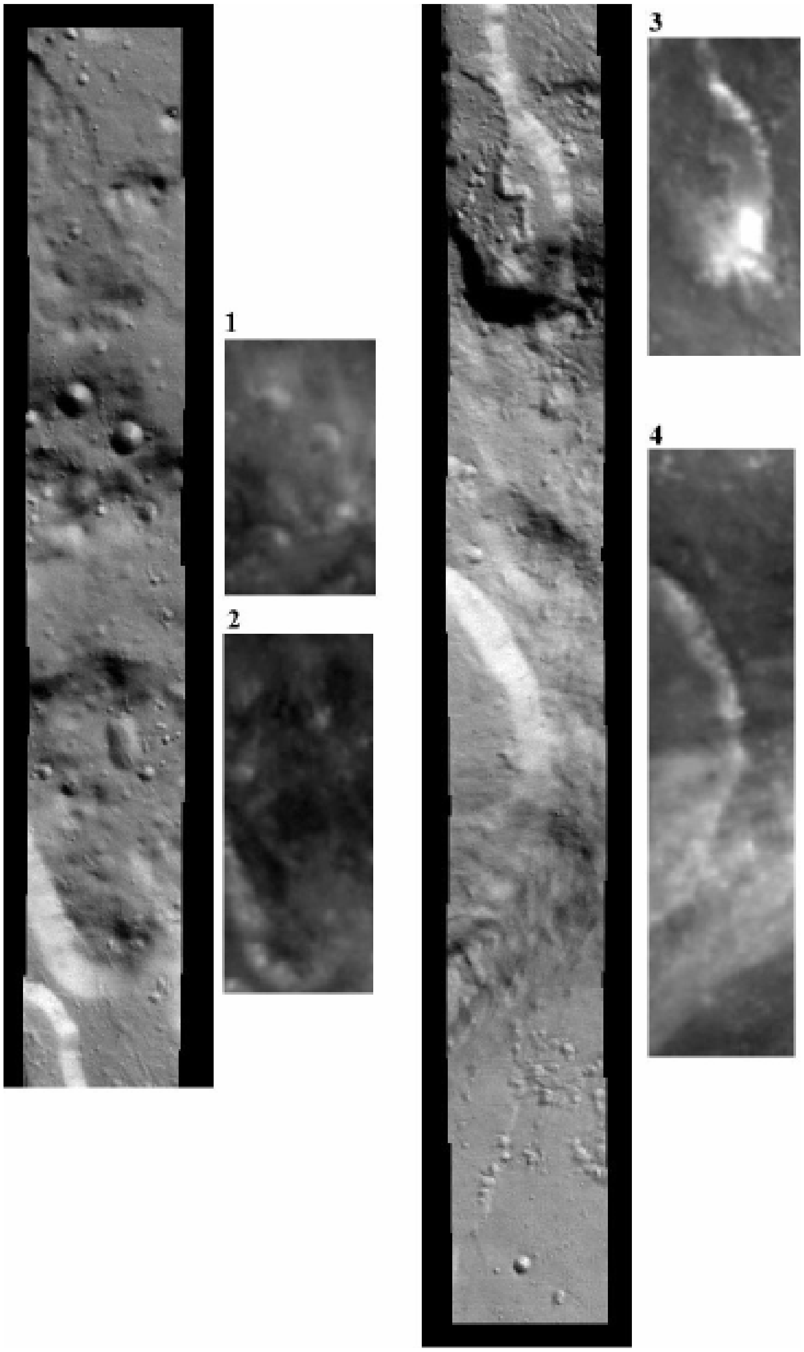

Figure 2.53. Aristarchus Plateau LWIR mosaic (strips) and corresponding UVVIS images (panels) (taken from Lawson and Jakosky 2001). Latitude range: 22°–28°N, longitude: 310.8°E.LWIR resolution: 100 m; LWIR temp range: 320-380 K. Numbered parts correspond to sections discussed in the text.

by black pixels and divided into two portions; the northernmost point of the mosaic is at the top of the left strip, and the southernmost point is at the bottom of the right strip. To the right of each LWIR mosaic strip are UVVIS 750-nm images of the same area of the lunar surface; the brightness stretch across the four UVVIS panels is constant. The Aristarchus Plateau is a 2-km elevated crustal block approximately 170 × 200 km which slopes downward to the north-northwest and is surrounded by the younger mare basalts of Oceanus Procellarum. The 42-km-diameter impact crater Aristarchus lies on the plateau's southwestern edge, and the older, partially embayed 35-km-diameter crater Herodotus lies just west of Aristarchus. The plateau contains the densest concentration of lunar sinuous rilles, most of which originate from cobra-head craters. A dark-mantle deposit, with the lowest reflectivity of any large lunar area blankets the entire plateau (Wilhelms 1987; McEwen et al. 1994; Weitz et al. 1998).

At very low phase angles the temperature and reflectance response is primarily governed by the variation in single-scattering albedo regardless of the presence of topography. As the phase angle increases, the influence of surface roughness grows. Finally, at moderate to high phase angles the effect of surface roughness dominates. In the absence of large-scale topography, the lunar surface temperature and reflectance response at all phase angles is governed by the variation in single-scattering albedo. LWIR-measured temperature variations yield local topographic information at high incidence angles that is unavailable via the reflectance, whereas UVVIS-measured reflectance variations yield local topographic information at low incidence angles that is unavailable via the temperature. The largest factors affecting the lunar surface daytime temperatures are the albedo and the incidence angle of solar insolation.

10.6.2. Neutron spectrometer measurements of subsurface temperature. The flux of thermal neutrons that leak out from planets depend mostly on surface composition, but also on surface temperature. The temperature dependence reflects the fact that in equilibrium, the rate of moderating the neutron flux from the epithermal range to the thermal range must exactly balance the rate of neutron absorption by elements in the soil. Because most absorption cross sections in the thermal energy range depend inversely on the neutron speed, the loss of neutron flux (density times speed) to absorption depends only on the neutron number density. This density should not, therefore, depend on temperature. Instead, the flux of neutrons in the thermal energy range should increase with increasing temperature.

With numerical simulations of this effect using the Monte Carlo Neutral Particle transport code MCNPX, Little et al. (2003) showed that the effect is most prominent in materials having a low macroscopic absorption cross section (such as the feldspathic lunar highlands) because the thermal-neutron population is relatively largest for that composition. On the other hand, the effect is insignificant for material having a large macroscopic cross section (such as the mare basalts). They also showed that the depth being sampled by leakage thermal-neutron fluxes was centered at about 30 g cm^{-2} below the surface. For a density of 2 g cm^{-2}, this depth is 15 cm. Because most models of the thermal structure of the lunar surface (e.g., Vasavada et al. 1999) indicate that this depth is below the diurnal thermal wave, the temperature of such a layer should depend only on latitude (λ). Indeed, Figure 2.54 shows that a preliminary comparison of the latitudinal variation of the flux of thermal neutrons above the feldspathic highlands were shown to be consistent with a $\cos^{1/4}(\lambda)$ temperature law (Little et al. 2003) as was determined using the Clementine LWIR data (Lawson and Jakosky 2001). The net effect on the thermal neutron flux from equator to pole amounted to about 13.5%.

10.6.3. Infrared night-time and eclipse observations of the Moon. Ground-based telescopic infrared-scanner measurements of the Moon during eclipse, normalized to initial temperature and time of observation, show numerous thermal anomalies and that these anomalies often correlate with stratigraphic ages of craters and crater count ages of individual maria (Shorthill and Saari 1965; Fudali 1966; Saari et al. 1966). The Apollo 17 Infrared Scanning Radiometer collected high-quality temperature data for portions of both the night and

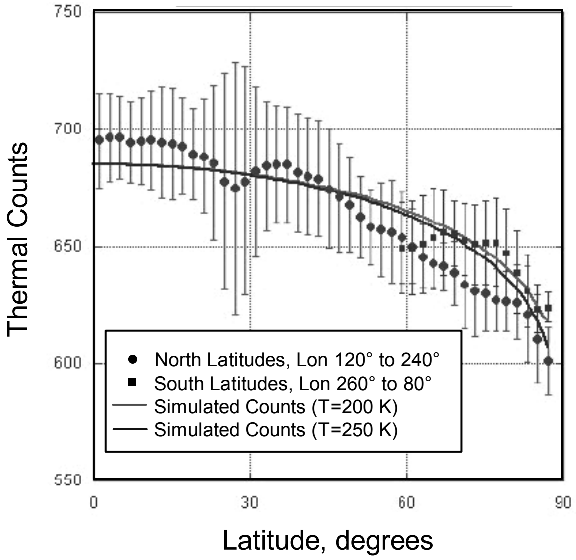

Figure 2.54. Latitude dependence of lunar surface temperature measured with thermal neutrons. The points show measured thermal neutron count rate in feldspathic highlands regions either for northern latitudes (●) or southern latitudes (■). The solid line is a $\cos^{1/4}(\lambda)$ temperature dependence for $T = 250$ K at the equator.

day side of the Moon (Mendell and Low 1975). These data showed that nighttime temperature anomalies were observed and that they often correlated with geologic features. This experiment showed that areas with high thermal inertia (indicated by high nighttime temperatures) also had higher frequencies of exposed rock. Mendell (1976) suggested, that with an appropriate dose of geologic common sense, these or similar data might be used for age dating.

Recent observations of the southern near side of the Moon in partial eclipse in the thermal infrared at high resolution show results similar in spatial resolution and character to the Apollo 17 radiometer results, but for a different portion of the Moon (Wilcox et al. 2005). As reported by Mendell and Low (1975), mare surfaces are dotted with small anomalies, small impact craters having excavated cobble-rich material from thin mare regoliths. Highland regolith almost entirely lacks anomalies owing to small craters suggesting the highland regolith is free of blocks to depths on the order of 100 m. These data, coupled with radar measurements at a range of wavelengths, should allow detailed understanding of the regolith structure at the meter scale.

10.7. Radar remote sensing of the regolith

Earth-based radar measurements, acquired using the delay-Doppler technique (Pettengill et al. 1974), provide synoptic views of the lunar surface over a range of wavelengths from 3.8 cm to 7.5 m (e.g., Zisk et al. 1974; Thompson 1987; Thompson 1978). These maps have been used to study regional pyroclastic deposits (Zisk et al. 1977), mare titanium abundance (Schaber et al. 1975; Campbell et al. 1997), and variations in large-scale regolith properties (Thompson et al. 1979). Recent work has improved considerably the effective spatial resolution of these observations through the use of focused processing (Stacy et al. 1997; Campbell et al. 2003), and permitted derivation of detailed topography using interferometric techniques (Margot et al. 2000).

The radar echo from the Moon is modulated by a number of factors: surface topography on scales of several meters to many kilometers, the abundance of wavelength-scale rocky debris on the surface or suspended within the fine-grained dust, and the bulk microwave loss properties of the regolith. Longer radar wavelengths are sensitive to the abundance of larger-diameter rocks, and can penetrate to greater depth for any particular value of the regolith loss factor. Attenuation of the radar signals with depth is controlled primarily by ilmenite in basaltic or basalt-contaminated deposits. Losses in highland-dominated materials are typically low, and may be controlled by a number of possible minerals.

Radar data can reveal properties of the regolith deeper than apparent to visible imaging. Ghent et al. (2005) found that virtually all large, young craters on the Moon have extensive "haloes" of low 70-cm radar return concentric to rugged, radar-bright materials of the continuous ejecta blanket (Fig. 2.55). It is most likely that these haloes are due to a lower abundance of 10-cm to meter-scale rocks on and within the regolith than is typical of "well-gardened" highlands and maria across the Moon. In effect, the impact process reduces the block abundance of a large surrounding region. This deep view also allows direct imaging buried mare deposits (cryptomare), for example in the region west of Oceanus Procellarum (Campbell and Hawke 2005).

Ongoing work is opening new opportunities for Earth-based radar studies of the Moon. By using focused processing (similar to synthetic aperture radar), high spatial resolution can be achieved over a large illuminated area (Stacy et al. 1997; Campbell and Hawke 2005). At 12.6-cm radar wavelength, spatial resolution as fine as 20 meters per pixel has been achieved using these techniques. Applications include studies of the polar shadowed terrain, detailed analysis of pyroclastic deposits that may provide useful resources for eventual exploitation, and improved understanding of regional differences in regolith properties linked with basin ejecta patterns.

10.8. Hydrogen and the lunar poles

10.8.1. Importance of hydrogen. The elemental composition of planetary bodies provides a very important diagnostic of the processes that shaped their formation and evolution. The giant molecular cloud from which the Sun and its planetary system formed was very rich in H. It is generally thought that 90% by number was H, about 8% was He, and all of the heavier elements comprised the remaining 2%. Although the Sun contains all elements in these proportions, the various planetary bodies of the solar system sustained considerable chemical fractionation that depended on the location within the solar nebula where they coalesced and the mix of mechanisms that guided their evolution. The H content of the terrestrial planets is generally low compared to that of the Sun, but increases gradually with increasing heliocentric distance. Beyond Mars, the abundance of H takes a large jump in all of the gas-rich giant planets and comets that populate the outer solar system (see also Chapter 7).

An early result of the Apollo program was that the composition of the Moon was deficient in all volatile elements relative to the Earth, especially so in H. Whereas most dry basalts on

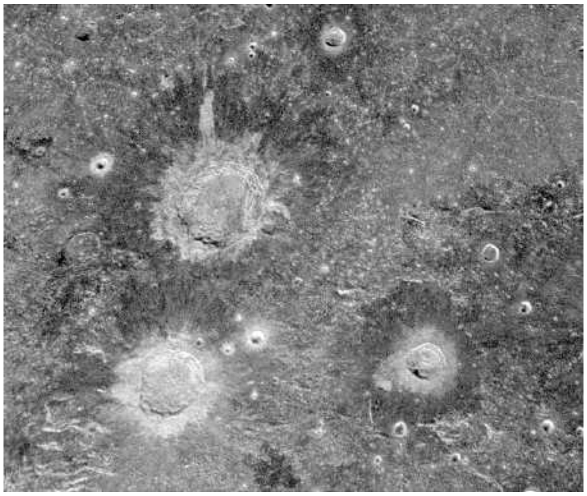

Figure 2.55. 70-cm wavelength radar image, collected using the Arecibo and Greenbank radio telescopes, of three large lunar craters (Aristoteles, at upper left, is 87 km diameter). The brightness variations reflect differences in decimeter-scale rocks on the surface or suspended within the upper 3-10 m of the regolith. Many large, young lunar craters have associated "haloes" of low 70-cm radar return that indicate rock-poor ejecta deposits outside rock-rich continuous ejecta.

Earth contain the equivalent of 1% water by weight, similar rocks on the Moon contain the equivalent of about 0.045% water. In addition, there are no reservoirs of water on the Moon such as is contained in the terrestrial oceans, glaciers, and polar ice packs. This striking difference has been used to infer that the Moon formed, or evolved through a single or series of catastrophic heating events in which most of the Moon's inventory of volatiles was either stripped or evaporated away. Hydrogen, being the lightest volatile, is thought to have been completely lost during this period. Hydrogen that has been detected within lunar samples from the present lunar surface is thought to have been implanted in the outer amorphous layers of regolith grains by the solar wind (Section 8.3).

Speculation regarding reservoirs of H that might exist on the present-day surface of the Moon is centered on the very cold regions near both lunar poles that form the floors of craters permanently shaded from the Sun (Watson et al. 1961; Arnold 1979). This H is thought to have been delivered in the form of water molecules through impacts of comets, meteoroids, and dust particles with the Moon. After delivery, the water molecules slowly migrated to the poles while undergoing loss to interplanetary space due to ionization by solar UV and pickup by the solar wind. Once at polar latitudes, the residual component of water molecules becomes trapped by the cold surfaces of the permanently-shaded polar craters (Butler et al. 1993; Butler 1997).

There are several reasons for special interest in detecting and locating enhanced reservoirs of H on the Moon. Foremost is that layered horizons within these deposits provide a history of past impacts that can be interpreted using the isotopic ratios of all volatile elements within individual layers and their thickness, to determine the size and origin of the delivery agent. Next, is that water is an essential ingredient for the support of any extended human presence on the Moon. An assay of its lunar inventory (or by proxy, that of H) is needed to conduct advanced planning for future scientific and commercial human missions to the Moon (see Chapter 6). And finally, the H content of non-polar surface soils provides a potential marker of soil maturity.

10.8.2. Epithermal neutron measurements of H. Neutrons generated by galactic cosmic rays that leak from planets provide a sensitive measure of H within near-surface regolith layers. This sensitivity stems from the fact that neutrons and protons have the same mass. The fractional energy transferred per elastic collision is thus greater for protons than for all other nuclei, which are heavier. On average, neutrons lose half their energy per collision with H and so moderate to low energies very quickly when H is present. They consequently travel very quickly from the energy range in which they are born (the fast neutron range), to the energy range in which they are absorbed (the thermal range). At equilibrium, the intensity of neutrons in the intermediate energy range (predominantly the epithermal range) is reduced in proportion to the enhancement in energy-transfer rate. The measurement signature of enhanced H in planetary leakage neutrons is therefore a reduced flux in the intermediate energy range.

Another factor that regulates the amount of neutron flux-reduction is the cross section for elastic scattering. Here again, H is outstanding because the (n,p) cross section is 20 barns, independent of energy, E, below $E = {\sim}20$ keV, and decreases slowly as the neutron energy increases. It is equal to about 5 barns at $E = 1$ MeV, which is about equal to elastic cross sections for most elements heavier than H. The detectability of H using neutrons is therefore greatest in the energy range between the upper thermal energy limit, about 0.4 eV, and 20 keV. Although it diminishes steadily at higher energies, the neutron-detection technique is still useful and significant at the low energy end of the fast-neutron range (0.5 MeV $< E <$ 10 MeV). The technique is not applicable in the thermal energy range because detection in this range is masked by the fact that thermal fluxes depend critically on the macroscopic absorption cross section, which varies over a range of 300% for the different compositions of lunar surface material (Feldman et al. 2000b).

Although the characteristic signature of H as a reduction in the flux of epithermal neutrons is very specific, it is not unique. Several REE such as Gd and Sm, support extremely large and sharp resonances in their neutron absorption cross sections in the energy range between 0.4 eV and 10 eV (see Section 10.2.2). The effect of these resonances on the equilibrium neutron flux spectrum can sometimes be significant, thereby masking the reduction effect due to H (Maurice et al. 2000). This effect is not present at fast neutron energies. Detection of a reduction of leakage neutrons in both ranges of energy in the proportions dictated by both the composition of the major rock-forming elements and the known elastic-scattering cross sections then provides a unique signature of H. This effect was used to verify the presence of enhanced H near the south pole of the Moon by Feldman et al. (2000b) (Plate 2.11).

Although enhanced abundances of H near both lunar poles is evident in neutron measurements made using the Lunar Prospector neutron spectrometers, identification of their host molecule as water requires more information. Arguments in this regard were provided by Feldman et al. (2001). Two models of enhanced H emplacement have been published in the literature. The first, presented earlier, is the delivery of water to the Moon from impacts of comets, meteoroids, and/or dust particles, followed by a random walk to the poles where they are permanently trapped on surfaces sufficiently cold that their characteristic evaporation time is longer than a few billion years (Watson et al. 1961; Arnold 1979; Butler et al. 1993; Butler 1997; Crider and Vondrak 2000). The second is the delivery of H to the Moon from the solar wind and related plasmas near the Earth (Crider and Vondrak 2000; Starukhina and Shkuratov 2000). Typical energies of these plasma protons are between 1 keV and 4 keV, which results in burial depth within the amorphous coatings of regolith grains to the order of 1000 Å. At sufficiently low temperatures, diffusive loss of implanted protons from these amorphous layers is sufficiently low that the H is trapped for times longer than several billion years. However, estimates of characteristic loss times for all major minerals known to be present on the Moon yield times longer than the age of the solar system for temperatures lower than about 200 K (Feldman et al. 2001). But temperatures lower than this limit are predicted (Vasavada et al. 1999) to exist within several large, flat-floored, only intermittently-shaded craters near the north pole. However these craters are observed to support H concentrations that are much lower than those within neighboring permanently-shaded craters whose temperatures are predicted (Vasavada et al. 1999) to be less than 100 K. While the difference in temperature between 200 K and 100 K cannot account for the needed difference in H diffusion times, it can account for the difference in water-ice sublimation times (Feldman et al. 2001). The presence of water molecules therefore provides a natural explanation of the observed difference in H concentration. Nevertheless, an association between variable concentrations of H in non-polar surface soils and the Clementine spectral-reflectance maturity index (Lucey et al. 2000) has been reported (Johnson et al. 2002) and shown to be in quantitative agreement with the H content of returned Apollo and Luna soil samples (Feldman et al. 2001).

10.8.3. Radar measurements of lunar poles. The discovery of deposits at the poles of Mercury consistent with water ice prompted the lunar radar community to make similar observations of the lunar poles. While experiments have detected local anomalies (Nozette et al. 1994), the most recent ground-based measurements of the poles have shown these local anomalies are not similar to the Mercury polar deposits, and that floors of permanently shaded craters that can be observed do not show evidence of thick ice deposits (Campbell et al. 2003). This places a strong constraint on the distribution and abundance of H-bearing materials at the poles; if in the form of water ice, they must be well mixed with regolith, or at most exist in the form of thin, centimeter scale layers.

11. THE LUNAR ATMOSPHERE

11.1. Introduction

The possible existence of a lunar atmosphere has both fascinated and challenged astronomers for hundreds of years. Galileo searched for evidence of clouds, and Kepler imagined an Earth-like climate. Landings during the Apollo era brought instruments that measured a weak atmospheric pressure. Decades later, new spectrographic and imaging instruments detected sodium and potassium gas that extended to surprisingly large distances, making the Moon's gaseous environment appear as comet-like. The sources of the lunar atmosphere involve transport of the materials to the surface and their release by the impact of sunlight, solar-wind plasma and meteorites upon the surface to release atoms and perhaps molecules. Solar radiation and the gravitational influence of the Earth play dramatic roles in the subsequent evolution of the lunar atmosphere.

The first studies of a possible lunar atmosphere were carried out by Galileo, who devoted considerable effort to a systematic search (Mendillo 2001). He carried out the very first stellar occultation experiment, finding no sign of an atmosphere. Sensors brought to the surface of the Moon by Apollo astronauts detected a very low atmospheric pressure and detected atoms of He and Ar (Hodges 1975; Stern 1999). The concentration of gases was found to be approximately 10^7 particles/cm^3 during the day and about 10^5 particles/cm^3 at night. Such densities are still comparable to vacuum conditions in comparison to the gas content at the surface of the Earth (10^{19} cm^{-3}). Initial concerns that the instruments were merely detecting gases that evaporated off the lunar modules were ultimately dismissed in favor of accepting a weak atmosphere produced by capture of solar-wind particles (such as He) or the radioactive decay of elements in the lunar soil (such as Ar from decay of K). As interests turned to other areas in the solar system, the Moon's minor atmosphere received little attention for many years.

11.2. Remote sensing of the Moon's atmosphere

An astonishing discovery by Potter and Morgan (1985) was the presence of very bright emission of the yellow D lines of Na at Mercury; shortly afterwards they found the near-infrared emission of K (Potter and Morgan 1986). A comprehensive summary of this work appears in Hunten et al. (1988). At that time, the much fainter emissions from the Moon had not been discovered; they were found by looking past the sunlit limb by Potter and Morgan (1988a) and Tyler et al. (1988). In the same way as comets, the rocky surfaces of Mercury, the Moon and some asteroids emit gases that escape into space, providing a transient atmosphere to study. The elements Na and K are not particularly abundant in the solar system but are relatively easy to detect because they scatter sunlight very efficiently. They are not the major constituents of the atmospheres of the Moon (or Mercury), but they do serve as excellent "tracers" of other gases presumably there but more difficult to detect. For example, the total number of Na plus K atoms detected just above the Moon's surface is barely 100 atoms/cm^3, far below the concentrations suggested for total abundances in the Apollo data.

Plate 2.12 provides a dramatic example of Na abundance profiles versus height above the limb. They confirm the discovery by Potter and Morgan (1988b) that the Na atoms extend to much higher altitudes than they would if they were at the temperature of the local surface. A small thermal component can, however, be detected near the subsolar point. Higher velocities have been suggested to be the result of sputtering by impact of ions or solar photons; micrometeoroid impact could also be involved. Evidently these other processes are more important than thermal evaporation everywhere except the warmest region at and near the subsolar point. We will return to these points below after a further discussion of the observations.

As demonstrated in Plate 2.12, it is necessary to use high-dispersion spectroscopy for studies near the limb to reduce the signals from the scattered light of the lunar limb and disk. For altitudes more than one or two lunar radii, the much more sensitive technique of imaging through narrow-band filters can be used. These new low-light-level imaging techniques, capable of taking a picture of the full extent of the atmosphere, provided the next step in understanding the Na atmosphere of the Moon. Images of the Na brightness in two dimensions show that the atmosphere extends to several times the radius of the Moon (Fig. 2.56). If the brightness levels were very much higher, the Moon's Na atmosphere would be visible to the naked eye as a large cloud (nebula) spanning several degrees of the night sky. This large extent implies that many Na atoms have relatively high speeds, approaching the escape speed (2.3 km/sec); yet, the pattern of brightness decreases with distance (*d*) as d^{-4} showing that there are slower Na atoms as well. To test the mechanisms responsible for sputtering processes with the required release speed distributions, several research groups are making lunar observations during meteor showers and at times when the solar wind is shielded from the surface by the Earth's magnetic field.

11.3. Lunar atmosphere generated by meteors

There have been several reports of possible enhancements in the Moon's atmosphere during a meteor shower (Hunten et al. 1992; Cremonese and Verani 1997; Verani et al. 1998, 2001). A particularly strong case occurred during the Leonids "storm" in November 1998. Using a wide-angle (180° all-sky) field of view, Smith et al. (1999) described a persistent Na "spot" seen on the nights after the peak meteor events of 17 November 1998. The unusual aspect of their observations was that they were made near new Moon phase, i.e., when the Moon cannot be observed directly owing to its location between the Earth and the Sun. Their analysis and companion computer simulations (Wilson et al. 1999) showed that Na atoms released by the meteor-regolith impacts at a rate of 7×10^{21} s^{-1} were accelerated away from the Moon by the radiation pressure of sunlight. In approximately two days (i.e., on 19 November), a cloud of Na gas swept past the Earth where it was focused into a beam by the Earth's gravitational field. Thus, in viewing the sky in the direction opposite from both the Moon and the Sun, the distant lunar tail was observed. Figure 2.57 summarizes the observational and modeling description of this effect. Subsequent observations reported by Smith et al. (2001) show that the lunar Na spot (and therefore the distant atmospheric tail) is a permanent feature of the Earth-Moon system, occasionally modulated in prominence by transient sources of sputtering.

11.4. Sputtering sources

The source of the Na gas on the Moon is a research topic very much in active debate (Stern 1999). Liberating gases from the surface material (regolith) requires the impact of micrometeorites or solar-wind ions and electrons, or sunlight. These are called sputtering agents, and laboratory experiments show that they indeed can free atoms and molecules from surfaces with sufficient energy to move away from the surface. Both hot and cold gaseous populations are possible from these processes, and the degree to which the thermal and

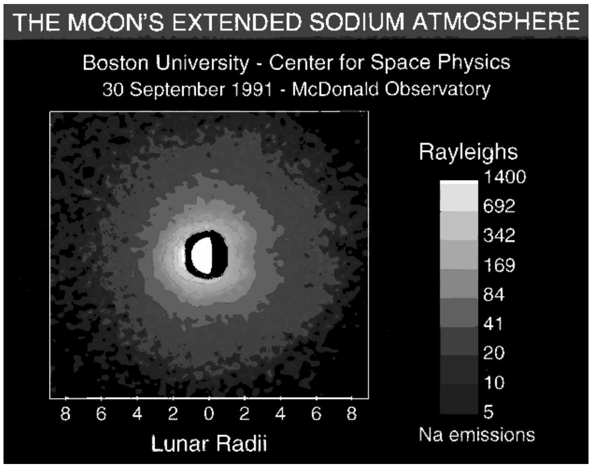

Figure 2.56. Image of the sodium atmosphere surrounding the Moon near quarter phase. The sodium brightness units shown are far below those capable of being seen by the unaided human eye. The Rayleigh unit is defined as $10^6/4\pi$ photons per square centimeter per second per steradian.

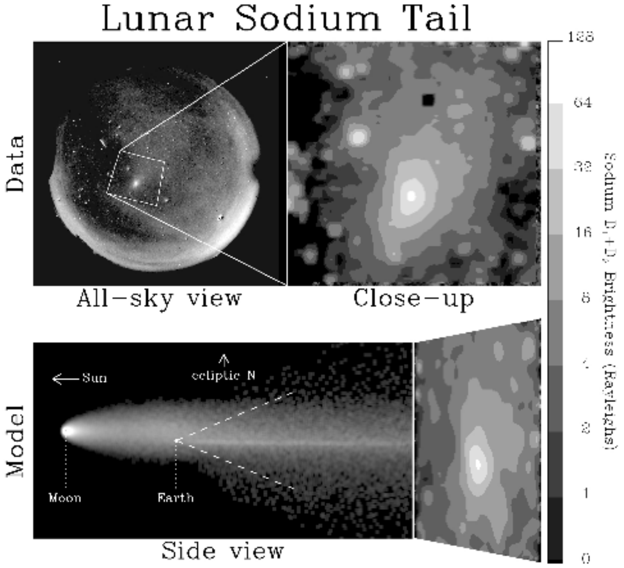

Figure 2.57. *Top panel:* (*Left*) all-sky image showing the sodium "spot" discovered on 19 November 1998. (*Right*) magnified portion of the feature. *Bottom panel:* (*Left*) computer model showing (to scale) neutral sodium originating from the Moon, accelerated by radiation pressure to the Earth where a portion is gravitationally focused into a column of enhanced sodium brightness. (*Right*) This simulated "spot" is shown as it would appear to a wide-angle camera system (dashed lines) on the night side of the Earth.

suprathermal components dominate close and distant regions is still under study (Sprague et al. 1992, 1998; Hunten et al. 1998). Sputtered gases are either pulled back to the regolith by gravity, pushed away by solar radiation pressure, or lost by photoionization and removal by the magnetic field in the solar wind (see Plate 2.12). The term surface-boundary-exosphere (SBE) is applied to an atmosphere produced by vaporization of surface material under conditions where collisions aloft are so rare that the liberated gases can have long parabolic trajectories back to the surface, or can escape directly from it.

11.5. Sources, recycling and sinks

The discussion of sources and sinks can be assisted by the illustration in Fig. 2.58. It is useful to distinguish between source processes (often very slow) that bring material to the surface and loss processes that release them from the surface into the atmosphere or space.

The need for some kind of source process is demonstrated as follows: The loss rate of Na atoms, in global mean, is 5×10^3 atoms per cm^2 per second. If material near the surface contains 1% Na by weight, all of it could be depleted in 10^7 years. Possible mechanisms for replacing it are regolith turnover, addition of meteoritic material, or diffusion from deeper layers. Hunten and Sprague (1997) and Morgan et al. (1988, 1989) suggest that regolith turnover is adequate, with an augmentation by meteoritic material.

Any atom that is released into the atmosphere must return to the surface unless it is ionized or otherwise lost to space. Half the ions find themselves in a downward electric field and are carried back to the surface. Sprague et al. (1992) discuss the fate of these recycled atoms, suggesting that the average one executes about 50 such hops, each lasting about 1000 sec.

The relation of the various source and release processes was studied by Sprague et al. (1992) with the use of a set of height profiles (0–700 km) of intensity measured at five solar

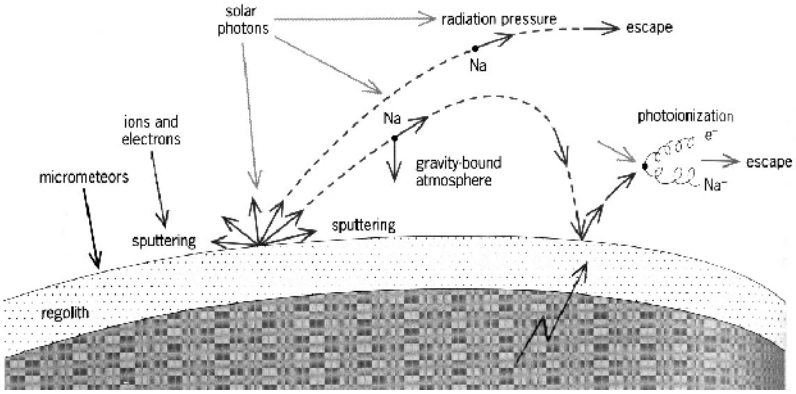

Figure 2.58. A schematic illustration of the processes that release and govern the subsequent motion of sodium atoms (Na) ejected from the regolith of the Moon.

zenith angles from 3 to 80°. The rates, which had to be assumed, have now been measured in the laboratory (Madey et al. 1998, Yakshinskiy and Madey 2000, Yakshinskiy et al. 2000). They are slower than the assumed ones by a factor of 1700 for photo-stimulated desorption (PSD) and 4000 for thermal evaporation. Thus, nearly the same results are obtained for the atmosphere if the number of atoms adsorbed per unit area of surface is increased by a factor of 3000; the value is then 3×10^{10} cm^{-2} at 9° from the subsolar point, increasing by a factor of 4 near the terminator. Thermal evaporation dominates by a factor ~ 3 near the subsolar point and rapidly becomes negligible elsewhere. Sputtering by solar-wind protons has been shown to be less important as a source (see the next section).

11.6. Lunar atmosphere seen during eclipses

For approximately four days each month, the Moon passes through the Earth's magnetic envelope (magnetosphere) thereby shielding its surface from solar-wind plasma impact. To see if the lunar atmosphere is affected by this removal of a sputtering agent, observations of the tenuous Na gas have to be made during the nights spanning the bright full Moon. This presents a serious, if not impossible, impediment to wide-angle imaging systems. Such observations can however be made during the totality phase of a lunar eclipse. Under such conditions, the bright lunar disk (and therefore scattered light) is very much reduced, and yet sunlight beyond the penumbra is still at full strength to illuminate any distant Na that may be present. Mendillo et al. (1999) reported on four such experiments and found that the robust, extended nature of the Moon's atmosphere is not affected in any drastic way by the absence of a solar-wind sputtering source. Thus, of the three proposed mechanisms for generating the extended lunar atmosphere, photon-sputtering is always present on one hemisphere and is thus considered to be the dominant source; ever-present micrometeorites are a secondary source, one certainly enhanced during meteor showers; solar wind sputtering appears to be the least significant source. Its weakness is traceable mainly to the small proton flux, 3×10^{8} cm^{-2} sec^{-1}, while that of photons effective in producing PSD is 2×10^{14} cm^{-2} sec^{-1}.

11.7. Summary

Studies of the Moon's atmosphere, once a topic of only speculation, is now an active research field in comparative atmospheric science. State-of-the-art observational tools have transformed the available database and numerical simulations offer insights and tests of physical processes. Future observational work will center on attempts to identify species other than Na and K (i.e., the major constituents), probably requiring dedicated space-based ultraviolet observations. Modeling efforts will concentrate on the variability patterns associated with sources (i.e., as illustrated in Fig. 2.58); laboratory experiments will explore surface sputtering efficiencies and yields. Thus, our closest cosmic neighbor continues to fascinate us, and its role as a laboratory-in-space for the study of surface-boundary-exospheres will continue to enrich the study of primitive bodies in the solar system.

12. REFERENCES

Adams JB (1974) Visible and near-infrared diffuse reflectance spectra of pyroxenes as applied to remote sensing of solid objects in the solar system. J Geophys Res 79:4829-4836

Adams JB (1975) Interpretation of visible and near-infrared diffuse reflectance spectra of pyroxenes and other rock-forming minerals. *In*: Infrared and Raman Spectroscopy of Lunar and Terrestrial Minerals. Karr Jr C (ed) Academic Press, p 91-116

Adams JB, Charette MP, Rhodes JM (1975) Chemical fractionation of the lunar regolith by impact melting. Science 190:380-381

Adams JB, Filice AL (1967) Spectral reflectance 0.4 to 2.0 microns of silicate rock powders. J Geophys Res 72:5705-5715

Adams JB, Goulaud LH (1978) Plagioclase feldspars: visible and near infrared diffuse reflectance spectra as applied to remote sensing. Proc Lunar Planet Sci Conf 9:2901-2909

Adams JB, Hörz F, Gibbons RV (1979) Effects of shock-loading on the reflectance spectra of plagioclase, pyroxene and glass. Proc Lunar Planet Sci Conf 10:1-3

Adams JB, Pieters CM, McCord TB (1974) Orange glass: Evidence for regional deposits of pyroclastic origin on the Moon. Proc Lunar Sci Conf 5:171-186

Adler I, Trombka J, Schmadeback R, Lowman P, Blodget H, Yin L, Eller E, Podwysocki M, Weidner JR, Bickel AL, Lum RKL, Gerard J, Gorenstein P, Bjorkholm P, Harris B (1973) Results of the Apollo 15 and 16 x-ray fluorescence experiment. Proc Lunar Sci Conf 4:2783-2791

Adler I, Trombka JI (1980) Orbital chemistry-lunar surface analysis from the X-ray and gamma ray remote sensing experiments. *In:* Chemistry of the Moon: Physics and Chemistry of the Earth, Volume 10. Ahrens LH (ed) Pergamon, p 17-43

Agrell SO, Peckett A, Boyd FR, Haggerty SE, Bunch TE, Cameron EN, Dence MR, Douglas JAV, Plant AG, Traill RJ, James OB, Keil K, Prinz M (1970) Titanian chromite, aluminian chromite, and chromian ulvöspinel from Apollo 11 rocks. Proc Apollo 11 Lunar Sci Conf 1:81-86

Ali MZ, Ehmann WD (1977) Chemical characterization of lunar core 60010. Proc Lunar Sci Conf 8:2967-2981

Allen CC, Morris RV, McKay DS (1995) Experimental space weathering of lunar soils. Meteoritics 30(5):479-480

Allen CC, Morris RV, McKay DS (1996) An experimental analog to maturing lunar soil. Lunar Planet Sci 27:13-14

Allen CC, Morris RV, McKay DS (1996) Oxygen extraction from lunar soils and pyroclastic glass. J Geophys Res 101: 26085-26095

Allton JH (1989) Catalog of Apollo Lunar Surface Geological Sampling Tools and Containers. JSC-23454, NASA Johnson Space Center, Houston, p 97

Anand M, Taylor LA, Nazarov MA, Patchen A (2003) Petrologic comparisons of lunar mare basalt meteorites Dh-287A and NWA 032. Lunar Planet Sci 34:1787 (CD-ROM)

Anand M, Taylor LA, Neal C, Patchen A, Kramer G (2004) Petrology and geochemistry of LAP 02205: A new low-Ti mare-basalt meteorite. Lunar Planet Sci XXXV:1626 (CD-ROM)

Anders E, Grevesse N (1989) Abundances of the elements: meteoritic and solar. Geochim Cosmochim Acta 53:197-214

Andre CG, Wolfe RW, Adler I, Clark PE, Weidner JR, Philpotts JA (1977) Chemical character of the partially flooded Smythii Basin based on Al/Si orbital x-ray data. Proc Lunar Sci Conf 8(1):925-931

Antonenko I, Head JW, Mustard JF, Hawke BR (1995) Criteria for the detection of lunar cryptomaria. Earth Moon Planets 69:141-172

Arai T, Warren PH (1999) Lunar meteorite Queen Alexandra Range 94281: Glass compositions and other evidence for launch pairing with Yamato 793274. Meteorit Planet Sci 34:209-234

Arnold JR (1979) Ice in the Lunar Polar Regions. J Geophys Res 84:5659-5668

Basu A, McKay DS (1985) Chemical variability and origin of agglutinitic glass. Proc Lunar Planet Sci Conf 16:D87-D94

Basu A, Wentworth SJ, McKay DS (2001) Occurrence and distribution of Fe^0-globules in lunar agglutinates. Lunar Planet Sci XXXII:1942 (CD-ROM)

Bell PM, Mao HK (1972) Crystal-field effects of iron and titanium in selected grains of Apollo 12, 14, and 15 rocks, glasses, and fine fractions. Proc Lunar Sci Conf 3(1):545-553

Bernatowicz TJ, Hohenberg CM, Podosek FA (1979) Xenon component organization in 14301. Proc Lunar Planet Sci Conf 10:1587-1616

Bernatowicz TJ, Nichols RH, Jr., Hohenberg CM (1994) Origin of amorphous rims on lunar soil grains. Lunar Planet Sci XXV:105-106

Bickel CE (1977) Petrology of 78155 - an early, thermally metamorphosed polymict breccia. Proc Lunar Planet Sci Conf 8:2007-2027

Bielefeld MJ, Reedy RC, Metzger AE, Trombka JI, Arnold JR (1976) Surface chemistry of selected lunar regions. Proc Lunar Sci Conf 7:2661-2676

Binder AB (1998) Lunar Prospector: overview. Science 281:1475-1476

Blanchard DP, Jacobs JW, Brannon JC, Brown RW (1976) Drive tube 60009: A chemical study of magnetic separates of size fractions from five strata. Proc Lunar Sci Conf 7:281-294

Blanchard DP, Korotev RL, Brannon JC, Jacobs JW, Haskin LA, Reid AM, Donaldson CH, Brown RW (1975) A geochemical and petrographic study of 1-2 mm fines from Apollo 17. Proc Lunar Sci Conf 6:2321-2341

Blewett DT, Hawke BR (2001) Remote sensing and geological studies of the Hadley-Apennine region of the Moon. Meteorit Planet Sci 36(5):701-730

Blewett DT, Lucey PG, Hawke BR, Jolliff BL (1997) Clementine images of the lunar sample-return stations: refinement of FeO and TiO_2 mapping techniques. J Geophys Res 102:16,319-16,325

Bogard DD, Morris RV, Hirsch WC, Jr. HVL (1980) Depositional and irradiational history of the Hadley Rille core 15010/11. Proc Lunar Planet Sci Conf 11:1511-1529

Bogard DD, Morris RV, Johnson P, Lauer HVJ (1982) The Apennine Front core 15007/8: irradiational and depositional history. Proc Lunar Planet Sci Conf 13:A221-A231

Borchardt R, Stöffler D, Spettel B, Palme C, Wänke H, Wacker K, Jessberger EK (1986) Composition, structure, and age of the Apollo 16 subregolith basement as deduced from the chemistry of post-Imbrium melt bombs. Proc Lunar Planet Sci Conf 17. J Geophys Res 91:E43-E54

Boynton WV, Chou C-L, Bild RW, Baedecker PA, Wasson JT (1976) Element distribution in size fractions of Apollo-16 soils; evidence for element mobility during regolith processes. Earth Planet Sci Lett 29:21-33

Britt DT, Pieters CM (1994) Darkening in black and gas-rich ordinary chondrites - the spectral effects of opaque morphology and distribution. Geochim Cosmochim Acta 58(18):3905-3919

Brownlee DE, Hörz F, Bradley J (1992) Interplanetary meteoroid debris in LDEF metal craters. Second LDEF Post-Retrieval Symposium Abstracts, NASA CP-10097, p. 47. NASA Langley Research Center

Brownlee DE, Hörz F, Laurance M, Bernhard RP, Warren J, Bradley J (1991) The composition of meteoroids impacting LDEF. 54th Annual Meeting of the Meteoritical Society, LPI Contrib No 766:38

Bruckenthal EA, Pieters CM (1984) Spectral effects of natural shock on plagioclase feldspar. Proc Lunar Planet Sci Conf 15:96-97

Burns RG (1970) Crystal field spectra and evidence for cation ordering in olivine minerals. Am Mineral 55:1608-1632

Burns RG (1985) Electronic spectra of minerals. *In*: Chemical Bonding and Spectroscopy in Mineral Chemistry. Berry FJ, Vaughan DJ (eds) Chapman and Hall, p 63-101

Burns RG (1993) Mineralogical Applications of Crystal Field Theory. Cambridge University Press

Busche FD, Prinz M, Keil K, Bunch TE (1972) Spinels and the petrogenesis of some Apollo 12 igneous rocks. Am Mineral 57:1729-1747

Butler B (1997) The migration of volatiles on the surfaces of Mercury and the Moon. J Geophys Res 102:19283-19291

Butler BJ, Muhleman DO, Slade MA (1993) Mercury; full-disk radar images and the detection and stability of ice at the North Pole. J Geophys Res 98:15003-15023

BVSP (1981) Basaltic Volcanism on the Terrestrial Planets. Pergamon Press

Cameron EN (1971) Opaque minerals in certain lunar rocks from Apollo 12. Proc Lunar Sci Conf 2:193-206

Campbell BA, Campbell DB, Chandler JF, Hine AA, Nolan MC, Perillat PJ (2003) Radar mapping of the lunar poles. Nature 426:137-138

Campbell BA, Hawke BR (2005) Radar mapping of lunar cryptomaria east of Orientale basin. J Geophys Res doi: 10.1029/2005JE002425

Campbell BA, Hawke BR, Thompson TW (1997) Long-wavelength radar studies of the lunar maria. J Geophys Res 102:19,307-19,320

Cassidy W, Hapke B (1975) Effects of darkening processes on surfaces of airless bodies. Icarus 25:371-383

Chambers JG, Taylor LA, Patchen A, McKay DS (1995) Quantitative mineralogical characterization of lunar high-ti mare basalts and soils for oxygen production. J Geophys Res 100:14391-14401

Champness PE, Dunham AC, Gibb FGF, Giles HN, MacKenzie WS, Stumpfl EF, Zussman J (1971) Mineralogy and petrology of some Apollo 12 samples. Proc Lunar Sci Conf 2:359-376

Charette MP, McCord TB, Pieters CM, Adams JB (1974) Application of remote spectral reflectance measurements to lunar geology classification and determination of titanium content of lunar soils. J Geophys Res 79(11):1605-1613

Charette MP, Taylor SR, Adams JB, McCord TB (1977) The detection of soils of Fra Mauro basalt and anorthositic gabbro composition in the lunar highlands by remote spectral reflectance techniques. Proc Lunar Sci Conf 8: 1049-1061

Cintala MJ, Hörz F (1992) An experimental evaluation of mineral-specific comminution. Meteorit Planet Sci 27:395-403

Cirlin EH, Goldberg IB, Housley RM, Weeks RA, Perhac R (1975) Ferromagnetic resonance as a method of studying the micrometeorite bombardment history of lunar fines. Lunar Sci Conf 6:146-148

Cirlin EH, Housley RM, Goldberg IB, Paton NE (1974) Ferromagnetic resonance as a method for studying regolith dynamics and breccia formation. Lunar Sci Conf 5:121-122

Clark PE, Adler I (1978) Utilization of independent solar flux measurements to eliminate nongeochemical variation in X-ray fluorescence data. Proc Lunar Planet Sci Conf 9:3029-3036

Clark PE, Hawke BR (1981) Compositional variation in the Hadley Apennine region. Proc Lunar Planet Sci Conf 12: 727-749

Clark PE, McFadden LA (2000) New results and implications for lunar crustal iron distribution using sensor data fusion techniques. J Geophys Res 105:4291-4316

Cloutis EA, Gaffey MJ (1991) Pyroxene spectroscopy revisited - spectral-compositional correlations and relationship to geothermometry. J Geophys Res 96:22809-22826

Cremonese G, Verani S (1997) High resolution observations of the sodium emission from the Moon. Adv Space Res 19:1561-1569

Crider DH, Vondrak RR (2000) The solar wind as a possible source of lunar polar hydrogen deposits. J Geophys Res 105:26773-26782

Cushing JA, Taylor GJ, Norman MD, Keil K (1999) The granulitic impactite suite: Impact melts and metamorphic breccias of the early lunar crust. Meteorit Planet Sci 34:185-195

Dalton J, Hollister LS, Kulick CG, Hargraves RB (1974) The nature of the chromite to ulvöspinel transition in mare basalt 15555. Lunar Planet Sci V:160-162

Davis Jr PA (1980) Iron and titanium on the Moon from orbital gamma-ray spectrometry with implications for crustal evolutionary models. J Geophys Res 85(B6):3209-3224

Davis PA, Bielefeld MJ (1981) Inelastic neutron scatter iron concentrations of the Moon from orbital gamma ray data. J Geophys Res 86:11919

Davis PA, Spudis PD (1985) Petrologic province maps of the lunar highlands derived from orbital geochemical data. Proc Lunar Planet Sci Conf 16. J Geophys Res 90:D61-D74

Davis PA, Spudis PD (1987) Global petrologic variations on the Moon: a ternary-diagram approach. Proc Lunar Planet Sci Conf 17:E387-E395

Delano JW (1986) Pristine lunar glasses: criteria, data and implications. Proc Lunar Planet Sci Conf 16. J Geophys Res 90:D201-D213

Delano JW, Ringwood AE (1978) Siderophile elements in the lunar highlands: Nature of the indigenous component and implications for the origin of the Moon. Proc Lunar Planet Sci Conf 9:111-159

Dence MR, Douglas JAV, Plant AG, Traill RJ (1970) Petrology, mineralogy and deformation of Apollo 11 samples. Proc Apollo 11 Lunar Sci Conf 1:315-340

Deutsch A, Stöffler D (1987) Rb-Sr analyses of Apollo 16 melt rocks and a new age estimate for the Imbrium basin: Lunar basin chronology and the early heavy bombardment of the Moon. Geochim Cosmochim Acta 51:1951-1964

Dickinson T, Taylor GJ, Keil K, Schmitt RA, Hughes SS, Smith MR (1985) Apollo 14 aluminous mare basalts and their possible relationship to KREEP. Proc Lunar Planet Sci Conf 15. J Geophys Res 90(Supplement):C365-C374

Donaldson CH, Usselman TM, Wiliams RJ, Lofgren GE (1975) Experimental modeling of the cooling history of Apollo 12 olivine basalts. Proc Lunar Sci Conf 6:843-869

Dowty E (1977) Phosphate in Angra Dos Reis: structure and composition of the $Ca_3(PO_4)_2$ minerals. Earth Planet Sci Lett 35:347-351

Dowty E, Keil K, Prinz M (1974a) Igneous rocks from Apollo 16 rake samples. Lunar Science V:174-176

Dowty E, Prinz M, Keil K (1974b) Ferroan anorthosite: a widespread and distinctive lunar rock type. Earth Planet Sci Lett 24:15-25

Dymek RF (1986) Characterization of the Apollo 15 feldspathic basalt suite. *In*: Geology and Petrology of the Apollo 15 Landing Site, LPI Tech. Rpt. 86-03. Spudis PD, Ryder G (eds) Lunar and Planetary Institute, p 52-57

Eberhardt P, Geiss J, Graf H, Groegler N, Krahenbuehl U, Schwaller H, Schwarzmuller J, Stettler A (1970) Trapped solar wind noble gases, exposure age and K/Ar-age in Apollo 11 lunar fine material. Lunar Sci Conf 1:1037-1070

El Goresy A, Prinz M, Ramdohr P (1976) Zoning in spinels as an indicator of the crystallization histories of mare basalts. Proc Lunar Sci Conf 7:1261-1279

El Goresy A, Ramdohr P, Taylor LA (1971a) The opaque minerals in the lunar rocks from Oceanus Procellarum. Proc Lunar Sci Conf 2:219-235

El Goresy A, Ramdohr P, Taylor LA (1971b) The geochemistry of the opaque minerals in Apollo 14 crystalline rocks. Earth Planet Sci Lett 13:121-129

Elphic RC, Lawrence DJ, Feldman WC, Barraclough BL, Maurice S, Binder AB, Lucey PG (1998) Lunar Fe and Ti abundances: comparison of Lunar Prospector and Clementine data. Science 281:1493-1496

Elphic RC, Lawrence DJ, Feldman WC, Barraclough BL, Maurice S, Binder AB, Lucey PG (2000) Lunar rare earth element distribution and ramifications for FeO and TiO_2: Lunar Prospector neutron spectrometer observations. J Geophys Res 105:20,333-20,345

Elphic RC, Lawrence DJ, Feldman WC, Barraclough BL, Maurice S, Lucey PG, Blewett DT, Binder AB (2002) The Lunar Prospector neutron spectrometer constraints on TiO_2. J Geophys Res 107(E4):10.1029/2000JE001460

Etchegaray-Ramirez MI, Metzger AE, Haines EL, Hawke RB (1983) Thorium concentrations in the lunar surface; IV, Deconvolution of the Mare Imbrium, Aristarchus, and adjacent regions. Proc Lunar Planet Sci Conf 13:A529-A543

Eugster O (1999) Chronology of dimict breccias and the age of South Ray crater at the Apollo 16 site. Meteorit Planet Sci 34:385-391

Eugster O, Terribilini D, Polnau E, Kramers J (2001) The antiquity indicator argon-40/argon-36 for lunar surface samples calibrated by uranium-235-xenon-136 dating. Meteorit Planet Sci 36:1097-1115

Evans LG, Reedy RC, Trombka JI (1993) Introduction to planetary remote sensing gamma ray spectroscopy. *In*: Remote Geochemical Analysis: Elemental and Mineralogical Composition. Pieters CM, Englert PAJ (eds) Cambridge Univ. Press, p 167-198

Evensen NM, Murthy VR, Coscio Jr. MR (1974) Provenance of KREEP and the exotic component: Elemental and isotopic studies of grain size fractions in lunar soils. Proc Lunar Sci Conf 5:1401-1417

Feldman W, Maurice S, Lawrence DJ, Little RC, Lawson SL, Gasnault O, Wiens RC, Barraclough BL, Elphic RC, Prettyman TH, Steinberg JT, Binder AB (2001) Evidence for water ice near the lunar poles. J Geophys Res 106(E10):23,231-23,251

Feldman WC, Ahola K, Barraclough BL, Belian RD, Black RK, Elphic RC, Everett DT, Fuller KR, Kroesche J, Lawrence DJ, Lawson SL, Longmire JL, Maurice S, Miller MC, Prettyman TH, Storms SA, Thornton GW (2004) Gamma-ray, neutron, and alpha-particle spectrometers for the Lunar Prospector mission. J Geophys Res 109:doi 10.1029/2003JE002207

Feldman WC, Barraclough BL, Fuller KR, Lawrence DJ, Maurice S, Miller MC, Prettyman TH, Binder AB (1999) The Lunar Prospector gamma-ray and neutron spectrometers. Nucl Instrum Methods Phys Res(Sect, A 422):562-566

Feldman WC, Barraclough BL, Maurice S, Elphic RC, Lawrence DJ, Thomsen DR, Binder AB (1998a) Major compositional units of the Moon: Lunar Prospector thermal and fast neutrons. Science 281:1489-1493

Feldman WC, Lawrence DJ, Elphic RC, Barraclough BL, Maurice S, Genetay I, Binder AB (2000a) Polar hydrogen deposits on the Moon. J Geophys Res 105:4175-4195

Feldman WC, Lawrence DJ, Elphic RC, Vaniman DT, Thomsen DR, Barraclough BL, Maurice S, Binder AB (2000b) The chemical information content of lunar thermal and epithermal neutrons. J Geophys Res 105:20347-20363

Feldman WC, Maurice S, Binder AB, Barraclough BL, Elphic RC, Lawrence DJ (1998b) Fluxes of fast and epithermal neutrons from lunar prospector: evidence for water ice at the lunar poles. Science 281:1496-1500

Fink D, Klein J, Middleton R, Vogt S, Herzog GF, Reedy RC (1998) ^{41}Ca, ^{26}Al, and ^{10}Be in lunar basalt 74275 and ^{10}Be in the double drive tube 74002/74001. Geochim Cosmochim Acta 62:2389-2402

Fischer EM, Pieters CM (1994) Remote determination of exposure degree and iron concentration of lunar soils using VIS-NIR spectroscopic methods. Icarus 111(2):475-488

Fischer EM, Pieters CM (1995) Lunar-surface aluminum and iron concentration from Galileo solid-state imaging data, and the mixing of mare and highland materials. J Geophys Res 100(E11):23279-23290

Fischer EM, Pieters CM (1996) Composition and exposure age of the Apollo 16 Cayley and Descartes regions from Clementine data: normalizing the optical effects of space weathering. J Geophys Res 101(E1):2225-2234

Folk RL (1980) Petrology of Sedimentary Rocks. Hemphill Publishing Co.

Fruland RM, Morris RV, McKay DS, Clanton US (1977) Apollo 17 ropy glasses. Proc Lunar Sci Conf 8:3095-3111

Fudali RF (1966) Implications of the nonuniform cooling behavior of the eclipsed Moon. Icarus 5(1-6):536-544

Gaddis LR, Pieters CM, Hawke BR (1985) Remote sensing of lunar pyroclastic mantling deposits. Icarus 61:461-489

Gaddis LR, Staid MI, Tyburczy JA, Hawke BR (2003) Compositional analyses of lunar pyroclastic deposits. Icarus 161:262-280

Garrison JR, Taylor LA (1980) Genesis of highland basalt breccias: A view from 66095. *In*: Proc. Conf. Lunar Highlands Crust. Papike JJ, Merrill RB (eds) Pergamon Press, p 395-417

Gasnault O, Feldman WC, Maurice S, Genetay I, d'Uston C, Prettyman TH, Moore KR (2001) Composition from fast neutrons: application to the Moon. Geophys Res Lett 28:3797-3800

Genetay I, Maurice S, Feldman WC, Gasnault O, Lawrence DJ, Elphic RC, d'Uston C, Binder AB (2003) Elemental content from 0 to 500 keV neutrons: Lunar Prospector results. Planet Space Sci 51:271-280

Ghent RR, Leverington DW, Campbell BA, Hawke BR, Campbell DB (2005) Earth-based observations of radar-dark crater haloes on the Moon: Implications for regolith properties. J Geophys Res 110: doi:10.1029/2004JE002366

Gibbons RV, Hörz F, Schaal RB (1976) The chemistry of some individual lunar soil agglutinates. Proc Lunar Sci Conf 7:405-422

Giguere TA, Taylor GJ, Hawke BR, Lucey PG (2000) The titanium contents of lunar mare basalts. Meteorit Planet Sci 35(1):193-200

Gillis JJ, Jolliff BL, Elphic RC (2003) A revised algorithm for calculation TiO_2 concentrations from Clementine **UVVIS** data: a synthesis of rock, soil, and remotely sensed TiO_2 concentrations. J Geophys Res 108(E2):5009, doi:10.1029/2001JE001515

Gillis JJ, Jolliff BL, Lawrence DJ, Lawson SL, Prettyman TH (2002) The Compton-Belkovich region of the Moon: Remotely sensed observations and lunar sample association. Proc Lunar Planet Sci Conf XXXIII:1967 (CD-ROM)

Gillis JJ, Korotev RL, Jolliff BL (2004) Lunar surface geochemistry: Global concentrations of Th, K, and FeO as derived from Lunar Prospector and Clementine data. Geochim Cosmochim Acta 68(18):3791-3805

Gillis JJ, Lucey PG (2004) Clementine 2.7 micron data: mapping the mare and searching for water. Proc Lunar Planet Sci Conf 35:2158

Gillis JJ, Lucey PG, Campbell BA, Hawke BR (2005) Clementine 2.7 micron data and 70-cm Earth-based radar data provide additional constraints for **UVVIS**-based estimates of TiO_2 content for lunar mare basalts. Proc Lunar Planet Sci Conf XXXVI:2254

Gnos E, Hofmann BA, A. A-K, Lorenzetti S, Eugster O, Whitehouse MJ, Villa IM, Jull AJT, Eikenberg J, Spettel B, Krähenbühl U, Franchi IA, Greenwood RC (2004) Pinpointing the source of a lunar meteorite: implications for the evolution of the Moon. Science 305:657-659

Gold T (1955) The lunar surface. Monthly Notices Royal Astron Soc 115:585-604

Goldstein JI, Axon HJ, Agrell SO (1972) The grape cluster, metal particle 63344,1. Earth Planet Sci Lett 28:217-224

Goldstein JI, Hewins RH, Axon HJ (1974) Metal silicate relationships in Apollo 17 soils. Proc Lunar Conf 5:653-671

Gose WA, Morris RV (1977) Depositional history of the Apollo 16 deep drill core. Proc Lunar Sci Conf 8:2909-2928

Gose WA, Strangway DW, Pearce GW (1978) Origin of magnetization in lunar breccias; an example of thermal overprinting. Earth Planet Sci Lett 38:373-384

Graf JC (1993) Lunar Soils Grain Size Catalog. NASA Reference Publication 1265, NASA

Grande M (2001) The D-CIXS X-ray spectrometer on ESA's SMART-1 mission to the Moon. Earth Moon Planets 85: 143-152

Grier JA, McEwen AS, Lucey PG, Milazzo M, Strom RG (2001) Optical maturity of ejecta from large rayed lunar craters. J Geophys Res 106(E12):32847-32862

Grove TL (1982) Use of lamellae in lunar clinopyroxenes as cooling rate speedometers: An experimental calibration. Am Mineral 67:251-268

Haggerty SE (1971) Compositional variations in lunar spinels. Nature Phys Sci 233:156-160

Haggerty SE (1972a) Luna 16: An opaque mineral study and a systematic examination of compositional variations of spinels from Mare Fecunditatis. Earth Planet Sci Lett 13:328-352

Haggerty SE (1972b) Chemical characteristics of spinels in some Apollo 15 basalts. *In*: The Apollo 15 Lunar Samples. Chamberlain JW (ed) Lunar Science Institute, p 92-97

Haggerty SE (1973a) Luna 20: mineral Chemistry of spinel, pleonaste, chromite, ulvöspinel, ilmenite, and rutile. Geochim Cosmochim Acta 37:857-867

Haggerty SE (1973b) Armalcolite and genetically associated opaque minerals in the lunar samples. Proc Lunar Sci Conf 4:777-797

Haggerty SE (1978) Luna 24: systematics in spinel mineral chemistry in the context of an intrusive petrogenetic grid. *In*: Mare Crisium: The View From Luna 24. Merrill RB, Papike JJ (eds) Pergamon, p 523-536

Haggerty SE, Boyd FR, Bell PM, Finger LW, Bryan WB (1970) Opaque minerals and olivine in lavas and breccias from Mare Tranquillitatis. Proc Apollo 11 Lunar Sci Conf 3:513–538

Hapke B (2001) Space weathering from Mercury to the asteroid belt. J Geophys Res 106(E5):10039-10073

Hapke B, Cassidy W, Wells EN (1975) Effects of vapor-phase deposition processes on the optical, chemical and magnetic properties of the lunar regolith. The Moon 13:339-353

Hapke B, Cohen A, Cassidy W, Wells E (1970) Solar radiation effects of the optical properties of Apollo 11 lunar samples. Proc of the Apollo 11 Lunar Sci Conf 3:2199-2212

Haselton JD, Nash WP (1975) A model for the evolution of opaques in mare lavas. Proc Lunar Sci Conf 6:747-755

Hashizume K, Chaussidon M, Marty B, Robert F (2000) Solar wind record on the Moon: deciphering presolar from planetary nitrogen. Science 290:1142-1145

Haskin LA (1985) Chapter 4. Petrogenetic modeling - Use of rare earth elements. *In*: Rare Earth Element Geochemistry, Developments in Geochemistry 2. Henderson P (ed) Elsevier, p 115-152

Haskin LA, Gillis JJ, Korotev RL, Jolliff BL (2000) The materials of the lunar Procellarum KREEP Terrane: a synthesis of data from geomorphological mapping, remote sensing, and sample analyses. J Geophys Res 105:20,403-20,415

Haskin LA, Korotev RL (1977) Test of a model for trace element partition during closed-system solidification of a silicate liquid. Geochim Cosmochim Acta 41:921-939

Haskin LA, Korotev RL, Rockow KM, Jolliff BL (1998) The case for an Imbrium origin of the Apollo thorium-rich impact-melt breccias. Meteorit Planet Sci 33:959-975

Haskin LA, Warren PH (1991) Lunar chemistry. *In*: Lunar Sourcebook: A User's Guide to the Moon. Heiken G, Vaniman DT, French BM (eds) Cambridge University Press, p 357-474

Hawke BR, Head JW (1978) Lunar KREEP volcanism: geologic evidence for history and mode of emplacement. Proc Lunar Planet Sci Conf 9:3285-3309

Hawke BR, Lucey PG, Bell JF, Spudis PD (1990) Ancient mare volcanism. LPI-LAPST Workshop on Mare Volcanism and Basalt Petrogenesis: Astounding Fundamental Concepts (AFC) Developed Over the Last Fifteen Years. p 5-6

Hawke BR, Peterson CA, Blewett DT, Bussey DBJ, Lucey PG, Taylor GJ, Spudis PD (2003) Distribution and modes of occurrence of lunar anorthosite. J Geophys Res 108(E6):10.1029/2002JE001890

Hazen RM, Bell PM, Mao HK (1978) Effects of compositional variation on absorption spectra of lunar pyroxenes. Proc Lunar Sci Conf 9:2919-2934

Hazen RM, Mao HK, Bell PM (1977) Effects of compositional variation on absorption spectra of lunar olivines. Proc Lunar Sci Conf 8:1081-1090

Head JW (1974) Lunar dark mantle deposits: Possible clues to the distribution of early mare deposits. Proc Lunar Sci Conf 5:207-222

Head JW (1976) Lunar volcanism in space and time. Rev Geophys Space Phys 14:265-300

Head JW, Wilson L (1992) Lunar mare volcanism: stratigraphy, eruption conditions, and the evolution of secondary crusts. Geochim Cosmochim Acta 56:2155-2175

Head JW, Wilson L, Wilhelms D (1997) Lunar mare basalt volcanism; early stages of secondary crustal formation and implications for petrogenetic evolution and magma emplacement processes. Lunar Planet Sci XXVIII:545-546

Heiken G, McKay DS (1974) Petrography of Apollo 17 soils. Proc Lunar Sci Conf 5:843-860

Heiken G, McKay DS, Fruland RM (1973) Apollo 16 soils: Grain size analysis and petrography. Proc Lunar Planet Sci Conf 4:251-265

Heiken G, Vaniman DT, French BM (1991) Lunar Sourcebook: A User's Guide to the Moon. Cambridge University Press

Heiken GH, Morris RV, McKay DS, Fruland RM (1976) Petrographic and ferromagnetic resonance studies of the Apollo 15 deep drill core. Proc Lunar Sci Conf 7:93-111

Herzog GF (1994) Applications of accelerator mass spectrometry in extraterrestrial materials. Nucl Instr Methods B 92:492-499

Hewins RH, Goldstein JI (1975) The provenance of metal in anorthositic rocks. Proc Lunar Sci Conf 6:343-362

Hidaka H, Ebihara M, Yoneda S (2000) Neutron capture effects on samarium, europium, and gadolinium in Apollo 15 deep drill-core samples. Meteorit Planet Sci 35:581-589

Higgins SJ, Taylor LA, Chambers JG, Patchen A, McKay DS (1996) X-ray digital-imaging petrography: Technique development for lunar mare soils. Meteorit Planet Sci 31(3):356-361

Hodges RJ (1975) Formation of the lunar atmosphere. The Moon 14:139-157

Hood LL, Coleman PJ, Wilhelms DE (1979) Lunar nearside magnetic anomalies. Proc Lunar Planet Sci Conf 19:99-113

Hood LL, Schubert G (1980) Lunar magnetic-anomalies and surface optical-properties. Science 208(4439):49-51

Hood LL, Williams CR (1989) The lunar swirls: distribution and possible origins. Proc Lunar Planet Sci Conf 19: 99-113

Hood LL, Zakharian A, Halekas J, Mitchell DL, Lin RP, Acuña MH, Binder AB (2001) Initial mapping and interpretation of lunar crustal magnetic anomalies using Lunar Prospector magnetometer data. J Geophys Res 106:27,825-27,840

Hörz F, Cintala MJ, See TH, Cardenas F, Thompson TD (1984) Grain size evolution and fractionation trends in an experimental regolith. Proc Lunar Planet Sci Conf 15:C183-C196

Housley RM, Cirlin EH, Goldberg IB, Crowe H (1976) Ferromagnetic resonance studies of lunar core stratigraphy. Proc Lunar Sci Conf 7:13-26.

Housley RM, Cirlin EH, Goldberg IB, Crowe H, Weeks RA, Perhac R (1975) Ferromagnetic resonance as a method of studying the micrometeorite bombardment history of the lunar surface. Proc Lunar Sci Conf 6:3173-3186

Housley RM, Cirlin EH, Paton N, Goldberg IB (1974) Solar wind and micrometeorite alteration of the lunar regolith. Proc Lunar Sci Conf 5:2623-2642

Hu HN, Taylor LA (1977) Lack of chemical fractionation in major and minor elements during agglutinate formation. Proc Lunar Sci Conf 8:3645-3656

Hu HN, Taylor LA (1978) Soils from Mare Crisium: Agglutinitic glass chemistry and soil development. *In:* Mare Crisium: The View from Luna 24. Merrill RB, Papike JJ (eds) Pergamon Press, p 291-302

Hubbard NJ, Meyer CJ, Gast PW, Wiesmann H (1971) The composition and derivation of Apollo 12 soils. Earth Planet Sci Lett 10:341-350

Hunten DM, Cremonese G, Sprague AL, Hill RE, Verani S, Kozlowski RW (1998) The Leonid meteor shower and the lunar sodium atmosphere. Icarus 136:298-303

Hunten DM, Kozlowski RWH, Sprague AL (1992) A possible meteor shower on the Moon. Geophys Res Lett 18: 2101-2104

Hunten DM, Morgan TH, Shemansky DE (1988) The Mercury atmosphere. *In*: Mercury. Vilas F, Chapman CR, Matthews MS (eds) University of Arizona Press, p 562-612

Hunten DM, Sprague AL (1997) Origin and character of the lunar and mercurian atmospheres. Adv Space Res 10: 1551-1560

James OB (1995) Siderophile elements in lunar impact melts: Nature of the impactors. Lunar Planet Sci XXVI:671-672

James OB (1996) Siderophile elements in lunar impact melts define nature of the of the impactors. Lunar Planet Sci XXVII:603-604

James OB, Flohr MK (1983) Subdivision of the Mg-suite noritic rocks into Mg-gabbronorites and Mg-norites. J Geophys Res 88:A603-A614

James OB, Flohr MK, Lindstrom MM (1984) Petrology and geochemistry of lunar dimict breccia 61015. Proc Lunar Planet Sci Conf 15. J Geophys Res 89:C63-C86

James OB, Hammarstrom JG (1977) Petrology of four clasts from consortium breccia 73215. Proc Lunar Sci Conf 8: 2459-2494

Jerde EA, Morris RV, Warren PH (1990) In quest of lunar regolith breccias of exotic provenance: a uniquely anorthositic sample from the Fra Mauro (Apollo 14) highlands. Earth Planet Sci Lett 98:90-108

Jerde EA, Warren PH, Morris RV, Heiken GH, Vaniman DT (1987) A potpourri of regolith breccias; "new" samples from the Apollo 14, 16, and 17 landing sites. Proc Lunar Planet Science Conf 17:E526-E536

Johnson JR, Feldman WC, Lawrence DJ, Maurice S, Swindle TD, Lucey PG (2002) Lunar Prospector epithermal neutrons from impact craters and landing sites: Implications for surface maturity and hydrogen distribution. J Geophys Res 107(E2):10.1029/2000JE001430

Johnson JR, Larson SM, Singer RB (1991a) A reevaluation of spectral ratios for lunar mare TiO_2 Mapping. Geophys Res Lett 18(11):2153-2156

Johnson JR, Larson SM, Singer RB (1991b) Remote sensing of potential lunar resources, 1. Near-side compositional properties. J Geophys Res 96(E3):18,861-18,882

Johnson TV, Saunders RS, Matson DL, Mosher JA (1977) A TiO_2 abundance map for the northern maria. Proc Lunar Sci Conf 8:1029-1036

Jolliff BL (1991) Fragments of quartz monzodiorite and felsite in Apollo 14 soil particles. Lunar Planet Sci 21:101-118

Jolliff BL (1993) A monazite-bearing clast in Apollo 17 melt breccia. Lunar Planet Sci XXIV:725-726

Jolliff BL (1998) Large-scale separation of K-frac and REEP-frac in the source regions of Apollo impact-melt breccias, and a revised estimate of the KREEP composition. Int Geology Rev 40:916-935

Jolliff BL, Floss C, McCallum IS, Schwartz JM (1999) Geochemistry, petrology, and cooling history of 14161,7373: a plutonic lunar sample with textural evidence of granitic-fraction separation by silicate-liquid immiscibility. Am Mineral 84:821-837

Jolliff BL, Gillis JJ, Haskin L, Korotev RL, Wieczorek MA (2000) Major lunar crustal terranes: surface expressions and crust-mantle origins. J Geophys Res 105:4197-4216

Jolliff BL, Haskin LA (1995) Cogenetic rock fragments from a lunar soil: evidence of a ferroan noritic-anorthosite pluton on the Moon. Geochim Cosmochim Acta 59:2345-2374

Jolliff BL, Haskin LA, Colson RO, Wadhwa M (1993) Partitioning in REE-saturating minerals: theory, experiment, and modelling of whitlockite, apatite, and evolution of lunar residual magmas. Geochim Cosmochim Acta 57: 4069-4094

Jolliff BL, Haskin LA, Korotev RL, Papike JJ, Shearer CK, Pieters C, Cohen BA (2003) Scientific expectations from a sample of regolith and rock fragments from the interior of the lunar South Pole-Aitken basin. Lunar Planet Sci XXXIV:1989 (CD-ROM)

Jolliff BL, Korotev RL, Haskin LA (1991) Geochemistry of 2-4 mm particles from Apollo 14 soil (14161) and implications regarding igneous components and soil-forming processes. Proc Lunar Planet Sci Conf 21:193-219

Jolliff BL, Korotev RL, Rockow KM (1998) Geochemistry and petrology of lunar meteorite Queen Alexandra Range 94281, a mixed mare and highland regolith breccia, with special emphasis on very-low-Ti mafic components. Meteorit Planet Sci 33:581-601

Jolliff BL, Rockow KM, Korotev RL, Haskin LA (1996) Lithologic distribution and geologic history of the Apollo 17 site: the record in soils and small rock particles from the highland massifs. Meteorit Planet Sci 31:116-145

Jull AJT, Cloudt S (1996) Evidence for recent gardening or disturbance of lunar core 76001 from solar-cosmic-ray records of ^{14}C. Lunar Planet Sci XXVII:627-628

Jull AJT, Cloudt S, Donahue DJ, J.M. S, Reedy RC, Masarik J (1998) ^{14}C depth profiles in Apollo 15 and 17 cores and lunar rock 68815. Geochim Cosmochim Acta 62:3025-3036

Jull AJT, Lal D, McHargue LR, Burr GS, Donahue DJ (2000) Cosmogenic and implanted radionuclides studied by selective etching of lunar soils. Nucl Instr Methods B 172:867-872

Kaula WM, Schubert G, Lingenfelter RE, Sjogren WL, Wollenhaupt WR (1972) Analysis and interpretation of lunar laser altimetry. Proc Lunar Sci Conf 3:2189-2204

Kaula WM, Schubert G, Lingenfelter RE, Sjogren WL, Wollenhaupt WR (1974) Apollo laser altimetry and inferences as to lunar structure. Proc Lunar Sci Conf 5:3049-3058

Keil K, Kurat G, Green JA (1972) Lithic fragments, glasses and chondrules from Luna 16 fines. Earth Planet Sci Lett 13:243-256

Keller L, McKay D (1997) The nature and origin of rims on lunar soil grains. Geochim Cosmochim Acta 61:2331-2340

Keller LP, Clemett SJ (2001) Formation of nanophase iron in the lunar regolith. Lunar Planet Sci XXXII:2097 (CD-ROM)

Keller LP, McKay DS (1993) Discovery of vapor deposits in the lunar regolith. Science 261:1305-1307

Keller LP, Wentworth S, McKay D (1998) Space Weathering: Reflectance spectroscopy and TEM analysis of individual lunar soil grains. Proc Lunar Planet Sci Conf 29:1762

Keller LP, Wentworth SJ, McKay DS, Taylor LA, Pieters C, Morris RV (1999) Space weathering in the fine size fractions of lunar soils: Soil maturity effects. Workshop on New Views of the Moon II, p. 32-34. Lunar and Planetary Institute, Houston, Texas

Keller LP, Wentworth SJ, McKay DS, Taylor LA, Pieters C, Morris RV (2000) Space weathering in the fine size fractions of lunar soils: mare/highland differences. Lunar Planet Sci XXXI:1655

Kerridge JF (2001) Isotopic variability of nitrogen in lunar regolith. Science 293:U1-U2

King TVV, Ridley WI (1987) Relation of the Spectroscopic Reflectance of Olivine to Mineral Chemistry and Some Remote-Sensing Implications. J Geophys Res-Solid Earth Planets 92(B11):11457-11469

Klein CJ, Drake JC, Frondel C (1971) Mineralogical, petrological, and chemical features of four Apollo 12 lunar microgabbros. Proc Lunar Sci Conf 2:265-284

Korotev RL (1976) Geochemistry of grain size fractions of soils from the Taurus-Littrow valley floor. Proc Lunar Sci Conf 7:695-726

Korotev RL (1983a) Geochemical study of individual 1-2 mm particles from Apollo 16 soil 67712. Lunar Planet Sci Conf XIV:399-400

Korotev RL (1983b) Geochemical study of individual 1-2 mm particles from Apollo 16 soil 65502. Lunar Planet Sci Conf XIV:397-398

Korotev RL (1987a) The nature of the meteoritic components of Apollo 16 soil. As inferred from correlations of iron, cobalt, iridium, and gold with nickel. Proc Lunar Planet Sci Conf 17. J Geophys Res 92:E447-E461

Korotev RL (1987b) The meteoritic component of Apollo 16 noritic impact melt breccias. Proc Lunar Planet Sci Conf 17. J Geophys Res 92:E491-E512

Korotev RL (1987c) Mixing levels, the Apennine Front soil component, and compositional trends in the Apollo 15 soils. Proc Lunar Planet Sci Conf 17. J Geophys Res 92:E411-E431

Korotev RL (1991) Geochemical stratigraphy of two regolith cores from the central highlands of the Moon. Proc Lunar Planet Sci Conf 21:229-289

Korotev RL (1994) Compositional variation in Apollo 16 impact-melt breccias and inferences for the geology and bombardment history of the Central Highlands of the Moon. Geochim Cosmochim Acta 58:3931-3969

Korotev RL (1996) On the relationship between the Apollo 16 ancient regolith breccias and feldspathic fragmental breccias, and the composition of the prebasin crust in the central highlands of the moon. Meteorit Planet Sci 31: 403-412

Korotev RL (1997) Some things we can infer about the moon from the composition of the Apollo 16 regolith. Meteorit Planet Sci 32:447-478

Korotev RL (2000) The great lunar hot spot and the composition and origin of the Apollo mafic ("LKFM") impact-melt breccias. J Geophys Res 105:4317-4345

Korotev RL, Gillis JJ (2001) A new look at the Apollo 11 regolith and KREEP. J Geophys Res 106(E6):12,339-12,354

Korotev RL, Haskin LA (1988) Europium mass balance in polymict samples and implications for plutonic rocks of the lunar crust. Geochim Cosmochim Acta 52:1795-1813

Korotev RL, Jolliff BL (2000) Siderophile element concentrations in two metal fragments from the Apollo 16 regolith. Lunar Planet Sci XXXI:1385 (CD-ROM)

Korotev RL, Jolliff BL (2001) The curious case of the lunar magnesian granulitic breccias. Lunar Planetary Science 32:1013 (CD-ROM)

Korotev RL, Jolliff BL, Campbell AJ, Humayun M (2003a) Laser-ablation ICP-MS analyses of meteoritic metal grains in lunar impact-melt breccias. Lunar Planet Sci XXXIV:1487 (CD-ROM)

Korotev RL, Jolliff BL, Rockow KM (1996) Lunar meteorite Queen Alexandra Range 93096 and the iron concentration of the lunar highland surface. Meteorit Planet Sci 31:909-924

Korotev RL, Jolliff BL, Zeigler RA (2000) The KREEP components of the Apollo 12 regolith. Lunar Planet Sci XXXI: 1363 (CD-ROM)

Korotev RL, Jolliff BL, Zeigler RA, Gillis JJ, Haskin LA (2003b) Feldspathic Lunar Meteorites and Their Implications for Compositional Remote Sensing of the Lunar Surface and the Composition of the Lunar Crust. Geochim Cosmochim Acta 67:4895-4923

Korotev RL, Kremser DT (1992) Compositional variations in Apollo 17 soils and their relationship to the geology of the Taurus-Littrow site. Proc Lunar Planet Sci Conf 22:275-301

Korotev RL, Morris RV (1993) Composition and maturity of Apollo 16 regolith core 60013/14. Geochim Cosmochim Acta 57:4813-4826

Korotev RL, Morris RV, Jolliff BL, Schwarz C (1997a) Lithological variation with depth and decoupling of maturity parameters in Apollo 16 regolith core 68001/2. Geochim Cosmochim Acta 61:2989-3002

Korotev RL, Morris RV, Lauer HVJ (1984) Stratigraphy and geochemistry of the Stone Mountain core (64001/2). Proc Lunar Planet Sci Conf 15:C143-C160

Korotev RL, Rockow KM, Jolliff BL, Haskin LA (1997b) Lithic fragments of the Cayley plains. Lunar Planet Sci XXVIII:753-754

Laul JC, Lepel EA, Vaniman DT, Papike JJ (1979) The Apollo 17 drill core: Chemical systematics of grain-size fractions. Proc Lunar Planet Sci Conf 10:1269-1298

Laul JC, Papike JJ (1980) The Apollo 17 drill core: Chemistry of size fractions and the nature of the fused soil component. Proc Lunar Planet Sci Conf 11:1395-1413

Laul JC, Papike JJ, Simon SB (1981) The lunar regolith: Comparative studies of the Apollo and Luna sites. Chemistry of soils from Apollo 17, Luna 16, 20, and 24. Proc Lunar Planet Sci Conf 12B:389-407

Laul JC, Rode OD, Simon SB, Papike JJ (1987) The lunar regolith; chemistry and petrology of Luna 24 grain size fractions. Geochim Cosmochim Acta 51:661-673

Laul JC, Vaniman DT, Papike JJ, Simon S (1978) Chemistry and petrology of size fractions of Apollo 17 deep drill core 70009-70006. Proc Lunar Planet Sci Conf 9:2065-2097

Lawrence DJ, Elphic RC, Feldman WC, Prettyman T, Gasnault O, Maurice S (2003) Small-area thorium features on the lunar surface. J Geophys Res 108(E9):doi 10.1029/2003/JE002050

Lawrence DJ, Feldman WC, Barraclough BL, Binder AB, Elphic RC, Maurice S, Thomsen DR (1998) Global elemental maps of the Moon: the Lunar Prospector gamma-ray spectrometer. Science 281:1484-1489

Lawrence DJ, Feldman WC, Barraclough BL, Binder AB, Elphic RC, Maurice S, Miller MC, Prettyman TH (2000) Thorium abundances on the lunar surface. J Geophys Res 105:20,307-20,331

Lawrence DJ, Feldman WC, Barraclough BL, Elphic RC, Maurice S, Binder AB, Miller MC, Thomsen DR (1999) High resolution measurements of absolute thorium abundance on the lunar surface. Geophys Res Lett 26(17): 2681-2683

Lawrence DJ, Feldman WC, Elphic RC, Little RC, Prettyman TH, Maurice S, Lucey PG, Binder AB (2002) Iron abundances on the lunar surface as measured by the Lunar Prospector gamma-ray and neutron spectrometers. J Geophys Res 107(E12):10.1029/2001JE001530

Lawson SL, Jakosky BM (2001) Lunar surface thermophysical properties derived from Clementine LWIR and **UVVIS** images. J Geophys Res 106(E11):27,911-27,932

Lawson SL, Jakosky BM, Park H-S, Mellon MT (2000) Brightness temperature of the lunar surface: Calibration and global analysis of the Clementine long-wave infrared camera data. J Geophys Res 105(E2):4273-4290

Le Mouélic S, Langevin Y, Erard S (1999) The distribution of olivine in the crater Aristarchus inferred from Clementine NIR data. Geophys Res Lett 26(9):1195-1198

Le Mouélic S, Langevin Y, Erard S, Pinet P, Chevrel S, Daydou Y (2000) Discrimination between maturity and composition of lunar soils from integrated Clementine **UV-VIS**ible/near-infrared data: Application to the Aristarchus Plateau. J Geophys Res 105(E4):9445-9455

Le Mouélic S, Lucey PG, Langevin Y, Hawke BR (2002) Calculating iron contents of lunar highland materials surrounding Tycho crater from integrated Clementine **UV-VIS**ible and near-infrared data. J Geophys Res 107(E10):5074, doi:10.1029/2000JE001484

Leya I, Lange HJ, Lüpke M, Neupert U, Daunke R, Fanenbruck O, Michel R, Rösel R, Meltzow B, Schiekel T, Sudbrock F, Herpers U, Filges D, Bonani G, Dittrich-Hannen B, Suter M, Kubik PW, Synal HA (2000a) Simulation of the interaction of galactic cosmic-ray protons with meteoroids: On the production of radionuclides in thick gabbro and iron targets irradiated isotropically with 1.6 GeV protons. Meteorit Planet Sci 35:287-318

Leya I, Neumann S, Wieler R, Michel R (2001) The production of cosmogenic nuclides by galactic cosmic-ray particles for 2p exposure geometries. Meteorit Planet Sci 36:1547-1561

Leya I, Wieler R, Halliday AN (2000b) Cosmic-ray production of tungsten isotopes in lunar samples and meteorites and its implications for Hf-W cosmochemistry. Earth Planet Sci Lett 175:1-12

Lin RP, Mitchell DL, Curtis DW, Anderson KA, Carlson CW, McFadden J, Acuña MH, Hood LL, Binder AB (1998) Lunar surface magnetic fields and their interaction with the solar wind: results from lunar prospector. Science 281:1480-1484

Lindstrom MM, Lindstrom DJ (1986) Lunar granulites and their precursor anorthositic norites of the early lunar crust. Proc Lunar Planet Sci Conf 16th in J Geophys Res 91:D263-D276

Lindstrom MM, Mittlefehldt DW, Morris RV, Martinez RR, Wentworth S (1995) QUE93069, a more mature regolith breccia for the Apollo 25th anniversary. Lunar Planet Sci XXVI:849-850

Lindstrom MM, Schwarz C, Score R, Mason B (1991) MacAlpine Hills 88104 and 88105 lunar highland meteorites: General description and consortium overview. Geochim Cosmochim Acta 55:2999-3007

Lingenfelter RE, Canfield EH, Hess WN (1961) The lunar neutron flux. J Geophys Res 66:2665-2671

Little RC, Feldman WC, Maurice S, Genetay I, Lawrence DJ, Lawson SL, Gasnault O, Barraclough BL, Elphic RC, Prettyman TH, Binder AB (2003) Latitude variation of the subsurface lunar temperature: Lunar Prospector thermal neutrons. J Geophys Res 108(E5):10.1029/2001JE001497

Love SG, Brownlee DE (1993) A direct measurement of the terrestrial mass accretion rate of cosmic dust. Science 262: 550-553

Lovering JF, Wark DA, Gleadow AJW, Britten R (1974) Lunar monazite: A late-stage (mesostasis) phase in mare basalts. Earth Planet Sci Lett 21:164-168

Lucey PG (1998) Model near-infrared optical constants of olivine and pyroxene as a function of iron content. J Geophys Res 103:1703-1714

Lucey PG (2002) Radiative transfer model constraints on the shock state of remotely sensed lunar anorthosites. Geophys Res Lett29(10):124-1 to 124-3

Lucey PG (2004) Mineral maps of the Moon. Geophys Res Lett 31(8): doi:10.1029/2003GL019406

Lucey PG, Blewett DT, Hawke BR (1998) Mapping the FeO and TiO2 content of the lunar surface multispectral imagery. J Geophys Res 103(E2):3679-3699

Lucey PG, Blewett DT, Jolliff BL (2000a) Lunar iron and titanium abundance algorithms based on final processing Clementine **UVVIS** images. J Geophys Res 105(E8):20,297-20,305

Lucey PG, Blewett DT, Taylor GJ, Hawke BR (2000b) Imaging of lunar surface maturity. J Geophys Res 105(E8): 20377-20386

Lucey PG, Hawke BR (1987) Probable outcrops of Mg-gabbronorite in the lunar highlands detected by near-infrared remote sensing. Proc Lunar Planet Sci Conf 18:578

Lucey PG, Hawke BR, Pieters CM, Head JW, McCord TB (1986) A compositional study of the Aristarchus region of the Moon using near-infrared reflectance spectroscopy. J Geophys Res-Solid Earth Planets 91(B4):D344-D354

Lucey PG, Taylor GJ, Malaret E (1995) Abundance and distribution of iron on the Moon. Science 268(5214):1150-1153

Madey TE, Yakshinskiy BV, Ageev VN, Johnson RE (1998) Desorption of alkali atoms from oxide surfaces: relevance to origins of Na and K in atmospheres of Mercury and the Moon. J Geophys Res 103:5873-5887

Manatt SL, Elleman DD, Vaughn RW, Chan SI, Tsay F-D, Huntress WT Jr. (1970) Magnetic resonance of lunar samples. Science 167:709-711

Margot J, Campbell DB, Jurgens RF, Slade MA (2000) Digital elevation models of the Moon from Earth-based radar interferometry. IEEE Geosci Rem Sens 38:1122-1133

Marvin UB (1983) The discovery and initial characterization of Allan Hills 81005; the first lunar meteorite. Geophys Res Lett 10:775-778

Marvin UB, Lindstrom MM, Holmberg BB, Martinez RR (1991) New observations on the quartz monzodiorite-granite suite. Proc Lunar Planet Sci Conf 21:119-135

Marvin UB, Wood JA, Taylor GJ, Reid JB Jr., Powell BN, Dickey JS Jr., Bower JF (1971) Relative proportions and probable sources of rock fragments in the Apollo 12 soil samples. Proc Lunar Sci Conf 2:679-699

Masarik J, Nishiizumi K, Reedy RC (2001) Production rates of cosmogenic helium-3, neon-21, and neon-22 in ordinary chondrites and the lunar surface. Meteorit Planet Sci 36:643-650

Mathew KJ, Marti K (2001) Lunar nitrogen: indigenous signature and cosmic-ray production rate. Earth Planet Sci Lett 184:659-669

Maurice S, Feldman WC, Lawrence DJ, Elphic RC, Gasnault O, d'Uston C, Genetay I, Lucey PG (2000) High-energy neutrons from the Moon. J Geophys Res 105:20,365-20,375

Maurice S, Lawrence DJ, Feldman WC, Elphic RC, Gasnault O (2004) Reduction of neutron data from Lunar Prospector. J Geophys Res 109:doi 10.1029/2003JE002208

McCallum IS, O'Brien HE (1996) Stratigraphy of the lunar highlands crust: depth of burial of lunar samples from cooling rate studies. Am Mineral 81:1166-1175

McConnochie TH, Buratti BJ, Hillier JK, Tryka KA (2002) A search for water ice at the lunar poles with Clementine images. Icarus 156(2):335-351

McCord TB (1969) Color differences on the lunar surface. J Geophys Res 74(12):3131-3142

McCord TB, Adams JB (1973) Progress in remote optical analysis of lunar surface composition. The Moon 7:453-474

McCord TB, Clark RN, Hawke BR, McFadden LA, Owensby PD, Pieters CM, Adams JB (1981) Moon: near-infrared spectral reflectance, a good first look. J Geophys Res 86(B11):10,883-10,892

McCord TB, Johnson TV (1969) Relative spectral reflectivity 0.4-1m of selected areas of the lunar surface. J Geophys Res 74(17):4395-4401

McCord TB, Johnson TV (1970) Lunar spectral reflectivity (0.30 to 2.50 microns) and implications for remote mineralogical analysis. Science 169:855-858

McEwen AS, Robinson MS (1997) Mapping of the moon by Clementine. Comparative Studies Moon Mercury 19(10): 1523-1533

McEwen AS, Robinson MS, Eliason EM, Lucey PG, Duxbury TC, Spudis PD (1994) Clementine observations of the Aristarchus Region of the Moon. Science 266(5192):1858-1862

McKay DS, Basu A, Nace G (1980) Lunar core 15010/11; grain size, petrology, and implications for regolith dynamics. Proc Lunar Planet Sci Conf 11:1531-1550

McKay DS, Basu A, Waits G (1978a) Grain size and the evolution of Luna 24 soils. *In:* Mare Crisium: The View from Luna 24. Merrill RB, Papike JJ (eds) Pergamon Press, p 125-136

McKay DS, Bogard DD, Morris RV, Korotev RL, Johnson P, Wentworth SJ (1986) Apollo 16 regolith breccias: characterization and evidence for early formation in the mega-regolith. Proc Lunar Planet Sci Conf 16. J Geophys Res :D277-D303

McKay DS, Dungan MA, Morris RV, Fruland RM (1977) Grain size, petrographic, and FMR studies of double core 60009/10: a study of soil evolution. Proc Lunar Sci Conf 8:2929-2952

McKay DS, Fruland RM, Heiken GH (1974) Grain size and the evolution of lunar soil. Proc Lunar Sci Conf 5:887-906

McKay DS, Heiken G, Basu A, Blanford G, Simon S, Reedy R, French B, Papike JJ (1991) The lunar regolith. *In:* The Lunar Source Book: A User's Guide to the Moon. Heiken G, Vaniman D, French B, (eds) Cambridge Univ. Press, p 285-356

McKay DS, Heiken GH, Waits G (1978b) Core 74001/2; grain size and petrology as a key to the rate of *in situ* reworking and lateral transport on the lunar surface. Proc Lunar Planet Sci Conf 9:1913-1932

McKay DS, Williams RJ (1979) A geologic assessment of potential lunar ores. *In:* Space Resources and Space Settlement, NASA SP-428. Billingham J, Gilbreath W, O'Leary B (eds) NASA, p 243-256

McKay GA, unnamed coauthors (1986) Topic 2: Apollo 15 KREEP basalt. *In:* Geology and Petrology of the Apollo 15 Landing Site, LPI Tech Rpt 86-03. Spudis PD, Ryder G (eds) Lunar and Planetary Institute, p 14-16

McKay GA, Weill DF (1977) KREEP petrogenesis revisited. Proc Lunar Sci Conf 8:2339-2355

McKinley JP, Taylor GJ, Keil K, Ma M-S, Schmitt RA (1984) Apollo 16; impact melt sheets, contrasting nature of the Cayley Plains and Descartes Mountains, and geologic history. Proc Lunar Planet Sci Conf 14:514-524

Melendrez DE, Johnson JR, Larson SM, Singer RB (1994) Remote sensing of potential lunar resources, 2. High spatial resolution mapping of spectral reflectance ratios and implications for near side mare TiO_2 content. J Geophys Res 99(E3):5601-5619

Mendell WW (1976) Degradation of large, period II lunar craters. Proc Lunar Planet Sci Conf 7:2705-2716

Mendell WW, Low FJ (1975) Infrared orbital mapping of lunar features. Proc Lunar Planet Sci Conf 6:2711-2719

Mendillo M (2001) The atmosphere of the moon. Earth Moon Planets 85-86:271-277

Mendillo M, Baumgardner J, Wilson J (1999) Observational test for the solar wind origin of the Moon's extended sodium atmosphere. Icarus 137:13-23

Metzger AE (1993) Composition of the Moon as determined from orbit by gamma ray spectroscopy. *In:* Remote Geochemical Analysis: Alemental and Mineralogical Composition. Pieters CM, Englert PAJ (eds) Cambridge Univ. Press, p 341-365

Metzger AE, Haines EL, Parker RE, Radocinski RG (1977) Thorium concentrations in the lunar surface. 1. Regional values and crustal content. Proc Lunar Sci Conf 8:949-999

Metzger AE, Parker RE (1979) The distribution of titanium on the lunar surface. Earth Planet Sci Lett 45:155-171

Metzger AE, Trombka JI, Peterson LE, Reedy RC, Arnold JR (1973) Lunar surface radioactivity: Preliminary results of the Apollo 15 and Apollo 16 gamma-ray spectrometer experiments. Science 179:800-803

Meyer CJ, McKay DS, Anderson DH, Butler PJ (1975) The source of sublimates on the Apollo 15 green and Apollo 17 orange glass samples. Proc Lunar Sci Conf 6:1673-1699

Michel R (1999) Long-lived radionuclides as tracers in terrestrial and extraterrestrial matter. Radiochimica Acta 87: 47-73

Michel R, Bodemann R, Busemann H, Daunke R, Gloris M, Lange HJ, Klug B, Krins A, Leya I, Lüpke M, Neumann S, Reinhardt H, Schnatz-Büttgen M, Herpers U, Schiekel T, Sudbrock F, Holmqvist B, Condé H, Malmborg P, Suter M, Dittrich-Hannen B, Kubik PW, Synal HA, Filges D (1997) Cross sections for the production of residual nuclides by low- and medium-energy protons from the target elements C, N, O, Mg, Al, Si, Ca, Ti, V, Mn, Fe, Co, Ni, Cu, Sr, Y, Zr, Nb, Ba and Au. Nucl Instr Methods B 129:153-193

Morgan TH, Zook HA, Potter AE (1988) Impact-driven supply of sodium and potassium to the atmosphere of Mercury. Icarus 74:156-170

Morgan TH, Zook HA, Potter AE (1989) Production of sodium vapor from exposed regolith in the inner solar system. Proc Lunar Planet Sci Conf 19:297-304

Morris RV (1976) Surface exposure indices of lunar soils: a comparative FMR study. Proc Lunar Sci Conf 7:315-335

Morris RV (1977) Origin and evolution of the grains-size dependence of the concentration of fine-grained metal in lunar soils: the maturation of lunar soils to a steady-state stage. Proc Lunar Planet Sci Conf 8:3719-3747

Morris RV (1978a) The surface exposure (maturity) of lunar soils; some concepts and I_s/FeO compilation. Proc Lunar Planet Sci Conf 9:2287-2297

Morris RV (1978b) *In situ* reworking (gardening) of the lunar surface: evidence from the Apollo cores. Proc Lunar Planet Sci Conf 9:1801-1811

Morris RV (1980) Origins and size distribution of metallic iron particles in the lunar regolith. Proc Lunar Planet Sci Conf 11:1697-1712

Morris RV (1985) Determination of optical penetration depths from reflectance and transmittance measurements on albite powders. Lunar Planet Sci XVI:581-582

Morris RV, Gibbons RV, Hörz F (1975) FMR thermomagnetic studies up to 900ºC of lunar soils and potential magnetic analogues. Geophys Res Lett 2:461-464

Morris RV, Gose WA (1976) Ferromagnetic resonance and magnetic studies of cores 60009/60010 and 60003: Compositional and surface-exposure stratigraphy. Proc Lunar Sci Conf 7:1-11

Morris RV, Gose WA (1977) Depositional history of core section 74001; depth profiles of maturity, FeO, and metal. Proc Lunar Sci Conf 8:3113-3122

Morris RV, Korotev RL, Lauer HVJ (1989) Maturity and geochemistry of the Van Serg crater core (79001/2) with implications for micrometeorite composition. Proc Lunar Planet Sci Conf 19:269-284

Morris RV, Lauer HVJ (1980) The case against UV photostimulated oxidation of magnetite. Geophys Res Lett 7:605-608

Morris RV, Lauer HVJ, Gose WA (1979) Characterization and depositional and evolutionary history of the Apollo 17 deep drill core. Proc Lunar Planet Sci Conf 10:1141-1157

Morris RV, See TH, Hörz F (1983) Some evidence concerning the source material of large glass objects from the Moon. Proc Lunar Planet Sci Conf 14:528-529

Morris RV, See TH, Hörz F (1986) Composition of the Cayley Formation at Apollo 16 as inferred from impact melt splashes. Proc Lunar Planet Sci Conf 17:E21-E42

Naney MT, Crowl DM, Papike JJ (1976) The Apollo 16 drill core: Statistical analysis of glass chemistry and the characterization of a high alumina-silica poor (HASP) glass. Proc Lunar Sci Conf 7:155-184

Nash DB, Salisbury JW, Conel JE, Lucey PG, Christensen PR (1993) Evaluation of infrared-emission spectroscopy for mapping the Moons surface-composition from lunar orbit. J Geophys Res 98(E12):23535-23552

Neal CR, Taylor LA (1989) The nature of barium partitioning between immiscible melts: A comparison of experimental and natural systems with reference to lunar felsite petrogenesis. Proc Lunar Planet Sci Conf 19:209-218

Neal CR, Taylor LA (1992) Petrogenesis of mare basalts: a record of lunar volcanism. Geochim Cosmochim Acta 56: 2177-2211

Neal CR, Taylor LA, Lindstrom MM (1988) Apollo 14 mare basalt petrogenesis: assimilation of KREEP-like components by a fractionating magma. Proc Lunar Planet Sci Conf 18:139-153

Neal CR, Taylor LA, Patchen AD (1989) High alumina (HA) and very high potassium (VHK) basalt clasts from Apollo 14 breccias. Part 1. Mineralogy and petrology: Evidence of crystallization from evolving magmas. Proc Lunar Planet Sci Conf 19:137-145.

Nehru CE, Prinz M, Dowty E, Keil K (1974) Spinel-group minerals and ilmenite in Apollo 15 rock samples. Am Mineral 59:1220-1234

Nehru CE, Warner RD, Keil K (1976) Electron Microprobe Analyses of Opaque Mineral Phases from Apollo 11 Basalts. University of New Mexico Special Publication 17

Nishiizumi K, Caffee MW (2001) Beryllium-10 from the Sun. Science 294:352-354

Nishiizumi K, Caffee MW, Jull AJT, Reedy RC (1996) Exposure history of lunar meteorites Queen Alexandra range 93069 and 94269. Meteorit Planet Sci 31:893-896

Nishiizumi K, Fink D, Klein J, Middleton R, Masarik J, Reedy RC, Arnold JR (1997) Depth profile of ^{41}Ca in an Apollo 15 drill core and the low-energy neutron flux in the Moon. Earth Planet Sci Lett 148:545-552

Nishiizumi K, Kohl CP, Arnold JR, Finkel RC, Caffee MW, Masarik J, Reedy RC (1995) Final results of cosmogenic nuclides in lunar rock 64455. Lunar Planet Sci XXVI:1055-1056

Nishiizumi K, Masarik J, Caffee MW, Jull AJT (1999) Exposure histories of pair lunar meteorites EET 96008 and EET 87521. Lunar Planet Sci XXX:1980 (CD-ROM)

Noble SK, Pieters CM, Taylor LA, Morris RV, Allen CC, McKay DS, Keller LP (2001) The optical properties of the finest fraction of lunar soil: implications for space weathering. Meteorit Planet Sci 36:31-42

Norman MD, Ryder G (1980) Geochemical constraints on the igneous evolution of the lunar crust. Proc Lunar Planet Sci Conf 11:317-331

Nozette S, Rustan P, Pleasance LP, Horan DM, Regeon P, Shoemaker EM, Spudis PD, Acton CH, Baker DN, Blamont JE, Buratti BJ, Corson MP, Davies ME, Duxbury TC, Eliason EM, Jakosky BM, Kordas JF, Lewis IT, Lichtenberg CL, Lucey PG, Malaret E, Massie MA, Resnick JH, Rollins CJ, Park HS, McEwen AS, Priest RE, Pieters CM, Reisse RA, Robinson MS, Simpson RA, Smith DE, Sorenson TC, Breugge RWV, Zuber MT (1994) The Clementine Mission to the Moon - Scientific Overview. Science 266:1835-1839

Okada T, Kato M, Fujimura A, Tsunemi H, Kitamoto S (1999) X-ray fluorescence spectrometry with the SELENE orbiter. Adv Space Res 23:1833-1836

Palme H (1977) On the age of KREEP. Geochim Cosmochim Acta 41:1791-1801

Papike JJ (1987) Chemistry of the rock-forming silicates: ortho, ring, and single-chain structures. Rev Geophys 25: 1483-1526

Papike JJ (1988) Chemistry of the rock-forming silicates: multiple-chain, sheet, and framework silicates. Rev Geophys 26:407-444

Papike JJ (1998a) Planetary Materials. Rev Mineralogy, Volume 36. Mineralogical Society of America, Washington DC

Papike JJ (1998b) Comparative planetary mineralogy: chemistry of melt-derived pyroxene, feldspar, and olivine. Rev Mineral 36:7-1–7-11

Papike JJ, Bence AE, Brown GE, Prewitt CT, Wu CH (1971) Apollo 12 clinopyroxenes: exsolution and epitaxy. Earth Planet Sci Lett 10:307-315

Papike JJ, Cameron M (1976) Crystal chemistry of silicate minerals of geophysical interest. Rev Geophys Space Phys 14:37-80

Papike JJ, Hodges FN, Bence AE, Cameron M, Rhodes JM (1976) Mare basalts: crystal chemistry, mineralogy, and petrology. Rev Geophys Space Phys 14(4):475-540

Papike JJ, Ryder G, Shearer CK (1998) Lunar samples. Rev Mineral 36:5-1–5-234

Papike JJ, Simon SB, Laul JC (1982) The lunar regolith: chemistry, mineralogy, petrology. Rev Geophys Space Phys 20(4):761-826

Papike JJ, Simon SB, White C, Laul JC (1981) The relationship of the lunar regolith <10 μm fraction and agglutinates; Part I, A model for agglutinate formation and some indirect supportive evidence. Proc Lunar Planet Sci Conf 12: 409-420

Papike JJ, Spilde MN, Adcock CT, Fowler GW, Shearer CK (1997) Trace element fractionation by impact-induced volatilization: SIMS study of lunar HASP Samples. Am Mineral 82:630-634

Papike JJ, Taylor LA, Simon SE (1991) Lunar minerals. *In:* Lunar Sourcebook: A User's Guide to the Moon, Heiken G, Vaniman DT, French BM (eds) Cambridge University Press, p 121-181

Pearce GW, Strangway DW, Gose WA (1974) Magnetic properties of Apollo samples and implications for regolith formation. Proc Lunar Sci Conf 5:2815-2826

Pettengill GH, Zisk SH, Thompson TW (1974) The mapping of lunar radar scattering characteristics. The Moon 10: 3-16

Pieters CM (1982) Copernicus crater central peak - lunar mountain of unique composition. Science 215:59-61

Pieters CM (1983) Strength of mineral absorption features in the transmitted component of near-infrared reflected light - 1st results from Relab. J Geophys Res 88(NB11):9534-9544

Pieters CM (1986) Composition of the lunar highland crust from near-infrared spectroscopy. Rev Geophys 24:557-578

Pieters CM (1993) Compositional diversity and stratigraphy of the lunar crust derived from reflectance spectroscopy. *In:* Remote Geochemical Analysis: Elemental and Mineralogical Composition (Topics in remote sensing 4). Englert PAJ, Pieters CM (eds) Cambridge University Press, p 309-339

Pieters CM, Fischer EM, Rode O, Basu A (1993) Optical effects of space weathering - the role of the finest fraction. J Geophys Res 98:20817-20824

Pieters CM, Head JW, Gaddis L, Jolliff B, Duke M (2001a) Rock types of South Pole-Aitken basin and extent of basaltic volcanism. J Geophys Res 106:28001-28022

Pieters CM, Head JW, Gaddis LR, Jolliff BL, Duke M (2001b) The character and possible origin of olivine hill in South Pole-Aitken Basin. Proc Lunar Planet Sci Conf XXXII:#1810

Pieters CM, Hill PM, Magee KP, Sunshine JM (1988) Water on the Moon? Potential detection of recent cometary impacts in the Earth/Moon environment using LGO/VIMS. Lunar Planet Sci 19:935-936

Pieters CM, McCord TB (1976) Characterization of lunar mare basalt types: A remote sensing study using reflection spectroscopy of surface soils. Proc Lunar Sci Conf 7:2677-2690

Pieters CM, Taylor LA (2003) Systematic global mixing and melting in lunar soil evolution. Geophys Res Lett 30(20): 2048, doi:10.1029/2003GL018212

Pieters CM, Taylor LA, Noble SK, Keller LP, Hapke B, Morris RV, Allen CC, McKay DS, Wentworth S (2000) Space weathering on airless bodies: Resolving a mystery with lunar samples. Meteorit Planet Sci 35(5):1101-1107

Pieters CM, Tompkins S (1999) Tsiolkovsky crater: a window into crustal processes on the lunar farside. J Geophys Res 104:21935-21949

Pieters CM, Tompkins S, Head JW, Hess PC (1997) Mineralogy of the mafic anomaly in the South Pole-Aitken Basin: implication for excavation of the lunar mantle. Geophys Res Lett 24(15):1903-1906

Pieters CM, Wilhelms DE (1985) Origin of olivine at Copernicus. J Geophys Res 90:C415-C420

Pillinger CT, Davis PR, Eglinton G, Gowar AP, Jull AJT, Maxwell JR, Housley RM, Cirlin EH (1974) The association between carbide and finely divided metallic iron in lunar fines. Proc Lunar Sci Conf 5:1949-1961

Polnau E, Eugster O (1998) Cosmic-ray produced, radiogenic, and solar noble gases in lunar meteorites Queen Alexandra Range 94269 and 94281. Meteorit Planet Sci 33:313-319

Potter AE, Morgan TH (1985) Discovery of sodium in the atmosphere of Mercury. Science 229:651-653

Potter AE, Morgan TH (1986) Potassium in the atmosphere of Mercury. Icarus 67:336-340

Potter AE, Morgan TH (1988a) Extended sodium atmosphere of the Moon. Geophys Res Lett 15:1515-1518

Potter AE, Morgan TH (1988b) Discovery of sodium and potassium vapor in the atmosphere of the Moon. Science 241:675-680

Prettyman TH, Feldman WC, Lawrence DJ, McKinney GW, Binder AB, Elphic RC, Gasnault O, Maurice S, Moore KR (2002a) Library least squares analysis of Lunar Prospector gamma ray spectra. Lunar Planet Sci XXXIII: 2012 (CD-ROM)

Prettyman TH, Lawrence DJ, Vaniman DT, Elphic RC, Feldman WC (2002b) Classification of regolith materials from lunar prospector data reveals a magnesium-rich province. *In:* The Moon Beyond 2002: Next steps in Lunar Science and Exploration, LPI Contr. Abstract #1128. Lunar and Planetary Institute

Quick JE, Albee AL, Ma M-S, Murali AV, Schmitt RA (1977) Chemical composition and possible immiscibility of two silicate melts in 12013. Proc Lunar Sci Conf 8:2153-2189

Quick JE, James OB, Albee AL (1981) Petrology and petrogenesis of lunar breccia 12013. Proc Lunar Planet Sci Conf 12B:117-172

Rao MN, Garrison DH, Bogard DD, Reedy RC (1994) Determination of the flux and energy distribution of energetic solar protons in the past 2 Myr using lunar rock 68815. Geochim Cosmochim Acta 58:4231-4245

Rava B, Hapke B (1987) An Analysis of the Mariner 10 color ratio map of Mercury. Icarus 71(3):397-429

Reed SJB, Taylor SR (1974) Meteoritic metal in Apollo 16 samples. Meteorit Planet Sci 9:23-34

Reedy RC (1978) Planetary gamma-ray spectroscopy. Proc Lunar Planet Sci Conf 9:2961-2984

Reedy RC (1998) Studies of modern and ancient solar energetic particles. Proc Indian Acad Sci (Earth Planet Sci) 107: 433-440

Reedy RC (2000) Predicting the production rates of cosmogenic nuclides. Nucl Instr Methods B 172:782-785

Reedy RC, Arnold JR, Lal D (1983) Cosmic-ray record in solar system matter. Science 219:127-135

Reedy RC, Nishiizumi K (1998) Factors affecting the interpretation of solar-proton-produced nuclides and some chlorine-36 results. Lunar Planet Sci XXIX:1698 (CD-ROM)

Reid AM, Meyer C, Harmon RS, Brett R (1970) Metal grains in Apollo 12 igneous rocks. Earth Planet Sci Lett 9:1-5

Rhodes JM, Adams JB, Blanchard DP, Charette MP, Rodgers KV, Jacobs JW, Brannon JC, Haskin LA (1975) Chemistry of agglutinate fractions in lunar soils. Proc Lunar Sci Conf 6:2291-2307

Rhodes JM, Rodgers KV, Shih C, Bansal BM, Nyquist LE, Wiesmann H, Hubbard NJ (1974) The relationships between geology and soil chemistry at the Apollo 17 landing site. Proc Lunar Sci Conf 5:1097- 1117

Robinson MS, Jolliff BL (2002) Apollo 17 landing site: Topography, photometric corrections, and heterogeneity of the surrounding highland massifs. J Geophys Res 107(E11):doi 10.1029/2001JE001614

Ross M, Bence AE, Dwornik EJ, Clark JR, Papike JJ (1970) Mineralogy of lunar clinopyroxenes, augite and pigeonite. Proc Lunar Sci Conf 1:839-848

Ross M, Huebner JS, Dowty E (1973) Delineation of the one atmosphere augite-pigeonite miscibility gap for pyroxenes from lunar basalt 12021. Am Mineral 58:619-635

Roush TL, Lucey PG (1988) A search for water on the moon at the Reiner Gamma formation, a possible site of cometary coma impact. Proc Lunar Planet Sci Conf 18:397-402

Rubin AE (1997) Mineralogy of meteorite groups. Meteorit Planet Sci 32:231-247

Rutherford MJ, Dixon S, Hess P (1980) Ilmenite saturation at high pressure in KREEP basalts: origin of KREEP and high TiO_2 in mare basalts. Lunar Planet Sci XI:966-967

Ryder G (1985) Catalog of Apollo 15 Rocks. Curatorial Publication 20787. NASA Johnson Space Center

Ryder G (1994) Coincidence in time of the Imbrium basin impact and Apollo 15 KREEP volcanic flows: the case for impact-induced melting. Spec Pap Geol Soc Am 293:11-18

Ryder G, Norman MD, Score RA (1980) The distinction of pristine from meteorite-contaminated highland rocks using metal compositions. Proc Lunar Planet Sci Conf 11:471-479

Ryder G, Stoeser DB, Wood JA (1977) Apollo 17 KREEPy basalt: a rock type intermediate between KREEP and mare basalts. Earth Planet Sci Lett 35:1-13

Ryder G, Wood JA (1977) Serenitatis and Imbrium impact melts: implications for large-scale layering in the lunar crust. Proc Lunar Sci Conf 8:655-668

Saari JM, Shorthill RW, Deaton TK (1966) Infrared and visible images of the eclipsed moon of December 19, 1964. Icarus 5:635-659

Salisbury JW, Basu A, Fischer EM (1997) Thermal infrared spectra of lunar soils. Icarus 130:125-139

Salpas PA, Taylor LA, Lindstrom MM (1987) Apollo 17 KREEPy basalts: evidence for the non-uniformity of KREEP. J Geophys Res 92:E340-E348

Sands DG, De Laeter JR, Rosman KJR (2001) Measurements of neutron capture effects on Cd, Sm and Gd in lunar samples with implications for the neutron energy spectrum. Earth Planet Sci Lett 186:335-346

Sato M, Hickling NL, McLane JE (1973) Oxygen fugacity values of Apollo 12, 14, and 15 lunar samples and reduced state of lunar magmas. Proc Lunar Sci Conf 4:1061–1079

Schaal RB, Hörz F (1977) Shock metamorphism of lunar and terrestrial basalts. Proc Lunar Sci Conf 8:1697-1729

Schaber GG, Thompson TW, Zisk SH (1975) Lava flows in Mare Imbrium: An evaluation of anomalously low Earth-based radar reflectivity. The Moon 13:395-423

Schnabel C, Xue S, Ma P, Herzog GF, Fifield K, Cresswell RG, di Tada ML, Hausladen P, Reedy RC (2000) Nickel-59 in surface layers of lunar basalt 74275: implications for the solar alpha particle flux. Lunar Planet Sci XXXI: 1778 (CD-ROM)

Schonfeld E (1974) The contamination of lunar highlands rocks by KREEP: interpretation by mixing models. Proc Lunar Sci Conf 5:1269-1286

Schultz PH (1976a) Moon morphology: interpretations based on Lunar Orbiter photography. University of Texas Press

Schultz PH (1976b) Floor-fracture lunar craters. Moon 15:241-273

Schultz PH, Srnka LJ (1980) Cometary collisions on the Moon and Mercury. Nature 284:22-26

Shervais JW, McGee JJ (1998) Ion and electron microprobe study of troctolites, norite, and anorthosites from Apollo 14: evidence for urKREEP assimilation during petrogenesis of Apollo 14 Mg-suite rocks. Geochim Cosmochim Acta 62:3009-3023

Shervais JW, Taylor LA, Lindstrom MM (1988) Olivine vitrophyres: a nonpristine high-Mg component in lunar breccia 14321. Proc Lunar Planet Sci Conf 18:45-57

Shih C-Y, Nyquist LE, Bogard DD, Wooden JL, Bansal BM, Wiesmann H (1985) Chronology and petrogenesis of a 1.8 g lunar granitic clast: 14321, 1062. Geochim Cosmochim Acta 49:411-426

Shih C-Y, Nyquist LE, Wiesmann H (1993) K-Ca chronology of lunar granites. Geochim Cosmochim Acta 57:4827-4841

Shorthill RW, Saari JM (1965) Nonuniform cooling of the eclipsed Moon: a listing of thirty prominent anomalies. Science 150:210-212

Simon SB, Papike JJ (1985) Petrology of the Apollo 12 highland component. J Geophys Res 90:D47-D60

Simon SB, Papike JJ, Gosselin DC, Laul JC (1985) Petrology and chemistry of Apollo 12 regolith breccias. J Geophys Res 90:D75-D86

Simon SB, Papike JJ, Gosselin DC, Laul JC (1986) Petrology, chemistry, and origin of Apollo 15 regolith breccias. Geochim Cosmochim Acta 50:2675-2691

Simon SB, Papike JJ, Laul JC (1981) The lunar regolith: Comparative studies of the Apollo and Luna sites. Petrology of soils from Apollo 17, Luna 16, 20, and 24. Proc Lunar Planet Sci Conf 12B:371-388

Simon SB, Papike JJ, Shearer CK, Laul JC (1983) Petrology of the Apollo 11 highland component. Proc Lunar Planet Sci Conf 14:B103-B138

Sippel RF (1971) Luminescence petrography of the Apollo 12 rocks and comparative features in terrestrial rocks and meteorites. Proc Lunar Sci Conf 2:247-263

Sisterson JM, Kim K, Beverding A, Englert PAJ, Caffee MW, Vincent J, Castaneda C, Reedy RC (1997) Measuring excitation functions needed to interpret cosmogenic nuclide production in lunar rocks. Eds. *In:* Applications of Accelerators in Research and Industry, 392. Duggan JL, Morgan IL (eds) AIP Conf. Proc., p 811-814

Smith JV (1974) Lunar mineralogy: a heavenly detective story, Presidential Address, Part I. Am Mineral 59:231-243

Smith JV, Steele IM (1976) Lunar Mineralogy, a heavenly detective story. Am Mineral 61:1059-1116

Smith SM, Wilson JK, Baumgardner J, Mendillo M (1999) Discovery of the distant sodium tail and its enhancement following the Leonid meteor shower. Geophys Res Lett 26:1649-1652

Smith SM, Wilson JK, Baumgardner J, Mendillo M (2001) Monitoring the Moon's transient atmosphere with an all-sky imager. Adv Space Res 27:1181-1187

Smrekar S, Pieters CM (1985) Near-Infrared spectroscopy of probable impact melt from 3 large lunar highland craters. Icarus 63:442-452

Snyder GA, Taylor LA, Jerde EA (1994) Evolved QMD-melt parentage for lunar highlands alkali suite cumulates: Evidence from ion-probe rare-earth element analyses of individual minerals. Lunar Planet Sci XXV:1311-1312

Snyder GA, Taylor LA, Liu Y-G, Schmitt RA (1992) Petrogenesis of the western highlands of the Moon: Evidence from a diverse group of whitlockite-rich rocks from the Fra Mauro Formation. Proc Lunar Planet Sci Conf 22: 399-416

Sonett CP, Giampapa MS, Mathews MS (1991) The Sun in Time, 990 p, Univ. Arizona Press, Tucson

Spettel B, Dreibus G, Burghele A, Jochum KP, Schultz L, Weber HW, Wlotzka F, Wänke H (1995) Chemistry, petrology, and noble gases of lunar highland meteorite Queen Alexandra Range 93069. Meteorit Planet Sci 30:581-582

Sprague AL, Kozlowski WH, Hunten DM, Wells WK, Grosse FA (1992b) The sodium and potassium atmosphere of the Moon and its interaction with the surface. Icarus 96:27-42

Sprague AL, Kozlowski WH, Hunten DM, Wells WK, Grosse FA (1998) Observations of sodium in the lunar atmosphere during International Lunar Atmosphere Week, 1995. Icarus 131:372-381

Sprague AL, Witteborn FC, Kozlowski RW, Cruikshank DP, Bartholomew MJ, Graps AL (1992a) The Moon – mid-infrared (7.5-Mu-M to 11.4-Mu-M) spectroscopy of selected regions. Icarus 100(1):73-84

Spudis P, Pieters C (1991) Global and regional data about the Moon. *In:* Lunar Sourcebook: A Users Guide to the Moon. Heiken GH, Vaniman DT, French BM (eds) Cambridge University Press, p 595-632

Spudis PD, Davis PA (1986) A chemical and petrological model of the lunar crust and implications for lunar crustal origin. Proc Lunar Planet Sci Conf 17. J Geophys Res 91:E84-E90

Spudis PD, Hawke BR (1986) The Apennine Bench formation revisited. *In*: Workshop on the Geology and Petrology of the Apollo 15 Landing Site. LPI Tech. Report 86-03. Spudis PD, Ryder G (eds) Lunar and Planetary Institute, p 105-107

Spudis PD, Hawke BR, Lucey P (1984) Composition of Orientale basin deposits and implications for the lunar basin-forming process. J Geophys Res 89:C197-C210

Spudis PD, Ryder G (1981) Apollo 17 impact melts and their relation to the Serenitatis basin. Multi-Ring Basins. Proc Lunar Planet Sci Conf 12A:133-148

Spudis PD, Ryder G (1985) Geology and petrology of the Apollo 15 landing site - Past, present, and future understanding. EOS, Trans Am Geophys Union 66:721,724-726

Stacy NJS, Campbell DB, Ford PG (1997) Radar mapping of the lunar poles: A search for ice deposits. Science 276: 1527

Staid MI, Pieters CM (2000) Integrated spectral analysis of mare soils and craters: application to eastern nearside basalts. Icarus 145:122-139

Staid MI, Pieters CM (2001) Mineralogy of the last lunar basalts: results from Clementine. J Geophys Res 106:27,887-27,900

Starukhina LV, Shkuratov YG (2000) The lunar poles: water ice or chemically trapped hydrogen? Icarus 147:585-587

Stern SA (1999) The lunar atmosphere: history status current problems and context. Rev Geophys 37:453-491

Stewart DB (1975) Apollonian metamorphic rocks - the products of prolonged subsolidus equilibration. Lunar Sci Conf 6:774-776

Stöffler D, Bischoff A, Borchardt R, Burghele A, Deutsch A, Jessberger EK, Ostertag R, Palme H, Spettel B, Reimold WU, Wacker K, Wänke H (1985) Composition and evolution of the lunar crust in the Descartes Highlands, Apollo 16. Proc Lunar Planet Sci Conf 15. J Geophys Res 90:C449-C506

Stöffler D, Knoll H-D, Marvin UB, Simonds CH, Warren PH (1980) Recommended classification and nomenclature of lunar highland rock—A committee report. *In:* Proceedings of the Conference on the Lunar Highland Crust. Papike JJ, Merrill RB (eds) Pergamon Press, p 51-70

Stöffler D, Ostertag R, Reimold WU, Borchardt R, Malley J, Rehfeldt A (1981) Distribution and provenance of lunar highland rock types at North Ray Crater Apollo 16. Proc Lunar Planet Sci Conf 12:185-207

Sunshine JM, Pieters CM (1993) Estimating modal abundances from the spectra of natural and laboratory pyroxene mixtures using the modified gaussian model. J Geophys Res 98:9075-9087

Sunshine JM, Pieters CM (1998) Determining the composition of olivine from reflectance spectroscopy. J Geophys Res 103:13675-13688

Takeda H, Miyamoto M, Ishii T, Lofgren GE (1975) Relative cooling rates of mare basalts at the Apollo 12 and 15 sites as estimated from pyroxene exsolution data. Proc Lunar Sci Conf 6:987-996

Taylor GJ, Warner RD, Keil K, Ma M-S, Schmitt RA (1980) Silicate liquid immiscibility, evolved lunar rocks and the formation of KREEP. *In:* Proceedings of the Conference on the Lunar Highland Crust. Papike JJ, Merrill RB (eds) Pergamon Press, p 339-352

Taylor GJ, Warren P, Ryder G, Delano J, Pieters C, G. L (1991) Lunar Rocks. *In:* Lunar Sourcebook: A Users Guide to the Moon. Heiken GH, Vaniman DT, French BM (eds) Cambridge University Press, p 183-284

Taylor GJ, Wentworth S, Warner RD, Keil K (1978) Agglutinates as recorders of fossil soil compositions. Proc Lunar Planet Sci Conf 9:1959-1967

Taylor LA (1988) Generation of native Fe in lunar soil. Proceedings of the Space ‘88 Conference. American Society of Civil Engineers, Albuquerque, NM, p 67-77

Taylor LA, Chambers JG, Patchen A, Jerde EA, McKay DS, Graf J, Order RR (1993) Evaluation of lunar rocks and soils for resource utilization: detailed image analysis of raw material and beneficiated products. Lunar Planet Sci XXIV:1409-1410

Taylor LA, Kullerud G, Bryan WB (1971) Opaque mineralogy and textural features of Apollo 12 samples and a comparison with Apollo 11 rocks. Proc Lunar Sci Conf 2:855-871

Taylor LA, McCallister RH (1972) Experimental investigation of significance of zirconium partitioning in lunar ilmenite and ulvöspinel. Earth Planet Sci Lett 17:105-111

Taylor LA, McCallister RH, Sardi O (1973) Cooling histories of lunar rocks based on opaque mineral geothermometers. Proc Lunar Sci Conf 4:819-828

Taylor LA, Meek TT (2005) Microwave sintering of lunar soil: properties, theory, and practice. J Aerospace Engr 18: 188-196

Taylor LA, Morris RV, Keller LP, Pieters CM, Patchen A, Taylor DH, Wentworth SJ, McKay DS (2000) Major contributions to spectral reflectance opacity by non-agglutinitic, surface-correlated nanophase iron. Lunar Planet Sci XXXI:1842 (CD-ROM)

Taylor LA, Onorato PIK, Uhlmann DR, Coish RA (1978) Subophitic basalts from Mare Crisium: cooling rates. *In:* Mare Crisium: The View from Luna 24. Merrill RB, Papike JJ (eds) Pergamon Press, p 473-482

Taylor LA, Patchen A, Morris RV, Taylor D, Pieters CM, Keller LP, McKay DS, Wentworth S (1999) Chemical and mineralogical characterization of the 44-20, 20-10, and <10 micron fractions of lunar mare soils. Lunar Planet Sci XXX:1885 (CD-ROM)

Taylor LA, Patchen A, Taylor DS, Chambers JG, McKay DS (1996) X-ray digital imaging petrography of lunar soils: Modal analyses of minerals and glasses. Icarus 124:500-512

Taylor LA, Pieters C, Keller LP, Morris RV, McKay DS, Patchen A, Wentworth S (2001a) The effects of space weathering on Apollo 17 mare soils: petrographic and chemical characterization. Meteorit Planet Sci 36:285-299

Taylor LA, Pieters CM, Morris RV, Keller LP, McKay DS (2001b) Lunar mare soils: Space weathering and the major effects of surface-correlated nanophase Fe. J Geophys Res 106:27,985-28,000

Taylor LA, Pieters CM, Patchen A, Taylor D, Wentworth S, McKay D (1998) Optical properties and abundances of minerals and classes in the 10 to 44 size fraction of mare soils: Lunar Planet Sci XXIX:1160 (CD-ROM)

Taylor LA, Pieters CM, Patchen A, Taylor DH, Morris RV, Keller LP, McKay DS (2003) Mineralogical characterization of lunar highland soils. Lunar Planet Sci 34:1774 (CD-ROM)

Taylor LA, Shervais JW, Hunter RH, Laul JC (1983) Ancient (4.2 AE) highlands volcanism: the gabbronorite connection? Lunar Planet Sci 14:777-778

Taylor LA, Taylor DH (2000) Considerations for return to the Moon and lunar base site selection Workshops. J Aerospace Engineering 10:68-79

Taylor LA, Uhlmann DR, Hopper RW, Misra KC (1975) Absolute cooling rates of lunar rocks: theory and application. Proc Lunar Sci Conf 6:181-191

Taylor SR (1975) Lunar Science: A Post-Apollo View; Scientific Results and Insights from the Lunar Samples. Pergamon Press

Taylor SR (1982) Planetary Science: A Lunar Perspective. Lunar and Planetary Institute

Thalmann C, Eugster O, Herzog GF, Klein J, Krähenbühl U, Vogt S, Xue S (1996) History of lunar meteorites Queen Alexandra Range 93069, Asuka 881757, and Yamato 793169 based on noble gas isotopic abundances, radionuclide concentrations, and chemical composition. Meteorit Planet Sci 31:857-868

Thompson TW (1978) High resolution lunar radar map at 7.5 m wavelength. Icarus 36:174-188

Thompson TW (1987) High resolution lunar radar map at 70-cm wavelength. Earth Moon Planets 37:59-70

Thompson TW, Roberts WJ, Hartmann WK, Shorthill RW, Zisk SH (1979) Blocky craters: Implications about the lunar megaregolith. Moon and Planets 21:319-342

Toksöz MN, Dainty AM, Solomon SC, Anderson KR (1974) Structure of the Moon. Rev Geophys 12:539-567

Tompkins S, Pieters CM (1999) Mineralogy of the lunar crust: Results from Clementine. Meteorit Planet Sci 34:25-41

Tsay F-D, Chan SI, Manatt SL (1971a) Magnetic resonance studies of Apollo 11 and Apollo 12 samples. Proc Lunar Sci Conf 2:2515-2528

Tsay F-D, Chan SI, Manatt SL (1971b) Ferromagnetic resonance of lunar samples. Geochim Cosmochim Acta 35: 865-875

Tuniz C, Bird JR, Fink D, Herzog GF (1998) Accelerator Mass Spectrometry. CRC Press, Boca Raton, Florida

Tyler AL, Kozlowski RWH, Hunten DM (1988) Observations of sodium in the tenuous lunar atmosphere. Geophys Res Lett 15:1141-1144

Uhlmann DR, Onorato PIK, Yinnon H, Taylor LA (1979) Partitioning as a cooling rate indicator. Lunar Planet Sci X: 1253-1255

Usselman TM, Lofgren GE (1976) The phase relations, textures, and mineral chemistries of high titanium mare basalts as a function of oxygen fugacity and cooling rate. Proc Lunar Sci Conf 7:1345-1363

Usselman TM, Lofgren GE, Donaldson CH, Williams RJ (1975) Experimentally reproduced textures and mineral chemistries of high-titanium mare basalts. Proc Lunar Sci Conf 6:997-1020

Vaniman D, Heiken G, Mendell W, Olhoeft G, Reedy R (1991) The lunar environment. *In:* Lunar Sourcebook: A Users Guide to the Moon. Heiken GH, Vaniman DT, French BM (eds) Cambridge University Press, p 27-60

Vaniman DT, Bish DL (1990) Yoshiokaite, a new Ca,Al-silicate mineral from the Moon. Am Mineral 75:676-686

Vaniman DT, Papike JJ (1977) Very low Ti (VLT) basalts; a new mare rock type from the Apollo 17 drill core. Proc Lunar Sci Conf 8:1443-1471

Vaniman DT, Papike JJ (1980) Lunar highland melt rocks: Chemistry, petrology, and silicate mineralogy. *In:* Proceedings of the Conference on the Lunar Highland Crust. Papike JJ, Merrill RB (eds) Pergamon Press, p 271-337

Vasavada AR, Paige DA, Wood SE (1999) Near-surface temperatures on Mercury and the Moon and the stability of polar ice deposits. Icarus 141:179-193

Verani SC, Barbieri C, Benn CR, Cremonese G, Mendillo M (2001) The 1999 Quadrantids and the lunar Na atmosphere. Mon Not R Astron Soc 327:244-248

Verani SC, Benn C, Cremonese G (1998) Meteor stream effects on the lunar sodium atmosphere. Planet Space Sci 46: 1003-1006

Via WN, Taylor LA (1976) Chemical aspects of agglutinate formation; relationships between agglutinate composition and the composition of the bulk soil. Proc Lunar Sci Conf 7:393-403

Vilas F, Domingue DL, Jensen EA, McFadden LA, Coombs R, Mendell W (1999) Aqueous alteration on the Moon. Lunar Planet Sci XXX:1343

Vogt S, Herzog GF, Reedy RC (1990) Cosmogenic nuclides in extraterrestrial materials. Rev Geophys 28:253-275

Walker RJ, Papike JJ (1981) The relationship of the lunar regolith, <10 µm fraction and agglutinates; Part II, Chemical composition of agglutinate glass as a test of the "fusion of the finest fraction" (F (super 3)) model. Proc Lunar Planet Sci Conf 12:421-432

Warner JL, Phinney WC, Bickel CE, Simonds CH (1977) Feldspathic granulitic impactites and pre-final bombardment lunar evolution. Proc Lunar Sci Conf 8:2051-2066

Warren PH (1985) The magma ocean concept and lunar evolution. Ann Rev Earth Planet Sci 13:201-240

Warren PH (1988) The origin of pristine KREEP: effects of mixing between urKREEP and the magmas parental to the Mg-rich cumulates. Proc Lunar Planet Sci Conf 18:233-241

Warren PH (1990) Lunar anorthosites and the magma-ocean plagioclase-flotation hypothesis: importance of FeO enrichment in the parent magma. Am Mineral 75:46-58

Warren PH (1993) A concise compilation of petrologic information on possibly pristine nonmare Moon rocks. Am Mineral 78:360-376

Warren PH (1994) Lunar and martian meteorite delivery services. Icarus 111:338-363

Warren PH (2001a) Porosities of lunar meteorites: strength, porosity, and petrologic screening during the meteorite delivery process. J Geophys Res 106:10101-10111

Warren PH (2001b) Early lunar crustal genesis: the ferroan anorthosite epsilon-neodymium paradox. Meteorit Planet Sci 36:A 219

Warren PH (2005) "New" lunar meteorites: implications for composition of the global lunar surface, lunar crust, and the bulk Moon. Meteorit Planet Sci 40:477-506

Warren PH, Jerde EA, Kallemeyn GW (1987) Pristine Moon rocks: A "large" felsite and a metal-rich ferroan anorthosite. Proc Lunar Planet Sci Conf 17. J Geophys Res 92:E303-E313

Warren PH, Taylor GJ, Keil K, Marshall C, Wasson JT (1981) Foraging westward for pristine nonmare rocks; complications for petrogenetic models. Proc Lunar Planet Sci Conf 12:21-40

Warren PH, Taylor GJ, Keil K, Shirley DN, Wasson JT (1983) Petrology and chemistry of two "large" granite clasts from the Moon. Earth Planet Sci Lett 64:175-185

Warren PH, Wasson JT (1977) Pristine nonmare rocks and the nature of the lunar crust. Proc Lunar Sci Conf 8:2215-2235

Warren PH, Wasson JT (1978) Compositional-petrographic investigation of pristine nonmare rocks. Proc Lunar Planet Sci Conf 9:185-217

Warren PH, Wasson JT (1979a) The origin of KREEP. Rev Geophys 17:73-88

Warren PH, Wasson JT (1979b) The compositional-petrographic search for pristine nonmare rocks: Third foray. Proc Lunar Sci Conf 10:583-610

Warren PH, Wasson JT (1980) Further foraging for pristine nonmare rocks: Correlations between geochemistry and longitude. Proc Lunar Planet Sci Conf 11:431-470

Wasson JT, Boynton WV, Chou C-L, Baedecker PA (1975) Compositional evidence regarding the influx of interplanetary materials onto the lunar surface. Moon 13:121-141

Watson K, Murray BC, Brown H (1961) The behavior of volatiles on the lunar surface. J Geophys Res 66:3033

Weitz CM, Head JW, Pieters CM (1998) Lunar regional dark mantle deposits: geologic, multispectral, and modeling studies. J Geophys Res 103:22725-22759

Wentworth SJ, Keller LP, McKay DS, Morris RV (1999) Space weathering on the Moon: patina on Apollo 17 samples 75075 and 76015. Meteorit Planet Sci 34:593-603

Wentworth SJ, McKay DS, Lindstrom DJ, Basu A, Martinez RR, Bogard DD, Garrison DH (1994) Apollo 12 ropy glasses revisited. Meteorit Planet Sci 29:323-333

Whitaker EA (1972) Lunar color boundaries and their relationship to topographic features. The Moon 4:348-355

Wieczorek MA, Phillips RJ (2000) The Procellarum KREEP terrane: implications for mare volcanism and lunar evolution. J Geophys Res 105:20,417-20,430

Wieler R (1998) The solar noble gas record in lunar samples and meteorites. Space Sci Rev 85:303-314

Wieler R, Baur H (1995) Fractionation of Xe, Kr, and Ar in the solar corpuscular radiation deduced by closed system etching of lunar soils. Astrophys J 453:987-997

Wilcox BB, Lucey PG, T. CJ (2005) Space weathering and thermal properties of fresh craters on the Moon. Lunar Planet Sci XXXVI:2293 (CD-ROM)

Wilhelms DE (1987) The geologic history of the Moon. US Geol. Surv. Prof. Paper 1348

Wilhelms DE, McCauley JF (1971) Geologic map of the near side of the moon. Miscellaneous geologic investigations; USGS Map I-703, p. 1 map. U.S. Geological Survey, Washington, D.C.

Williams KL, Taylor LA (1974) Optical properties and chemical compositions of Apollo 17 armalcolites. Geology 2: 5-8

Wilson JK, Smith SM, Baumgardner J, Mendillo M (1999) Modeling an enhancement of the extended lunar atmosphere during the Leonid meteor shower of 1998. Geophys Res Lett 26:1645-1648

Wlotzka F, Spettel B, Wänke H (1973) On the composition of metal from Apollo 16 fines and the meteoritic component. Proc Lunar Sci Conf 4:1483-1491

Wood RW (1912) Selective absorption of light on the Moon's surface and lunar petrography. Astrophys J 36:75

Yakshinskiy BV, Madey TE (2000a) Desorption induced by electronic transitions of Na from SiO_2: relevance to planetary exospheres. Surf Sci 451:160–165

Yakshinskiy BV, Madey TE, Ageev VN (2000b) Thermal desorption of sodium atoms from thin SiO_2 films. Surf Rev Lett 7:75-87

Yin L, Trombka JI, Adler I, Bielefeld M (1993) X-ray remote sensing techniques for geochemical analysis of planetary surfaces. *In:* Remote Geochemical Analysis: Elemental and Mineralogical Composition. Pieters CM, Englert PAJ (eds) Cambridge Univ. Press, p 199-212

Zisk SH, Hodges CA, Moore HJ, Shorthill RW, Thompson TW, Whitaker EA, Wilhelms DE (1977) The Aristarchus-Harbinger region of the Moon: Surface geology and history from recent remote sensing observations. The Moon 17:59-99

Zisk SH, Pettengill GH, Catuna GW (1974) High-resolution radar maps of the lunar surface at 3.8-cm wavelength. The Moon 10:17-50Campbell HW, Hess PC, Rutherford MJ (1978) Ilmenite crystallization in non-mare basalts. Lunar Planet Sci IX:149-151